Clinical translation of hyperpolarized magnetic resonance for cardiovascular and metabolic diseases

Submitted for the degree of Doctor of Philosophy in Cardiovascular Medicine

Kellogg College, Trinity 2016, University of Oxford

Andrew JM Lewis MRCP

Acknowledgements

The work presented in this thesis would not have been possible without the expertise and support of a truly outstanding group of colleagues in Oxford and beyond. In particular, I thank my supervisors Damian Tyler, Oliver Rider, and Stefan Neubauer for their tireless patience, good humour, and inspirational vision throughout this project.

One of the most rewarding aspects of conducting research in biomedical imaging has been the almost unparalleled opportunity to work with researchers from across the scientific disciplines. When faced with seemingly insurmountable problems, I have greatly valued the insight, tenacity, and frequently brilliance, of Jack Miller, Angus Lau, Mike Dodd, Lucia Giles, Jane Francis, Vicky Ball, and Carolyn Carr among many others. Their expertise and perspectives are a continued source of inspiration.

Above all, I thank Emily, to whom this thesis is dedicated, and my parents for love and unwavering encouragement throughout.

Andrew Lewis
September 2016

Abstract

Cardiovascular diseases continue to pose an unacceptable societal burden, mandating the development of new and improved methods for their diagnosis, monitoring and treatment. Current cardiovascular magnetic resonance imaging techniques provide exquisite structural and functional information, but their ability to assess the molecular processes underlying cardiac function in health and disease is limited by inherent insensitivity. Hyperpolarized magnetic resonance is a new technology which overcomes this limitation, creating molecular contrast agents with an improvement in magnetic resonance signal of up to five orders of magnitude. One key molecule, hyperpolarized [1-^{13}C]pyruvate, shows particular promise for the assessment of cardiac energy metabolism and other fundamental biological processes with clinical relevance.

This thesis describes a programme of translational research in hyperpolarized magnetic resonance conducted with the aims of identifying priority disease states for translational hyperpolarized MR studies, and of enabling first human cardiovascular studies using the technique. We identify important and new potential roles for hyperpolarized magnetic resonance in both the diagnosis, and potentially treatment, of heart disease associated with metabolic diseases and also in ischaemic heart disease.

Hyperpolarized [1-^{13}C]pyruvate also has high potential for rapid clinical translation from the laboratory to patients with cardiovascular disease, though the production and administration of clinical-grade hyperpolarized molecules poses significant challenges. We present strategies to overcome these challenges, and describe the first human cardiovascular experience with hyperpolarized magnetic resonance.

Contents

Chapter 1: Hyperpolarized magnetic resonance and cardiovascular disease 1
1.1 Abstract 1
1.2 The societal burden of cardiovascular disease 2
1.3 Strengths and limitations of CMR in cardiovascular disease 3
1.4 Current CMR techniques are limited by inherent insensitivity 5
1.4.1 Low sample polarization at clinical field strengths and temperatures 7
1.4.2 Sample polarization is a fundamental determinant of NMR sensitivity 8
1.4.3 Strategies to overcome low signal to noise ratio in CMR 13
1.5 Hyperpolarized magnetic resonance as a novel approach to increasing SNR 16
1.5.1 Brute force polarization 16
1.5.2 Parahydrogen induced polarization (PHIP) 16
1.5.3 Optical pumping 17
1.5.4 Dynamic nuclear polarization 17
1.6 Development of biological applications of DNP 22
1.6.1 Dissolution DNP for hyperpolarized liquid state NMR 22
1.6.2 Hyperpolarized ^{13}C MR as a probe of metabolism 26
1.6.3 Acquisition strategies for hyperpolarized ^{13}C experiments 33
1.6.4 Analysis of data from hyperpolarized ^{13}C experiments 35
1.6.5 Hyperpolarized [1-^{13}C]pyruvate as a probe of cardiac energy metabolism 36
1.7 Clinical translational issues for cardiovascular DNP 41
1.7.1 Pyruvate as a molecule for human administration 42
1.7.2 Hyperpolarization hardware suitable for sterile use intent 43
1.7.3 The SPINlab™ sterile fluid path 44
1.7.4 Sample polarization and dissolution 45
1.7.5 Quality control 46
1.8 Aims of this programme of work 47
1.9 Appendix 1A: References 49

Chapter 2: Clinical translation of hyperpolarized MR for type II diabetes 59
2.1 Abstract 59
2.2 Design of a first-in-human cardiovascular hyperpolarized [1-^{13}C]pyruvate study 60

2.3 Rationale for selection of type II diabetes as a study disease state 60
2.4 Preclinical work to address potentially confounding factors 62
2.4.1 The effects of diurnal variation and dietary intake 62
2.4.2 Effect of metformin upon heart and liver pyruvate metabolism 67
2.4.3 Metformin does not change whole cell [NAD^+]:[NADH] ratio 74
2.4.4 Metformin induced changes in lactate production reflect an increase in the cytosolic, but not mitochondrial redox state. 75
2.4.5 Discussion of findings 76
2.5 Towards clinical studies using hyperpolarized [1-^{13}C]pyruvate 79
2.5.1 Design of the clinical study 80
2.5.2 Regulatory considerations for human hyperpolarized MR studies 82
2.5.3 Installation of the SPINlab™ hyperpolarizer 84
2.5.4 Installation of the quality control (QC) accessory 86
2.5.5 Administration of hyperpolarized pyruvate 91
2.5.6 Selection of receiver coil and acquisition strategy 94
2.6 First human experiment 95
2.7 Limitations and future work 98
2.8 Conclusions: challenges and opportunities in clinical DNP 99
2.9 Appendix 2A: Methods for preclinical studies 101
2.9.1 Model 101
2.9.2 Hyperpolarized magnetic resonance spectroscopy 101
2.9.3 Metformin administration 102
2.9.4 Preclinical echocardiography 102
2.9.5 Tissue analysis 102
2.9.6 Statistical analysis 103
2.10 Appendix 2B: Methods for clinical study 104
2.10.1 Personal contribution 104
2.10.2 Clinical echocardiography 104
2.10.3 CMR methods 104
2.11 Appendix 2C: References 106

Chapter 3: Mechanistic and energetic insights into obesity cardiomyopathy 111

3.1 Abstract 111
3.2 Background 112
3.2.1 Obesity related heart disease 112
3.2.2 Cardiac energy metabolism in obesity cardiomyopathy 113
3.3 Hypotheses 117
3.4 Methods development and results 119
3.4.1 Selection of a clinically relevant model to study obesity cardiomyopathy 119
3.4.2 Overview of experimental design 120

3.4.3 Characterisation of model 120
3.4.4 Obesity compromised cardiac high energy phosphate metabolism 124
3.4.5 Selection of pharmacological intervention to increase PDH flux 126
3.4.6 Liraglutide and calorie restriction restored myocardial carbohydrate metabolism, normalising energetics and diastolic function 130
3.5 Discussion 134
3.5.1 Cardiac metabolism as a therapeutic target in obesity cardiomyopathy 134
3.5.2 Clinical translational approaches 137
3.5.3 Limitations and future work 138
3.6 Conclusions 139
3.7 Appendix 3A: Methods 140
3.7.1 Model 140
3.7.2 Echocardiography 140
3.7.3 Hyperpolarized [1-^{13}C] and [2-^{13}C]pyruvate magnetic resonance spectroscopy 141
3.7.4 Cardiac perfusion 141
3.7.5 ^{31}P spectroscopy 142
3.7.6 Western blotting 142
3.7.7 High performance liquid chromatography 143
3.8 Appendix 3B: References 144

Chapter 4: Hyperpolarized MRI of cardiac inflammation and repair 151

4.1 Abstract 151
4.2 Background 152
4.2.1 Myocardial infarction 152
4.2.2 Inflammation following myocardial infarction 152
4.2.3 Imaging cardiac inflammation 155
4.3 Hypotheses 157
4.4 Methods development and results 158
4.4.1 Development of a model of myocardial infarction 158
4.4.2 Development of flow cytometric approach 160
4.4.3 MI causes high hyperpolarized [1-^{13}C]lactate signal at both day 3 and 7, reflecting macrophage driven inflammation 168
4.4.4 Development of hyperpolarized MR in cell suspensions 172
4.4.5 RAW264.7 activation increases hyperpolarized [1-^{13}C]lactate label flux 174
4.4.6 Glycolysis is essential for macrophage proinflammatory cytokine production 175
4.4.7 Hyperpolarized [1-^{13}C]lactate signal as a potential therapeutic target 189
4.5 Discussion 191
4.5.1 Mechanisms of macrophage activation in MI 192
4.5.2 Clinical translational challenges and opportunities of inflammation imaging 193
4.5.3 Technical developments in hyperpolarized MRI of inflammation 195
4.5.4 Clinical applications of hyperpolarized MR inflammation imaging 197

4.5.5 Limitations 197
4.5.6 Conclusions 198
4.6 Appendix 4A: Methods 199
4.6.1 Myocardial infarction 199
4.6.2 Macrophage depletion 199
4.6.3 Hyperpolarized MR imaging 199
4.6.4 Flow cytometry 200
4.6.5 Cell culture 201
4.6.6 Hyperpolarized MR in cell suspensions 202
4.6.7 qPCR 202
4.6.8 Enzyme linked immunosorbent assay (ELISA) 203
4.7 Appendix 4B: References 204
Chapter 5: Future perspectives 211
5.1 Hyperpolarized cardiovascular MR: the next decade 211
5.1.1 Hyperpolarized [1-^{13}C]pyruvate as a clinical tool 211
5.1.2 New molecules in hyperpolarized magnetic resonance 213
5.1.3 Conclusions 215

Chapter 1: Hyperpolarized magnetic resonance and cardiovascular disease

1.1 Abstract

The identification of improved methods to diagnose and monitor cardiovascular diseases in humans is a key component of strategies to deliver better outcomes for patients with cardiovascular disease. Current cardiovascular magnetic resonance (CMR) imaging techniques provide exquisite structural and functional information about the heart, but their ability to assess the molecular processes underlying cardiac function are limited by inherent insensitivity. Hyperpolarized magnetic resonance refers to a range of techniques in which this insensitivity can be overcome by altering the magnetic properties of contrast agents, leading to an improvement in MR signal of up to five orders of magnitude. In proof-of-concept studies, hyperpolarized magnetic resonance using the dynamic nuclear polarization method provided unprecedented insight into a range of cardiac cellular processes *in vivo* in model systems, providing a rationale for early translation to clinical applications. However, the properties of hyperpolarized magnetic resonance pose many unique translational challenges which must be overcome prior to human studies.

1.2 The societal burden of cardiovascular disease

Cardiovascular disease, an umbrella term for diseases involving the heart and circulatory system, is a major cause of death in the United Kingdom (UK) and worldwide. Cardiovascular disease is the leading cause of death in women and of premature death in men in the UK, whilst coronary artery disease remains the largest single cause of death[1]. Overall, 155,000 deaths are attributed to cardiovascular diseases every year in the UK, an average death rate of one every three minutes.

Many forms of cardiovascular disease also cause debilitating symptoms and limit the quality of the lives of people affected. More than 700,000 people in the UK live with heart failure, which can cause breathlessness, limitation of exercise tolerance and oedema. These symptoms lead to diminished quality of life in many affected patients, and current therapies for heart failure are only partially effective for the relief of symptoms and extension of life.

The economic impact of cardiovascular disease is also substantial, accounting for direct healthcare costs of £11 billion per year, and almost £15 billion when accounting for the indirect costs associated with premature deaths. Estimates of the worldwide costs of cardiovascular disease suggest a global burden of US$860 billion[2] and are projected to increase dramatically by 2030[3].

Cardiovascular diseases thus pose an unacceptable societal burden, and the identification and development of new and better strategies for their diagnosis and treatment is an urgent healthcare priority.

1.3 Strengths and limitations of CMR in cardiovascular disease

Accurate diagnosis is fundamental to the effective treatment of cardiovascular disease and cardiovascular medicine currently employs a broad armamentarium of diagnostic imaging modalities. The most widely used approaches to image the heart and vascular system clinically include ultrasound, X-ray computed tomography (CT), single photon emission computed tomography (SPECT), invasive angiography, and cardiovascular magnetic resonance imaging (CMR), all of which have strengths and weaknesses[4]. Emerging imaging technologies include positron emission tomography (PET), optical coherence tomography and vascular ultrasound and are used in specialist centres.

The use of CMR for clinical diagnosis and research has expanded rapidly in Europe[5] and worldwide due to strengths that include the ability to image in unlimited planes, to quantify flow, to characterise myocardial tissue and to define cardiac function with a greater degree of precision than is possible with other modalities[6-8]. In research settings, the precision and flexibility of CMR has provided new insights into the understanding of many cardiovascular diseases by enabling 'deep phenotyping' of the hearts of humans with clearly defined diagnoses[9-11]. The high accuracy and precision of CMR derived estimates of cardiac dimensions and function substantially reduces the numbers of participants needed to achieve statistical power when these indices are selected as endpoints in pharmaceutical and other interventional trials[12]. Importantly, CMR has the potential to extend beyond imaging of the macroscopic structure of the heart and vascular systems to the non-invasive assessment of the molecular processes underpinning cardiac function by assessing the non-proton nuclei involved in these processes[13].

Despite these strengths, CMR has been less successful in gaining clinical traction in the United States and its wider uptake and application worldwide are limited by relatively long scan times and high installation and running costs[14]. These financial costs of CMR are due in large part to the need to maintain superconducting magnets at high static fields and to employ expert scanner operators. Although the benefits of CMR have been recognised by recommendations in international guidelines in some scenarios[15, 16], a 'killer application' leading to unequivocal clinical benefit over other modalities is arguably lacking. Furthermore, research insights into heart disease have often had the greatest success in the macroscopic characterisation of structure, function and fibrosis using proton based imaging. The only non-proton based spectroscopic technique to have significant cardiovascular research impact in human participants is ^{31}P magnetic resonance spectroscopy (MRS) for the assessment of cardiac energetics, which has shown prognostic significance in heart failure[17] and provided insight into mechanisms of energy delivery in failing hearts[18, 19]. However, this technique is technically challenging and is not used routinely outside of research settings in specialist centres and there remains no routine clinical indication for ^{31}P MRS[20].

Non-proton MR studies following the administration of carbon-13 (^{13}C) labelled substrates have been used in preclinical laboratories since the 1980s to study the processes of cardiac energy metabolism that underlie, and are inextricably linked to, mechanical function[21, 22]. These experiments have generally been conducted in isolated perfused hearts by measuring the pattern of ^{13}C label incorporation into the glutamate pool following the administration of labelled tracers including [^{13}C]acetate, [^{13}C]pyruvate and [^{13}C]acetyl CoA[23]. In addition to contributing to the elucidation of mechanisms of normal cardiac metabolism, this method has also provided insight into cardiac metabolism in disease states such as diabetes[24] and ischaemia[25]. However,

perfused heart preparations require fixed substrate and haemodynamic loading conditions, which may not fully recapitulate *in vivo* disease phenotypes[26], and long acquisitions times generally restrict these experiments to the metabolic steady state. There remains, therefore, significant potential to develop non-proton based CMR technologies, and ^{13}C MR in particular, with the intention of gaining novel and important insights into mechanisms of cardiovascular diseases.

1.4 Current CMR techniques are limited by inherent insensitivity

Many of the current limitations and costs of CMR and MRS reflect the fact that nuclear magnetic resonance (NMR) based techniques are inherently insensitive and have a low ratio of signal to background noise (SNR).

First demonstrated in the context of condensed physics matter independently and near-simultaneously by Bloch[27] and Purcell[28] in 1946, NMR is a versatile technique for the assessment of certain atomic nuclei which have a particular form of angular momentum called spin. The net nuclear spin quantum number, I, is determined by the subatomic composition of the nucleus such that if there are an even number of both protons and neutrons then the nucleus has no spin, if there are an odd number of both neutrons and protons, the nucleus has integer spin and if the sum of the number of neutrons and protons is odd, then the nucleus has half integer spin. This value determines whether the nucleus is suitable for study with NMR based techniques, as only nuclei with non-zero spin are amenable to study using NMR based techniques (Table 1.1).

Nucleus	Protons	Neutrons	Spin quantum number (*I*)
^{1}H	1	0	1/2
^{2}H	1	1	1
^{12}C	6	6	0
^{13}C	6	7	1/2
^{23}Na	11	12	3/2
^{31}P	15	16	1/2

Table 1.1: Composition of key nuclei and resultant spin quantum number. Only non-zero spin nuclei can be assessed using NMR based techniques.

Nuclei with non-zero spin have both charge and angular momentum, giving rise to a small magnetic field which is termed a magnetic moment. When non-zero spin nuclei exist in a group, the magnetic moment of a nucleus can interact with those of nearby nuclei, a phenomenon termed magnetism. Assuming that these nuclear magnetic moment interactions are weak, they can also interact with a strong external magnetic field in an interaction dependent upon the energy magnitude of the magnetic moment, μ, and the flux density of the external field, B.

The possible values of μ are constrained by the laws of quantum physics, including the discrete solutions of Schrodinger's wave equation. In brief, the number of energy eigenstates a spin can occupy is determined according to the spin quantum number, I:

$$N_{possible\ energy\ states} = 2I + 1 \qquad 1.1$$

Thus, for spin 1/2 nuclei in a strong external field, μ has two potential values reflecting either a low or high energy eigenstate (analogous to the 'spin up' and 'spin down' positions in classical mechanics, Figure 1.1).

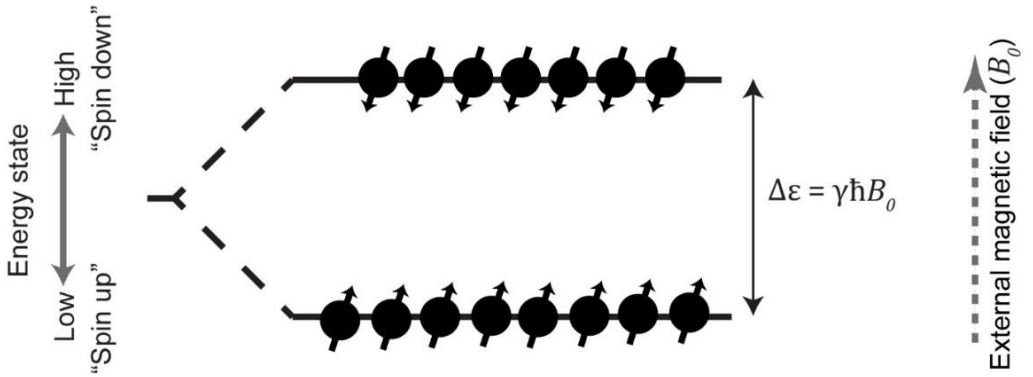


Figure 1.1: Zeeman splitting into two energy levels for a group of spin 1/2 nuclei in an external magnetic field. The energy difference between the levels, $\Delta\varepsilon$, is determined according to the gyromagnetic ratio of the nucleus and the strength of the external field.

The energy difference between these two eigenstates, $\Delta\varepsilon$, is proportional to the applied field, B_0, the nuclear specific gyromagnetic ratio, γ, and Planck's constant divided by 2π, $\hbar$, according to equation 1.2:

$$\Delta\varepsilon = \gamma\hbar B_0 \qquad 1.2$$

When nuclear spins are present in large numbers in an external field, as is the case in NMR experiments, the interaction gives rise to a weak form of sample magnetism called paramagnetism.

1.4.1 Low sample polarization at clinical field strengths and temperatures

At clinically relevant field strengths and biological temperatures, there is a very small difference in the sizes of the populations of nuclei occupying the high and low energy states, with the low energy state slightly favoured. The magnitude of the difference in the sizes of the populations occupying the high and low energy states is referred to as the sample polarization and is a critical determinant of the signal available to all NMR based techniques. The degree of sample polarization is determined by the external magnetic field strength, the sample temperature and the gyromagnetic ratio of the nucleus. Although individual nuclei can alternate between eigenstates, the population

distribution for a large sample of nuclei is determined by the Boltzmann distribution (described in equation 1.3), where k_B is the Boltzmann constant, and T is the sample temperature:

$$\frac{N_{\text{low energy}} - N_{\text{high energy}}}{N_{\text{low energy}} + N_{\text{high energy}}} = \tanh\left(\frac{\gamma\hbar B_0}{2k_B T}\right) \qquad 1.3$$

Boltzmann distribution estimates of sample polarization at clinical field strengths and biological temperature demonstrate that the statistical excess of nuclei entering the low energy state at clinical field strengths and biological temperatures is only approximately ten in every one million spins (Table 1.2). Low sample polarization is a fundamental reason for the intrinsically low sensitivity of CMR and represents an important opportunity to overcome the lack of signal.

	Sample polarization		
	1.5T	**3T**	**7T**
^{1}H	0.00099%	0.00197%	0.00461%
^{13}C	0.00025%	0.00050%	0.00116%
^{31}P	0.00040%	0.00080%	0.00187%

Table 1.2: Low sample polarization for biologically relevant nuclei at biological temperatures.

1.4.2 Sample polarization is a fundamental determinant of NMR sensitivity

All NMR based techniques exploit spin transitions between high and low energy states to generate signal in experiments that consist of at least two components:

1. *Induction of energy state transitions using RF energy*

In the first component of a basic NMR experiment, bulk spin energy state transitions from the thermal equilibrium state are induced by the application of an oscillating magnetic field, or radiofrequency (RF) pulse, by a pulse generator and set of transmit coils within the NMR system.

This induced field is termed B_1, and the frequency of the RF necessary to induce energy state transitions, ω, is determined according to the Larmor equation:

$$\omega = \gamma B_0 \qquad 1.4$$

When a population of nuclei are irradiated by an oscillating transverse magnetic field at the Larmor frequency, spin transitions from the low to the high energy state or from the high to the low energy state are induced. Because there are more nuclei in the low energy state than in the high energy state at thermal equilibrium, the net effect of RF irradiation is to increase the number of spins in the high energy state.

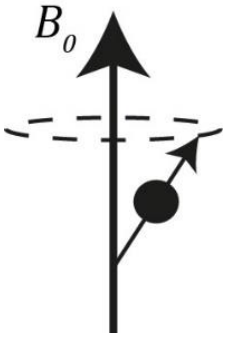


Figure 1.2: Precession of a magnetic moment about an external magenetic field, B_0.

The maximum absorption of RF occurs when the spin populations are inverted - i.e. all spins that were in the low energy state at thermal equilibrium have been promoted to the high energy state and *vice versa*. For simple NMR spectroscopic experiments, RF pulses of half, or less, of the energy required to invert the spin populations are generally used to maximise signal, and these intermediate states are described according to classical mechanics by the flip angle α, where a flip angle of 180° corresponds to spin population net inversion, and a flip angle of 90° is half of this.

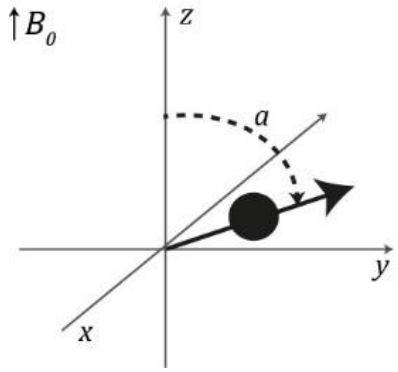


Figure 1.3: Net magnetisation is tipped into the x-y plane during application of RF at the Larmor frequency and is described according to the flip angle, α.

As an approximation, for simple on-off ('hard') RF pulses, the flip angle is determined by the gyromagnetic ratio, the strength of the RF pulse field $B_{1,}$ and the time for which the RF pulse is applied, t_p according to equation 1.5:

$$\alpha = \gamma B_1 t_p \qquad 1.5$$

In addition to tipping the longitudinal magnetization M_z towards the transverse plane, the RF pulse also introduces a component of magnetization in the M_{xy} plane, leading to a temporary statistical 'phase coherence', Figure 1.4:

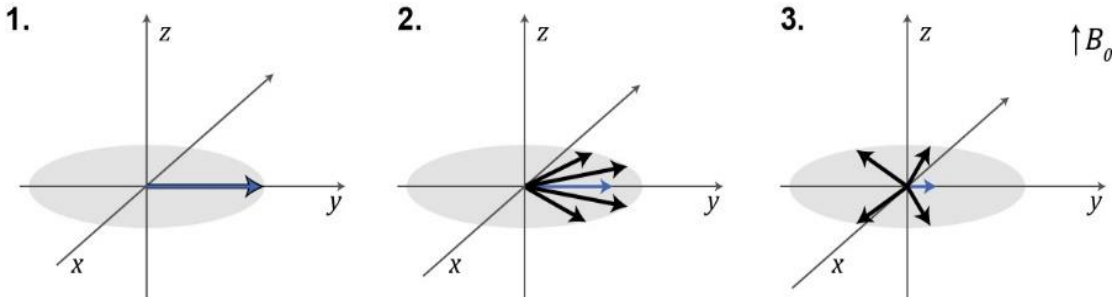


Figure 1.4: RF irradiation introduces a component of magnetization in the M_{xy} plane (panel 1, net M_{xy} plane magnetization represented as blue arrow), which decays when the RF pulse is switched off (panels 2 and 3).

1.4.2.1 *Measurement of spin relaxation*

In the second part of the MR experiment, the RF pulse is switched off and the nuclear spin system begins to return to the thermal equilibrium state. The return to thermal equilibrium is the product of two separate relaxation processes. The first process involves the loss of energy from the excited spin system into the much larger surrounding molecular lattice through dipole-dipole interactions and results in recovery of magnetization in the z direction. This process is random and the recovery of M_z at a given time, t, is exponential and defined according to one of the series of Bloch equations:

$$M_z(t) = M_{z,eq} - [M_{z,eq} - M_z(0)]e^{-t/T_1} \quad 1.6$$

T_1 is the time taken for the longitudinal magnetization to recover to 63% of its value at thermal equilibrium.

The second relaxation process results the from loss of phase coherence and the decay of M_{xy} following dephasing due to interactions with other spins with slightly different precessional frequencies, characterised by the decay time constant T_2 according to equation 1.7.

$$M_{xy}(t) = M_{xy}(0)e^{-t/T_2} \quad 1.7$$

T_2 is the time taken for the transverse magnetization to decay to 37% of its initial value.

Thus, although T_1 and T_2 occur simultaneously, they are different processes and T_2 is always shorter than T_1 (Figure 1.5).

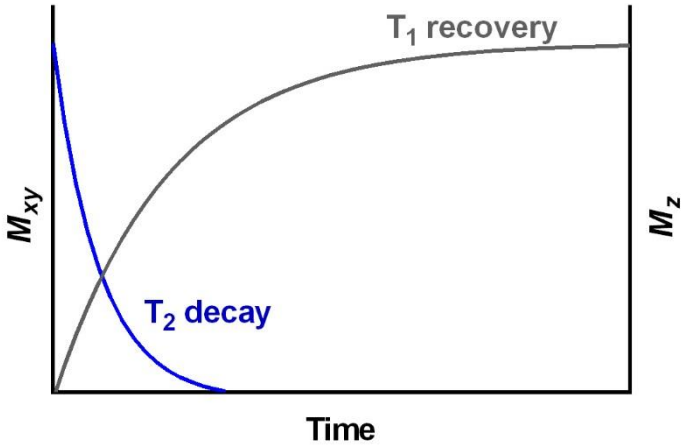


Figure 1.5: T_1 recovery and T_2 decay are simultaneously occurring, though separate, relaxation mechanisms.

As the spins return to thermal equilibrium, an oscillating current is induced in the receiver coils of the NMR system giving rise to a free induction decay (FID, Figure 1.6). The frequency of the FID is determined by the Larmor frequency of the nucleus and the rate and the amplitude decays according to T_2 (or T_2^* when allowing for the effects of field inhomogeneity).

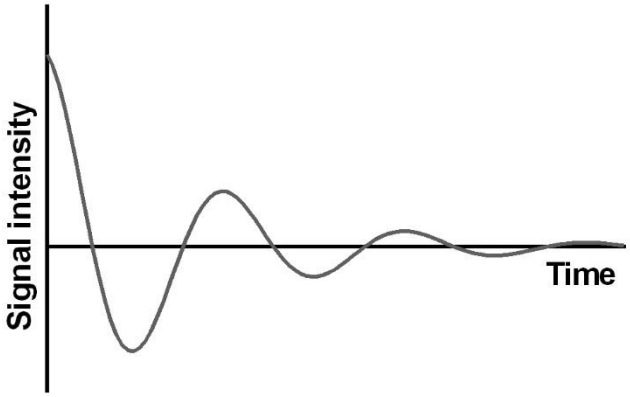


Figure 1.6: Free induction decay induced in the receiver coil by spin relaxation.

One unique strength of NMR over other cardiovascular imaging techniques is the ability to differentiate molecules despite their containing the same NMR active nuclei. This property arises due to the effect of electron shielding upon the magnetic field experienced by the spins, and thus different molecules will precess at different

frequencies according to their chemical compositions leading to different FID signals. This modifies the Larmor equation such that:

$$\omega = \gamma(1 - \sigma)B_0 \qquad 1.8$$

Where σ is the electron shielding constant.

The representation of complex FIDs containing signals from several spins with different Larmor frequencies is generally simplified by converting the plot from the time domain to the frequency domain by means of a mathematical Fourier transform (Figure 1.7).

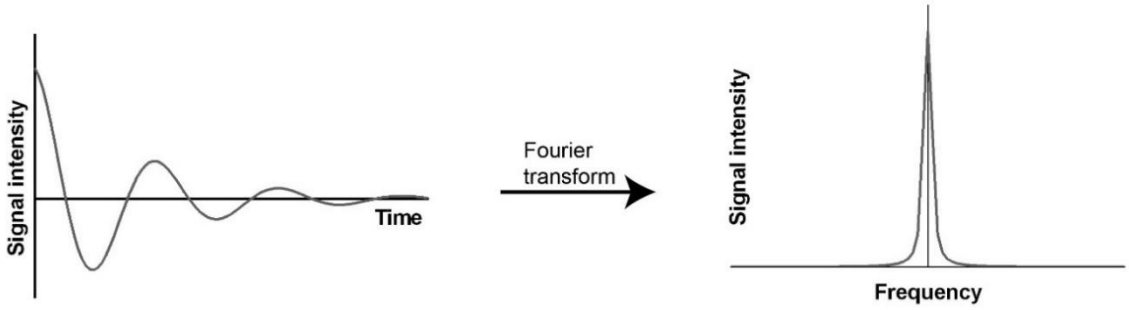


Figure 1.7: Free induction decays are generally transformed from the time to the frequency decay using a Fourier transform for MR spectroscopy.

1.4.3 Strategies to overcome low signal to noise ratio in CMR

The intensity of the induced signal recorded by the receiver coil is proportional to the rate of change of the magnetization (determined by the Larmor frequency), the coil efficiency, B_1 and M_0. Because the statistical excess of nuclei in the low energy state, and hence M_0, is extremely small, the ratio of the signal of interest from the sample to that of signal arising from random noise is very low.

For conventional proton based CMR imaging, the inherent insensitivity in NMR is mitigated by the high natural abundance of protons in the tissues of interest. However,

it is the major limitation for the development of NMR techniques using non-proton nuclei such as ^{13}C and ^{31}P. ^{13}C NMR is further limited by the fact that only 1% of naturally abundant carbon occurs as the stable isotope ^{13}C; almost all the remainder occurs as ^{12}C which has zero net spin and is therefore not NMR active[30]. Furthermore, as illustrated in Table 1.2, the lower gyromagnetic ratio of ^{13}C further reduces the sample polarization at a given field strength and temperature relative to protons, limiting the available SNR.

The two major strategies for increasing SNR in NMR experiments are to either increase the number of acquisitions or alternatively increase the static magnetic field strength, but the degree of increase in SNR that is practically possible with either of these measures is limited, and is unlikely to enable clinical ^{13}C MR with current technologies:

1. *Increasing the number of acquisitions (averages)*

Because NMR signals from samples are highly reproducible, though low in intensity, MR experiments generally rely upon repeated measures of the same sample. As the noise component of the signal is random, it will average with the square root of the number of excitations, whereas the sample component of the signal will increase linearly. Thus, increases in SNR are approximately proportional to the square root of the number of excitations, and hence acquisition time:

$$SNR \propto \sqrt{N_{excitations}} \qquad 1.9$$

However, the extent to which the number of signal averages can be increased in CMR is significantly limited by the need, in general, for breath-holding to minimise respiratory motion. This usually limits individual acquisition sequences to approximately 20 seconds[31], unless respiratory navigator gating is used. Longer sequences also lead to longer examination times which increases costs, reduces patient

throughput and increases the risk of an adverse event when scanning critically ill patients.

2. *Increasing the magnetic field strength*

Although it is possible to increase sample polarization, and hence SNR, by increasing the field strength of the magnet (for example, from 1.5T to 3T or 7T)[32, 33], the expense of an MR system increases greater than linearly (and near exponentially) with the field strength of the magnet, and ultra-high field systems are associated with further intrinsic limitations due to a greater heating effect from radiofrequency energy deposition. The shortening of RF wavelength also leads to non-uniform transmit fields, which increases spatial variation in SNR and contrast-to-noise ratio (CNR)[33]. Furthermore, the increasing number of patients with implantable electronic cardiac devices will be, at least for the foreseeable future, excluded from ultra-high field examinations[34], restricting both the possible clinical benefit and also the accessibility of patient groups with diseases such as heart failure for study.

Thus, although non-proton MR holds significant biological interest, the SNR is not sufficient for clinically practical ^{13}C MR assessment of the cardiovascular system using current technology. The overall result of these factors is impractically long acquisition

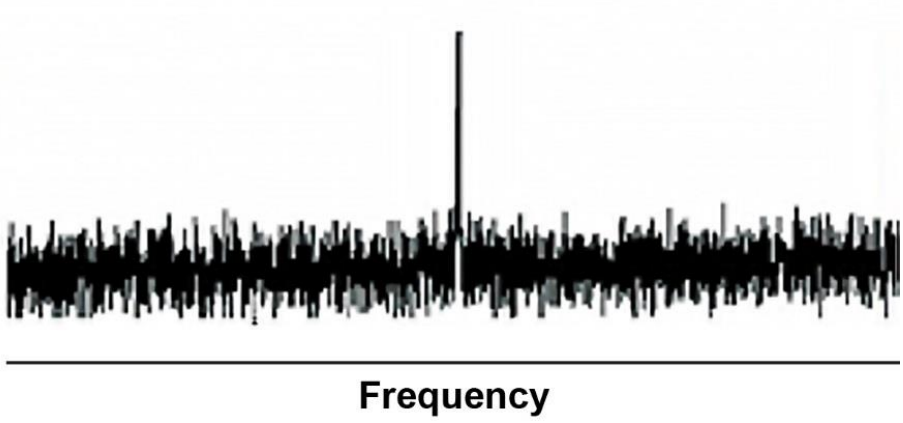


Figure 1.8: Poor quality spectrum from a [^{13}C] enriched pyruvate sample despite 3 hour acquisition at 7 T. Redrawn from Schroeder et al[35].

times and poor quality spectroscopy, as illustrated by this spectrum acquired over 3 hours from a ^{13}C labelled phantom sample using a 7 T MR system[35] (Figure 1.8).

1.5 Hyperpolarized magnetic resonance as a novel approach to increasing SNR

Hyperpolarization refers to a range of techniques which offer an alternative approach to overcoming the relatively low signal obtained from conventional NMR experiments[36]. For biological purposes, all hyperpolarization techniques involve the preparation of a substance in an external system, which is then administered to the biological system of interest. Importantly, hyperpolarization techniques can induce far greater nuclear polarization than would be realistically possible by increasing the field strength of static magnets, with polarization gains of up to 4-5 orders of magnitude now routinely achieved with some techniques. There are four main methods of hyperpolarization, all of which temporarily enhance the polarization of an NMR active nucleus of interest in a system external to the imaging magnet:

1.5.1 Brute force polarization

Brute force polarization exploits the greater Boltzmann nuclear polarization at low temperatures in a strong magnetic field[37]. However, this approach is slow to produce hyperpolarized samples because of excessively long T_1 values at low temperatures and the maximum degree of polarization that can be achieved is relatively small, limiting the potential for cardiovascular applications.

1.5.2 Parahydrogen induced polarization (PHIP)

Molecular hydrogen consists of two atoms, the nuclei of which possess two possible spin eigenstates, allowing four potential spin combinations. The majority of naturally

abundant hydrogen (75%) exists as orthohydrogen, but the remainder exists as para-hydrogen, the relative proportion of which can be enhanced by cooling to temperatures under 20 K. The spin order inherent to parahydrogren can be exploited and transferred to an unsaturated carbon bond on a molecule of interest by a hydrogenation reaction followed by the application of RF or field cycling to transfer polarization from the proton to an adjacent ^{13}C nucleus; a process which occurs at room temperature[38]. Although PHIP techniques can in principle be applied to many molecules, are rapid and are relatively cheap, the degree of polarization which can be achieved is relatively limited and few molecules that can be hyperpolarized using PHIP have yet shown potential clinical relevance[39].

1.5.3 Optical pumping

Optical pumping is primarily a method for the hyperpolarization of noble gases, which are used for lung imaging[40]. The noble gas to be hyperpolarized (most frequently xenon) is mixed with a vapor of either alkali-metal or metastable atoms and irradiated with circularly polarized light. This increases the electron polarization within the vapour, which is transferred to the nuclei of the noble gas during collisions. Optical pumping occurs in the gas state and no cardiovascular applications have yet been described.

1.5.4 Dynamic nuclear polarization

Of the four methods, dynamic nuclear polarization has to date shown the greatest biological promise in cardiovascular and other disease states and is the focus of the work described in this thesis.

The concept of enhanced nuclear polarization during microwave irradiation of the electron spin resonance (ESR) was first described theoretically by Overhauser in 1953[41]. Despite early criticism, the effect was demonstrated experimentally by Carver and

Slichter later that year[42]. These investigators used a lithium sample in a low magnetic field to demonstrate enhancement of the ^{7}Li resonance during the application of RF energy, which was termed the Overhauser effect. Applications to either analytical chemistry or biology were limited for several decades by the lack of availability of microwave sources that could provide irradiation at a sufficiently high frequency (gigahertz range) to saturate electron spin resonances in high static fields.

However, a similar effect of polarization enhancement during microwave irradiation near the electron Larmor frequency was later shown to exist in non-conducting solid samples[43]. Hyperpolarization experiments were performed during the 1980s in solid carbon samples[43, 44] and demonstrated the potential of the technique to provide huge signal increases. In addition to applications in analytical chemistry, the technique also proved useful in particle physics for the production of spin polarized targets for neutron scattering experiments[45].

The dynamic nuclear polarization (DNP) method of hyperpolarization exploits the much higher polarization of electrons than nuclei at low temperatures in magnetic fields (Figure 1.9) and induces 'transfer' of this electron polarization to the nucleus.

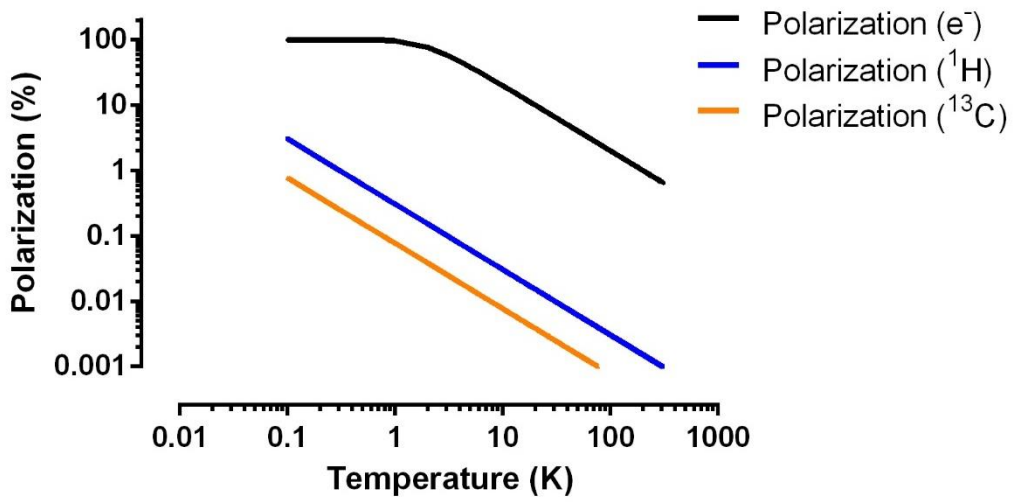


Figure 1.9: Temperature dependence of electron and nuclear polarization at 3 T.

The electron system can be either an endogenous or exogenous paramagnetic system, which can be modified through the addition of free radical sources, such as TEMPO (2,2,6,6-tetramethylpiperidine-1-oxyl) or OXO63 (tris[8-carboxy-2,2,6,6-tetrakis(2-hydroxymethyl)benzo[1,2-d:4,5-d′]bis(1, 3)dithio-4-yl]methyl radical), or alternatively by photo-induction of endogenous radicals[46]. Following the application of microwave irradiation at a frequency near the electron Larmor frequency, ω_e, the high electron polarization is transferred to the nuclear spin system, resulting in nuclear hyperpolarization.

The frequency of microwave irradiation required to cause DNP is determined by the magnetic field strength and the properties of the free electron source and nucleus of interest. The maximal NMR sample signal amplitude occurs during irradiation at approximately the ω_e ± the nuclear Larmor frequency ω_n, Figure 1.10.

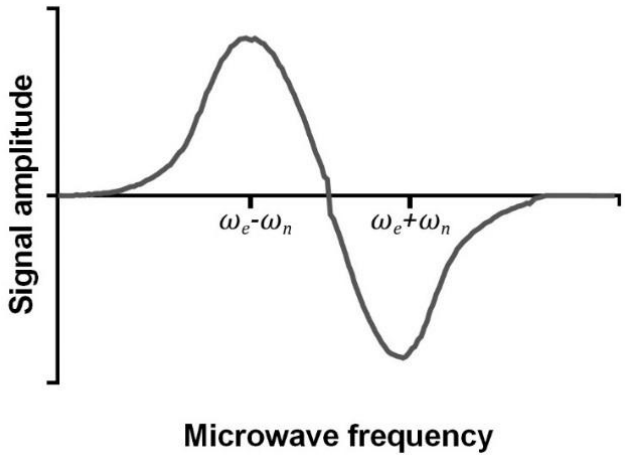


Figure 1.10: NMR signal enhancement resulting from microwave irradiation around the electron Larmor frequency, ω_e. Optimum polarization occurs during irradiation at ω_e ± the nuclear Larmor frequency ω_n.

The mechanisms by which microwave irradiation at these frequencies leads to transfer of electronic to nuclear polarization in solid state DNP experiments are incompletely understood, but have been described using model spin systems and quantum mechanical approaches. Three major mechanisms of DNP are recognised and the relative contribution of each to hyperpolarization depends upon the conditions of the DNP experiment, including the linewidth of the EPR spectrum of the radical, the number of electrons and the nuclear Larmor frequency[47]. Quantum mechanical descriptions recognise the solid and cross effects whereas thermal mixing is a thermodynamic description:

1. *The solid effect*

Solid effect DNP is most likely to occur during hyperpolarization with a free electron source which has a linewidth much smaller than the nuclear Larmor frequency[48]. The laws of quantum mechanics generally permit only certain energy state transitions according to the NMR effect (irradiation at nuclear Larmor frequency) and electron paramagnetic resonance (EPR) effects (irradiation at electron Larmor frequency) whilst

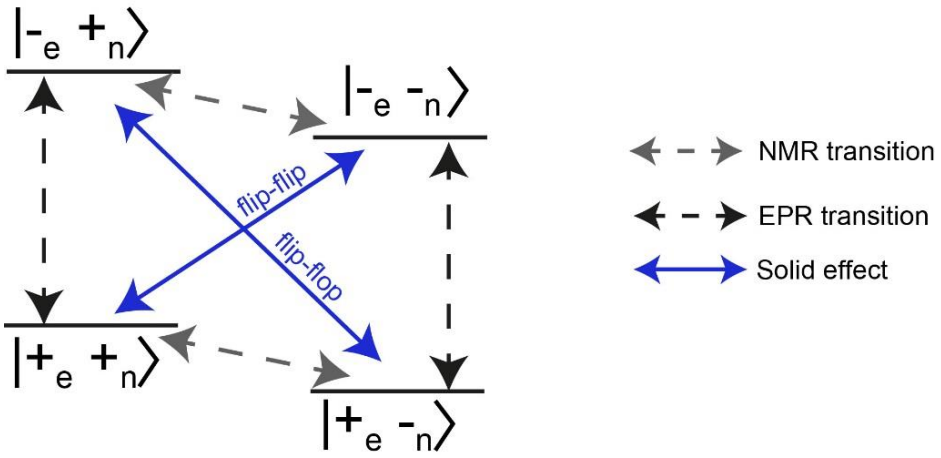


Figure 1.11: Solid effect DNP evokes 'forbidden' electron/nucleus energy state transitions, adapted from [48, 50].

other transitions involving simultaneous electron and nuclear transition (known as 'flip-flop' and 'flip-flip', Figure 1.11) are highly unlikely to occur without significant external energy input and have been termed 'forbidden'[49, 50].

Solid effect DNP occurs when microwave irradiation at an appropriate frequency induces 'flip-flop' and 'flip-flip' transitions, leading to polarization transfer to the nuclear system.

2. Cross effect

The cross effect is modelled in a three or greater spin system and occurs when the inhomogeneous spectral breadth of the radical is greater than the nuclear Larmor frequency and the linewidth of the radical EPR spectrum remains narrow[50]. Unlike the solid effect, the cross effect relies upon permitted transitions and occurs when the EPR transition between two dipolar coupled electrons is saturated, leading to either positive or negative nuclear enhancement depending upon which transition is saturated[51].

3. Thermal mixing

The thermal mixing effect is described in thermodynamic terms and relies upon the concept of spin temperature[52]. Spin temperature is a description of energy which

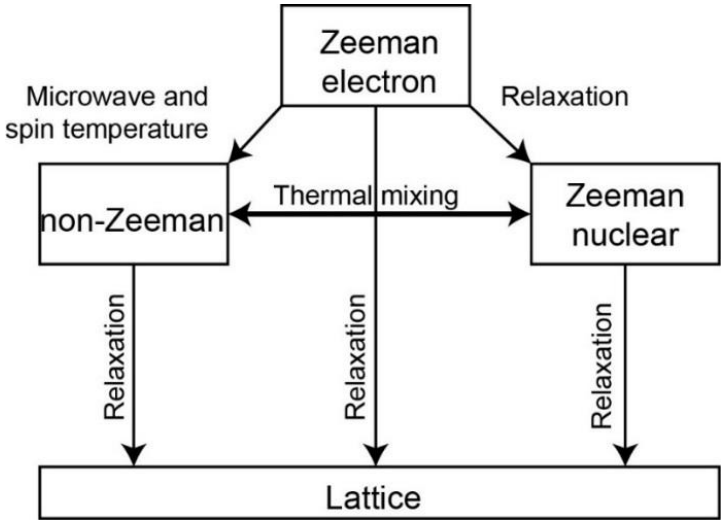


Figure 1.12: Thermal couplings of four thermal reservoirs during microwave irradiation. Redrawn from original by Goldman[52]

considers the Zeeman and dipolar Hamiltonians of electrons as commuting reservoirs which cannot ordinarily exchange energy. However, under conditions of microwave irradiation, energy transfers from the electron dipolar reservoir into the electronic and nuclear Zeeman reservoirs and from there to the lattice. This results in a cooling of the nuclear spin temperature (despite an increase in energy), enhancing nuclear polarization (Figure 1.12).

1.6 Development of biological applications of DNP

1.6.1 Dissolution DNP for hyperpolarized liquid state NMR

Despite having been well established for chemical NMR in the late 1990s, the DNP process required samples to be frozen at temperatures approaching absolute zero. This restricted the process to molecules in the solid state, with limited apparent biological applicability.

The application of the DNP technique to liquid state NMR was made possible by the discovery by Ardenkjær-Larsen and colleagues that polarization was transiently

preserved after rapid melting of a hyperpolarized solid state sample using a bolus of superheated liquid[53]. Following rapid melting to near room temperature, the sample remained highly polarized though the polarization decayed according to the T_1 time of the molecule. These investigators demonstrated that this effect could be exploited to provide a short window for unprecedented signal enhancement in biological imaging applications[54].

The rapid melting of solid state samples undergoing DNP poses a significant engineering challenge, which was addressed by designing custom hardware. A prototype hyperpolarizer of a design similar to that used by Ardenkjær-Larsen and colleagues in the first DNP experiments was acquired by the University of Oxford in

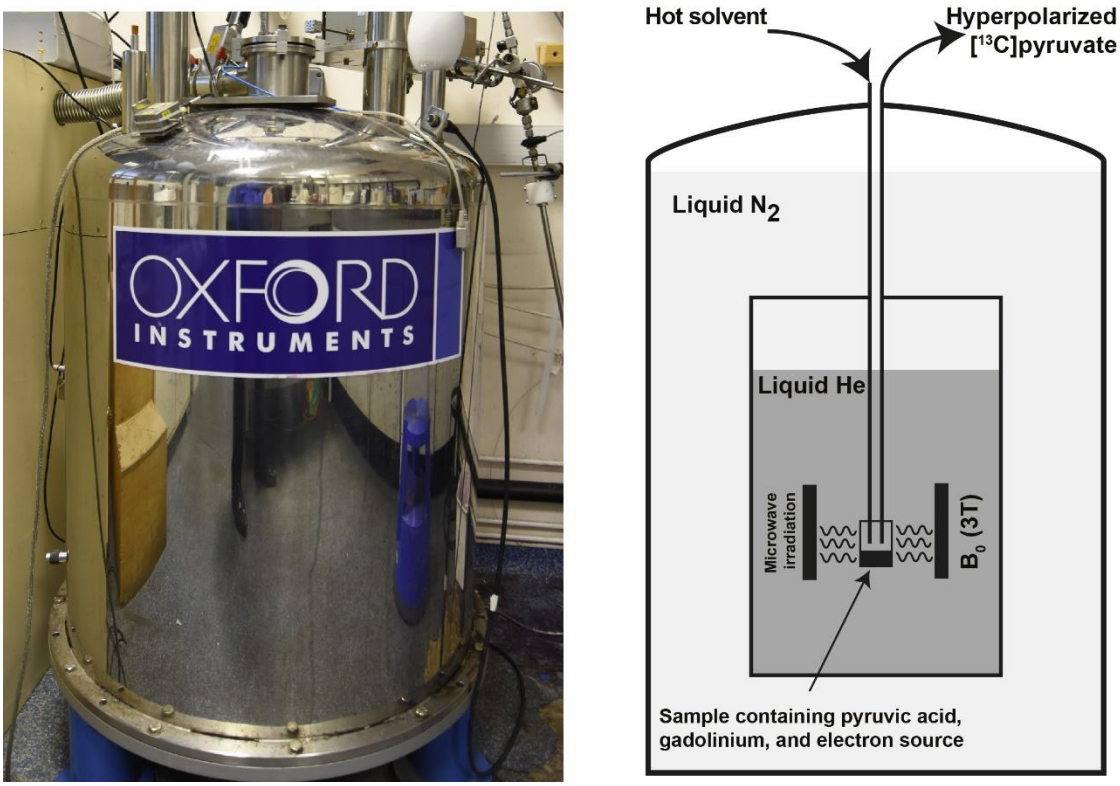


Figure 1.13: Image of prototype preclinical hyperpolarizer (left panel) and schematic representation (right panel) of key components of the system necessary for hyperpolarization of [^{13}C]pyruvic acid.

2005 and is shown along with a schematic demonstrating the key components in Figure 1.13.

The prototype polarizer has a superconducting magnet at 3.35 T with a variable temperature insert cooled with a flow of liquid helium. The chamber is connected to high performance vacuum pumps to create a vapour pressure of ~0.8 mbar, in order to reduce the sample temperature to ~1 K. An external microwave source capable of providing microwave irradiation at gigahertz frequency is sited externally, with microwaves directed to the sample via a waveguide.

Samples to be hyperpolarized using DNP are prepared externally. In the first dissolution DNP experiments using prototype systems, the OXO63 radical was added to ^{13}C labelled urea as a free electron source[54]. One important prerequisite for DNP is that the radical be distributed uniformly through the sample, and thus a glassing agent (glycerol in the [^{13}C]urea experiment) is also required to avoid crystal formation. This sample is then placed in a container connected to the bottom of a Teflon™ tube, and then lowered into the polarizer. The sample is immersed in liquid helium at the isocentre of the static field and cooled to ~1 K by the application of a vacuum prior to

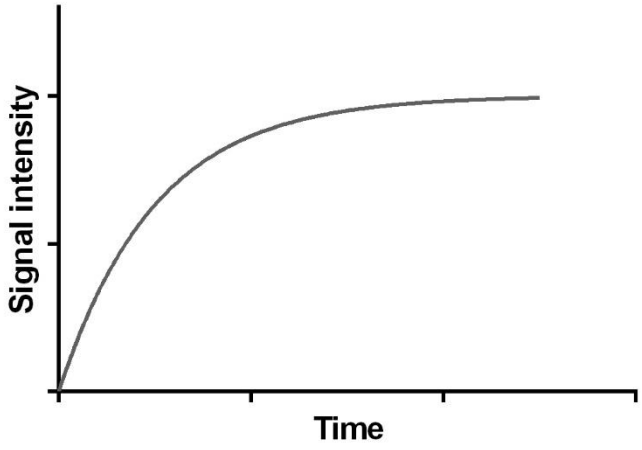


Figure 1.14: Increase in sample polarization (build-up) following an exponential (or biexponential) curve.

and during microwave irradiation. The increase in the sample polarization within the polarizer can be monitored using integrated NMR apparatus, producing a build-up curve from which a time constant can be estimated (illustrated in Figure 1.14).

After the sample has achieved a sufficient degree of polarization (usually around 30 minutes to 1 hour for the commonly used substrates), the sample is rapidly melted to a temperature compatible with biological use. Immediately prior to melting, the microwave irradiation is stopped, and the sample lifted out of the liquid helium. An injection wand with two tubes is rapidly inserted into the sample holder, and a bolus of boiling solvent (water in early experiments) rapidly injected into one of the two tubes in the injection wand. The arrival of the boiling solvent in the sample holder melts the frozen, polarized sample into the liquid state which is then ejected through the other tube within the injection wand tube into a container. The residual polarization can then be measured following transfer to nearby NMR apparatus.

Following dissolution, the polarization of hyperpolarized samples decays according to the rate of the spin interaction with the surrounding lattice, or T_1 decay, leading to a window of preservation of the polarization of generally seconds to minutes for molecules commonly used for potential biological application. Because of this, dissolution is conducted as quickly as possible and DNP polarizers are colocated with NMR systems to minimise the time between dissolution and administration, and hence maximise signal. Increases in signal-to-noise ratio of >10,000 fold were reported for [^{13}C]urea, and the biological applicability of hyperpolarized urea demonstrated for rapid ^{13}C angiography in rodents[53, 54].

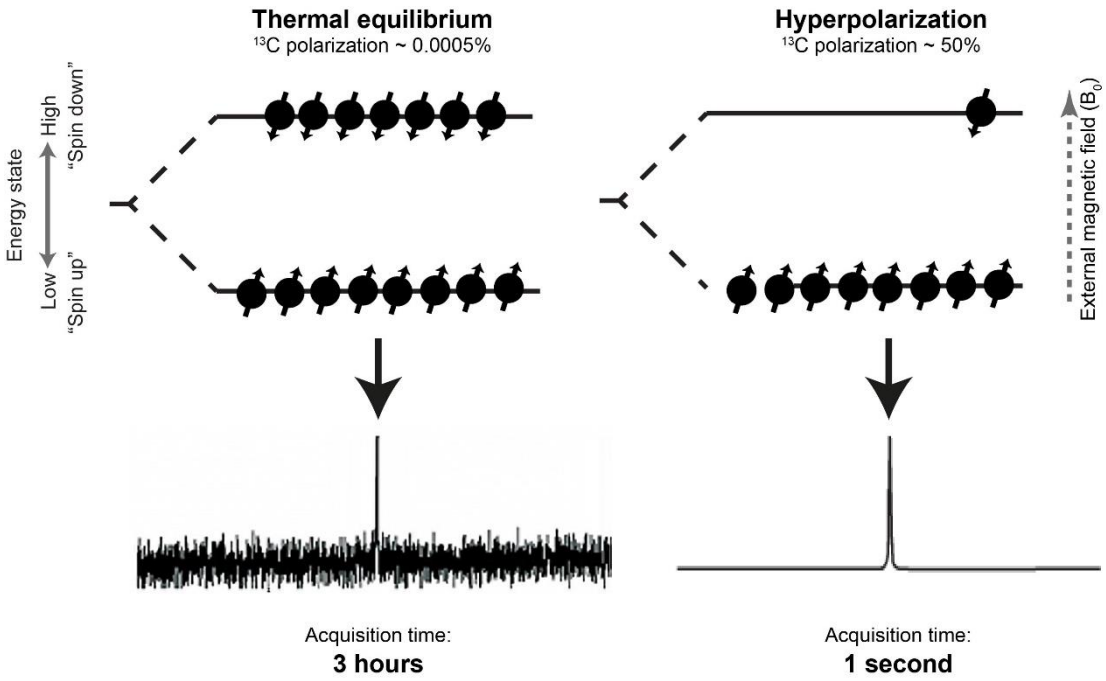


Figure 1.15: Comparison of sample polarization and resulting spectrum at thermal equilibrium and during hyperpolarization.

Comparison between the spectrum of the same ^{13}C labelled sample in Figure 1.15 before and after hyperpolarization demonstrates the potential of hyperpolarized NMR using DNP to dramatically increase the quality of the information and shorten the acquisition time.

1.6.2 Hyperpolarized ^{13}C MR as a probe of metabolism

One unique strength of MR spectroscopy is the differentiation of molecules according to the frequencies of their free induction decays (chemical shift) which are determined by their chemical structure and the degree of electron shielding of the nucleus[55]. This offers the potential for hyperpolarized MR to assess the biological interconversion of substances *in vivo*, representing a unique advantage of the technique over other tracer technologies such as PET which generally assess only tracer uptake. Because the T_1 of ^{13}C labelled biological molecules is no longer than seconds to minutes, the application

of hyperpolarized MR is well suited to the study of rapid enzymatic processes *in vivo*. This property is particularly compatible with applications as a probe of metabolism.

In order to be suitable for use as a hyperpolarized substrate for metabolism, the molecule must have a sufficiently long T_1 to retain sufficient polarization during dissolution, administration and metabolism and must form a glass-like substance when frozen in the hyperpolarizer. In order to be of biological interest, the molecule must also be at an important point of metabolic control, to provide information about a biological mechanism of interest. These complex and sometimes competing requirements have so far been most successfully combined with the hyperpolarization of pyruvate, which occupies a central position and important role within mammalian metabolism.

1.6.2.1 Hyperpolarized [^{13}C]pyruvate

The pyruvate molecule is a three carbon chain, and is the end product of glycolysis, linking glucose uptake to the tricarboxylic acid (TCA) cycle (Figure 1.16). Hyperpolarized [^{13}C]pyruvate MR can be performed with a ^{13}C label at either the first ([1-^{13}C]) or second ([2-^{13}C]) position of pyruvate (less commonly at both, [1, 2-^{13}C]), enabling measurement of flux through enzyme catalysed pathways downstream. The third carbon position can also be labelled, but the short T_1 time of [3-^{13}C]pyruvate renders it unsuitable as a biological probe. Pyruvate is rapidly transported across cardiac cell membranes by the family of monocarboxylate transporters[56].

There are three major metabolic fates of the [^{13}C] label in hyperpolarized [1-^{13}C]pyruvate which can be exchanged into [1-^{13}C]alanine, [1-^{13}C]lactate and [^{13}C]bicarbonate pools in reactions catalysed by alanine aminotransferase, lactate dehydrogenase and pyruvate dehydrogenase respectively[57] (Figure 1.16).

[^{13}C]Bicarbonate in turn equilibrates with $^{13}CO_2$ in the pH dependent carbonic anhydrase reaction.

The ^{13}C label in [2-^{13}C]pyruvate also exchanges with the lactate and alanine pools but avoids PDH mediated decarboxylation and enters acetyl coenzyme A, though the small pool size and very rapid turnover of acetyl CoA means that no resonance attributable to [^{13}C]acetyl CoA is usually detectable (Figure 1.17). The [^{13}C] label within the acetyl CoA pool is propagated downstream leading to resonances attributable to [1-^{13}C]acetylcarnitine and also first span TCA cycle metabolites including [1-^{13}C]citrate and [5-^{13}C]glutamate.

Thus, hyperpolarized magnetic resonance using [^{13}C]pyruvate can provide a much more comprehensive overview of energy metabolism at the level of carbohydrate oxidation than is possible with any competing metabolic imaging technology.

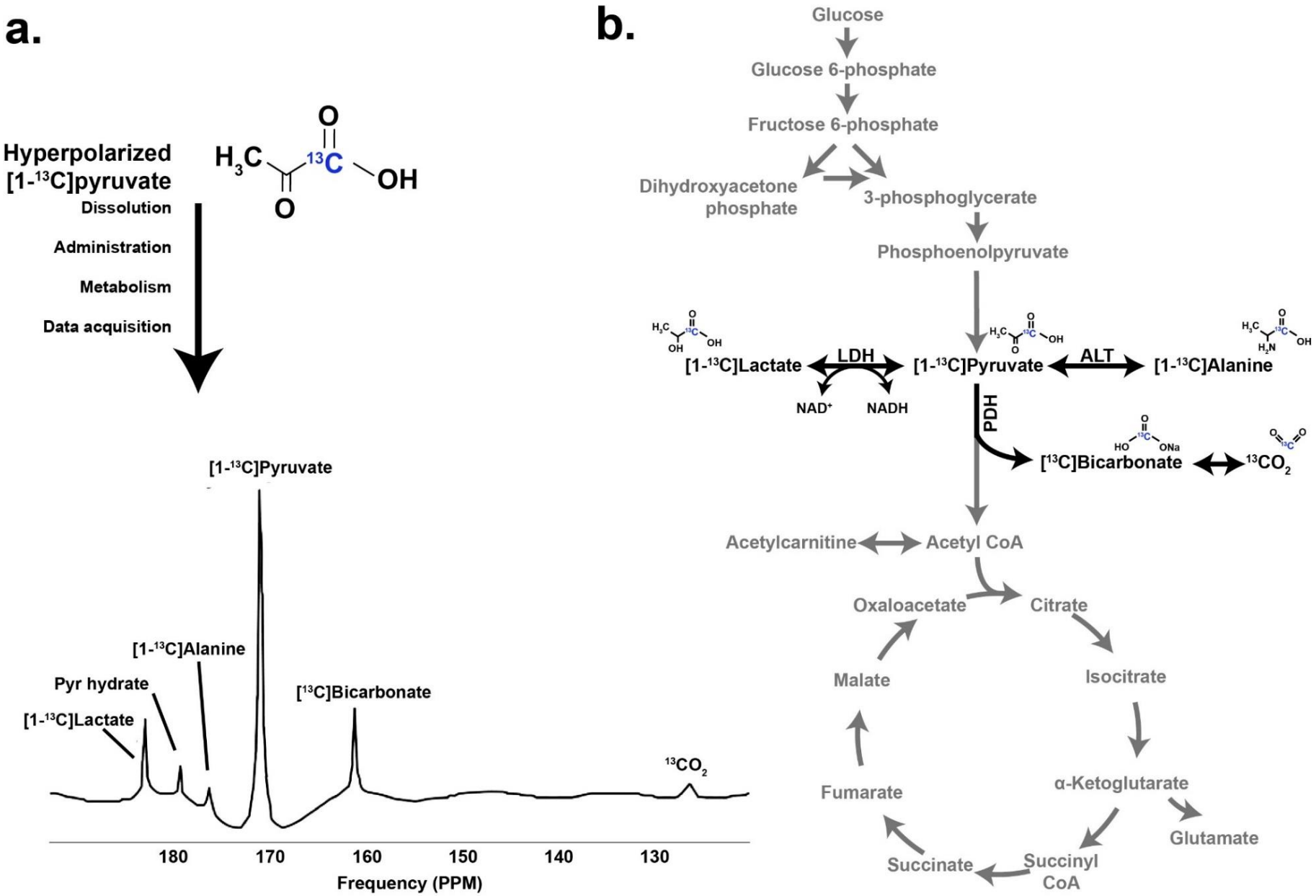


Figure 1.16, panel a: Hyperpolarized [1-13C]pyruvate molecule and resulting spectrum following label incorporation in biological system following administration of hyperpolarized [1-13C]pyruvate. Panel b: biochemical basis for label exchange in a biological system.

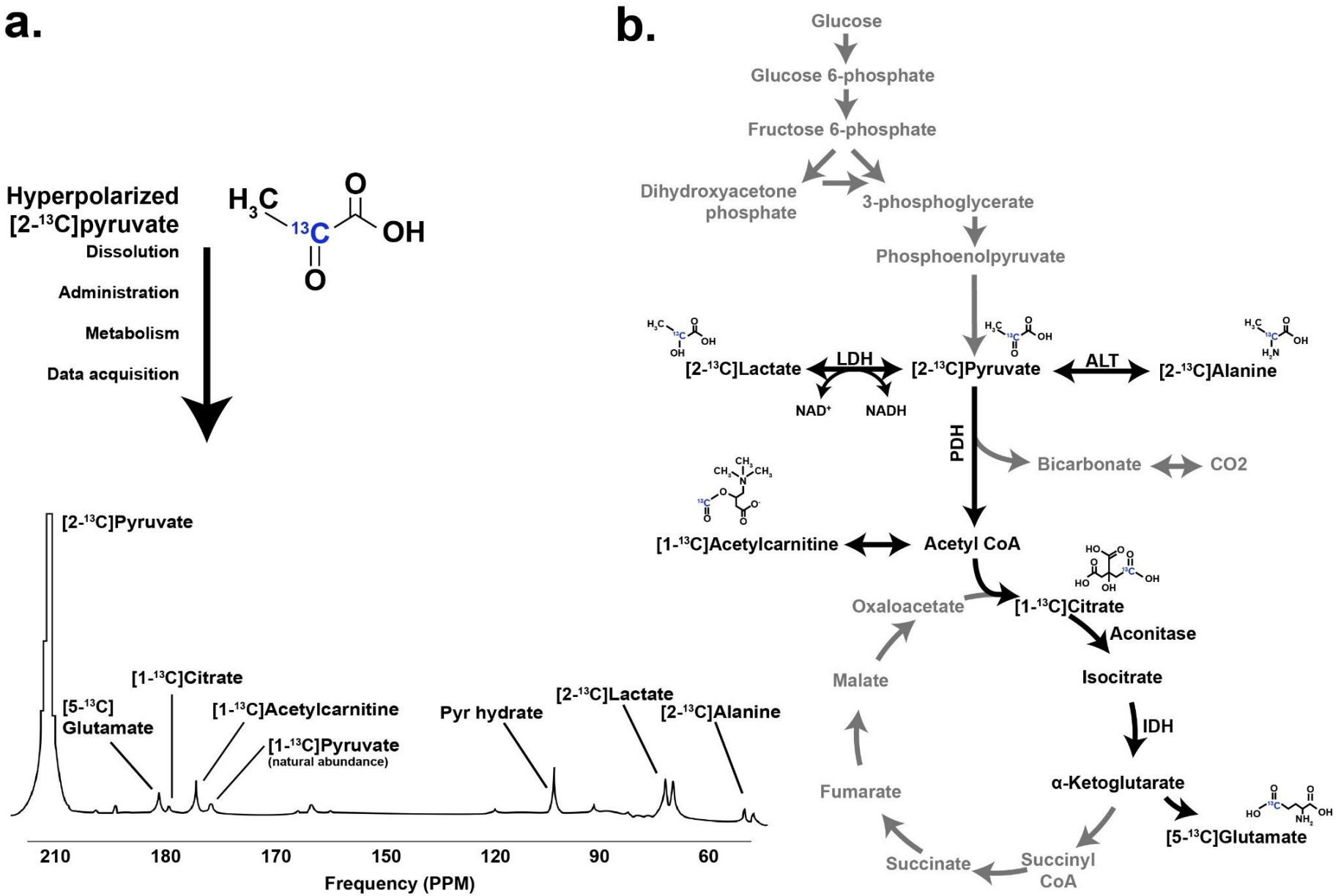


Figure 1.17 panel a: Hyperpolarized [2-13C]pyruvate molecule and resulting spectrum following label incorporation in biological system following administration of hyperpolarized [2-13C]pyruvate. Panel b: biochemical basis for [2-13C]pyruvate label exchange in a biological system.

1.6.2.2 *Dose selection for hyperpolarized pyruvate experiments*

Although the signal enhancement provided by DNP is of the order of 4-5 orders of magnitude, many of the metabolic processes that can be studied occur biologically at only low millimolar concentrations, and it is generally necessary to administer a supraphysiological dose of hyperpolarized substrate in order to adequately quantify resonances resulting from label incorporation into downstream metabolites. However, the administration of substances at supraphysiological doses has the potential to alter the very reactions that it was the intention to study, introducing a potential source of bias to experiments. The concentrations of substrates administered during DNP are generally much higher than those required for PET and arguably cannot be termed 'tracers'.

The optimal dose of a hyperpolarized substrate is likely to be the minimum dose required to ensure adequate tissue delivery to saturate a rate limiting reaction of interest, whilst producing sufficient signal to ensure robust and reliable quantitation[58]. The optimal dose will therefore vary according to the organ and reaction of interest. For rodent cardiac applications, a dose of 1 ml of 40-80 mM hyperpolarized [1-^{13}C]pyruvate has been shown to achieve saturation of the [1-^{13}C]bicarbonate resonance, whilst [1-^{13}C]alanine and [1-^{13}C]lactate demonstrated linear dependence, implying that PDH activity, rather than cellular uptake rate via monocarboxylate transporters, was rate limiting[58].

1.6.2.3 *Other molecules with biological potential using DNP*

In addition to pyruvate and urea, many other molecules have shown potential to be used as hyperpolarized probes. For cardiac energy metabolism applications, one limitation of hyperpolarized pyruvate is that it can directly assess only carbohydrate metabolism, though the majority of cardiac ATP is, under usual physiological conditions, synthesised from fatty acids. Hyperpolarized [1-^{13}C]acetate is converted to acetyl carnitine and can used as an indirect measure of acetyl CoA synthetase activity[59] whilst [1-^{13}C]butyrate has favourable

polarization properties and a T_1 of around 20 seconds, and demonstrates label exchange with glutamate, β-hydroxybutyrate, glutamate, acetoacetate and acetylcarnitine in isolated perfused hearts[60]. However, these short chain fatty acids do not undergo beta oxidation, and medium and long chain fatty acids are the major source of reducing equivalents for ATP generation in the heart and their physiological relevance is therefore unclear. Recently, hyperpolarization of the medium chain fatty acid [1-^{13}C]octanoate was described, though *in vivo* signal decay was rapid, and only a single resonance was detected and was attributed to [1-^{13}C]acetylcarnitine[61].

In addition to the study of cardiac energy metabolism, the other major application of preclinical DNP has been in oncology. In tumour cell lines and *in vivo* models, the conversion [1,4-$^{13}C_2$]fumarate to [1,4-$^{13}C_2$]malate has been shown to be a marker of cell death and treatment response in tumours, as intact cell membranes are usually impermeable to fumarate[62]. The same molecule also demonstrated utility as a biomarker in acute kidney injury[63], though it appears to be relatively insensitive in cardiac applications where late gadolinium enhancement techniques already demonstrate excellent sensitivity[64]. In more specific oncological applications, hyperpolarized [1-^{13}C]α-ketoglutarate[65] and [1-^{13}C]glutamate[66] were used to assess tumour isocitrate dehydrogenase 1 (IDH1) mutational status, though whether there are potential cardiac applications of these molecules is not currently clear. The exchange of hyperpolarized [^{13}C]bicarbonate with $^{13}CO_2$ in the pH dependent carbonic anhydrase reaction provides *in vivo* pH mapping in tumours[67], and a similar approach using [1-^{13}C]pyruvate (was successfully applied to cardiac applications in ischaemia[68].

Essentially all ^{13}C labelled hyperpolarized molecules have a T_1 of under 1 minute, which precludes their use as substrates to assess slower biological processes such as antibody

binding and synthetic processes. However, nanoparticles of silicon have the unusual property of containing natural abundant spin 1/2 ^{29}Si in a nuclear spin free ^{28}Si lattice, which 'shields' ^{29}Si from the usual dipole-dipole interactions resulting in T_1 times of the order of hours[69]. Although silicon nanoparticles are not themselves metabolised, they can be prepared to enable conjugation to biological targeting ligands[70]. No cardiovascular applications of ^{29}Si nanoparticles have yet been described, although potential applications in atherosclerosis are obvious.

1.6.3 Acquisition strategies for hyperpolarized ^{13}C experiments

The exploitation of the signal gains from hyperpolarized magnetic resonance require that that careful consideration is given to the MR acquisition sequence used. The choice of acquisition strategy is an important component of experimental design depending upon the biological question to be answered. There are three main acquisition strategies:

1. *Non-localised*

The simplest acquisition strategy involves the application of a broad frequency RF pulse to induce bulk spin state transitions in all ^{13}C labelled metabolites, and recording of the subsequent free induction decay in the receiver coil. This approach was successfully applied in the setting of the isolated perfused rat heart to demonstrate the initial feasibility of using hyperpolarized [1-^{13}C]pyruvate to measure enzyme catalysed reaction steps[57], and is also useful for assessing the whole-body response to metabolic shifts, including those induced systemically using drugs[71].

2. *Slice selection*

An important strength of hyperpolarized MR experiments is that they can be conducted in fully equipped MR systems which include gradient sets for spatial localisation. By applying a linear field slice selection gradient across the direction of the slice to be excited before the acquisition and applying an RF pulse of a sufficiently narrow bandwidth, the resulting spectrum can be restricted to include only data from the selected slice, which can be placed across an organ of interest[72]. This approach is relatively straightforward from a sequence design perspective, and is useful in cardiac applications, as the surrounding lung and skeletal muscle contribute little to pyruvate metabolism relative to the heart (illustrated in Figure 1.18).

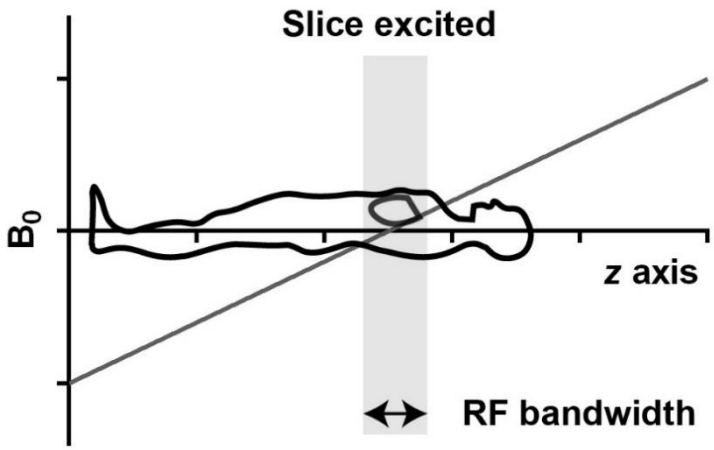


Figure 1.18: Principle of slice selection using gradient field and narrow bandwidth RF pulse.

Because the heart and liver lie in essentially separate axial slices, it has also been possible to refine the early iterations of slice selective acquisition to sequentially acquire spectra from alternating axial slices covering the heart and liver. A single hyperpolarized tracer injection was therefore shown to provide information about both organs (in press).

3. Hyperpolarized ^{13}C imaging

Although slice selective spectroscopy is useful for the study of spatially homogenous myocardial disease processes such as those seen in systemic metabolic disorders, it is not useful for assessing regional processes such as ischaemic heart disease and certain cardiomyopathies[73]. The imaging of hyperpolarized ^{13}C label exchange is thus an important goal, but efficient sampling of the finite magnetization at a useful spatial and temporal resolution poses significant challenges in sequence design and MR hardware requirements.

The most successful implementations of MR imaging in rodent MR systems have used custom designed imaging sequences including selective RF excitation of individual metabolites, which helps to convert sample polarization to signal as efficiently as possible[74]. These complex RF pulses usually necessitate high gradient strength and slew rates, though a custom designed local implementation was shown to sidestep these limitations in a preclinical MR system[75]. The RF pulses in this implementation are followed by a 3D echo planar imaging readout gradient, allowing the imaging of label exchange with a resolution of 2 x 2 x 3.8 mm^3.

1.6.4 Analysis of data from hyperpolarized ^{13}C experiments

As with all MR based techniques, absolute quantification of hyperpolarized ^{13}C substrate concentration is difficult as many factors influence the signal intensity received by the MR system, including, but not limited to, the degree of sample polarization, the time taken from dissolution to administration, the rate of administration and the homogeneity of the magnetic field, all of which are variable between experiments.

Because of this, most early analysis techniques for hyperpolarized MR were based upon the ratios of maximum peak areas for the metabolite of interest to the pyruvate signal, for example the [1-^{13}C]bicarbonate:[1-^{13}C]pyruvate or [1-^{13}C]lactate:[1-^{13}C]pyruvate ratios[72].

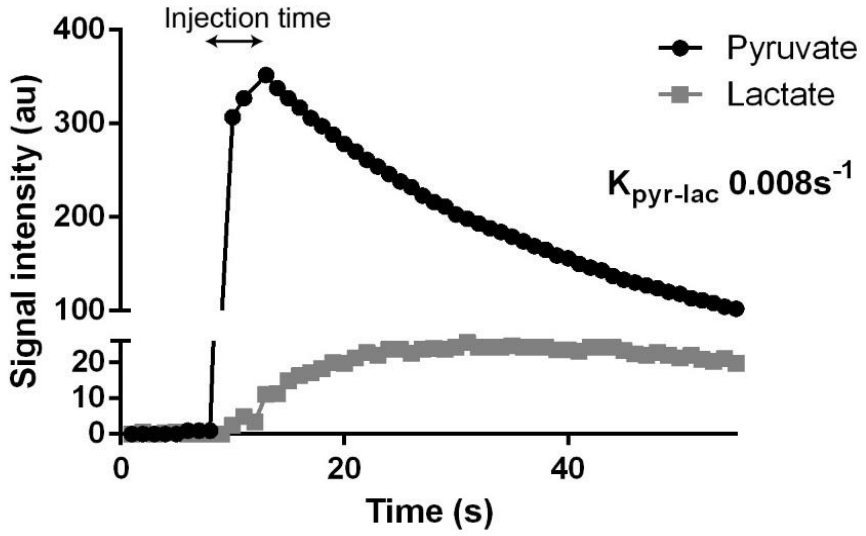


Figure 1.19: NMR signal intensity curves following injection of hyperpolarized [1-^{13}C]pyruvate and subsequent ^{13}C label exchange into lactate. A pseudo first order rate constant, $K_{pyr-lac}$, can be estimated by fitting mathematical models to the curves.

This approach helps to minimise variability due to differing signal input functions, but is relatively crude and does not allow for different rates of injection or differing rates of signal decay due to higher flip angles or more frequent sampling by the MR system. A more sophisticated approach is to fit a mathematical model to the curves resulting from change in pyruvate and metabolite signal over time using kinetic models to estimate rate constants for the K_{pyr-x}, reactions[76], illustrated with [1-^{13}C]pyruvate and [1-^{13}C]lactate in in Figure 1.19.

1.6.5 Hyperpolarized [1-^{13}C]pyruvate as a probe of cardiac energy metabolism

Pyruvate has a central role in cardiac energy metabolism. In order to fulfil its mechanical function as a pump, the heart generates and consumes chemical energy in the form of adenosine triphosphate (ATP)[13]. ATP is synthesised within mitochondria in a process driven by an electrochemical proton gradient driven by electrons in the form of the reducing equivalents NADH and flavin adenine dinucleotide (FADH.) The sources of reducing equivalents for ATP synthesis are dietary fuels, including fatty acids and carbohydrates,

and, to a lesser extent, amino acids and ketone bodies. In the normal heart in the fasted, resting state, the majority of acetyl CoA entering the tricarboxylic acid cycle is derived from the beta oxidation of free fatty acids (overall 70-90% of ATP synthesis)[77]. Almost all of the remainder is derived from the oxidation of pyruvate, with a small contribution from the glycolysis process itself. In the fed state or during increased workload or hypoxia, there is a significant and adaptive increase in the relative contribution of carbohydrate metabolism to ATP generation[78]. Pyruvate dehydrogenase is thus an enzyme which occupies a critical physiological role at a key point of metabolic control.

The mammalian PDH complex consists of three catalytic subunits, E1-3, and activity is regulated both by allosteric end-product inhibition (by high ratios of the reduced and oxidised forms of nicotinamide adenine dinucleotide ($NADH/NAD^+$) and acetyl-CoA/CoA ratios) and also by a phosphorylation and dephosphorylation cycle.[79] Phosphorylation of PDH occurs at three serine residues on the alpha chain of the E1 subunit of the enzyme complex, and inhibits substrate binding, leading to a decrease in enzyme activity. PDH phosphorylation is catalysed by a family of four pyruvate dehydrogenase kinases (PDKs, designated PDK1-4 in the order in which they were cloned with PDK4 dominant in cardiac tissue[80]) which are responsive to increased $NADH/NAD^+$ and acetyl CoA/CoA ratios, whilst dephosphorylation is catalysed by two pyruvate dehydrogenase phosphatases (PDP1 and PDP2)[81]. Because the PDH mediated decarboxylation of hyperpolarized [1-^{13}C]pyruvate results in label incorporation into [1-^{13}C]bicarbonate, the rate of production of [1-^{13}C]bicarbonate must reflect PDH activity[82], providing a non-invasive readout of PDH flux. The [1-^{13}C]bicarbonate:[1-^{13}C]pyruvate ratio is therefore a novel index of the relative contribution of carbohydrate oxidation to overall cardiac energy metabolism[72].

In early experiments, spectral acquisitions from rodents confirmed the sensitivity of the technique to [1-^{13}C]bicarbonate production, and that the ratio of hyperpolarized bicarbonate to pyruvate was significantly greater in the fed than fasted state, consistent with activation of PDH[72]. The potential of the technique to provide a non-invasive assessment of disease state was also demonstrated in a model of type I diabetes, in which PDH flux was suppressed. The assumption that the [1-^{13}C]bicarbonate:[1-^{13}C]pyruvate ratio reflected PDH activity was subsequently confirmed in experiments demonstrating a strong linear correlation with *ex vivo* measures of PDH activity, using classical biochemical techniques[83] and also states of redox shift[84]. The [1-^{13}C]bicarbonate:[1-^{13}C]pyruvate was also responsive to pharmacological activation of PDH using the drug dichloroacetate (which binds to the pyruvate domain of PDK4 with ADP and inhibits activity by locking the active site in a closed conformational state[85]) providing proof-of-principle for the sensitivity of the method to drug induced changes[83].

Hyperpolarized MR estimates of PDH flux in the heart have also been used to assess models of clinically relevant disease states. It has long been established that cardiac substrate metabolism changes in disease states and the targeting of substrate metabolism with therapeutic intent has been investigated in many human cardiovascular diseases including diabetes[86], heart failure[87, 88], hypertrophic cardiomyopathy[89, 90] and ischaemia[91, 92] among many others. Almost all of these studies have suffered from an inability to measure cardiac substrate metabolism at repeated time points *in vivo* and it is therefore uncertain to what extent the variable efficacies reported can be directly attributed to changes in metabolism. In a rodent model of hypertension, a leading cause of heart failure, hyperpolarized MR estimates of PDH flux were increased, consistent with a metabolic shift towards an increase in glucose oxidation[93]. However, in a model of hyperthyroidism, PDH flux was reduced in the disease state, and restoration of PDH flux using dichloroacetate surprisingly improved

hyperthyroidism induced cardiac hypertrophy[94]. In models of ischaemic heart disease, impairment of PDH flux correlated with the degree of cardiac dysfunction[95] and in a large animal tachycardiomyopathy heart failure model, PDH flux was again reduced following the development of heart failure[96]. In a rodent model of type II diabetes, both PDH flux and diastolic cardiac function were impaired and restoration of PDH was also associated with improved function[97]. These studies and others suggest that PDH flux could be an important index of metabolism in human cardiovascular disease[98], with roles in both mechanistic understanding and also potentially in phase II dose ranging metabolic pharmacological studies.

Although the majority of preclinical cardiac work has focussed upon the assessment of PDH flux, the ability to assess ^{13}C label incorporation into [1-^{13}C]lactate may also have important clinical implications. The LDH reaction exists in a redox couple with the oxidised and reduced forms of the cofactor NAD, and the assessment of [1-^{13}C]lactate incorporation may be a novel probe of cardiac redox shifts acutely and glycolytic gene programme induction over a longer term. Because redox shifts are characterised by an increase in the [NADH]/[NAD^+] ratio and are a very early event in hypoxia and ischemia, hyperpolarized [1-^{13}C]pyruvate imaging could provide a novel and sensitive marker of ischaemia[98]. In coronary artery balloon occlusion experiments in a porcine model, a significant increase in [1-^{13}C]lactate production was shown following reperfusion, consistent with a shift towards a glycolytic phenotype in ischaemic tissue[99]. Recently, using a closed chest rodent model of acute ischaemia-reperfusion, higher label incorporation into [1-^{13}C]lactate was observed in reperfused myocardium , which resolved one week later[100].

1.6.5.1 Applications of clinical cardiovascular hyperpolarized MR beyond metabolic imaging

Although the majority of potential cardiovascular applications of hyperpolarized MR involve the assessment of metabolism, the significant increases in signal offer potential to overcome limitations in other CMR applications. Current CMR assessments of myocardial perfusion are based upon the change in signal intensity on myocardial T_1-weighted images during the infusion of a bolus of a gadolinium based contrast agent (GBCA), which shortens T_1[101]. They are therefore only an indirect assessment of myocardial perfusion as the change in signal intensity correlates linearly with the concentration of GBCA across only a narrow range. This necessitates specialist mathematical correction to enable absolute quantitation of perfusion, which is not widely available[102]. In contrast, the ^{13}C signal intensity during a perfusion study using hyperpolarized [^{13}C]urea would be expected to correlate essentially linearly with the concentration of the contrast agent, and was shown in preclinical models to increase during adenosine induced hyperaemia[103]. Importantly, the frequency of microwave irradiation required for polarization of [^{13}C]urea is sufficiently similar to that of [1-^{13}C]pyruvate that these molecules can be co-polarized and co-administered, providing a single infusion for assessment of cardiac perfusion and metabolism[104]. This approach could be particularly valuable for the assessment of cardiac perfusion/metabolism coupling during myocardial viability assessment, with advantages in acquisition time and ionising radiation dose when compared to existing PET techniques[105].

Finally, hyperpolarized ^{13}C labelled agents also have the potential to be used for interventional catheter tracking experiments. A prototype tri-lumen catheter containing a continuous flow of hyperpolarized $^{13}C_2$-hydroxyethylacrilate was used to enable passive catheter tracking in a porcine model, but the continuous flow requirements may restrict this application to PHIP polarization[106].

1.6.5.2 *Hyperpolarized [1-^{13}C]pyruvate MRS as a readout on wider cellular metabolism*

Mammalian cardiac energy metabolism involves hundreds of enzyme catalysed reactions, but hyperpolarized [1-^{13}C]pyruvate results in detectable label exchange into just three downstream metabolites. Despite this apparent limitation, the central position of pyruvate within metabolism in fact allows a much more comprehensive assessment of cellular metabolism than a simple numerical comparison would initially suggest. This is because although cellular metabolism has traditionally been thought of as a series of individual reactions and pathways, the remarkable flexibility and redundancy of metabolic networks in the heart is in fact better represented around a limited number of highly interconnected nodes[107].

Along with the lactate dehydrogenase catalysed interconversion of pyruvate and lactate, over 700 other cellular reactions are redox coupled to the ancient and evolutionarily conserved molecule NAD[108]. The ability to non-invasively assess just one of these therefore represents an opportunity to assess cellular metabolic responses at a much more comprehensive level than is initially apparent. PDH is another critical metabolic node, occupying a fundamental position at an important control point of glycolysis, carbohydrate oxidation and fatty acid oxidation via the Randle cycle[109]. Thus, although the individual steps of canonical metabolic processes such as glycolysis or beta oxidation cannot be assessed using hyperpolarized [1-^{13}C]pyruvate, it is nevertheless possible to make inferences of the prevailing cellular metabolic environment, reflecting fundamental responses to endogenous and exogenous influences.

1.7 Clinical translational issues for cardiovascular DNP

Hyperpolarized [^{13}C]pyruvate magnetic resonance is inherently attractive for translation to clinical cardiovascular applications as, unlike existing tracer techniques, hyperpolarized MR

results in no ionising radiation dose to patients, enabling non-invasive and repeated assessments in the same person at different time points. However, the very short window for data acquisition between dissolution and administration poses significant technical and regulatory challenges, as clinical diagnostic agents are usually carefully evaluated on a batch-to-batch basis to assure quality. The clinical translation of hyperpolarized ^{13}C labelled substances therefore requires careful consideration of the clinical safety profile of the molecule and of the relevant regulatory frameworks, which vary significantly between international jurisdictions.

1.7.1 Pyruvate as a molecule for human administration

In addition to its favourable properties for hyperpolarization and metabolic importance, pyruvate has a very good human safety profile. Pyruvate has been trialled with therapeutic intent in cardiovascular disease at supraphysiological doses far in excess of those required for hyperpolarized MR studies with no significant safety issues demonstrated, including during direct and prolonged intracoronary infusion[110-112].

Extrapolation of preclinical studies indicated that a potential dose range of 0.07-0.57 ml/kg body weight of 250 mM pyruvate solution could be infused at a rate of 5 ml/second. At the request of US regulatory agencies, these dose ranges were tested against a placebo infusion of equivalent volume and infusion rate in formal phase 1 clinical trial in healthy male and female volunteers.[113] Adverse events in both pyruvate and placebo arms were generally mild and universally non-serious, and included transient flushing, dysgeusia and dizziness. However, the proportion of adverse effects was higher at the 0.57 ml/kg dose than at lower doses, and included two non-serious AEs that were adjudicated to be related to the pyruvate infusion. A dose of up to 0.43ml/kg 250 mM pyruvate infused at up to 5 ml/s was therefore deemed appropriate for human studies.

Although the principles of GMP incorporate many separate requirements[114], the key challenge for hyperpolarized contrast agents is to ensure the sterility of the sample, which is not possible when using preclinical hyperpolarizers. This is because the hyperpolarization process takes place in an effectively open system, with no way to sterilise the sample holder or injection wands prior to dissolution. One solution to this problem is to house the entire prototype hyperpolarizer in a designated clean room, as was undertaken for first in human studies at one university[113], though this approach is expensive and not practical for widespread adoption. In order to enable clinical human DNP using sterile substrates, it was therefore necessary to design hyperpolarization hardware that could produce sterile substrates meeting the quality requirements imposed by GMP and other relevant policies.

1.7.2 Hyperpolarization hardware suitable for sterile use intent

The design of a new generation hyperpolarizer for sterile use intent was again initially conducted by Ardenkjaer-Larsen and colleagues and commercialised by GE Healthcare as the SPINlab™ before being transferred to a new GE owned subsidiary, Research Circle Technology Inc. The first SPINlab™ hyperpolarizer to be used for cardiovascular

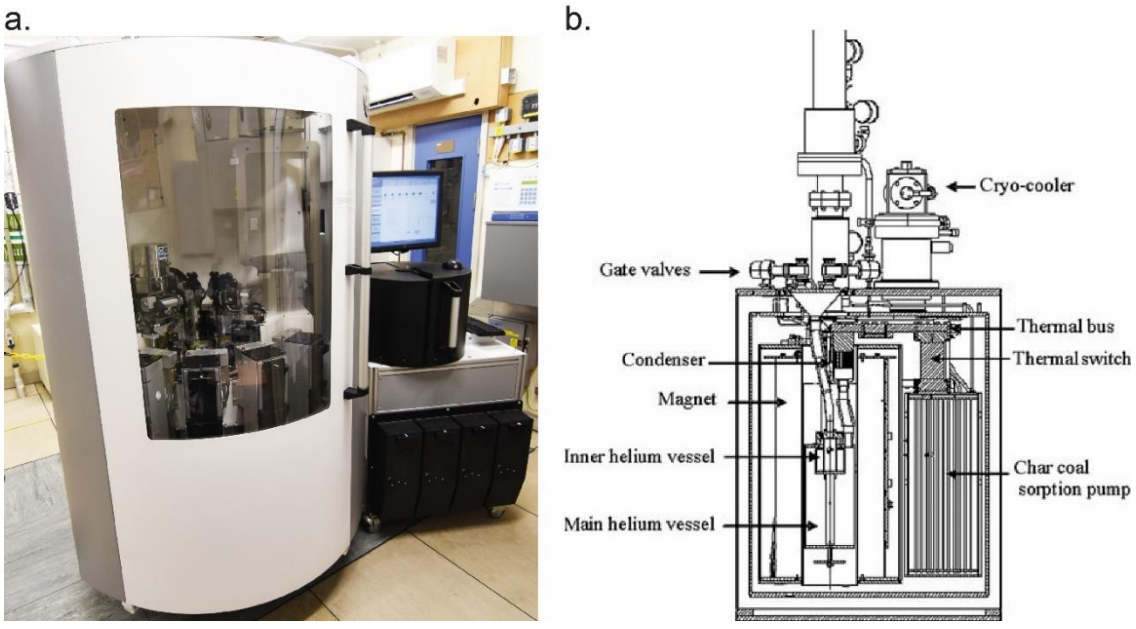


Figure 1.20: Panel a, SPINlab™ hyperpolarizer and Panel b, schematic of key components, reproduced from[115].

applications was acquired by the University of Oxford in 2013 with financial support from the British Heart Foundation.

The fundamental difference between the SPINlab™ and previous hyperpolarizers is the capability to apply the DNP process to the sample and solvent whilst they are within a single use sterile barrier, which is termed a sterile fluid path (SFP). In addition to suitability for sterile use intent, the SPINlab™ has other advantages over the earlier systems including the ability to simultaneously polarise four samples, an increased degree of automation of sample loading, an increased sample volume and a closed cycle cryogenic regeneration system, to avoid cryogen consumption (Figure 1.20).

1.7.3 The SPINlab™ sterile fluid path

The SFP consists of a sample vial, a syringe designed to contain the dissolution medium, a filter to remove the electron radical and a receiver syringe for the final product, all connected with coaxial tubing (Figure 1.21). The fluid path is prepared externally in a laminar flow cabinet and the appropriate volume of pyruvic acid and radical added to the sample cup. The sample cup is then attached to the tubing and sealed using a laser welder. Sterile helium is blown into the vial and tubing dead space, in order to ensure adequate thermal conduction from the sample to the external helium temperature bath. Sterile water is added to the dissolution syringe and sterile neutralization medium added to the final receiver syringe. Because the sample needs to be retained exclusively within the sample cup until dissolution, the entire fluid path assembly is then frozen in the upright position prior to transport and maintained at a temperature of -20 °C or lower.

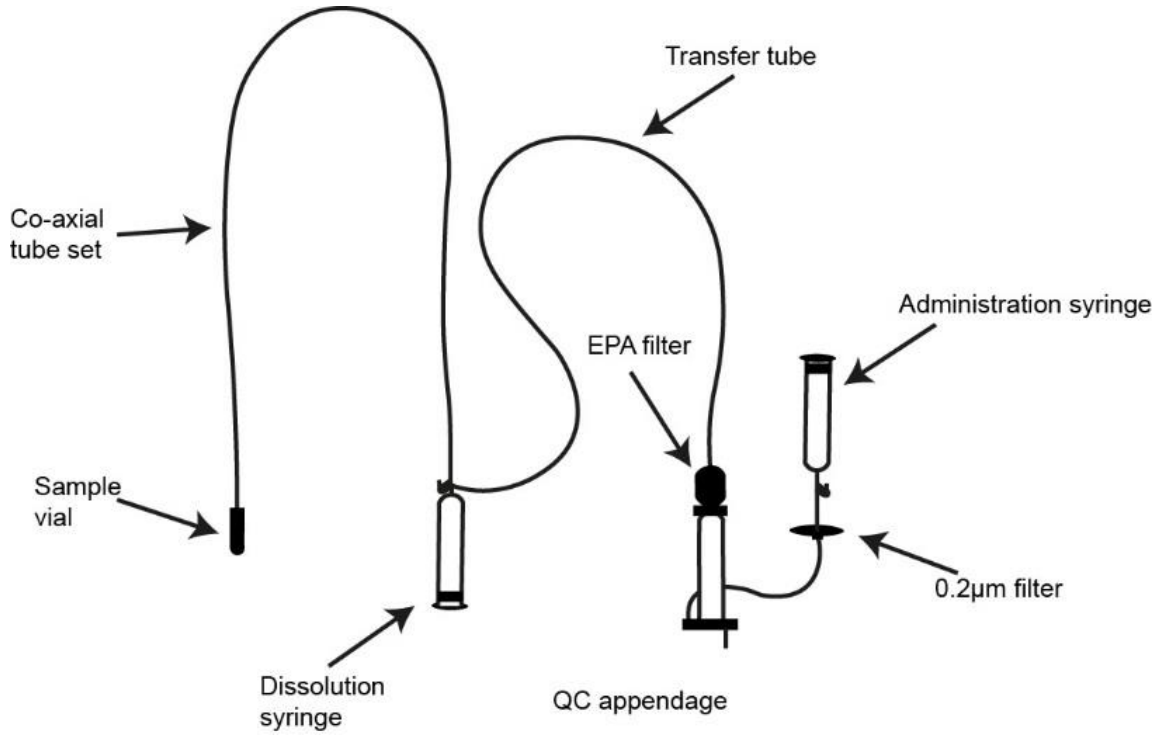


Figure 1.21: Schematic representation of the sterile fluid path for use in the SPINlab™ hyperpolarizer.

1.7.4 Sample polarization and dissolution

A series of positioning steps are followed during the lowering of the sample into the helium bath for hyperpolarization. These steps are designed to reduce the heat load delivered by the sample into the helium bath itself, and are essentially automated. After the sample is within the helium space, microwave irradiation is commenced and sample polarization monitored using integrated NMR apparatus. Because the SPINlab™ uses a 5 T magnetic field, as opposed to the 3.35 T fields used in previous hyperpolarizers, the time constant for hyperpolarization of [1-^{13}C]pyruvic acid is longer, but a higher degree of sample polarization can be achieved which, in conjunction with the filtration of paramagnetic radical, extends the window over which data can be acquired.

During hyperpolarization, the sterile water contained within the dissolution syringe is heated to >100°C. During dissolution, the hyperpolarized sample is lifted from the helium reservoir and heated water ejected into the coaxial tubing before entering the sample vial,

melting and mixing with the sample before being passed through the EPA filter into the quality control (QC) appendage syringe and neutralized.

1.7.5 Quality control

Because each hyperpolarized sample is prepared individually, it is also necessary to have rapid QC processes to ensure that important sample parameters of physiological relevance (temperature, pH, sample polarization, radical concentration, pyruvate concentration and sample volume) are within appropriate predefined ranges prior to injection. The SPINlab™ QC unit accessory incorporates a low field NMR system, a pyrometer, a spectrophotometer (for pyruvate and EPA concentration and pH measurements) as well as a heating system for the receiver syringe to ensure that the QC process is conducted at a consistent temperature.

Following dissolution, the hyperpolarized solution arrives in the receiver syringe and aliquots are simultaneously delivered to separate chambers within the syringe for measurement. The QC process takes approximately 30 seconds, and the results are displayed on the SPINlab™ display unit and manually compared to acceptance criteria prior to release.

The hyperpolarized product can then be released for consideration of administration to a human research participant.

1.8 Aims of this programme of work

The aims of the work described in thesis were to:

- Extend the use of established preclinical hyperpolarized MR spectroscopic techniques to clinically relevant disease models and interventions, testing the feasibility of a translational research pipeline to identify new applications of hyperpolarized [^{13}C]pyruvate in the diagnosis and management of cardiovascular diseases.
- Use preclinical models to answer questions of immediate relevance to the design and conduct of first-in-human hyperpolarized cardiovascular MR studies.
- Identify novel cardiovascular applications with translational potential for emerging preclinical advances in hyperpolarized MR techniques, including ^{13}C imaging.
- Support the governance applications and technical development necessary for first-in-human hyperpolarized cardiovascular MR studies and coordinate the conduct of these studies.

This remainder of this thesis describes the results of work directed to addressing these aims.

Chapter 2 focuses upon applications of hyperpolarized magnetic resonance to cardiovascular disease associated with diabetes, and includes preclinical work relating to the timing of glucose administration, the need for a washout period for concomitant medication, describes work validating the internal QC processes and the first human cardiovascular hyperpolarized MR experiment.

Chapter 3 describes a programme of basic science studying the interplay between metabolic substrate selection, myocardial energetics and function, utilising a clinically relevant model of the obesity cardiomyopathy.

Work in chapter 4 uses recent developments in hyperpolarized MR imaging to study the regional myocardial responses following myocardial infarction to understand the application of hyperpolarized magnetic resonance to cardiovascular inflammation.

1.9 Appendix 1A: References

1. Townsend N, Bhatnagar P, Wilkins E, Wickramasinghe K, and Rayner M, *Cardiovascular Disease Statistics* 2015: British Heart Foundation.

2. Bloom D, Cafiero E, Jané-Llopis E, Abrahams-Gessel S, Bloom L, and Fathima S *The global economic burden of non-communicable diseases: report by the World Economic Forum and the Harvard School of Public Health.* Geneva: World Economic Forum; 2011,

3. Fuster V *Global burden of cardiovascular disease: time to implement feasible strategies and to monitor results.* Journal of the American College of Cardiology 2014;64(5):520-522

4. Zamorano J L, Bax J, Knuuti J, Sechtem U, Lancellotti P, and Badano L, *The ESC Textbook of Cardiovascular Imaging* 2015: Oxford University Press.

5. Wagner A, Bruder O, Lombardi M, Schwitter J, van Rossum A C, Pilz G, Nothnagel D, Petersen S E, Nagel E, and Prasad S K *European Cardiovascular Magnetic Resonance (EuroCMR) registry-multi national tesults from 57 centers in 15 countries.* Journal of Cardiovascular Magnetic Resonance 2013;15(Suppl 1):O96

6. Pennell D J *Cardiovascular magnetic resonance.* Circulation 2010;121(5):692-705

7. Karamitsos T D, Francis J M, Myerson S, Selvanayagam J B, and Neubauer S *The role of cardiovascular magnetic resonance imaging in heart failure.* Journal of the American College of Cardiology 2009;54(15):1407-1424

8. Myerson S G *Heart valve disease: investigation by cardiovascular magnetic resonance.* Journal of Cardiovascular Magnetic Resonance 2012;14(7)

9. Dungu J N, Valencia O, Pinney J H, Gibbs S D, Rowczenio D, Gilbertson J A, Lachmann H J, Wechalekar A, Gillmore J D, and Whelan C J *CMR-based differentiation of AL and ATTR cardiac amyloidosis.* JACC: Cardiovascular Imaging 2014;7(2):133-142

10. Petersen S E, Selvanayagam J B, Wiesmann F, Robson M D, Francis J M, Anderson R H, Watkins H, and Neubauer S *Left ventricular non-compaction: insights from cardiovascular magnetic resonance imaging.* Journal of the American College of Cardiology 2005;46(1):101-105

11. Yilmaz A, Ferreira V, Klingel K, Kandolf R, Neubauer S, and Sechtem U *Role of cardiovascular magnetic resonance imaging (CMR) in the diagnosis of acute and chronic myocarditis.* Heart Failure Reviews 2013;18(6):747-760

12. Bottini P B, Carr A A, Prisant L M, Flickinger F W, Allison J D, and Gottdiener J S *Magnetic resonance imaging compared to echocardiography to assess left ventricular mass in the hypertensive patient.* American Journal of Hypertension 1995;8(3):221-228

13. Neubauer S *The failing heart—an engine out of fuel.* New England Journal of Medicine 2007;356(11):1140-1151

14. Moschetti K M S, Pinget C, Wagner A, Pilz G, Wasserfallen JB, Schulz-Menger J, Nothnagel D, Dill T, Frank H, Lombardi M, Bruder O, Mahrholdt H, Schwitter J. *Cost evaluation of cardiovascular magnetic resonance versus coronary angiography for the diagnostic work-up of coronary artery disease: application of the European Cardiovascular Magnetic Resonance registry data to the German, United Kingdom, Swiss, and United States health care systems.* Journal of Cardiovascular Magnetic Resonance 2012;14(35)

15. Windecker S, Kolh P, Alfonso F, Collet J-P, Cremer J, Falk V, Filippatos G, Hamm C, Head S J, and Jüni P *2014 ESC/EACTS Guidelines on myocardial revascularization.* European Heart Journal 2014;(35):2541–2619

16. Adler Y, Charron P, Imazio M, Badano L, Barón-Esquivias G, Bogaert J, Brucato A, Gueret P, Klingel K, and Lionis C *2015 ESC Guidelines for the diagnosis and management of pericardial diseases.* European Heart Journal 2015;36(42):2921-2964

17. Neubauer S, Horn M, Cramer M, Harre K, Newell J B, Peters W, Pabst T, Ertl G, Hahn D, and Ingwall J S *Myocardial phosphocreatine-to-ATP ratio is a predictor of mortality in patients with dilated cardiomyopathy.* Circulation 1997;96(7):2190-2196

18. Neubauer S, Krahe T, Schindler R, Horn M, Hillenbrand H, Entzeroth C, Mader H, Kromer E, Riegger G, and Lackner K *^{31}P magnetic resonance spectroscopy in dilated cardiomyopathy and coronary artery disease. Altered cardiac high-energy phosphate metabolism in heart failure.* Circulation 1992;86(6):1810-1818

19. Neubauer S, Horn M, Pabst T, Gödde M, Lübke D, Jilling B, Hahn D, and Ertl G *Contributions of ^{31}P-magnetic resonance spectroscopy to the understanding of dilated heart muscle disease.* European Heart Journal 1995;16:115-118

20. Holloway C J, Suttie J, Dass S, and Neubauer S *Clinical cardiac magnetic resonance spectroscopy.* Progress in Cardiovascular Diseases 2011;54(3):320-327

21. Bailey I A, Gadian D G, Matthews P M, Radda G K, and Seeley P J *Studies of metabolism in the isolated, perfused rat heart using ^{13}C NMR.* FEBS letters 1981;123(2):315-318

22. Taegtmeyer H *Cardiac metabolism as a target for the treatment of heart failure.* Circulation 2004;110(8):894-896

23. Malloy C R, Sherry A D, and Jeffrey F M H *Carbon flux through citric acid cycle pathways in perfused heart by ^{13}C NMR spectroscopy.* FEBS letters 1987;212(1):58-62

24. Chatham J C and Seymour A L *Cardiac carbohydrate metabolism in Zucker diabetic fatty rats.* Cardiovascular research 2002;55(1):104-112

25. Sherry A D, Malloy C R, Zhao P, and Thompson J R *Alterations in substrate utilization in the reperfused myocardium: a direct analysis by ^{13}C NMR.* Biochemistry 1992;31(20):4833-4837

26. Ziegler A, Zaugg C E, Buser P T, Seelig J, and Künnecke B *Non-invasive measurements of myocardial carbon metabolism using in vivo ^{13}C NMR spectroscopy.* NMR in biomedicine 2002;15(3):222-234

27. Bloch F *Nuclear induction.* Physical review 1946;70(7-8):460

28. Purcell E M, Torrey H, and Pound R V *Resonance absorption by nuclear magnetic moments in a solid.* Physical review 1946;69(1-2):37

29. McRobbie D, Moore E, Graves M, and Prince M, *MRI: From Picture to Proton* 2007: Cambridge University Press.

30. Clendinen C S, Lee-McMullen B, Williams C M, Stupp G S, Vandenborne K, Hahn D A, Walter G A, and Edison A S *^{13}C NMR metabolomics: applications at natural abundance.* Analytical chemistry 2014;86(18):9242-9250

31. Piechnik S K, Ferreira V M, Dall'Armellina E, Cochlin L E, Greiser A, Neubauer S, and Robson M D *Shortened Modified Look-Locker Inversion recovery (ShMOLLI) for clinical myocardial T1-mapping at 1.5 and 3 T within a 9 heartbeat breathhold.* Journal of Cardiovascular Magnetic Resonance 2010;12(1):69

32. Hess A T, Bissell M M, Ntusi N A, Lewis A J, Tunnicliffe E M, Greiser A, Stalder A F, Francis J M, Myerson S G, and Neubauer S *Aortic 4D flow: Quantification of signal-to-noise ratio as a function of field strength and contrast enhancement for 1.5 T, 3T, and 7T.* Magnetic Resonance in Medicine 2015;73(5):1864-1871

33. Rodgers C T, Clarke W T, Snyder C, Vaughan J T, Neubauer S, and Robson M D *Human cardiac ^{31}P magnetic resonance spectroscopy at 7 tesla.* Magnetic Resonance in Medicine 2014;72(2):304-315

34. Buendía F, Cano Ó, Sánchez-Gómez J M, Igual B, Osca J, Sancho-Tello M J, Olagüe J, and Salvador A *Cardiac magnetic resonance imaging at 1.5 T in patients with cardiac rhythm devices.* Europace 2011;13(4):533-538

35. Schroeder M A, Clarke K, Neubauer S, and Tyler D J *Hyperpolarized magnetic resonance A novel technique for the In vivo assessment of cardiovascular disease.* Circulation 2011;124(14):1580-1594

36. Tyler D J *Cardiovascular applications of hyperpolarized MRI.* Current Cardiovascular Imaging Reports 2011;4(2):108-115

37. Ardenkjaer-Larsen J H *On the present and future of dissolution-DNP.* Journal of Magnetic Resonance 2016;264:3-12

38. Natterer J and Bargon J *Parahydrogen induced polarization.* Progress in Nuclear Magnetic Resonance Spectroscopy 1997;31(4):293-315

39. Reineri F, Boi T, and Aime S *ParaHydrogen Induced Polarization of ^{13}C carboxylate resonance in acetate and pyruvate.* Nature Communications 2015;6:5858

40. Oros A-M and Shah N J *Hyperpolarized xenon in NMR and MRI.* Physics in Medicine and Biology 2004;49(20):R105

41. Overhauser A W *Polarization of nuclei in metals.* Physical Review 1953;92(2):411

42. Carver T and Slichter C *Polarization of nuclear spins in metals.* Physical Review 1953;92(1):212

43. Wind R A, Anthonio F, Duijvestijn M, Smidt J, Trommel J, and De Vette G *Experimental setup for enhanced ^{13}C NMR spectroscopy in solids using dynamic nuclear polarization.* Journal of Magnetic Resonance 1983;52(3):424-434

44. Duijvestijn M, Van Der Lugt C, Smidt J, Wind R, Zilm K, and Staplin D *^{13}C NMR spectroscopy in diamonds using dynamic nuclear polarization.* Chemical Physics Letters 1983;102(1):25-28

45. Abragam A and Goldman M *Principles of dynamic nuclear polarisation.* Reports on Progress in Physics 1978;41(3):395

46. Eichhorn T R, Takado Y, Salameh N, Capozzi A, Cheng T, Hyacinthe J-N, Mishkovsky M, Roussel C, and Comment A *Hyperpolarization without persistent radicals for in vivo real-time metabolic imaging.* Proceedings of the National Academy of Sciences 2013;110(45):18064-18069

47. Banerjee D, Shimon D, Feintuch A, Vega S, and Goldfarb D *The interplay between the solid effect and the cross effect mechanisms in solid state ^{13}C DNP at 95GHz using trityl radicals.* Journal of Magnetic Resonance 2013;230:212-219

48. Hovav Y, Feintuch A, and Vega S *Theoretical aspects of dynamic nuclear polarization in the solid state–the solid effect.* Journal of Magnetic Resonance 2010;207(2):176-189

49. Smith A A, Corzilius B, Haze O, Swager T M, and Griffin R G *Observation of strongly forbidden solid effect dynamic nuclear polarization transitions via electron-electron double resonance detected NMR.* The Journal of Chemical Physics 2013;139(21):214201

50. Maly T, Debelouchina G T, Bajaj V S, Hu K-N, Joo C-G, Mak–Jurkauskas M L, Sirigiri J R, van der Wel P C, Herzfeld J, and Temkin R J *Dynamic nuclear polarization at high magnetic fields.* The Journal of Chemical Physics 2008;128(5):052211

51. Hovav Y, Feintuch A, and Vega S *Theoretical aspects of dynamic nuclear polarization in the solid state–the cross effect.* Journal of Magnetic Resonance 2012;214:29-41

52. Goldman M *Overview of spin temperature, thermal mixing and dynamic nuclear polarization.* Applied Magnetic Resonance 2008;34(3-4):219-226

53. Ardenkjær-Larsen J H, Fridlund B, Gram A, Hansson G, Hansson L, Lerche M H, Servin R, Thaning M, and Golman K *Increase in signal-to-noise ratio of >10,000 times in liquid-state NMR.* Proceedings of the National Academy of Sciences 2003;100(18):10158-10163

54. Golman K, Ardenkjær-Larsen J H, Petersson J S, Månsson S, and Leunbach I *Molecular imaging with endogenous substances.* Proceedings of the National Academy of Sciences 2003;100(18):10435-10439

55. Bruhn H, Frahm J, Gyngell M L, Merboldt K D, Hänicke W, Sauter R, and Hamburger C *Noninvasive differentiation of tumors with use of localized ^{1}H MR spectroscopy in vivo: initial experience in patients with cerebral tumors.* Radiology 1989;172(2):541-548

56. Halestrap A P and Price N T *The proton-linked monocarboxylate transporter (MCT) family: structure, function and regulation.* Biochemical Journal 1999;343(2):281-299

57. Merritt M E, Harrison C, Storey C, Jeffrey F M, Sherry A D, and Malloy C R *Hyperpolarized ^{13}C allows a direct measure of flux through a single enzyme-catalyzed step by NMR.* Proceedings of the National Academy of Sciences 2007;104(50):19773-19777

58. Schroeder M A, Atherton H J, Cochlin L E, Clarke K, Radda G K, and Tyler D J *The effect of hyperpolarized tracer concentration on myocardial uptake and metabolism.* Magnetic Resonance in Medicine 2009;61(5):1007-1014

59. Bastiaansen J A, Cheng T, Mishkovsky M, Duarte J M, Comment A, and Gruetter R In vivo *enzymatic activity of acetylCoA synthetase in skeletal muscle revealed by ^{13}C turnover from hyperpolarized [1-^{13}C] acetate to [1-^{13}C] acetylcarnitine.* Biochimica et Biophysica Acta 2013;1830(8):4171-4178

60. Ball D R, Rowlands B, Dodd M S, Le Page L, Ball V, Carr C A, Clarke K, and Tyler D J *Hyperpolarized butyrate: A metabolic probe of short chain fatty acid metabolism in the heart.* Magnetic Resonance in Medicine 2014;71(5):1663-1669

61. Yoshihara H, Bastiaansen J A, Karlsson M, Lerche M H, Comment A, and Schwitter J *Myocardial fatty acid metabolism probed with hyperpolarized [1-^{13}C]octanoate.* Journal of Cardiovascular Magnetic Resonance 2015;17(Suppl 1):O101

62. Gallagher F A, Kettunen M I, Hu D-E, Jensen P R, Karlsson M, Gisselsson A, Nelson S K, Witney T H, Bohndiek S E, and Hansson G *Production of hyperpolarized [1, 4-$^{13}C_2$] malate from [1, 4-$^{13}C_2$] fumarate is a marker of cell necrosis and treatment response in tumors.* Proceedings of the National Academy of Sciences 2009;106(47):19801-19806

63. Clatworthy M R, Kettunen M I, Hu D-E, Mathews R J, Witney T H, Kennedy B W, Bohndiek S E, Gallagher F A, Jarvis L B, and Smith K G *Magnetic resonance imaging with hyperpolarized [1, 4-$^{13}C_2$] fumarate allows detection of early renal acute tubular necrosis.* Proceedings of the National Academy of Sciences 2012;109(33):13374-13379

64. Kim R J, Wu E, Rafael A, Chen E-L, Parker M A, Simonetti O, Klocke F J, Bonow R O, and Judd R M *The use of contrast-enhanced magnetic resonance imaging to identify reversible myocardial dysfunction.* New England Journal of Medicine 2000;343(20):1445-1453

65. Chaumeil M M, Larson P E, Yoshihara H A, Danforth O M, Vigneron D B, Nelson S J, Pieper R O, Phillips J J, and Ronen S M *Non-invasive in vivo assessment of IDH1 mutational status in glioma.* Nature Communications 2013;4

66. Chaumeil M M, Larson P E, Woods S M, Cai L, Eriksson P, Robinson A E, Lupo J M, Vigneron D B, Nelson S J, and Pieper R O *Hyperpolarized [1-^{13}C] glutamate: a metabolic imaging biomarker of IDH1 mutational status in glioma.* Cancer research 2014;74(16):4247-4257

67. Gallagher F A, Kettunen M I, Day S E, Hu D-E, Ardenkjær-Larsen J H, Jensen P R, Karlsson M, Golman K, Lerche M H, and Brindle K M *Magnetic resonance imaging of pH in vivo using hyperpolarized ^{13}C-labelled bicarbonate.* Nature 2008;453(7197):940-943

68. Schroeder M A, Swietach P, Atherton H J, Gallagher F A, Lee P, Radda G K, Clarke K, and Tyler D J *Measuring intracellular pH in the heart using hyperpolarized carbon dioxide and bicarbonate: a ^{13}C and ^{31}P magnetic resonance spectroscopy study.* Cardiovascular Research 2010;86(1):82-91

69. Aptekar J W, Cassidy M C, Johnson A C, Barton R A, Lee M, Ogier A C, Vo C, Anahtar M N, Ren Y, and Bhatia S N *Silicon nanoparticles as hyperpolarized magnetic resonance imaging agents.* ACS Nano 2009;3(12):4003-4008

70. Pan G-H, Barras A, Boussekey L, Qu X, Addad A, and Boukherroub R *Preparation and characterization of decyl-terminated silicon nanoparticles encapsulated in lipid nanocapsules.* Langmuir 2013;29(41):12688-12696

71. Hu S, Yoshihara H A, Bok R, Zhou J, Zhu M, Kurhanewicz J, and Vigneron D B *Use of hyperpolarized [1-^{13}C] pyruvate and [2-^{13}C] pyruvate to probe the effects of the anticancer agent dichloroacetate on mitochondrial metabolism in vivo in the normal rat.* Magnetic Resonance Imaging 2012;30(10):1367-1372

72. Schroeder M A, Cochlin L E, Heather L C, Clarke K, Radda G K, and Tyler D J *In vivo assessment of pyruvate dehydrogenase flux in the heart using hyperpolarized carbon-13 magnetic resonance.* Proceedings of the National Academy of Sciences 2008;105(33):12051-12056

73. Lau A Z, Chen A P, Ghugre N R, Ramanan V, Lam W W, Connelly K A, Wright G A, and Cunningham C H *Rapid multislice imaging of hyperpolarized ^{13}C pyruvate and bicarbonate in the heart.* Magnetic Resonance in Medicine 2010;64(5):1323-1331

74. Lau A Z, Chen A P, Hurd R E, and Cunningham C H *Spectral–spatial excitation for rapid imaging of DNP compounds.* NMR in Biomedicine 2011;24(8):988-996

75. Miller J J, Lau A Z, Teh I, Schneider J E, Kinchesh P, Smart S, Ball V, Sibson N R, and Tyler D J *Robust and high resolution hyperpolarized metabolic imaging of the rat heart at 7 t with 3d spectral-spatial EPI.* Magnetic Resonance in Medicine 2015;

76. Zierhut M L, Yen Y-F, Chen A P, Bok R, Albers M J, Zhang V, Tropp J, Park I, Vigneron D B, and Kurhanewicz J *Kinetic modeling of hyperpolarized ^{13}C 1-pyruvate*

metabolism in normal rats and TRAMP mice. Journal of Magnetic Resonance 2010;202(1):85-92

77. Stanley W C, Recchia F A, and Lopaschuk G D *Myocardial substrate metabolism in the normal and failing heart.* Physiological Reviews 2005;85(3):1093-1129

78. Camici P, Marraccini P, Marzilli M, Lorenzoni R, Buzzigoli G, Puntoni R, Boni C, Bellina C, Klassen G, and L'Abbate A *Coronary hemodynamics and myocardial metabolism during and after pacing stress in normal humans.* American Journal of Physiology - Endocrinology and Metabolism 1989;257(3):309-317

79. Sugden M C and Holness M J *Recent advances in mechanisms regulating glucose oxidation at the level of the pyruvate dehydrogenase complex by PDKs.* American Journal of Physiology - Endocrinology And Metabolism 2003;284(5):855-862

80. Pengfei W, Juichi S, Yu Z, Jaskiewicz J, Popov M K, and Harris A R *Starvation and diabetes increase the amount of pyruvate dehydrogenase kinase isoenzyme 4 in rat heart.* Biochemical Journal 1998;329(1):197-201

81. Sugden M C and Holness M J *Mechanisms underlying regulation of the expression and activities of the mammalian pyruvate dehydrogenase kinases.* Archives of Physiology and Biochemistry 2006;112(3):139-149

82. Golman K and Thaning M *Real-time metabolic imaging.* Proceedings of the National Academy of Sciences 2006;103(30):11270-11275

83. Atherton H J, Schroeder M A, Dodd M S, Heather L C, Carter E E, Cochlin L E, Nagel S, Sibson N R, Radda G K, and Clarke K *Validation of the in vivo assessment of pyruvate dehydrogenase activity using hyperpolarised 13C MRS.* NMR in biomedicine 2011;24(2):201-208

84. Schroeder M A, Atherton H J, Heather L C, Griffin J L, Clarke K, Radda G K, and Tyler D J *Determining the in vivo regulation of cardiac pyruvate dehydrogenase based on label flux from hyperpolarised [1-^{13}C] pyruvate.* NMR in Biomedicine 2011;24(8):980-987

85. Wynn R M, Kato M, Chuang J L, Tso S-C, Li J, and Chuang D *T Pyruvate dehydrogenase kinase-4 structures reveal a metastable open conformation fostering robust core-free basal activity.* Journal of Biological Chemistry 2008;283(37):25305-25315

86. Malmberg K, Rydén L, Efendic S, Herlitz J, Nicol P, Waldenstrom A, Wedel H, and Welin L *Randomized trial of insulin-glucose infusion followed by subcutaneous insulin treatment in diabetic patients with acute myocardial infarction (DIGAMI study): effects on mortality at 1 year.* Journal of the American College of Cardiology 1995;26(1):57-65

87. Bersin R M, Wolfe C, Kwasman M, Lau D, Klinski C, Tanaka K, Khorrami P, Henderson G N, de Marco T, and Chatterjee K *Improved hemodynamic function and mechanical efficiency in congestive heart failure with sodium dichloroacetate.* Journal of the American College of Cardiology 1994;23(7):1617-1624

88. Fragasso G, Palloshi A, Puccetti P, Silipigni C, Rossodivita A, Pala M, Calori G, Alfieri O, and Margonato A *A randomized clinical trial of trimetazidine, a partial free fatty acid oxidation inhibitor, in patients with heart failure.* Journal of the American College of Cardiology 2006;48(5):992-998

89. Abozguia K, Elliott P, McKenna W, Phan T T, Nallur-Shivu G, Ahmed I, Maher A R, Kaur K, Taylor J, Henning A, Ashrafian H, Watkins H and Frenneaux M *Metabolic modulator perhexiline corrects energy deficiency and improves exercise capacity in symptomatic hypertrophic cardiomyopathy.* Circulation 2010;122(16):1562-1569

90. Horowitz J D and Chirkov Y Y *Perhexiline and Hypertrophic Cardiomyopathy: A New Horizon for Metabolic Modulation.* Circulation 2010;122(16):1547-1549

91. Selker H P, Beshansky J R, Sheehan P R, Massaro J M, Griffith J L, D'Agostino R B, Ruthazer R, Atkins J M, Sayah A J, and Levy M K *Out-of-hospital administration of intravenous glucose-insulin-potassium in patients with suspected acute coronary syndromes: the IMMEDIATE randomized controlled trial.* Journal of the American Medical Association 2012;307(18):1925-1933

92. Diaz R, Paolasso E A, Piegas L S, Tajer C D, Moreno M G, Corvalán R, Isea J E, Romero G, and Latinoamérica E C *Metabolic Modulation of Acute Myocardial Infarction the ECLA Glucose-Insulin-Potassium Pilot Trial.* Circulation 1998;98(21):2227-2234

93. Dodd M S, Ball D R, Schroeder M A, Le Page L M, Atherton H J, Heather L C, Seymour A-M, Ashrafian H, Watkins H, and Clarke K *In vivo alterations in cardiac metabolism and function in the spontaneously hypertensive rat heart.* Cardiovascular Research 2012;95(1):69-76

94. Atherton H J, Dodd M S, Heather L C, Schroeder M A, Griffin J L, Radda G K, Clarke K, and Tyler D J *Role of pyruvate dehydrogenase inhibition in the development of hypertrophy in the hyperthyroid rat heart a combined magnetic resonance imaging and hyperpolarized magnetic resonance spectroscopy study.* Circulation 2011;123(22):2552-2561

95. Dodd M S, Atherton H J, Carr C A, Stuckey D J, West J A, Griffin J L, Radda G K, Clarke K, Heather L C, and Tyler D J *Impaired in vivo mitochondrial Krebs cycle activity after myocardial infarction assessed using hyperpolarized magnetic resonance spectroscopy.* Circulation: Cardiovascular Imaging 2014;7(6):895-904

96. Schroeder M A, Lau A Z, Chen A P, Gu Y, Nagendran J, Barry J, Hu X, Dyck J R, Tyler D J, and Clarke K *Hyperpolarized ^{13}C magnetic resonance reveals early-and late-onset changes to in vivo pyruvate metabolism in the failing heart.* European journal of heart failure 2013;15(2):130-140

97. Le Page L M, Rider O J, Lewis A J, Ball V, Clarke K, Johansson E, Carr C A, Heather L C, and Tyler D J *Increasing pyruvate dehydrogenase flux as a treatment for diabetic cardiomyopathy: a combined ^{13}C hyperpolarized magnetic resonance and echocardiography study.* Diabetes 2015;64(8):2735-2743

98. Rider O J and Tyler D J *Clinical implications of cardiac hyperpolarized magnetic resonance imaging.* Journal of Cardiovascular Magnetic Resonance 2013;15(1):1-9

99. Aquaro G D, Frijia F, Positano V, Menichetti L, Santarelli M F, Ardenkjaer-Larsen J H, Wiesinger F, Lionetti V, Romano S L, and Bianchi G *Three-dimensional magnetic resonance mapping of cardiac metabolism by hyperpolarized ^{13}C-pyruvate in a pig model of ischemia-reperfusion.* JACC: Cardiovascular Imaging 2013;6(6):743

100. O h-Ici D, Wespi P, Busch J, Wissmann L, Krajewski M, Weiss K, Sigfridsson A, Messroghli D, and Kozerke S *Hyperpolarized Metabolic MR Imaging of Acute Myocardial Changes and Recovery after Ischemia-Reperfusion in a Small-Animal Model.* Radiology 2015:151332

101. Gerber B L, Raman S V, Nayak K, Epstein F H, Ferreira P, Axel L, and Kraitchman D L *Myocardial first-pass perfusion cardiovascular magnetic resonance: history, theory, and current state of the art.* Journal of Cardiovascular Magnetic Resonance 2008;10(1):18

102. Morton G, Chiribiri A, Ishida M, Hussain S T, Schuster A, Indermuehle A, Perera D, Knuuti J, Baker S, and Hedström E *Quantification of absolute myocardial perfusion in patients with coronary artery disease: comparison between cardiovascular magnetic resonance and positron emission tomography.* Journal of the American College of Cardiology 2012;60(16):1546-1555

103. Lau A Z, Miller J J, Robson M D, and Tyler D J *Cardiac perfusion imaging using hyperpolarized ^{13}C urea using flow sensitizing gradients.* Magnetic Resonance in Medicine 2015;75(4):1474-83

104. Lau A Z, Miller J J, Robson M D, and Tyler D J *Simultaneous assessment of cardiac metabolism and perfusion using copolarized [1-^{13}C] pyruvate and ^{13}C-urea.* Magnetic Resonance in Medicine 2016;

105. Camici P G, Prasad S K, and Rimoldi O E *Stunning, hibernation, and assessment of myocardial viability.* Circulation 2008;117(1):103-114

106. Magnusson P, Johansson E, Månsson S, Petersson J S, Chai C M, Hansson G, Axelsson O, and Golman K *Passive catheter tracking during interventional MRI using hyperpolarized ^{13}C.* Magnetic Resonance in Medicine 2007;57(6):1140-1147

107. Caetano-Anollés G, Kim H S, and Mittenthal J E *The origin of modern metabolic networks inferred from phylogenomic analysis of protein architecture.* Proceedings of the National Academy of Sciences 2007;104(22):9358-9363

108. Wang Y, Li L, Ma C, Gao C, Tao F, and Xu P *Engineering of cofactor regeneration enhances (2S, 3S)-2, 3-butanediol production from diacetyl.* Scientific Reports 2013;3

109. Randle P, Garland P, Hales C, and Newsholme E *The glucose fatty-acid cycle its role in insulin sensitivity and the metabolic disturbances of diabetes mellitus.* The Lancet 1963;281(7285):785-789

110. Hermann H P, Pieske B, Schwarzmöller E, Keul J, Just H, and Hasenfuss G *Haemodynamic effects of intracoronary pyruvate in patients with congestive heart failure: an open study.* The Lancet 1999;353(9161):1321-1323

111. Hermann H P, Arp J, Pieske B, Kögler H, Baron S, Janssen P M, and Hasenfuss G *Improved systolic and diastolic myocardial function with intracoronary pyruvate in patients with congestive heart failure.* European Journal of Heart Failure 2004;6(2):213-218

112. Schillinger W, Hünlich M, Sossalla S, Hermann H-P, and Hasenfuss G *Intracoronary pyruvate in cardiogenic shock as an adjunctive therapy to catecholamines and intra-aortic balloon pump shows beneficial effects on hemodynamics.* Clinical Research in Cardiology 2011;100(5):433-438

113. Nelson S J, Kurhanewicz J, Vigneron D B, Larson P E, Harzstark A L, Ferrone M, van Criekinge M, Chang J W, Bok R, and Park I *Metabolic imaging of patients with prostate cancer using hyperpolarized [1-^{13}C] pyruvate.* Science Translational Medicine 2013;5(198):ra108

114. European Commission Health and Consumers Directorate General *EudraLex - Volume 4 Good manufacturing practice (GMP) Guidelines.* 2011;

115. Ardenkjaer-Larsen J H, Leach A M, Clarke N, Urbahn J, Anderson D, and Skloss T W *Dynamic nuclear polarization polarizer for sterile use intent.* NMR in biomedicine 2011;24(8):927-932

Chapter 2: Clinical translation of hyperpolarized MR for type II diabetes

2.1 Abstract

Hyperpolarized magnetic resonance using [1-^{13}C]pyruvate shows particular promise for the assessment of metabolic processes underlying cardiac functional impairment in disease states. In addition to posing a substantial clinical problem, type II diabetes has several properties which render it an attractive model system for proof-of-concept clinical hyperpolarization studies. This chapter describes preclinical work conducted with the aim of informing the design of a clinical study in type II diabetes, the installation and validation of clinical hyperpolarization equipment in Oxford, the timeline of the production of consumables for clinical hyperpolarization, and preliminary experience with human hyperpolarized ^{13}C spectroscopy.

2.2 Design of a first-in-human cardiovascular hyperpolarized [1-^{13}C]pyruvate study

Key considerations for the design of a successful proof-of-concept study using hyperpolarized [1-^{13}C]pyruvate for cardiovascular applications in humans include the requirements for a disease state which:

- is common and poses a substantial clinical problem
- affects the myocardium globally, and is therefore suitable for evaluation using both spectroscopic and imaging acquisition strategies
- is likely to show a substantial effect size upon hyperpolarized MR indices
- is likely to demonstrate future clinical applications of the method
- affects an easy to identify and relatively clinically homogenous patient group

Type II diabetes is a disease state that addresses these requirements and was selected for first human studies using hyperpolarized cardiovascular MR in this centre. Preclinical data from rodent models of diabetes provided a foundation for the design of a human study, though several specific questions remained to be clarified.

2.3 Rationale for selection of type II diabetes as a study disease state

Data from the Framingham study demonstrate that the incidence of congestive heart failure is increased in men (relative risk (RR) 2.4) and women (RR 5.1) with diabetes, independent of the effects of age, blood pressure, weight, dyslipidaemia and coronary artery disease status[1]. The concept of a distinct cardiomyopathy associated with diabetes was introduced following a pathological analysis of the hearts of four patients with advanced diabetes and

heart failure without other apparent cause[2], which demonstrated evidence of ventricular hypertrophy and fibrosis.

The term 'diabetic cardiomyopathy', though still contentious, is today generally used to refer to myocardial disease arising in the presence of diabetes and the absence of other known causal factors. It poses a substantial clinical problem, as the prevalence of type II diabetes is increasing rapidly; the number of people affected internationally is projected to grow from 135 million in 1995 to 300 million 2025[3]. Cardiovascular disease is a leading cause of premature mortality in this patient group[4].

CMR studies have advanced our understanding of the cardiovascular phenotype of diabetic cardiomyopathy. Alongside mild LV hypertrophy and diastolic dysfunction, abnormal cardiac energy metabolism is one consistent finding in such work and may represent a therapeutic target[5, 6]. For example, in a study of 21 patients with normal LV systolic function and no evidence of coronary artery disease, both rest and stress skeletal muscle and resting cardiac high energy phosphorus metabolism were abnormal and correlated with other markers of disease severity[7]. More recently, using a comprehensive panel of contemporary CMR sequences, patients with stable type II diabetes, in whom coronary artery disease was excluded by CT coronary angiography, were shown to manifest a cardiac phenotype that included concentric LV remodelling, impairment of energetics both at rest and to a greater degree during exercise stress, and impaired myocardial perfusion and oxygenation[8].

Altered substrate metabolism is a key candidate mechanism linking type II diabetes and other disease states to the development of cardiac energetic and functional impairment[9]. The evidence and mechanisms underlying this hypothesis are discussed more fully in Chapter 3, where this was a specific focus of research. In brief, dominant cardiac fat

metabolism is a highly consistent observation in both animal models of diabetes[10, 11] and humans with type II diabetes[12, 13]. The magnitude of the reciprocal impairment of carbohydrate metabolism is substantial, with a 65 % reduction in PDH flux reported in preclinical hyperpolarized MR studies[14]. The potential clinical importance of an ability to measure PDH flux *in vivo* was highlighted by the finding that pharmacological restoration of PDH flux in a model of diabetes was associated with improvement in cardiac diastolic function[15]. These data and others support a potential role for hyperpolarized CMR measures of PDH flux as both a biomarker and a therapeutic target in type II diabetes, therefore meeting the desirable criteria for an initial disease state for proof-of-principle clinical studies using hyperpolarized [1-^{13}C]pyruvate. There are, however, several potential confounding factors that warrant consideration during the design of such a study.

2.4 Preclinical work to address potentially confounding factors

2.4.1 The effects of diurnal variation and dietary intake

The first important potentially confounding factor to be understood during the design of a human hyperpolarized CMR study in type II diabetes is the effect of diurnal variation and dietary status (fed versus fasted), which can dramatically alter cardiac substrate metabolism. During the fasted, rested state, the healthy heart relies almost exclusively upon the beta oxidation of fatty acids for ATP generation, but following dietary intake of carbohydrates during feeding, there is a shift towards a greater degree of glucose metabolism, regulated in part by dynamic and coordinated gene programme expression[16]. Cardiac metabolism has thus been described as a continually "moving target"[17]. A failure to control for normal metabolic oscillation has been thought to underlie seemingly contradictory findings in historical experiments, and international consensus statements now recommend that

metabolic experiments are conducted at a similar time of day, in a defined fasted or fed state[17].

By consensus, it has been customary to mitigate this potentially confounding factor in preclinical rodent hyperpolarized MR experiments by scanning only in morning hours (0600-1200), in the fed state (as rodents feed overnight). The intention of standardising carbohydrate availability in this manner is to ensure that PDH flux is not unduly underestimated due to low carbohydrate availability. This approach is in contrast to the usual strategy in cardiovascular PET studies using ^{18}F-FDG, both preclinically and clinically, where the intention is usually to *suppress* cardiac glucose uptake as far as possible prior to imaging. This is because the usual clinical indications for PET involve the identification of focal areas of abnormally prominent glucose uptake which might indicate disease, and the high background signal from heart muscle can hinder the identification of these areas. Approaches used by the PET community for the suppression of cardiac glucose uptake include scanning in the fasted state[18], a diet high in fat and low in carbohydrate,[19] and the administration of lipolytic drugs such as heparin[20].

In order to standardise carbohydrate availability in human cardiovascular hyperpolarized MR studies, it will be necessary to conduct studies at a similar time of day in the fed state, though whether the variability of measures could be reduced by standardising the carbohydrate load in both clinical and preclinical settings is unknown.

2.4.1.1 Cardiac PDH flux increases rapidly following glucose infusion

In view of this uncertainty, we first used a rodent model to investigate the changes in hyperpolarized MR indices of cardiac metabolism that followed glucose administration whilst in the fasted state. The intention of the experiment was to understand the temporal changes in hyperpolarized MR indices of cardiac metabolism that occur following glucose

administration and to determine whether standardised carbohydrate provision could improve the reproducibility of preclinical hyperpolarized MR experiments. Because it is challenging to administer a consistent dose orally in this setting, we instead elected to use an intravenous infusion of 1 g/kg glucose solution following an overnight fast; this dose was chosen to reflect that routinely used for human oral glucose tolerance tests (OGTTs). At a predetermined time point (either 0, 1, 5, 15 or 30 minutes, n = 6 biological replicates per timepoint) following the intravenous glucose infusion (the 0 minute time point reflects co-infusion of glucose via a separate venous catheter), a 1 ml bolus of 80 mM hyperpolarized [1-^{13}C]pyruvate was infused intravenously via a tail vein catheter and cardiac metabolism assessed by recording the resulting NMR signals localised from an axial slice placed over the heart. The data were subsequently fitted to a kinetic model to estimate rates of label incorporation as previously described[21]; data from at least 5 of the 6 biological replicates at each timepoint were of sufficient quality (defined as scaled fitting error < 20%) for reliable model fitting and were included. Each time point following glucose infusion was tested on a separate morning, and findings were then compared to those measured in the usual fed state. Full experimental methodological details are described are described in Appendix 2A (page 101).

At the 0 minute time point (co-infusion of glucose and hyperpolarized [1-^{13}C]pyruvate), cardiac [1-^{13}C]bicarbonate (reflecting PDH flux) was low but detectable (0.0030 ± 0.0009 s^{-1}). There was a however a significant increase in PDH flux when glucose was infused 1 minute prior to hyperpolarized [1-^{13}C]pyruvate, which was sustained at each of the following time points subsequently assessed (mean PDH flux measured between 1 – 30 minutes following infusion 0.014 ± 0.003 s^{-1} versus mean PDH flux at 0 minutes 0.0030±05 and ** $P < 0.01$ by Kruskall-Wallis test).

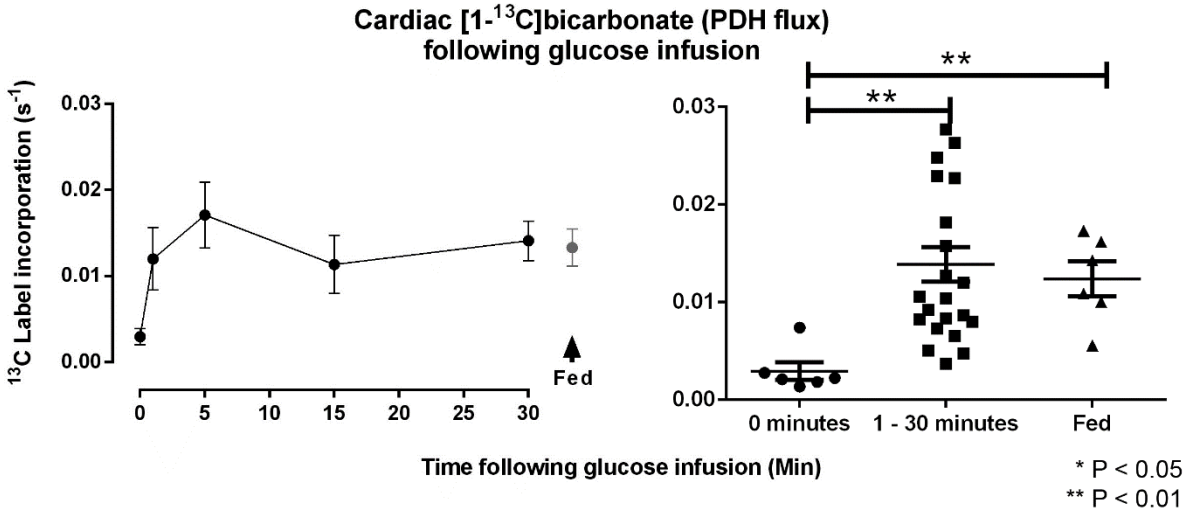


Figure 2.2: An intravenous glucose infusion leads to an increase in cardiac PDH flux within 1 minute, n = 5-6 evaluable datasets per time point; statistical comparison by Kruskall-Wallis test with multiple comparison correction by Dunn's test.

The magnitude of PDH flux measured at greater than or equal to 1 minute following the infusion was similar to that seen in the fed state (depicted as a separate point in Figure 2.1), though the glucose infusion strategy did not appear to reduce the variability of these hyperpolarized MR indices of metabolism. Therefore, these findings did not support a change from the current experimental practice (scanning in the fed state between the hours of 0600 – 1200) to the use of fasting and standardised glucose infusions to improve reproducibility in preclinical studies using hyperpolarized [1-^{13}C]pyruvate.

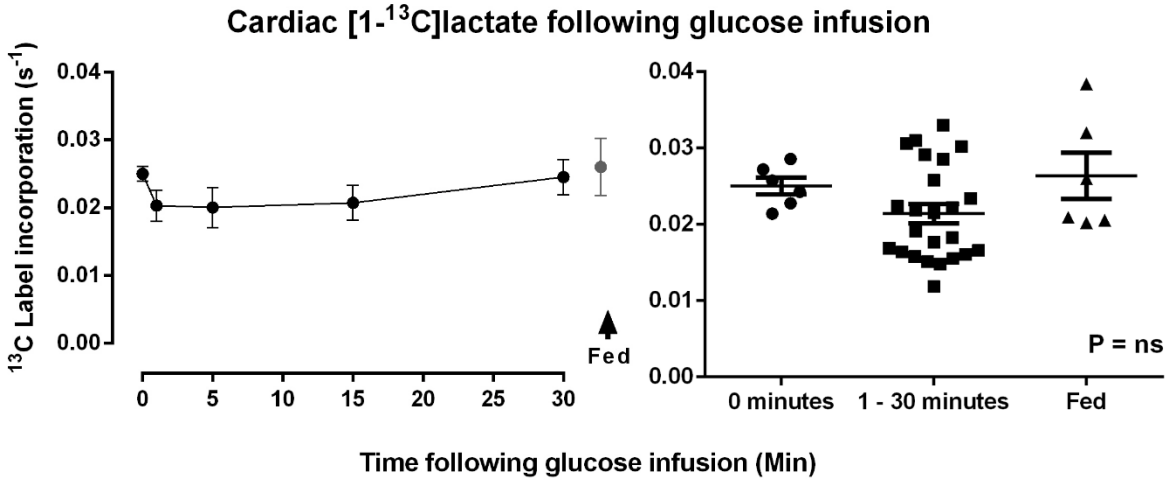


Figure 2.1: No significant change in cardiac [1-^{13}C]lactate label incorporation following glucose infusion; n = 5-6 evaluable datasets per time point; statistical comparison by Kruskall-Wallis test.

As expected, there were no significant changes in the rates of label incorporation into cardiac [1-^{13}C]lactate following glucose infusion (In view of this uncertainty, we first used a rodent model to investigate the changes in hyperpolarized MR indices of cardiac metabolism that followed glucose administration whilst in the fasted state. The intention of the experiment was to understand the temporal changes in hyperpolarized MR indices of cardiac metabolism that occur following glucose administration and to determine whether standardised carbohydrate provision could improve the reproducibility of preclinical hyperpolarized MR experiments. Because it is challenging to administer a consistent dose orally in this setting, we instead elected to use an intravenous infusion of 1 g/kg glucose solution following an overnight fast; this dose was chosen to reflect that routinely used for human oral glucose tolerance tests (OGTTs). At a predetermined time point (either 0, 1, 5, 15 or 30 minutes, n = 6 biological replicates per timepoint) following the intravenous glucose infusion (the 0 minute time point reflects co-infusion of glucose via a separate venous catheter), a 1 ml bolus of 80 mM hyperpolarized [1-^{13}C]pyruvate was infused intravenously via a tail vein catheter and cardiac metabolism assessed by recording the resulting NMR signals localised from an axial slice placed over the heart. The data were subsequently fitted to a kinetic model to estimate rates of label incorporation as previously described[21]; data from at least 5 of the 6 biological replicates at each timepoint were of sufficient quality (defined as scaled fitting error < 20%) for reliable model fitting and were included. Each time point following glucose infusion was tested on a separate morning, and findings were then compared to those measured in the usual fed state. Full experimental methodological details are described are described in Appendix 2A (page 101).

At the 0 minute time point (co-infusion of glucose and hyperpolarized [1-^{13}C]pyruvate), cardiac [1-^{13}C]bicarbonate (reflecting PDH flux) was low but detectable (0.0030 ± 0.0009 s^{-1}). There was a however a significant increase in PDH flux when glucose was infused 1

minute prior to hyperpolarized [1-^{13}C]pyruvate, which was sustained at each of the following time points subsequently assessed (mean PDH flux measured between 1 – 30 minutes following infusion 0.014 ± 0.003 s^{-1} versus mean PDH flux at 0 minutes 0.0030±05 and ** P < 0.01 by Kruskall-Wallis test).

) and no change in the rate of label incorporation into [1-^{13}C]alanine.

The rate of increase of PDH flux following a glucose infusion was surprising and suggests that redox and substrate mediated shifts are important in the acute control of cardiac PDH flux, in addition to the medium and long term changes that result from cyclical gene induction programmes[22]. The findings corroborate previous data suggesting that the healthy heart has substantial metabolic flexibility, a property which is likely to be diminished in type II diabetes[23].

2.4.2 Effect of metformin upon heart and liver pyruvate metabolism

A second factor with the potential to confound a clinical study is variability arising from the effects of concurrent medical therapy. In order to ensure a clinically homogenous cohort, we intended to study patients who have not received insulin therapy for type II diabetes, though the majority of patients with established type II diabetes receive oral antihyperglycaemic therapy.

The most commonly prescribed antihyperglycaemic drug for patients with type II diabetes is metformin, which is a biguanide. The popularity of metformin results from its efficacy for the improvement of cardiovascular outcomes in type II diabetes and a good safety profile, which includes a lower risk of weight gain or hypoglycaemia than is seen with other oral antihyperglycaemic therapies[24, 25]. However, despite long experience with this drug, the mechanisms by which metformin improves hyperglycaemia are uncertain, but have been thought to involve suppression of hepatic gluconeogenesis[26] either by activation of the

AMPK signalling pathway[27] or by inhibition of mitochondrial complex 1 leading to a decreased cellular energy charge[28]. Peripheral insulin sensitisation in hyperglycaemic states is also described, although the mechanisms by which this effect occurs are unclear. More recently, metformin was shown to inhibit the mitochondrial form of the redox shuttle glycerophosphate dehydrogenase (mGPD) in the liver[29]. One effect of mGPD inhibition is reduced redox coupled gluconeogenic conversion of glycerol and lactate into glucose.

The relative contribution of these putative mechanisms to the antihyperglycaemic effects of metformin are unknown, as are the effects of metformin upon hyperpolarized MR measures of cardiac metabolism. They are however important to understand in the context of clinical study design in which a majority of patients, but not their respective controls, are likely to use metformin therapy. Whether metformin has previously unrecognised direct cardiac effects is also of interest in its own right as metformin is more effective at reducing the risk of cardiovascular complications from diabetes than other antihyperglycaemic therapies[30, 31] and is considered an investigational treatment for heart failure even in the absence of diabetes[32, 33].

We next therefore used hyperpolarized [^{13}C]pyruvate MRS to determine whether metformin caused changes in pyruvate metabolism, and used a sequential dual slice spectroscopic acquisition sequence to acquire information from both the heart and liver in view of data suggesting that hepatic effects may be a key mechanism by which metformin reduces hyperglycaemia. One technical limitation of dual slice spectroscopy is that it is not possible to achieve the same degree of magnetic field homogeneity across two slices (as opposed to one slice) by shimming, which can reduce the quality of the spectra. In pilot work, we found that this effect made kinetic modelling less reliable, and, in contrast to the initial study of glucose infusion, reverted to the established method of comparison of

maximal spectral peak area ratios for the analysis of hyperpolarized MR data in this study. Again, full methodological details are provided in Appendix 2A (page 101)

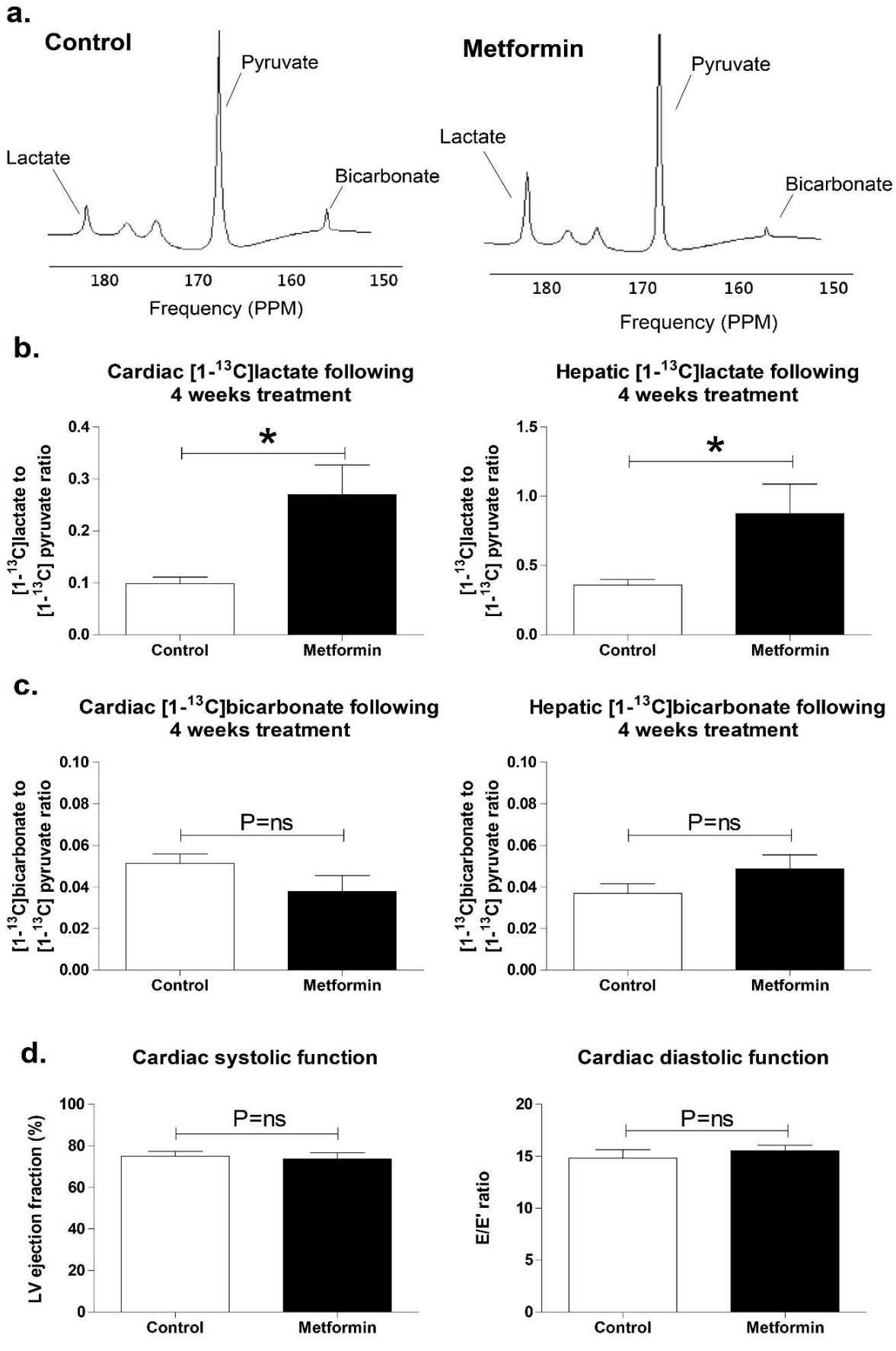


Figure 2.3: Panel a; representative spectra acquired from a slice covering the liver from control and metformin treated groups. Panels b and c; oral metformin treatment increases the hyperpolarized [1-^{13}C]lactate:[1-^{13}C]pyruvate ratio but not [1-^{13}C]bicarbonate:[1-^{13}C]pyruvate ratio. Panel d; metformin did not change either systolic or diastolic cardiac function. n = 10 per group to yield 8 – 10 evaluable datasets.

2.4.2.1 *Metformin treatment does not change PDH flux, but increases [1-^{13}C]lactate production*

We first treated healthy rats with metformin in drinking water for 4 weeks (250 mg/kg/day; dose selected following literature review, n = 6) prior to hyperpolarized [1-^{13}C]pyruvate MRS experiments. Comparison was made with a separate group receiving similarly flavoured water without metformin over the same duration (n = 6).

Treatment with oral metformin for four weeks had no effect upon either cardiac or hepatic pyruvate dehydrogenase flux (cardiac [1-^{13}C]bicarbonate:[1-^{13}C]pyruvate ratio 0.051 ± 0.004 versus 0.037 ± 0.007, P = 0.16 and hepatic [1-^{13}C]bicarbonate:[1-^{13}C]pyruvate ratio 0.049 ± 0.006 versus 0.037 ± 0.004, P = 0.19, Figure 2.3) or label incorporation into alanine (not shown). However metformin increased the [1-^{13}C]lactate:[1-^{13}C]pyruvate ratio in both the heart (0.27 ± 0.06 versus 0.10 ± 0.01, P = 0.02) and liver (0.87 ± 0.21 versus 0.36 ± 0.04, P = 0.04) and also increased the plasma lactate concentration (4.1 ± 0.3 versus 2.4 ± 0.3 mM, P = 0.002). As expected metformin had no effect upon either systolic or diastolic cardiac function, which was assessed using echocardiography (left ventricular ejection raction 75 ± 2% versus 74 ± 3%, P =0.74 and E/E' ratio 15 ± 1 versus 16 ± 1, P = 0.47, Figure 2.3, panel D).

2.4.2.2 *A single infusion of metformin rapidly increases [1-^{13}C]lactate production without changing PDH flux*

Whilst reassuring from the point of view of the design of a clinical study in which PDH flux was intended to be the primary outcome measure, the finding of an increased lactate signal was unexpected and raised questions about the mechanism underlying the effect. In order to determine whether the same effect of metformin upon cardiac and hepatic [1-^{13}C]lactate:[1-^{13}C]pyruvate ratios could be recapitulated acutely, we proceeded to perform hyperpolarized [1-^{13}C]pyruvate spectroscopy 45 minutes following a single intravenous infusion of either metformin (50mg dissolved in 1 ml 0.9% saline, dose selected following

literature review and pilot dose ranging studies in which no effect was observed at a dose of 10mg, n = 10) or an equal volume of saline (n = 10).

At this acute time point, metformin again increased the [1-^{13}C]lactate:[1-^{13}C]pyruvate ratio in both the heart (0.22 ± 0.04 versus 0.11 ± 0.01, P = 0.01, Figure 2.4, panel a) and liver (0.39 ± 0.04 versus 0.29 ± 0.02, P = 0.04) and again increased the plasma lactate concentration (2.9 versus 1.0 mM, P = 0.02). Metformin again had no effect upon either cardiac or hepatic pyruvate dehydrogenase flux (cardiac [1-^{13}C]bicarbonate:[1-^{13}C]pyruvate ratio 0.067 ± 0.009 versus 0.078 ± 0.006, P = 0.32 and hepatic [1-^{13}C]bicarbonate:[1-^{13}C]pyruvate ratio 0.046 ± 0.005 versus 0.051 ± 0.006, P = 0.54, Figure 2.4, panel b) or label incorporation into alanine.

In order to exclude the possibility that the increase in cardiac [1-^{13}C]lactate signal measured by spectroscopy might reflect metabolic shifts in the adjacent blood pool or skeletal muscle, we next investigated the effects of metformin upon pyruvate metabolism using a then-newly developed magnetic resonance imaging sequence[34]. Allowing for the inhomogeneous coverage of this early ^{13}C surface coil, a technical factor which reduces the signal acquired from the posterior aspect of the heart, almost all of the lactate signal localised to the left ventricular myocardium, whereas the large majority of the pyruvate signal localised to the ventricular cavity. This finding supports a direct effect of metformin upon the heart (Figure 2.4, panel c).

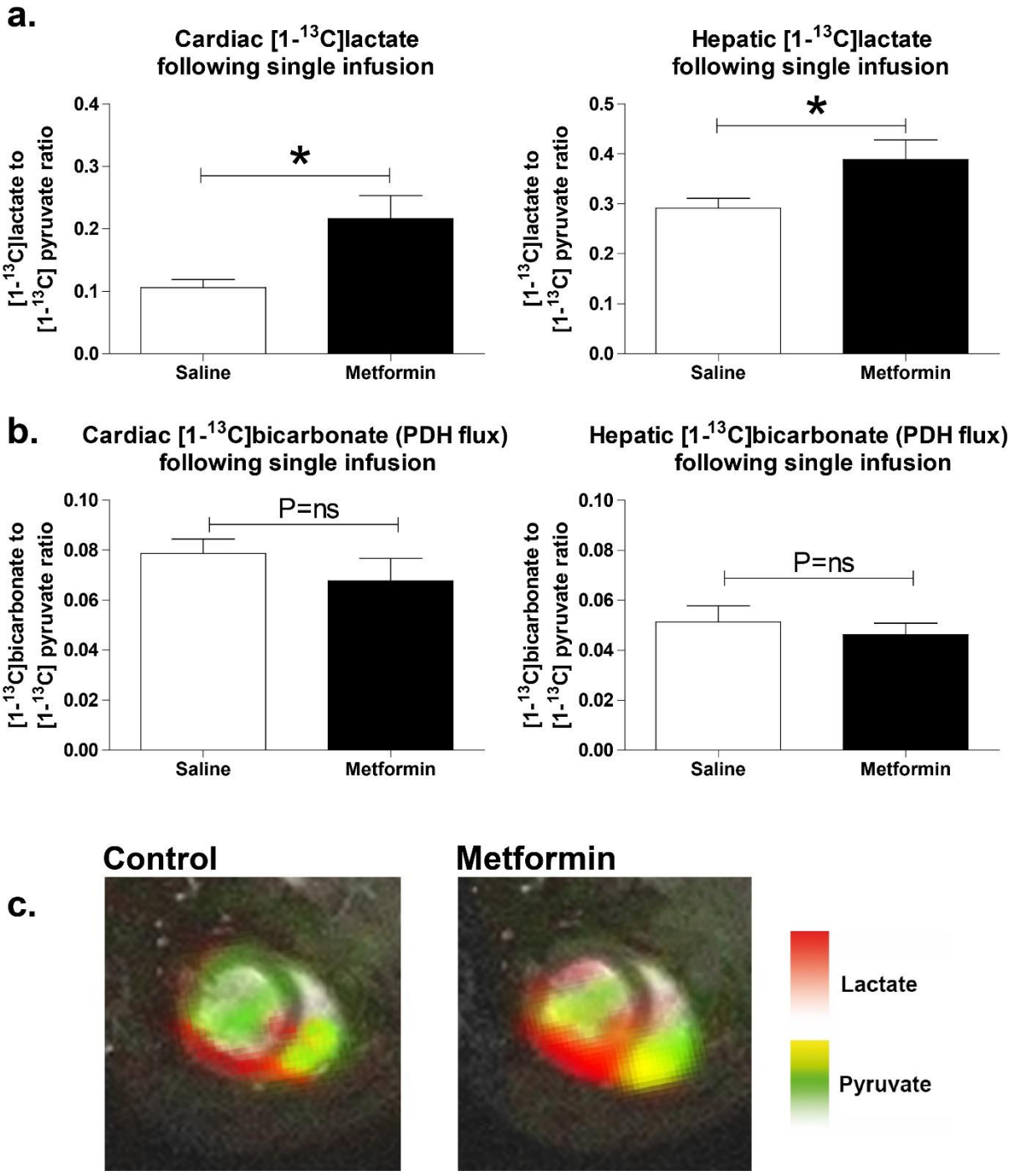


Figure 2.4: Panels a and b; a single metformin infusion increases the hyperpolarized [1-¹³C]lactate:[1-¹³C]pyruvate ratio but not [1-¹³C]bicarbonate:[1-¹³C]pyruvate ratio. Panel c; hyperpolarized magnetic resonance imaging demonstrates that almost the entirety of the lactate signal localises to the left ventricular myocardium.

2.4.3 Metformin does not change whole cell [NAD⁺]:[NADH] ratio

In considering the mechanisms by which metformin might increase lactate production in the heart, we were struck by the rapidity of the effect. The most likely mechanism of regulation of LDH activity over this short time frame is a redox shift, as the LDH catalysed interconversion of pyruvate and lactate exists in a redox couple with the oxidised and reduced forms of nicotinamide adenine dinucleotide (NAD). Alternative mechanisms, such as a more complex metabolic reprogramming at the messenger ribonucleic acid (RNA) level, seemed less likely. The recent discovery that metformin inhibits the mitochondrial form of the redox shuttle GPD in the liver was also pertinent, as mGPD is one of two

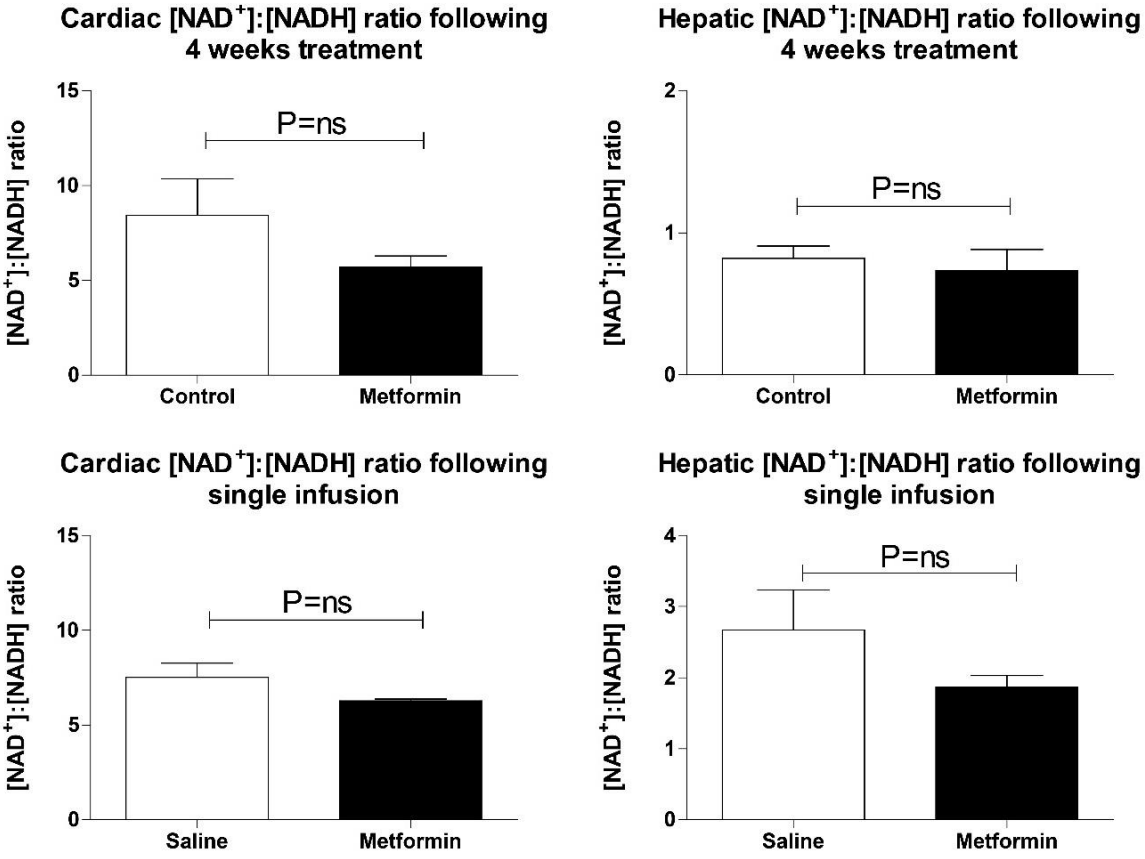


Figure 2.5: Neither acute nor chronic metformin treatments changes the whole cell redox state assessed by [NAD⁺]/[NADH] ratio, n = 6 per group, statistical comparison by unpaired T-tests.

major mitochondrial redox shuttles in the heart (the other being the malate-aspartate shuttle)[35].

To investigate whether the increase in heart and liver [1-^{13}C]lactate:[1-^{13}C]pyruvate ratio caused by metformin might reflect a redox shift resulting in a decrease in [NAD^+]:[NADH] ratio[29], we first measured [NAD^+]:[NADH] ratios in both heart and liver whole cell lysates following perchloric acid extraction using a commercially available assay kit based upon an enzyme cycling reaction. However, [NAD^+]:[NADH] ratios were unchanged by either longer term or acute metformin treatment (cardiac and hepatic [NAD^+]:[NADH] ratios 7 ± 1 versus 8 ± 2, P = 0.31 and 0.8 ± 0.1 versus 0.7 ± 0.1, P = 0.64 respectively following 4 week treatment and 6 ± 0.1 versus 8 ± 1, P = 0.14 and 2 ± 0.2 versus 3 ± 0.6, P = 0.14 following single infusion, Figure 2.5).

2.4.4 Metformin induced changes in lactate production reflect an increase in the cytosolic, but not mitochondrial redox state.

To understand the negative result at the whole cell level, we next considered the possibility that inhibition of mGPD might cause opposing shifts in redox state in the cytosolic and mitochondrial spaces, and that the total cellular [NAD^+]:[NADH] ratio may not be a reliable measure of compartmentalised redox shifts in opposing directions. We therefore proceeded to measure intracellular [lactate]:[pyruvate] ratios as a recognised surrogate for cytoplasmic redox state[36]. Metformin increased the intracellular [lactate]:[pyruvate] ratio, which is consistent with a shift in heart and liver cytosolic redox state and paralleled the changes in the hyperpolarized [1-^{13}C]lactate:[1-^{13}C]pyruvate ratio (cardiac and hepatic [lactate]:[pyruvate] ratios 46 ± 6 versus 30 ± 6, P = 0.04 and 60 ± 9 versus 27 ± 3, P=0.002 respectively following 4 week treatment and 50 ± 8 versus 25 ± 7, P = 0.0.2 and 72 ± 12 versus 16 ± 8, P = 0.002 following single infusion.

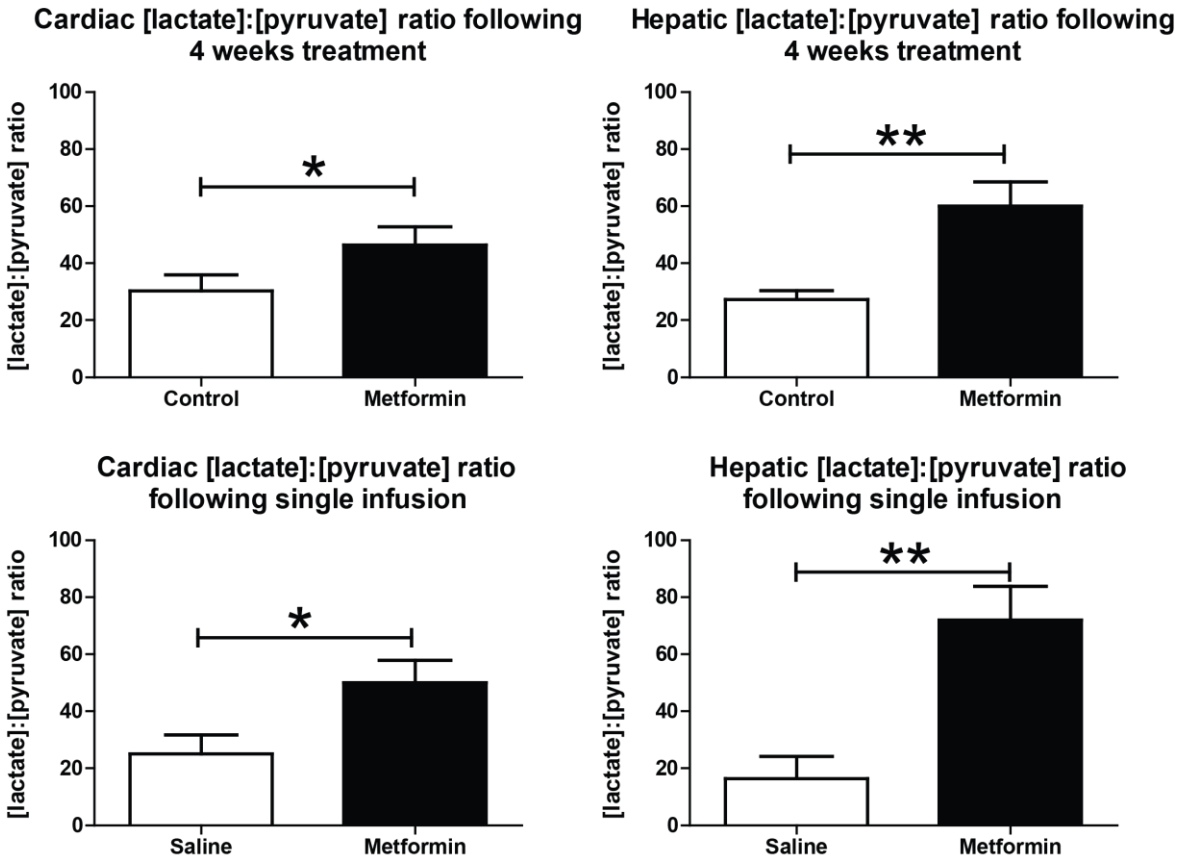


Figure 2.6: Both oral metformin treatment and a single metformin infusion treatment increase the cellular [lactate]:[pyruvate] ratio, implying an increase in the cytosolic redox stat, n = 6 per group, statistical comparison by unpaired T-tests.

2.4.5 Discussion of findings

This study demonstrated that metformin treatment increased the production of [1-^{13}C]lactate following a hyperpolarized [1-^{13}C]pyruvate infusion in both the heart and liver, a finding which was paralleled by an increase in the cytosolic, but not whole cell, redox state (illustrated in Figure 2.7).

In addition to demonstrating the sensitivity of hyperpolarized [1-^{13}C]pyruvate magnetic resonance to cytosolic redox shifts in the heart and liver, the unusual pharmacology of metformin (leading to compartmentalised redox shifts) helps to support the view that the interconversion of hyperpolarized [1-^{13}C]pyruvate and [1-^{13}C]lactate primarily reflects a cytosolic reaction, despite the recognition of mitochondrial capacity for lactate and pyruvate oxidation[37].

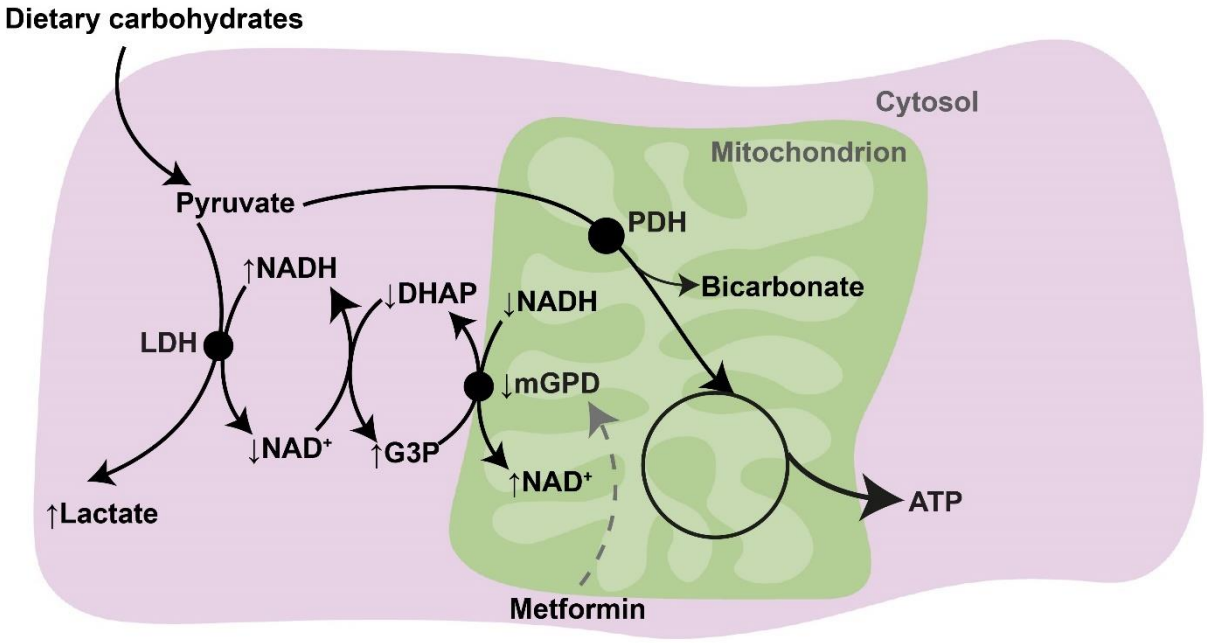


Figure 2.7: Illustration of mechanism by which inhibition of the mitochondrial form of the mitochondrial GPD redox shuttle may lead to compartmentalised redox shifts and an accumulation of cytosolic lactate. LDH - lactate dehydrogenase, NAD nicotinamide adenine dinucleotide, DHAP – dihydroxyacetone phosphate, G3P – glycerol-3-phosphate, - mGPD – mitochondrial form of glycerol-3-phosphate dehydrogenase, ATP – adenosine triphosphate.

Metformin caused changes in both hyperpolarized [1-^{13}C]lactate production and the intracellular [lactate]:[pyruvate] ratio within 45 minutes of administration, supporting a rapid, redox dependent mechanism, rather than a shift in the metabolic gene programme[29]. However, metformin has a complex pharmacokinetic profile and crosses plasma membranes slowly due to a net positive charge[38]. As a result, metformin achieves higher hepatic concentrations following longer term oral treatment than are possible with a single intravenous treatment at physiological doses[39]. The magnitude of the increase in the hyperpolarized [1-^{13}C]lactate:[1-^{13}C]pyruvate ratio in the liver was greater with longer term treatment, and it is tempting to speculate that this may reflect higher bioavailability as a consequence of the longer term treatment. However, the magnitude of the increase in liver [lactate]:[pyruvate] ratio was similar for both routes of metformin administration, a finding which did not corroborate this suggestion.

Although previously described in the liver, a metformin induced increase in cardiac cytosolic redox state has not been previously recognised. Metformin has historically been thought to improve cardiovascular outcomes in diabetes primarily by systemic reduction of hyperglycaemia, although the elucidation of direct cardiac effects is of interest as the risks and benefits of metformin treatment in heart failure with or without diabetes remain contentious[40].

The finding that metformin did not alter either cardiac or hepatic PDH flux in this study is consistent with previous data suggesting that the major mechanism by which metformin reduces hyperglycaemia is by reduction of endogenous glucose production by gluconeogenesis as opposed to an increase in peripheral glucose utilisation[41]. The finding is also consistent with data from ^{18}F-FDG PET studies demonstrating that metformin does not increase myocardial[12] or skeletal muscle[42] glucose uptake. However, because PDH is partially regulated by redox coupling and because mGPD inhibition would be expected to decrease the mitochondrial redox state, it is perhaps surprising that no increase in PDH activity was detected. The findings of this study and others therefore suggest that other mechanisms of PDH regulation, such as the well-defined phosphorylation/dephosphorylation cycle, are dominant over redox regulation in this setting.

In conclusion to this study, metformin increased hyperpolarized [1-^{13}C]lactate production without changing PDH flux, a finding which is likely to reflect a shift in cardiac and hepatic cytosolic redox state. In addition to demonstrating the sensitivity of hyperpolarized MR to cardiac redox shifts and identifying a previously unrecognised effect of metformin upon the heart, this study refined the design of the proposed clinical hyperpolarized MR study by highlighting the need for a washout period for metformin. Because the half-life of

metformin is around 6 hours (though longer extended release formulations are available), we concluded that the omission of the dose of metformin on the day of the study and the previous evening would be likely to be sufficient to mitigate this effect. The findings also invite a future mechanistic study of the effects of metformin in humans, as animal studies using metformin have been significantly confounded by the complex differences in inter-species dosing and bioavailability profiles[39] and it remains unclear to what extent inhibition of mGPD in isolation would be sufficient to cause significant cellular redox shifts in humans, where the malate-aspartate shuttle is thought to be the quantitatively dominant shuttle mechanism[43].

2.5 Towards clinical studies using hyperpolarized [1-^{13}C]pyruvate

Informed in part by the findings of these preclinical studies, the intention of the first human clinical study was to investigate cardiac metabolic flexibility in both healthy controls and people with type II diabetes. To do this, we planned to measure the changes in cardiac PDH flux that occur following an oral glucose tolerance test performed in the fasted state in both healthy volunteers and in people with type II diabetes. We aimed to test the hypotheses that:

- cardiac PDH flux would be low in both healthy controls and in people with type II diabetes in the fasted state
- following an oral glucose tolerance test, cardiac PDH flux would rise to a greater degree in healthy controls than in people with type II diabetes, reflecting cardiac metabolic inflexibility

Secondary aims of the study were to understand whether a shift in cardiac energy metabolism at the substrate level was associated with changes in systolic function, diastolic

function, myocardial triglyceride content, and high energy phosphorous metabolism and whether type II diabetes would affect these parameters. One technical aim of the study was to test both spectroscopic and imaging acquisition strategies for clinical hyperpolarized [1-^{13}C] pyruvate magnetic resonance.

2.5.1 Design of the clinical study

2.5.1.1 Study protocol

In order to address these aims, the study design was a single visit involving a series of clinical investigations performed both before and one hour after a standardised glucose tolerance test (75g carbohydrate, time point selected to coincide with peak plasma glucose concentration, study design is depicted in Figure 2.8).

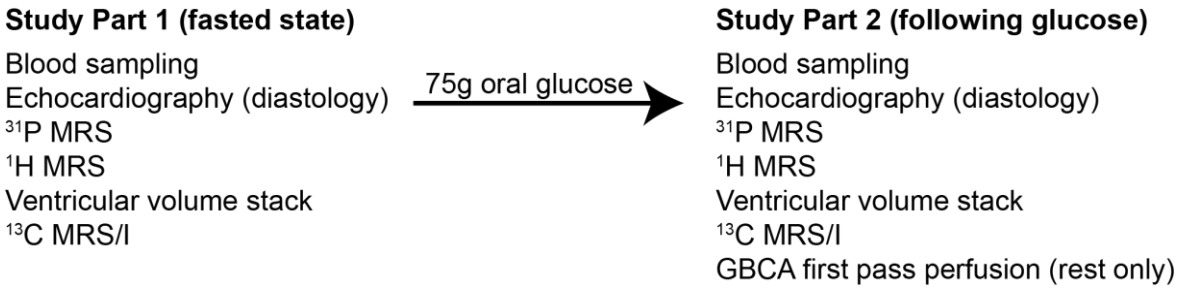


Figure 2.8: The study design consisted of a single visit with two sets of assessments; one before and one after a standardised glucose challenge to assess the metabolic flexibility of the hearts of people with type II diabetes.

2.5.1.2 The number of participants

There were no relevant human data from hyperpolarized [1-^{13}C]pyruvate experiments to inform a power calculation. Extrapolation of the magnitude and variability of PDH flux measures from preclinical rodent data (diabetes in fed state [^{13}C]bicarbonate:[1-^{13}C]pyruvate ratio 0.010 ± 0.007 (SD) versus control in fed state 0.020 ± 0.009, independent T-test analysis, α = 0.05 and β = 0.80) provided the basis for the estimate that 12 participants would be required in each group. To allow for potential higher variability in a 'real-world' setting, we aimed to recruit 15 participants in each group.

2.5.1.3 *Study inclusion and exclusion criteria*

In order to maximise the reliability of the findings, we aimed to identify a relatively clinically homogenous cohort of people with stable, insulin-naïve type II diabetes and age matched controls. Formal inclusion/exclusion criteria are shown in Table 2.1:

Inclusion criteria	Exclusion Criteria
All participants	Contra-indications to MR studies, such as metal implants, pacemakers, defibrillators
Participants who are able and willing to provide informed consent	Claustrophobia (relative caution rather than total exclusion)
Male or female	Any history of cardiovascular, endocrine, neurological, or neuromuscular disease (with the exception of type 2 diabetes for the participants with diabetes)
Aged 18 – 65 years	Uncontrolled hypertension (systolic > 140 mmHg, diastolic > 90 mmHg)
Additional inclusion for participants with type 2 diabetes	Hypercholesterolaemia (fasting cholesterol over 6.5 mmol/L, threshold chosen from British Hyperlipidaemia Society classification)
Stable Type 2 Diabetes for 3 months Not on insulin therapy	Diabetes (Fasting glucose of 7.1 mmol/L or greater, control participants only, threshold chosen from American Diabetes Association diagnostic criteria)
No change in medication for 3 months	History of, or investigation for, chest pains resulting in a diagnosis of ischaemic heart disease
Blood HBA1c of between 6 & 9%	Chronic kidney disease of a moderate or severe degree (eGFR < 30 mls/kg/min)
	Inability or loss of ability to give informed consent
	Current participation in another research trial
	A female who is pregnant, lactating or planning pregnancy during the course of the study.
	Any other cause, including a significant disease or disorder which, in the opinion of the investigator, may either put the participant at risk because of participation in the study, or may influence the result of the study, or the participant's ability to participate in the study

Table 2.1: Inclusion and exclusion criteria for clinical study with patients with type II diabetes.

2.5.2 Regulatory considerations for human hyperpolarized MR studies

All human hyperpolarized MR studies involve the administration of an agent that has been prepared externally and no hyperpolarized MR substrates have licensed indications for human use.

The administration of medicinal products to humans in clinical settings is governed by the Medicines Act (1968) and the Human Medicines Regulations (2012) whilst the administration of medicinal products in the context of a clinical trial of an investigational medicinal product (CTIMP) is governed by the European Clinical Trials Directive (Council Directive 2001/20/EC, with modifications from Council Directive 2004/27/EC).

Clinical Trials Authorisation (CTA) is required for CTIMPs, however a study is not automatically classified as a CTIMP simply because it involves the administration of a substance in the absence of a licensed indication[44]. The first test to be applied when determining the answer to this question is whether the substance to be administrated is classifiable as a medicinal product. Medicinal products (for the purposes of both the Human Medicines Regulations 2012 and Council Directive 2001/20/EC) are defined as those presented as having properties for treating or diagnosing human disease, either by restoring, correcting or modifying physiological functions by exerting a pharmacological, immunological or metabolic action or by making a medical diagnosis, or if it is an active substance in a pharmaceutical form. Although hyperpolarized [1-^{13}C]pyruvate is administered at a supraphysiological dose and is likely to have a slight and transient effect upon metabolism, it would be administered in this proposed study only with the intent of studying, rather than modifying, physiology and, as the diagnosis of diabetes has already been made (or not), would not be classifiable as a medicinal product on these grounds. Equally, although it could be argued that hyperpolarized [1-^{13}C]pyruvate is an active substance in a pharmaceutical form, there must still be an intention in the study to discover,

verify or compare the pharmacological effects, pharmacokinetics, pharmacodynamics, safety and/or efficacy of the substance in order for the study to be a CTIMP, none of which were proposed. The classification of human studies using hyperpolarized [1-^{13}C]pyruvate is thus determined by the specific study question being investigated, and a study such as this conducted with the exclusive intention of using hyperpolarized [1-^{13}C]pyruvate to study the physiology of a known disease process cannot be classified as a CTIMP. This distinction has significant ramifications for the conduct of the hyperpolarization process as the manufacture of IMPs for CTIMPs requires a manufacturing license from the Medicines and Healthcare Products Regulatory Agency (MHRA) which in turn places a different set of requirements upon the facility. The mixing of hyperpolarized [1-^{13}C]pyruvic acid with the dissolution buffers is very likely to be classifiable as 'manufacturing' if the intention is to use the final product as medicinal product (e.g. to make a new diagnosis). In the United States, the Food and Drug Administration classify and regulate the hyperpolarization and dissolution process as 'compounding', a term not recognised by regulatory bodies in Europe, and acknowledge hyperpolarized [1-^{13}C]pyruvate as an 'investigational new drug'.

The legislative framework covering the administration of substances to humans outside of licensed medicinal product indications and outside of investigational medicinal products (IMPs) within a CTIMP is less clearly established. The EU Clinical Trials Directive recognises a category of non-investigational medicinal products (NIMPs) which includes those administered within a CTIMP that do not meet the definition of an IMP, such as challenge agents or rescue therapies. However, NIMPs are not recognised or separately regulated outside the auspices of a CTIMP and thus this is not a useful classification for hyperpolarized [1-^{13}C]pyruvate in a physiological study. Although some forms of research, such as those conducted using ionising radiation or medical devices, are the subject of

separate legislation, research not falling into these categories is instead governed by policies of the UK Health Departments (codified as the Research Governance Framework for Health and Social Care in England[45]). This framework requires that studies undergo favourable review by an approved research ethics committee (REC) and be conducted according to the principles of Good Clinical Practice (GCP) in the 1996 statement of the International Conference on Harmonisation (ICH)[46]. GCP in turn requires that investigational products (not necessarily IMPs) should be manufactured, handled and stored in accordance with good manufacturing practice (GMP) and used in accordance with the protocol, establishing a framework of governance requirements for hyperpolarized [1-^{13}C]pyruvate studies in humans conducted with the intention of studying the physiology of disease processes, but not meeting criteria necessary to be classified as a CTIMP. Confirmation that the proposed study was not classifiable as a clinical trial as defined by EU Directive 2001/20/EC was sought from and provided by the MHRA in December 2012.

An application for ethical review of the study was subsequently submitted, and a favourable ethical opinion was provided by the South West – Exeter National Research Ethics Service (NRES) Committee in June 2013.

2.5.3 Installation of the SPINlab™ hyperpolarizer

With financial support from a British Heart Foundation (BHF) programme grant, a SPINlab™ hyperpolarizer was purchased from GE Healthcare and was installed at the University of Oxford Centre for Clinical Magnetic Resonance Research (OCMR) in December 2012.

In pilot work to test the performance of the SPINlab™ hyperpolarizer and to establish the feasibility of performing ^{13}C experiments using a clinical 3 T MR system (TIM Trio,

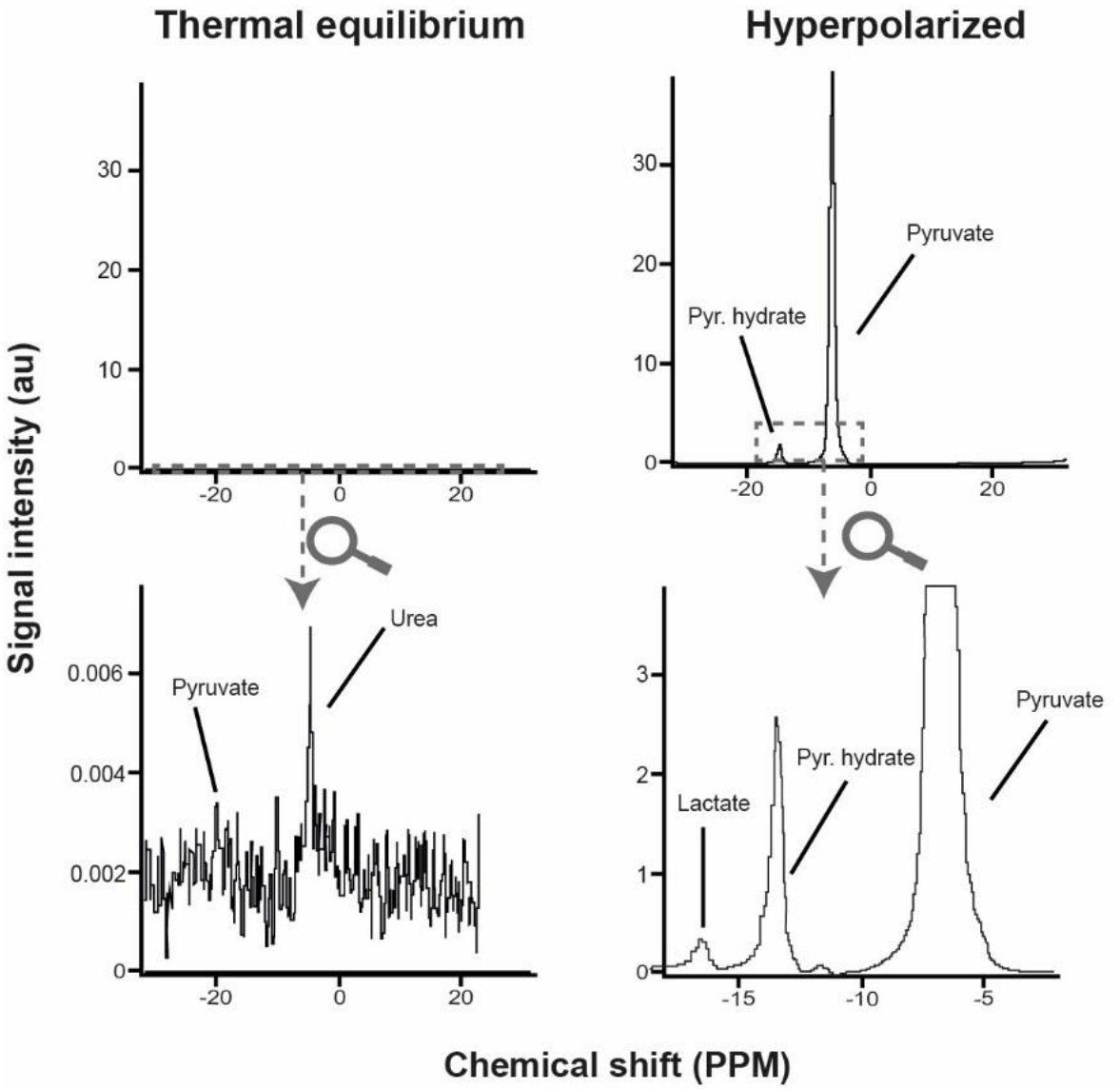


Figure 2.9: Initial ^{13}C spectra acquired using SPINlab™ hyperpolarizer and a clinical MR system. Signal to noise ratio is very low at thermal equilibrium, but is increased by 10-20,000 fold following hyperpolarization, with clear label exchange into [1-^{13}C]lactate.

Siemens), we first performed a 'before and after' experiment using an MR phantom containing [1-^{13}C]pyruvic acid, lactate dehydrogenase and NADH (to promote conversion of pyruvate to lactate) as well as a sample of [^{13}C]urea as a spectroscopic reference point. At thermal equilibrium, ^{13}C spectroscopy had very low signal to noise ratio as expected (Figure 2.9). In contrast, after hyperpolarization of pyruvic acid to a polarization of ~40 % and dissolution and neutralization to a [1-^{13}C]pyruvate solution, the SNR was increased by around 10-20,000 fold, with clear label incorporation into lactate detected.

2.5.4 Installation of the quality control (QC) accessory

As discussed in Chapter 1, the purpose of the QC accessory is to ensure that key parameters relating to the hyperpolarized product are within appropriate physiological ranges prior to clinical administration. The Oxford SPINlab™ hyperpolarizer was one of the first to be manufactured, and there was a significant delay before the design of the QC unit was finalized and production could begin. Following manufacture, the QC accessory was not installed in OCMR until April 2014; installation qualification tests performed by the manufacturer demonstrated satisfactory performance.

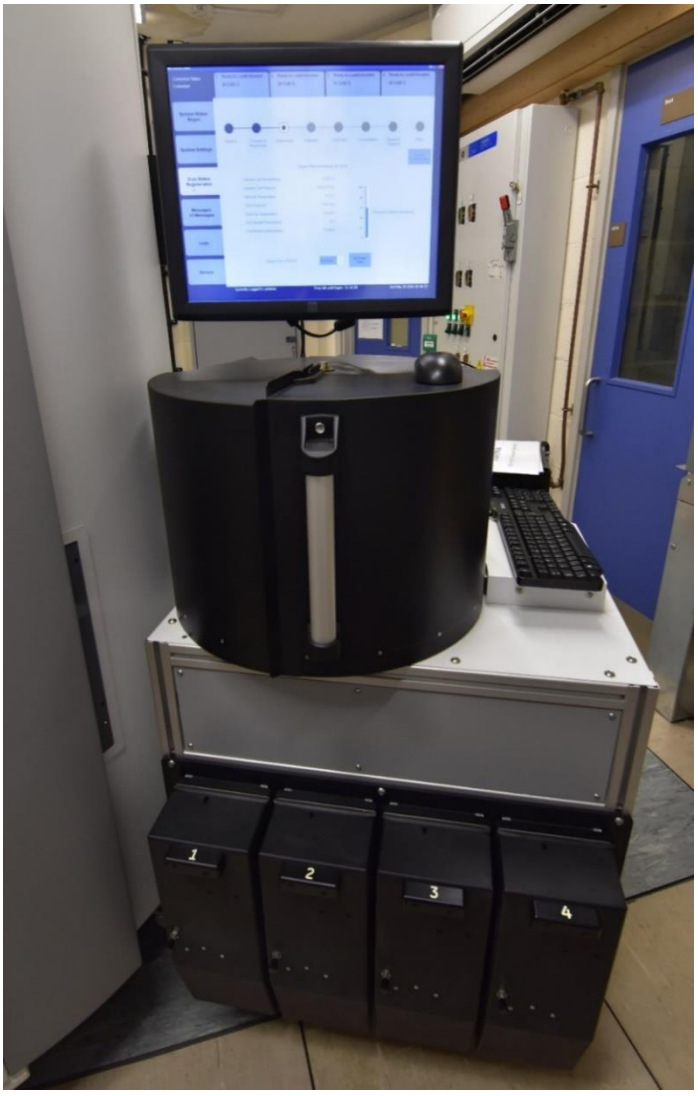


Figure 2.10: The SPINlab™ QC accessory.

In internal tests over the following months, the performance of the QC system measures was validated against offline measurements, which generally demonstrated good agreement across a wide dynamic range (for example, electron-paramagnetic agent (EPA) and pyruvate concentration, Figure 2.11). pH measures showed less strong correlation against a calibrated bench meter towards the limits of acceptable pH, though accuracy within the expected ranges remained reasonably good. There was a systematic difference in temperature measurements, attributable to sample cooling during the delay between the QC unit and subsequent offline measurement. The volume of all test samples exceeded 40 mls and all were correctly classified by the QC unit.

Production of sterile fluid paths

The identification of a robust production method for sterile fluid paths has been the main cause of delay for every centre pursuing the translation of hyperpolarized MR using DNP. In contrast to the commercially led hardware development, responsibility for the development and filling of sterile fluid paths for clinical use was in part devolved to the academic institutions who had purchased SPINlab™ hyperpolarizers.

The production of a sterile fluid path involves two main processes; the first is the manufacture and assembly of the plastic components and the second is the filling of the fluid path with the sample to be hyperpolarized, the polarizing agent and the dissolution medium.

2.5.4.1 Manufacture and sterilization of the sterile fluid path

Manufacture of the SPINlab™ fluid path was reported to be the most challenging design and production process ever undertaken by a medical consumable device firm[47]. The fluid path consists of numerous components, including valves, micro-bore tubing interfaces and

a unique seal design, and the final assembly must demonstrate tolerance to low pH and a temperatures ranging from 1 to 400 K.

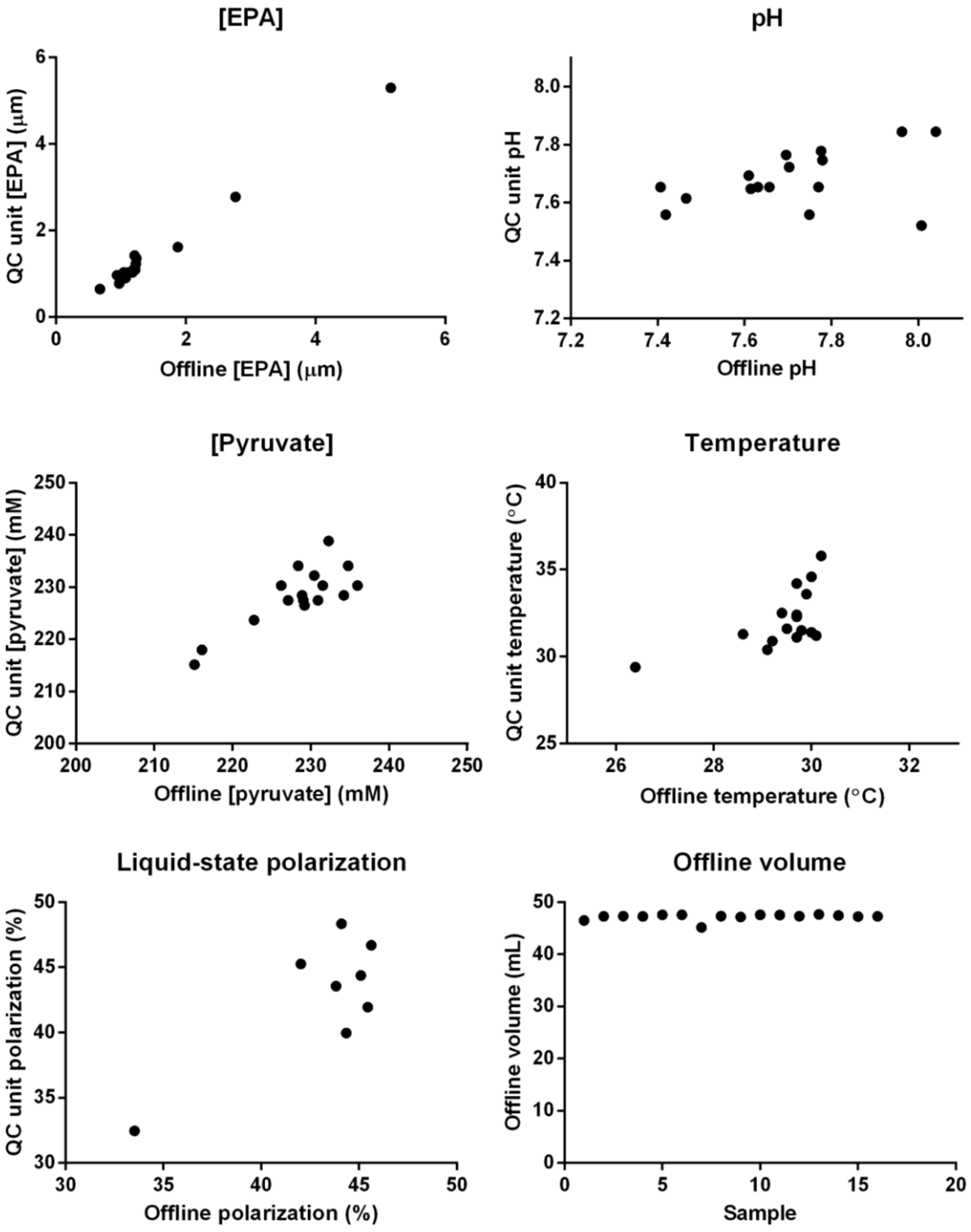


Figure 2.11: Measures of key parameters from the SPINlab™ QC accessory demonstrated good agreement with offline measurements within the expected ranges expected to be encountered during operation.

In addition to the difficulty of manufacture and assembly of the individual fluid path components, the maintenance of the sterility of the fluid path during and after filling also poses a logistical challenge. Conventional irradiation-based sterilization approaches for a completed and packaged medical product cannot be used once the fluid path has been filled, as gamma irradiation was found to destabilise the free electron source. This mandated the use of a certified clean room for the fluid path filling process, which in turn required that the fluid path to be filled must itself be confirmed to be sterile before it enters the sterile clean room environment.

The first commercial organisation contracted to manufacture sterile fluid paths for subsequent filling by international academic institutions was approached in 2013, and supplied non-sterile fluid paths over the following two years. It had, however, been unable to produce a product confirmed to be sterile by early 2015 and a second commercial organisation was therefore approached to lead production efforts. In the interests of expediency, this company was provided with a number of components sourced and manufactured by the previous organisation which were thought to be sterile. These components were mixed with independently manufactured new products to create a batch of fluid paths with sterile intent in mid-2015, which were exposed to electron beam irradiation and subsequently underwent formal endotoxin and sterility testing. This analysis demonstrated endotoxin limits well within acceptable limits, but also demonstrated mixed microbial growth confirming a failure of sterility and rendering the products unsuitable for clinical application. The cause of the sterility failure in this case was attributed to the use of existing components which may not themselves have been adequately sterilised prior to assembly, and a process to create new 'virgin' components was begun. It was not possible to simply increase the intensity of the electron beam irradiation, as to do so was shown the alter the optical transmission properties of the fluid path plastics, in turn invalidating the

(optical based) measurements performed by the SPINlab™ QC accessory. A new batch of fluid paths assembled from new components was finally confirmed to be sterile in October 2015, and an equal proportion of the fluid paths within this batch was shipped to the initial five international academic institutions pursuing clinical translation, including the University of Oxford.

2.5.4.2 *Filling of the sterile fluid path with the sample to be hyperpolarized and dissolution medium*

The filling of sterile fluid paths with precursor products to be hyperpolarized was undertaken by individual academic institutions. All five international institutions elected to begin with [1-^{13}C]pyruvic acid for clinical applications, and, in view of the substantial financial cost of sourcing a clean room and equipping it with the laser welding apparatus necessary to bond the sample cup to the coaxial tubing, it was decided that the University of Cambridge would undertake the filling process on behalf of both UK sites. This process was rehearsed, and was overseen by qualified persons (QPs) with expertise in pharmaceutical manufacturing from both UK sites.

2.5.4.3 *Validation of sterility of sterile fluid paths*

Following receipt of sterile fluid paths, it was necessary to confirm that sterility had been preserved during the filling, inter-institutional transport, hyperpolarization and dissolution processes. In order to assess this, four sterile fluid paths were filled at the University of Cambridge in early 2016 and two of these were shipped to OCMR, during which they were maintained at a temperature of less than -20 °C by packaging in dry ice, with temperature monitoring throughout transport. Both samples within the fluid paths were successfully hyperpolarized in OCMR, and one of the two samples was successfully hyperpolarized at the University of Cambridge. All three hyperpolarized samples subsequently underwent formal sterility and endotoxin testing at a commercial laboratory

and were confirmed to be sterile in February 2016, with an endotoxin level that was well within acceptable limits.

Following this validation of these processes, a further four sterile fluid paths were filled and shipped to OCMR for clinical use in March 2016.

2.5.5 Administration of hyperpolarized pyruvate

2.5.5.1 Quality control and release by a Qualified Person

Although the proposed study was not a CTIMP, we elected to undertake the study in a manner which would nevertheless be consistent with the principles of GMP and CTIMP regulation, providing a foundation for future clinical trials and manufacturing license application. One relevant requirement of GMP for the release of IMPs is that each batch of IMPs should only undergo release having been approved to do so by a QP, having satisfied themself that the manufacture has been conducted in accordance with relevant legislation.

Because the mixing of the hyperpolarized substrate and dissolution buffer within the SPINlab™ is classifiable as manufacturing if performed in the context of CTIMP, each dose of hyperpolarized pyruvate should therefore be individually released by a QP before administration. The uniquely short time interval that separates manufacture and administration of hyperpolarized [1-^{13}C]pyruvate requires the QP to be expert in rapid release. In addition to confirming the compliance of the precursor products with the principles of GMP and good laboratory practice (GLP) and having overseen the filling process, the QP and production staff must also be satisfied that the hyperpolarized product meets all QC requirements in order to be considered for release.

QC release criteria were defined and are shown in Table 2.2:

Parameter of interest	QC method	Acceptance criteria
Temperature	Infrared pyrometry	28 – 38 °C
pH	Ultraviolet absorbance	6.7 – 8.1
Sample polarization	Liquid-state NMR	> 16 %
Radical concentration	Visible absorbance	< 3 μM
Pyruvate concentration	Ultraviolet absorbance	220 – 280 mM
Sample volume	Capacitive level sensor	> 40 mL

Table 2.2: Sample parameters measured by the QC unit following dissolution, with associated reference limits for product to be considered for release.

Following the production of a hyperpolarized product with specifications within these ranges, the QP must also perform a visual inspection of the product against both dark and light backgrounds in order to satisfy himself or herself that filter integrity has been preserved.

If these criteria are all met and there are no other concerns, a green sticker is attached to the product to signify and confirm approval for release, and it is passed into the MR room for administration.

2.5.5.2 *Development of a process for the rapid administration of hyperpolarized pyruvate*

For preclinical applications, around 1 ml hyperpolarized pyruvate is administered via a tail vein catheter by a hand injection over around 10 seconds. For clinical purposes, the volume to be administered is determined by body weight and is usually >30 mls. An infusion rate of 5 mls per second is used, as infusion rates higher than this were associated with an increased incidence of non-serious adverse events in phase I studies. It is not possible to infuse hyperpolarized [1-^{13}C]pyruvate via an extension line at this rate using hand injection, necessitating the use of a power injector. However, the current generation of power

injectors for MR contrast agents are designed to enable the administration of the contents of syringes pre-prepared prior to the MR examination from the control room and are not designed to minimise the delay between loading and administration, as is necessary for a hyperpolarized MR study. In order to minimise the time taken for administration, and hence maximise the available signal in the experiment, we developed an approach in which, following release of the hyperpolarized product to be administered, one designated clinician was responsible for loading the syringe onto the power injector, clearing the excess air from the syringe and connecting the infusion line, whilst a second clinician in the control room made the decision to administer the product and commenced the infusion using the remote administration control system. With practice, this approach reduced the total time taken for administration to around 20 seconds, allowing the preservation of high degrees of polarization (> 30%) at the time of administration.

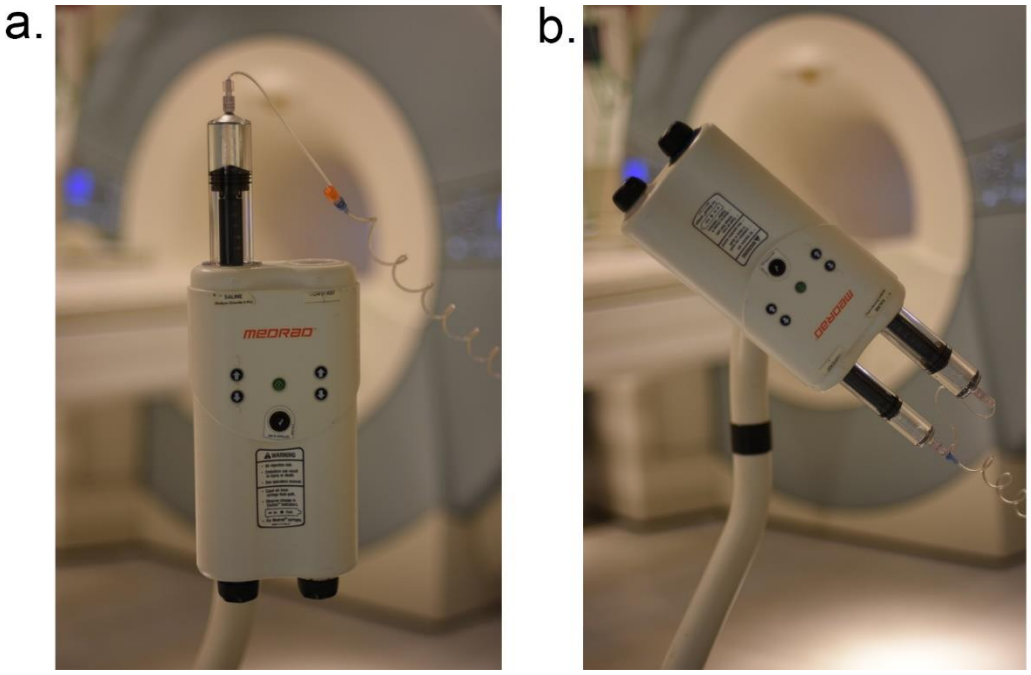


Figure 2.12: Power injector for hyperpolarized product administration. Panel a, injector pre-prepared ready to receive hyperpolarized [1-^{13}C]pyruvate syringe; panel b, power injector in administration position.

2.5.6 Selection of receiver coil and acquisition strategy

We elected to use a non-localised spectroscopic acquisition strategy using a ^{13}C loop coil placed on the chest wall over the apex of the left ventricle for initial experiments. We intended to use data acquired from the spectroscopic acquisition to measure key metabolite frequencies and estimate signal availability for future imaging strategies using selective radiofrequency excitation.



Figure 2.13: ^{13}C loop coil for use at 3 T; the coil is positioned over the cardiac apex for non-localised cardiac spectroscopy.

2.6 First human experiment

The world's first human cardiovascular hyperpolarized MR experiment was performed at OCMR in March 2016. We elected to initially study a healthy volunteer, and, following completion of the informed consent process, blood sampling, electrocardiography, echocardiography, ^{31}P spectroscopy, ^{1}H spectroscopy and an LV volume stack, proceeded to perform hyperpolarized [1-^{13}C]pyruvate spectroscopy in the fasted state. The product specifications, assessed using the QC accessory, were within predefined limits and the administration was successful. The subject reported a mild taste disturbance, as noted in phase I pyruvate trials, but there were no other concerns. Representative resulting spectra

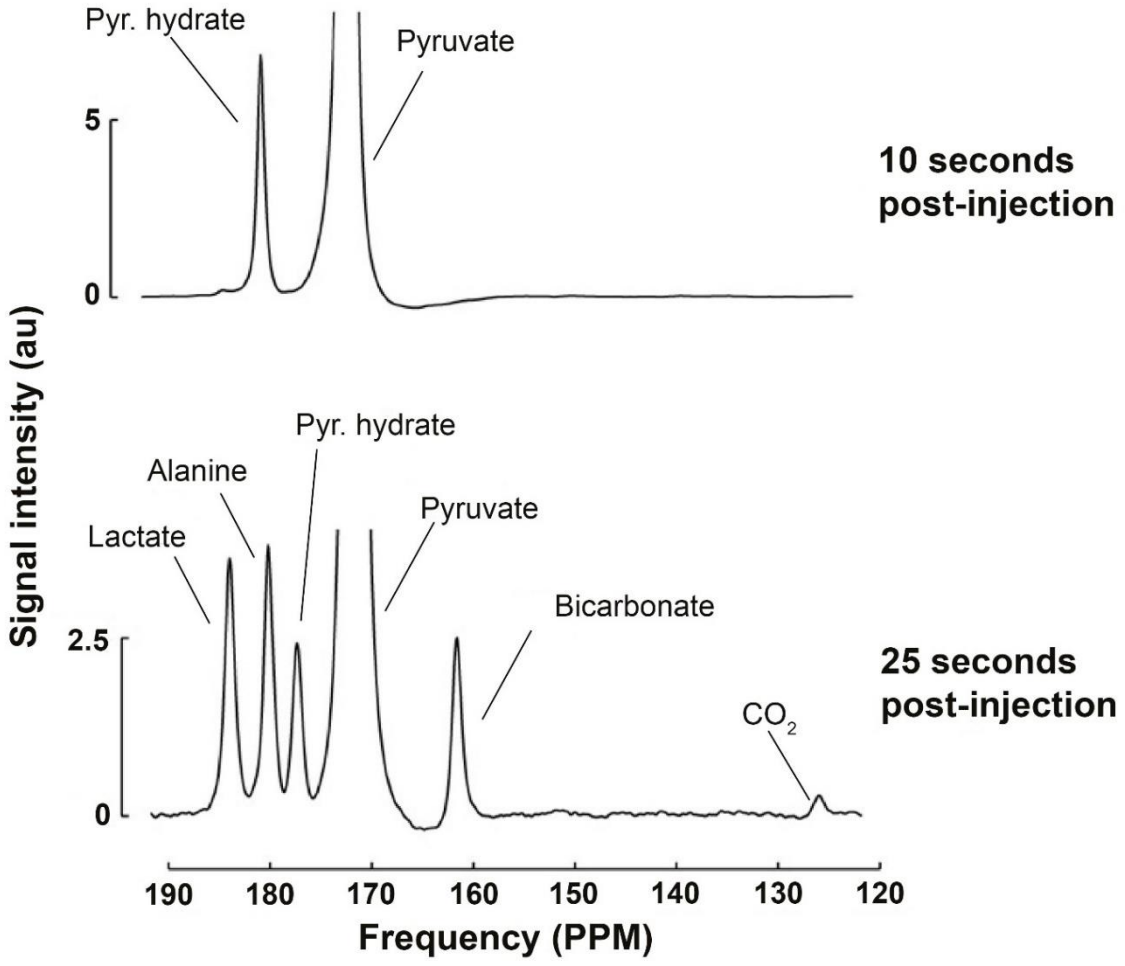


Figure 2.14: First human cardiovascular hyperpolarized [1-^{13}C]pyruvate experiment demonstrating high SNR pyruvate spectrum (top panel) and subsequent biological ^{13}C label exchange into downstream metabolites (bottom panel).

from the acquisition series are shown in Figure 2.14, and demonstrate both the signal enhancement and also label exchange into downstream biological metabolites.

A subsequent analysis of the evolution of the signal following injection demonstrated a distinct 'second pass' peak for pyruvate (Figure 2.15), as is seen with the change in myocardial signal intensity on T1-weighted images following a bolus infusion of gadolinium. This effect is not generally detectable in preclinical rodent applications, most likely on account of a smaller volume of distribution and more rapid heart rate, and represents an additional factor to be allowed for during kinetic modelling. The time course trace also demonstrates the rate of ^{13}C label incorporation into the downstream metabolites.

Following the first dissolution, we proceeded to the second phase of the experiment and administered an oral glucose challenge. However, the second solution of hyperpolarized pyruvate did not meet acceptable injection criteria on account of a pH measurement that

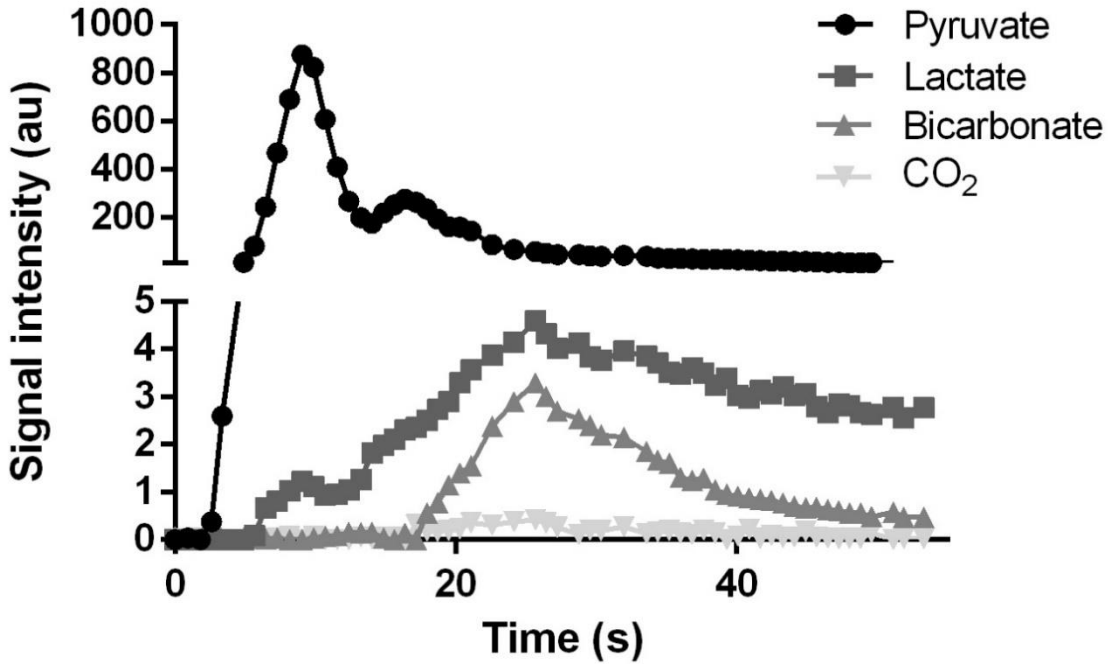


Figure 2.15: Time course analysis of signal intensity following infusion of hyperpolarized [1-^{13}C]pyruvate demonstrates evidence of ^{13}C label incorporation into downstream metabolites, as well as a second distinct pyruvate peak corresponding to the second-pass. This time course is data from a single participant.

was below the predetermined lower limit. The second half of the study visit was rescheduled for another day, but hyperpolarized pyruvate from the two remaining SFPs also failed QC testing due to low pH and were not released for administration. In contrast, subsequent offline pH testing of the same samples indicated acceptable pH. In considering reasons for the apparent misclassification of these samples, we extended the time window for sample mixing in the pH measurement cuvette. A large batch production run for plastics for further fluid paths was undertaken in April 2016. Routine sterility testing failed, and the batch was discarded.

Further clinical studies were undertaken in September 2016, when two successful dissolutions, one prior to an oral glucose tolerance test, and one administered 1 hour following the glucose were successfully performed. The resulting spectra demonstrated a higher [1-^{13}C]bicarbonate signal in the spectrum acquired following the glucose load (Figure 2.16), consistent with an increase in cardiac PDH flux. Subsequent kinetic modelling indicated an approximately four-fold increase in the rate of label incorporation

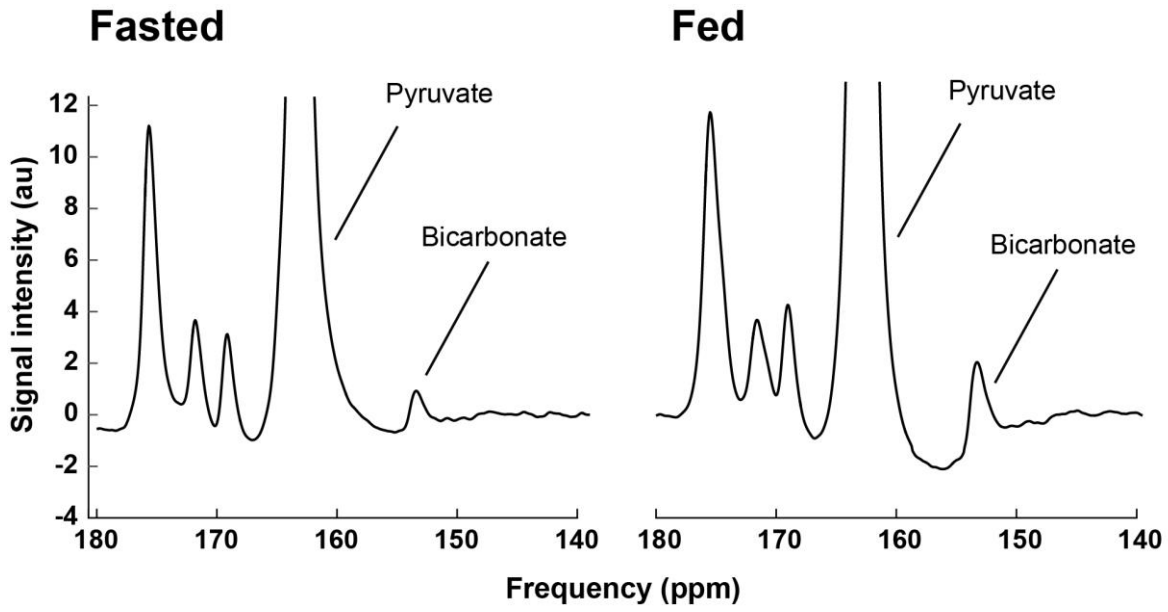


Figure 2.16: Hyperpolarized [1-^{13}C]pyruvate spectra acquired before and after an oral glucose tolerance test in a fasting health volunteer. Bicarbonate signal was increased following glucose administration, consistent with an increase in cardiac PDH flux.

into [1-^{13}C]bicarbonate, which is highly consistent with earlier preclinical studies, and suggests an effect size that may be unprecedented for human spectroscopy. Recruitment to this study continues, guided by the availability of sterile fluid paths.

2.7 Limitations and future work

One limitation of the glucose infusion study presented in section 2.4.1 is the absence of a saline treated control arm. The possibility that a stress response to infusion may have contributed to a change in heart rate therefore cannot be excluded but is considered unlikely.

The number of biological replicates presented in Figure 2.5 is relatively low (n=6), and a small effect size of metformin upon whole cell [NAD^+]:[NADH] ratio cannot be excluded, though the finding is consistent with that of previous work[29]. No data regarding the effects of metformin in a rodent model of diabetes is presented, and it is unclear whether similar changes in lactate metabolism would occur in models of type II diabetes. This would be an obvious area for future work, and could be combined with a human study to definitely address the inter-species variability issues that have confounded pharmacological studies with metformin for many years.

The work presented in this chapter establishes the feasibility of hyperpolarized magnetic resonance in humans, though it is not possible to draw any scientific conclusion from a single participant. Within the clinical study, it was not possible to include CT coronary angiogram to exclude epicardial coronary disease due to the length of the study visit and microvascular disease in type II diabetes is another potential confounding factor. However, late gadolinium imaging will rule out major previously undetected myocardial infarction.

2.8 Conclusions: challenges and opportunities in clinical DNP

Type II diabetes is a promising area for initial human cardiovascular studies using hyperpolarized [1-^{13}C]pyruvate as it poses a substantial clinical problem, affects the myocardium relatively uniformly and PDH flux may itself be a therapeutic target. Work presented in this chapter demonstrated that the healthy rodent heart has remarkable metabolic flexibility and is capable of substantially increasing PDH flux within 1 minute of a glucose infusion; initial human studies suggest a similar effect size. In addition, the commonly used antihyperglycaemic drug metformin has a previously unrecognised effect to increase cardiac hyperpolarized lactate production, a finding which appears to reflect an alteration in the cytosolic, but not whole cell, redox state. The findings helped to inform the design of a human study using hyperpolarized [1-^{13}C]pyruvate, before which it was necessary to perform a detailed series of governance and regulatory applications, validate the performance of both the SPINlab™ hyperpolarizer and its QC accessory, robustly establish the sterility of the products to be injected and develop new mechanisms for the administration of these agents. This work formed part of a major internal and external collaborative effort leading to the acquisition of the world's first cardiac hyperpolarized ^{13}C spectrum, though limited availability of suitable consumables delayed efforts to complete the study.

In reflecting upon the challenges posed by the translation of hyperpolarized MR, it is clear that international efforts to commence human applications have been slower than initially hoped, particularly in view of the optimism provided by the many apparently favourable translational properties of [1-^{13}C]pyruvate. The delays were primarily attributable to difficulty in manufacturing and sterilising the consumable sterile fluid paths. These difficulties in turn stemmed from the complexity of the high number of individual components and connections, which is in turn a product of the design of the SPINlab™

hyperpolarizer itself – a design which was finalised years before the first confirmed sterile fluid path had been produced. Although highly complex relative to other medical consumables, the fluid path appears, from an engineering perspective, to be deceptively simple when compared to the SPINlab™ hyperpolarizer hardware. From the commercial point of view of a company with expertise primarily in engineering rather than pharmaceutical manufacture, the fluid path may also be perceived to be associated with high potential liabilities in the event of an adverse patient event. These factors may have influenced the decision to commercialise primarily the SPINlab™ hyperpolarizer hardware and its QC accessory, whilst outsourcing responsibility for the provision of the consumables necessary to operate the hardware for human use to academic instructions. However, despite the high profile of the academic institutions involved, it is clear that the scale of the resources available in each centre was lower than that necessary to deliver the translation of a medicinal product across the original project timescales to the satisfaction of international regulatory bodies.

2.9 Appendix 2A: Methods for preclinical studies

2.9.1 Model

Male Wistar rats were used in studies in this chapter and all procedures were carried out in accordance with the UK Animals (Scientific Procedures) Act 1986. For magnetic resonance experiment, animals were anaesthetized using 3 % isoflurane (2.5 L/min O_2, 0.3 L/min N_2O) and anaesthesia was maintained with 2 % isoflurane thereafter. A tail vein catheter was inserted for intravenous injection of either glucose, metformin or saline and the hyperpolarised [^{13}C]pyruvate sample.

2.9.2 Hyperpolarized magnetic resonance spectroscopy

[1-^{13}C]pyruvic acid was hyperpolarized in a prototype hyperpolarizer as described previously[14]. Pre-polarised pyruvate was administered as a bolus of 1 ml of 80 mM solution over 10 s. Slice selective spectra were acquired interleaved over the following two minutes either from a single axial slice covering the heart (glucose infusion experiment) or from two axial slabs covering the heart and liver (metformin experiment). The spectroscopy sequence included a 350 μs sinc pulse, 1 cm thick excitation, 8 kHz bandwidth, 15° flip angle, TR 1s, both slices ECG gated). Experiments were performed on an Agilent 7 T preclinical horizontal bore scanner with a volume transmit/two channel surface receive array (Rapid Biomedical GmbH, Rimpar, Germany). Multicoil spectra were pre-whitened and added in phase. Spectra from the heart and liver were then temporally summed and quantified in jMRUI using the AMARES algorithm. For imaging experiments, a specifically designed MR sequence with spectral-spatial radiofrequency pulses with echo planar imaging gradients was used, as previously described[34].

2.9.3 Metformin administration

For initial studies of the chronic effects of metformin, rats were provided with either 250 mg/kg/day metformin in drinking water or control flavoured water without metformin for 4 weeks prior to hyperpolarized [1-^{13}C]pyruvate MRS experiments.

For subsequent studies of the acute effects of metformin, an intravenous infusion of either 50mg metformin or a saline infusion of the same volume was administered 45 minutes prior to the administration of hyperpolarized [1-^{13}C] pyruvate.

2.9.4 Preclinical echocardiography

Echocardiography was performed under light isoflurane anaesthesia using a Vivid I ultrasound scanner with 11.5 MHz 10S-RS probe (both from GE Healthcare). Systolic function was assessed from parasternal M-mode views. Diastolic function was assessed using pulsed wave Doppler examination directed to the mitral valve inflow (E wave) and tissue Doppler imaging of the medial mitral annulus (to derive E'). Analysis was performed using a commercially available software package (Xcelera, Philips Healthcare) by an expert operator blinded to experimental group.

2.9.5 Tissue analysis

Heart and liver tissue was homogenised and metabolites extracted using a perchloric acid based method and neutralised to pH 7 by adding sodium hydroxide. [Lactate] was determined using an automated assay system (Pentra 400, Horiba ABX Diagnostics), [pyruvate] was determined using a fluorescent assay (Cayman Chemical Company, Michigan, USA) and [NAD^+] and [NADH] ratios were determined using a colorimetric assay (Cambridge Bioscience, Cambridge, UK).

2.9.6 Statistical analysis

Data are reported as mean ± standard error of the mean (SEM) whilst statistical significance was determined as $p \leq 0.05$ and calculated using unpaired student t-tests or ANOVA with multiple comparison testing by Tukey's method unless otherwise described. No suitable pilot data were available to inform power calculations and the numbers assigned to experimental groups in each preclinical study were selected empirically.

2.10 Appendix 2B: Methods for clinical study

2.10.1 Personal contribution

The clinical study was conceived by Professors Tyler (DJT) and Rider (OJR). My personal contribution to the work was co-authorship of the protocol and ethical approval applications with OJR, and recruitment of the single participant presented. I was also responsible the clinical investigations and loading of the power injector with hyperpolarized substrate; OJR performed the imaging protocol and DJT was responsible for production of hyperpolarized pyruvate. Dr Jack Miller designed and ran the ^{13}C spectroscopy sequence and extracted resulting data leading the time course presented in Figure 2.15.

2.10.2 Clinical echocardiography

Echocardiography was performed using a CX50 echocardiography system (Philips Healthcare, The Netherlands). Because a CMR left ventricular volume stack was also performed, echocardiographic assessment was limited to diastology, including transmitral flow profile (E/A ratio), mitral annular tissue Doppler (to derive e') and pulmonary venous Doppler to derive systolic and diastolic wave velocities.

2.10.3 CMR methods

All clinical CMR experiments were performed using a multinuclear 3 T MR system (Tim Trio, Siemens Healthcare, Erlangen, Germany).

2.10.3.1 LV volume stack

Following acquisition of pilot images, horizontal and vertical long axis cine images were obtained using steady state free precession (SSFP) imaging. A short axis cine image stack was subsequently acquired, covering base to apex in 10 mm slices (7 mm slice thickness; 3 mm gap).

2.10.3.2 ^{31}P spectroscopy

^{31}P magnetic resonance spectroscopy was performed at 3 T and acquired with a 3 dimensional acquisition-weighted chemical shift imaging technique, as previously described[49]. Three 25 mm saturation bands were placed over the chest wall and liver. The central voxel for was placed in the mid interventricular septum, with rotation to maximise coverage of the septal myocardium.

2.10.3.3 ^{1}H spectroscopy

The ^{1}H MRS sequence was based on a conventional STEAM sequence that was modified to achieve a short TE of 10 ms, as previously described[50]. A voxel was placed in a mid-ventricular slice in the interventricular septum of a short axis image. Acquisition consisted of six breath-holds of about 16 s each, five breath-holds which allowed for the acquisition of 35 non-averaged water-suppressed spectra. Four non-averaged water spectra were subsequently acquired with a minimum TR of 4 s in a separate breath-hold by setting the water suppression RF pulse power to zero.

2.11 Appendix 2C: References

1. Kannel W B, Hjortland M, and Castelli W P *Role of diabetes in congestive heart failure: the Framingham study.* The American Journal of Cardiology 1974;34(1):29-34

2. Rubler S, Dlugash J, Yuceoglu Y Z, Kumral T, Branwood A W, and Grishman A *New type of cardiomyopathy associated with diabetic glomerulosclerosis.* The American Journal of Cardiology 1972;30(6):595-602

3. King H, Aubert R E, and Herman W H *Global burden of diabetes, 1995–2025: prevalence, numerical estimates, and projections.* Diabetes Care 1998;21(9):1414-1431

4. Stamler J, Vaccaro O, Neaton J D, and Wentworth D *Diabetes, other risk factors, and 12-yr cardiovascular mortality for men screened in the Multiple Risk Factor Intervention Trial.* Diabetes Care 1993;16(2):434-444

5. Civitarese A E and Ravussin E *Minireview: mitochondrial energetics and insulin resistance.* Endocrinology 2008;149(3):950-954

6. Diamant M, Lamb H J, Groeneveld Y, Endert E L, Smit J W, Bax J J, Romijn J A, de Roos A, and Radder J K *Diastolic dysfunction is associated with altered myocardial metabolism inasymptomatic normotensive patients with well-controlled type 2 diabetes mellitus.* Journal of the American College of Cardiology 2003;42(2):328-335

7. Scheuermann-Freestone M, Madsen P L, Manners D, Blamire A M, Buckingham R E, Styles P, Radda G K, Neubauer S, and Clarke K *Abnormal cardiac and skeletal muscle energy metabolism in patients with type 2 diabetes.* Circulation 2003;107(24):3040-3046

8. Levelt E, Rodgers C T, Clarke W T, Mahmod M, Ariga R, Francis J M, Liu A, Wijesurendra R S, Dass S, and Sabharwal N *Cardiac energetics, oxygenation, and perfusion during increased workload in patients with type 2 diabetes mellitus.* European Heart Journal 2015:ehv442

9. Poornima I G, Parikh P, and Shannon R P *Diabetic cardiomyopathy: the search for a unifying hypothesis.* Circulation Research 2006;98(5):596-605

10. Belke D D, Larsen T S, Gibbs E M, and Severson D L *Altered metabolism causes cardiac dysfunction in perfused hearts from diabetic (db/db) mice.* American Journal of Physiology-Endocrinology And Metabolism 2000;279(5):E1104-E1113

11. Chatham J C and Seymour A-M L *Cardiac carbohydrate metabolism in Zucker diabetic fatty rats.* Cardiovascular Research 2002;55(1):104-112

12. Hällsten K, Virtanen K, Lönnqvist F, Janatuinen T, Turiceanu M, Rönnemaa T, Viikari J, Lehtimäki T, Knuuti J, and Nuutila P *Enhancement of insulin-stimulated myocardial glucose uptake in patients with Type 2 diabetes treated with rosiglitazone.* Diabetic Medicine 2004;21(12):1280-1287

13. Rijzewijk L J, van der Meer R W, Lamb H J, de Jong H W, Lubberink M, Romijn J A, Bax J J, de Roos A, Twisk J W, and Heine R J *Altered myocardial substrate metabolism and decreased diastolic function in nonischemic human diabetic cardiomyopathy: studies*

with cardiac positron emission tomography and magnetic resonance imaging. Journal of the American College of Cardiology 2009;54(16):1524-1532

14. Schroeder M A, Cochlin L E, Heather L C, Clarke K, Radda G K, and Tyler D J *In vivo assessment of pyruvate dehydrogenase flux in the heart using hyperpolarized carbon-13 magnetic resonance.* Proceedings of the National Academy of Sciences 2008;105(33):12051-12056

15. Le Page L M, Rider O J, Lewis A J, Ball V, Clarke K, Johansson E, Carr C A, Heather L C, and Tyler D J *Increasing Pyruvate Dehydrogenase Flux as a Treatment for Diabetic Cardiomyopathy: A Combined ^{13}C Hyperpolarized Magnetic Resonance and Echocardiography Study.* Diabetes 2015:db141560

16. Van der Lee K A, Willemsen P H, Samec S, Seydoux J, Dulloo A G, Pelsers M M, Glatz J F, Van der Vusse G J, and Van Bilsen M *Fasting-induced changes in the expression of genes controlling substrate metabolism in the rat heart.* Journal of Lipid Research 2001;42(11):1752-1758

17. Taegtmeyer H, Young M E, Lopaschuk G D, Abel E D, Brunengraber H, Darley-Usmar V, Des Rosiers C, Gerszten R, Glatz J F, and Griffin J L *Assessing Cardiac Metabolism: A Scientific Statement From the American Heart Association.* Circulation Research 2016:RES. 0000000000000097

18. Ambrosini V, Zompatori M, Fasano L, Nanni C, Nava S, Rubello D, and Fanti S *18F-FDG PET/CT for the assessment of disease extension and activity in patients with sarcoidosis: results of a preliminary prospective study.* Clinical Nuclear Medicine 2013;38(4):e171-e177

19. Williams G and Kolodny G M *Suppression of myocardial ^{18}F-FDG uptake by preparing patients with a high-fat, low-carbohydrate diet.* American Journal of Roentgenology 2008;190(2):W151-W156

20. Morooka M, Moroi M, Ito K, Minamimoto R, Miyata Y, Okasaki M, and Kubota K *Heparin vs. long fasting method: which inhibits the FDG myocardial physiological uptake more strongly?* Journal of Nuclear Medicine 2013;54(supplement 2):1723-1723

21. Zierhut M L, Yen Y-F, Chen A P, Bok R, Albers M J, Zhang V, Tropp J, Park I, Vigneron D B, and Kurhanewicz J *Kinetic modeling of hyperpolarized [1-^{13}C]pyruvate metabolism in normal rats and TRAMP mice.* Journal of Magnetic Resonance 2010;202(1):85-92

22. Wray J A, Sugden M C, Zeldin D C, Greenwood G K, Samsuddin S, Miller-Degraff L, Bradbury J A, Holness M J, Warner T D, and Bishop-Bailey D *The epoxygenases CYP2J2 activates the nuclear receptor PPARα in vitro and in vivo.* PloS One 2009;4(10):e7421

23. Randle P, Garland P, Hales C, and Newsholme E *The glucose fatty-acid cycle its role in insulin sensitivity and the metabolic disturbances of diabetes mellitus.* The Lancet 1963;281(7285):785-789

24. UK Prospective Diabetes Study Group *Effect of intensive blood-glucose control with metformin on complications in overweight patients with type 2 diabetes (UKPDS 34).* The Lancet 1998;352(9131):854-865

25. Turner R C, Cull C A, Frighi V, Holman R R, and Group U P D S *Glycemic control with diet, sulfonylurea, metformin, or insulin in patients with type 2 diabetes mellitus: progressive requirement for multiple therapies (UKPDS 49).* JAMA 1999;281(21):2005-2012

26. Inzucchi S E, Maggs D G, Spollett G R, Page S L, Rife F S, Walton V, and Shulman G I *Efficacy and metabolic effects of metformin and troglitazone in type II diabetes mellitus.* New England Journal of Medicine 1998;338(13):867-873

27. Zhou G, Myers R, Li Y, Chen Y, Shen X, Fenyk-Melody J, Wu M, Ventre J, Doebber T, and Fujii N *Role of AMP-activated protein kinase in mechanism of metformin action.* Journal of Clinical Investigation 2001;108(8):1167

28. El-Mir M-Y, Nogueira V, Fontaine E, Avéret N, Rigoulet M, and Leverve X *Dimethylbiguanide inhibits cell respiration via an indirect effect targeted on the respiratory chain complex I.* Journal of Biological Chemistry 2000;275(1):223-228

29. Madiraju A K, Erion D M, Rahimi Y, Zhang X-M, Braddock D T, Albright R A, Prigaro B J, Wood J L, Bhanot S, and MacDonald M J *Metformin suppresses gluconeogenesis by inhibiting mitochondrial glycerophosphate dehydrogenase.* Nature 2014;510(7506):542-546

30. Schramm T K, Gislason G H, Vaag A, Rasmussen J N, Folke F, Hansen M L, Fosbøl E L, Køber L, Norgaard M L, and Madsen M *Mortality and cardiovascular risk associated with different insulin secretagogues compared with metformin in type 2 diabetes, with or without a previous myocardial infarction: a nationwide study.* European Heart Journal 2011;32(15):1900-1908

31. Eurich D T, Majumdar S R, McAlister F A, Tsuyuki R T, and Johnson J A *Improved clinical outcomes associated with metformin in patients with diabetes and heart failure.* Diabetes Care 2005;28(10):2345-2351

32. Gundewar S, Calvert J W, Jha S, Toedt-Pingel I, Ji S Y, Nunez D, Ramachandran A, Anaya-Cisneros M, Tian R, and Lefer D J *Activation of AMP-activated protein kinase by metformin improves left ventricular function and survival in heart failure.* Circulation Research 2009;104(3):403-411

33. Bhamra G S, Hausenloy D J, Davidson S M, Carr R D, Paiva M, Wynne A M, Mocanu M M, and Yellon D M *Metformin protects the ischemic heart by the Akt-mediated inhibition of mitochondrial permeability transition pore opening.* Basic Research in Cardiology 2008;103(3):274-284

34. Miller J J, Lau A Z, Teh I, Schneider J E, Kinchesh P, Smart S, Ball V, Sibson N R, and Tyler D J *Robust and high resolution hyperpolarized metabolic imaging of the rat heart at 7 T with 3D spectral-spatial EPI.* Magnetic Resonance in Medicine 2015;

35. Rupert B E, Segar J L, Schutte B C, and Scholz T D *Metabolic adaptation of the hypertrophied heart: role of the malate/aspartate and α-glycerophosphate shuttles.* Journal of Molecular and Cellular Cardiology 2000;32(12):2287-2297

36. Krebs H and Gascoyne T *The redox state of the nicotinamide-adenine dinucleotides in rat liver homogenates.* Biochemical Journal 1968;108:513-520

37. Baba N and Sharma H M *Histochemistry of lactic dehydrogenase in heart and pectoralis muscles of rat.* The Journal of Cell Biology 1971;51(3):621-635

38. Carvalho C, Correia S, Santos M S, Seiça R, Oliveira C R, and Moreira P I *Metformin promotes isolated rat liver mitochondria impairment.* Molecular and Cellular Biochemistry 2008;308(1-2):75-83

39. He L and Wondisford F E *Metformin action: concentrations matter.* Cell Metabolism 2015;21(2):159-162

40. Tahrani A, Varughese G, Scarpello J, and Hanna F *Metformin, heart failure, and lactic acidosis: is metformin absolutely contraindicated?* BMJ 2007;335(7618):508-512

41. Hundal R S, Krssak M, Dufour S, Laurent D, Lebon V, Chandramouli V, Inzucchi S E, Schumann W C, Petersen K F, and Landau B R *Mechanism by which metformin reduces glucose production in type 2 diabetes.* Diabetes 2000;49(12):2063-2069

42. Hällsten K, Virtanen K A, Lönnqvist F, Sipilä H, Oksanen A, Viljanen T, Rönnemaa T, Viikari J, Knuuti J, and Nuutila P *Rosiglitazone but not metformin enhances insulin- and exercise-stimulated skeletal muscle glucose uptake in patients with newly diagnosed type 2 diabetes.* Diabetes 2002;51(12):3479-3485

43. Baur J A and Birnbaum M J *Control of gluconeogenesis by metformin: does redox trump energy charge?* Cell Metabolism 2014;20(2):197-199

44. Medicines & Healthcare Products Regulatory Agency. *It it a clinical trial of a medicinal product?* Accessed 2016; Available from: https://www.gov.uk/government/uploads/system/uploads/attachment_data/file/317952/Algothrim.pdf.

45. Department of Health *Research governance framework for health and social care*, 2009: London

46. International Conference on Hamonisation of Technical Requirements for Registration of Pharmaceuticals for Human Use. *Guideline for Good Clinical Practice E6(R1).* 1996 Accessed May 2016]; Available from: http://www.ich.org/fileadmin/Public_Web_Site/ICH_Products/Guidelines/Efficacy/E6/E6_R1_Guideline.pdf.

47. Wi Medical Device Development Inc. Accessed May 2016; Available from: http://wiinc.net/spinlab/.

48. Sokoloff L, Reivich M, Kennedy C, Des Rosiers M, Patlak C S, Pettigrew K, Sakurada O, and Shinohara M *The [^{14}C]deoxyglucose method for the measurement of local cerebral glucose utilization: theory, procedure, and normal values in the conscious and anesthetized albino rat.* Journal of Neurochemistry 1977;28(5):897-916

49. Tyler D, Emmanuel Y, Cochlin L, Hudsmith L, Holloway C, Neubauer S, Clarke K, and Robson M *Reproducibility of ^{31}P cardiac magnetic resonance spectroscopy at 3 T.* NMR in Biomedicine 2009;22(4):405-413

50. Rial B, Robson M D, Neubauer S, and Schneider J E *Rapid quantification of myocardial lipid content in humans using single breath-hold ^{1}H MRS at 3 Tesla.* Magnetic Resonance in Medicine 2011;66(3):619-624

Chapter 3: Mechanistic and energetic insights into obesity cardiomyopathy

3.1 Abstract

Obesity is associated with a two-fold increased risk of developing heart failure and a distinct cardiac phenotype that has been termed 'obesity cardiomyopathy'. The mechanisms underlying the development of obesity cardiomyopathy are unclear, and no specific pharmacological treatment for this indication is currently available. Using a rodent model and multinuclear MRS, we show that obesity causes profound changes in cardiac energy metabolism, including suppression of PDH flux and impairment of cardiac energetics; findings which coexisted with diastolic functional impairment. Restoration of cardiac PDH flux, using either the glucagon like peptide 1 analogue Liraglutide or caloric restriction, was associated with normalisation of cardiac substrate selection and intermediary metabolism, restoration of the cardiac energetic state and reversal of diastolic functional impairment. These findings suggest that PDH flux may be a therapeutic target in obesity cardiomyopathy and provide a rationale for pilot clinical studies using hyperpolarized magnetic resonance in cardiovascular and metabolic diseases. An approach to clinical translation and potential roles in future mechanistic and dose ranging phase II pharmacological trials is discussed.

3.2 Background

3.2.1 Obesity related heart disease

Obesity, defined as a body mass index of ≥30 kg/m^2, is associated with a two-fold increased risk of developing heart failure[1] and a spectrum of cardiovascular changes that range from subclinical cardiac impairment to overt ventricular systolic dysfunction[2]. Worldwide, more than 2 billion people are either obese or overweight (defined as a body mass index of 25-30 kg/m^2), and obesity is thus likely to become a major driver of an increased societal burden of heart failure. No specific pharmacological therapy beyond those already used for the treatment of heart failure has been shown to improve symptoms or outcomes in obesity related heart disease and it therefore represents a major unmet health need.

The term obesity cardiomyopathy is used to describe structural and functional cardiac changes occurring in people with obesity in the absence of other causes[2, 3]. These changes most commonly include ventricular remodelling and impairment of cardiac diastolic function and the obesity epidemic may therefore be an important driver behind the increasing rates of hospital admission for heart failure with preserved ejection fraction (HFPEF), which now outnumber admissions for heart failure with reduced ejection fraction (HFREF)[4]. Obesity can also coexist with, and is likely to exacerbate, heart failure due to other causes (such as ischaemic heart disease or dilated cardiomyopathy, (Figure 3.1) as similar pathophysiological mechanisms apply. The relationship between obesity and clinical outcomes in advanced heart failure is incompletely understood, and has been associated with a paradoxical improvement in prognosis[5].

Although the pathophysiology of obesity related heart disease is almost certainly multifactorial[6], an increasing body of evidence suggests that abnormal cardiac substrate metabolism may be an important aspect of its development and maintenance. However,

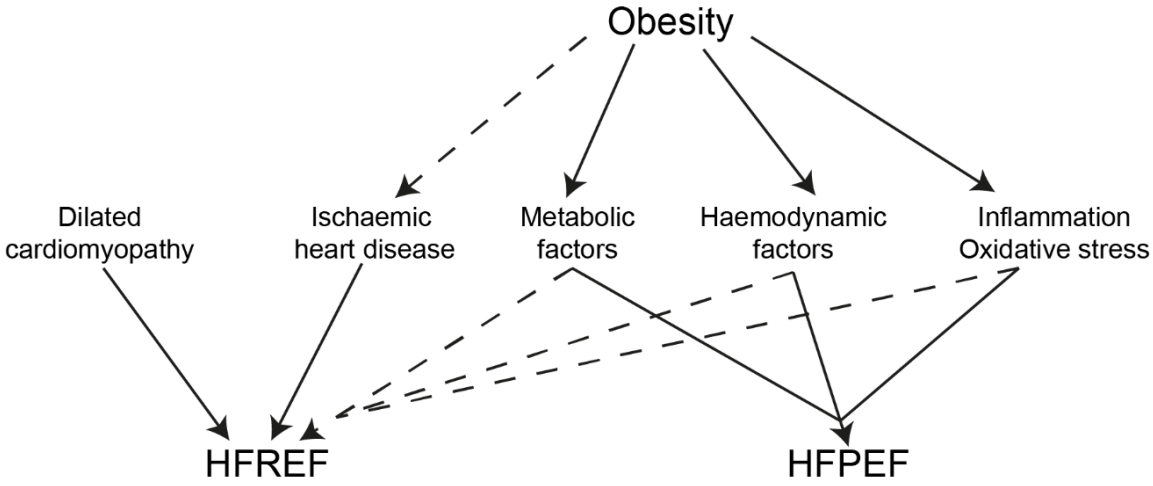


Figure 3.1: Obesity is independently associated with the development of heart failure (usually HFPEF) through a variety of mechanisms, but the same mechanisms are also likely to be detrimental to HFREF due to other causes such as dilated cardiomyopathy or ischaemic heart disease, for which obesity is a risk factor.

there is significant heterogeneity in experimental findings to date and whether cardiac substrate metabolism may be a valid pharmacological therapeutic target for this condition remains unknown, in part because conventional techniques cannot assess cardiac substrate metabolism and energetics, at repeated time points, *in vivo*.

3.2.2 Cardiac energy metabolism in obesity cardiomyopathy

3.2.2.1 Substrate selection and pyruvate dehydrogenase activity in obesity

Although the healthy adult heart derives the majority of acetyl coenzyme A (CoA) for adenosine triphosphate (ATP) synthesis from the beta oxidation of fatty acids, one key metabolic change in obesity is a further increase in fatty acid utilisation, which is paralleled by lower glucose uptake[7, 8].

In the heart, PDK4 is the major regulator of PDH activity[9], and is an important target of peroxisome proliferator-activated receptor (PPAR) signalling pathways. The PPARs belong to the nuclear receptor hormone superfamily and include three members (α, β/δ and γ) which are also differentially expressed according to tissue[10]. PPAR-α is the dominant isoform in the heart and has a large ligand binding pocket which allows the binding of multiple saturated and unsaturated fatty acid species[11] thus facilitating its function as both

an intracellular receptor for lipid molecules and also a transcription factor in the regulation of metabolic gene expression.

In obesity, circulating levels of fatty acids and triacylglycerols are high[12] and, as the heart is a highly efficient scavenger of fatty acids[13], result in increased cardiomyocyte lipid uptake and content[14]. These lipid species activate PPARs, which, in conjunction with heterodimerization with retinoic X receptors[15] and coactivation, lead to transcription of PPAR target genes. PPAR targets include genes involved in every step of cardiac fatty acid metabolism but also include PDK4 (and the remaining PDKs), which would be expected to result in a decrease in cardiac PDH activity and metabolic reprogramming of the heart to further increase fatty acid metabolism. PPAR mediated PDK4 transcription is predominantly mediated by the binding of PPAR coactivator/ERR-α to PDK4 promoter regions[16], though obesity is also associated with epigenetic PDK4 promoter modification[17]. Increased PDK levels in the heart are a consistent finding in models of obesity[18, 19], and, in conjunction with low-grade insulin resistance, impaired glucose uptake and allosteric end product inhibition of PDH[20], lead to suppressed cardiac carbohydrate oxidation in animal models[21]. Clinical positron emission tomography studies are generally consistent with the animal studies and report reductions in cardiac glucose uptake and oxygen efficiency, whilst fat uptake is increased[7, 22]. Normalization of PDK gene transcript levels[23], increased glucose metabolism, reduced fat oxidation and cardiac functional improvement[24] occur following caloric intake restriction/weight loss.

Direct and indirect genetic manipulation of PDH activity has provided further evidence that reduced PDH activity may have a role in the development of cardiac functional impairment in animal models of obesity cardiomyopathy. Complete genetic ablation of the heart/skeletal muscle form of PDH in mice leads to embryonic/neonatal mortality[25], which

is consistent with the observation that carbohydrate metabolism is the dominant source of reducing equivalents in the developing heart and is essential in the 'fetal phenotype'. Mice with heart and skeletal muscle specific knockout of the alpha-subunit of PDH have no detectable cardiac PDH activity, and, despite embryonic viability, do not survive weaning to standard chow due to heart failure[25]. High fat feeding prolongs the survival of these mice but leads to a severe cardiac phenotype, including ventricular hypertrophy and systolic dysfunction. Furthermore, cardiac specific overexpression of PPAR-α, resulting in markedly elevated PDK4 levels and a significant reduction in glucose oxidation, also causes cardiac dysfunction and hypertrophy[26].

3.2.2.2 Cardiac energetics in obesity

Although increased fatty acid metabolism and decreased glucose metabolism are reasonably well established components of the obesity cardiomyopathy phenotype, it is uncertain whether this loss of metabolic flexibility represents a legitimate therapeutic target, as the mechanistic links to cardiac functional deficit are less clearly defined. However, cardiac mitochondrial dysfunction is a consistent finding in models of obesity[27] and is a key candidate mechanism linking impaired substrate metabolism to functional deficit in obesity cardiomyopathy.

In humans, cardiac energetic status is generally assessed non-invasively using ^{31}P magnetic resonance spectroscopy to measure the concentrations of phosphocreatine (PCr) and ATP with localisation to the myocardium[28]. Obesity is associated with a reduction in cardiac PCr/ATP ratio at rest[29], and an even greater reduction during increased cardiac workload[30] when patients with obesity frequently experience undue dyspnoea. Thus, although obesity is a state of a chronic excess of circulating metabolic fuel, the heart is paradoxically energy deplete at the level of high energy phosphorus metabolism. These observations suggest that

obesity causes marked inefficiencies in the pathways linking substrate uptake, oxidation and ATP production, although no study has assessed the metabolic pathway, in its entirety, in the diseased state.

Although the majority of ATP produced by the heart is used to support systolic function, diastole is likely to be more susceptible to energetic deficit[31]. The reasons for this lie in the fact that the overall energetic state of the heart is defined not simply by ATP concentration, which is preserved until the development of advanced heart failure. Rather, the heart depends on high rates of both ATP delivery and also of clearance of the products of ATP hydrolysis, ADP and Pi, which inhibit ATPase reactions[32]. The ratio of ATP to ADP and Pi thus determines the available chemical driving force to overcome the thermodynamically unfavourable reactions involved in cardiac contraction and relaxation, including the myosin ATPase and the sarcoplasmic reticulum Ca^{2+} ATPase (SERCA). Even small increases in ADP concentration due to inhibition of the creatine kinase reaction lead to diastolic dysfunction, likely by slowing myosin ATPase associated cross bridge cycling[33]. In addition, the sarcoplasmic reticulum Ca^{2+} ATPase also depends upon a high chemical driving force in order to extrude cytosolic calcium and prevent diastolic calcium overload, another important cause of diastolic dysfunction[34]. Thus, although the actin-myosin ATPase consumes a greater quantity of ATP than the SERCA, SERCA function requires the highest chemical driving force of all cardiac ATPases (approximately -53 $kJ.mol^{-1}$)[35] and thus has the greatest susceptibility to energetic deficit.

The provision of a sufficient chemical driving force for ATPase reactions depends not only on the potential energy of the substrate but also on the efficiency of the biochemical processes that link substrate oxidation to mitochondrial redox power. Dominant fat metabolism in obesity is associated with the expression of uncoupling proteins (UCPs)

including UCP2, UCP3 (a PPAR-α target), adenine nucleotide transporter (ANT) and mitochondrial thioesterase-1 (MTE-1)[36]. These proteins have traditionally been thought to allow proton leak into the mitochondrial matrix, bypassing ATP generating pathways and partially dissipating the proton gradient required for ATP production[37]. In addition to evidence of increased mitochondrial uncoupling in hearts from obese animals, genetic deletion of UCP3 improves mitochondrial efficiency without altering substrate oxidation rates[38]. However, the precise role of UCPs in obesity remain to be fully elucidated, and UCP3 may act as a fatty acid transporter and acetyl CoA buffer[39]. Furthermore, mitochondrial uncoupling may have an important protective role in mitigating oxidative stress in obesity, as, when electron supply and the mitochondrial membrane potential exceed ADP availability or demand for ATP synthesis[40], excess electrons escape by reducing molecular oxygen, leading to the production of hydrogen peroxide. Additional mechanisms linking dominant fat metabolism to inefficient oxidative phosphorylation include the inefficient delivery of reducing equivalents to complex I by beta-oxidation[41] and oxidative post translational modifications of complex II[42], leading to impaired function.

3.3 Hypotheses

These data, and others, support a role for impaired carbohydrate metabolism in the development of obesity cardiomyopathy, potentially via the development of mitochondrial/energetic dysfunction, thus providing a rationale for investigating the role of pharmacological and non-pharmacological interventions that target substrate selection in obesity. However, there is significant heterogeneity in experimental findings to date and many studies have been limited by an inability to measure PDH flux *in vivo* whilst no study has investigated the links between PDH flux, high energy phosphorus metabolism and cardiac function in both systole and diastole.

Accordingly, it was hypothesised that:

1. Obesity would cause abnormal carbohydrate metabolism, impairing myocardial PDH flux.

2. Impaired PDH flux would be associated with changes in TCA cycle metabolism and cardiac energetics.

3. Normalisation of cardiac substrate metabolism, either pharmacologically or using caloric restriction, would ameliorate the energetic and functional deficit.

This chapter describes work using hyperpolarized ^{13}C magnetic resonance spectroscopy to measure flux through pyruvate dehydrogenase and the first span of the tricarboxylic acid cycle, perfused heart ^{31}P MRS energetic studies and echocardiographic functional studies using a rodent model of obesity cardiomyopathy.

3.4 Methods development and results

3.4.1 Selection of a clinically relevant model to study obesity cardiomyopathy

In order to study cardiac metabolism in obesity cardiomyopathy using hyperpolarized magnetic resonance, it was first necessary to establish a disease model that recapitulated the major components of the clinical phenotype. A commercially available rodent model of diet induced obesity (outbred Long Evans rats with high fat diet (Teklad TD.95217, 40% KCal from fat, Harlan Laboratories, UK) for 8 weeks) was initially selected. However, this model was unsuitable as there was no significant difference between the body mass of the two groups at arrival (at 10 weeks), precluding use as a meaningful model of human obesity. We therefore obtained a second model using an inbred strain (HsdBlu:LE) with a higher fat content diet (TD.06414, 60% KCal from fat, full details in section 3.7.1) which demonstrated satisfactory separation in growth curves from the control group (receiving TD2014S) and an overall 20% increase in body mass (440 ± 6 versus 351 ± 6 g, $P < 0.0001$, Figure 3.2).

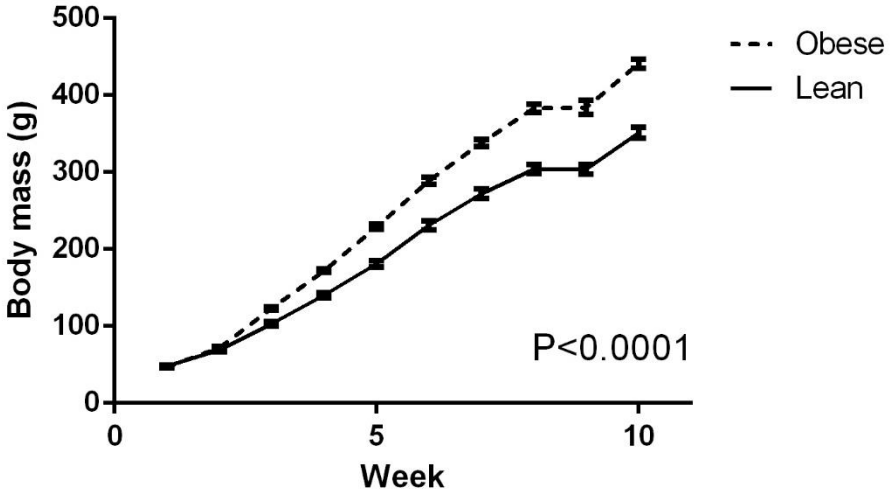


Figure 3.2: High fat feeding led to a ~20% increase in body mass in high fat fed (n = 36) versus lean controls (n = 12) over 10 weeks in this model. Statistical comparison by unpaired two-tailed T test of body mass at 10 weeks.

3.4.2 Overview of experimental design

An overview of the experimental design is presented in Figure 3.3. Following a baseline assessment to characterise the phenotype of the model, the obese groups were assigned to either pharmacological treatment (one week) or caloric restriction (to 70 % of usual intake for 28 days) prior to restudy.

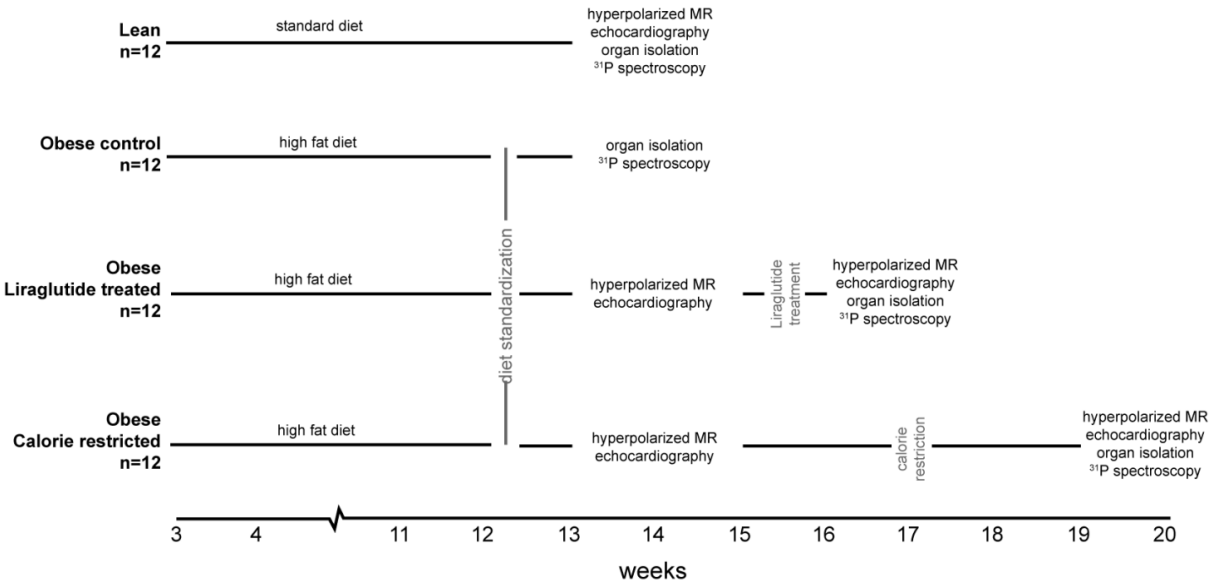


Figure 3.3: Overview of experimental design.

3.4.3 Characterisation of model

3.4.3.1 Obesity causes mild LV hypertrophy and diastolic, but not systolic, dysfunction

Transthoracic echocardiography was used to assess the cardiac phenotype in this model and was performed according to the optimised method described fully in Appendix 2A.

Obesity caused mild LV hypertrophy, with an increase in both septal (2.1 ± 0.1 versus 1.8 ± 0.1 mm, $P < 0.05$) and posterior wall thickness (2.3 ± 0.1 versus 2.0 ± 0.1 mm, $P < 0.05$, Figure 3.4) without significant cavity dilatation (LVIDD 6.2 ± 0.3 versus 6.6 ± 0.1 mm, P = ns). Obesity also caused mildly hyperdynamic systolic function (fractional shortening 53

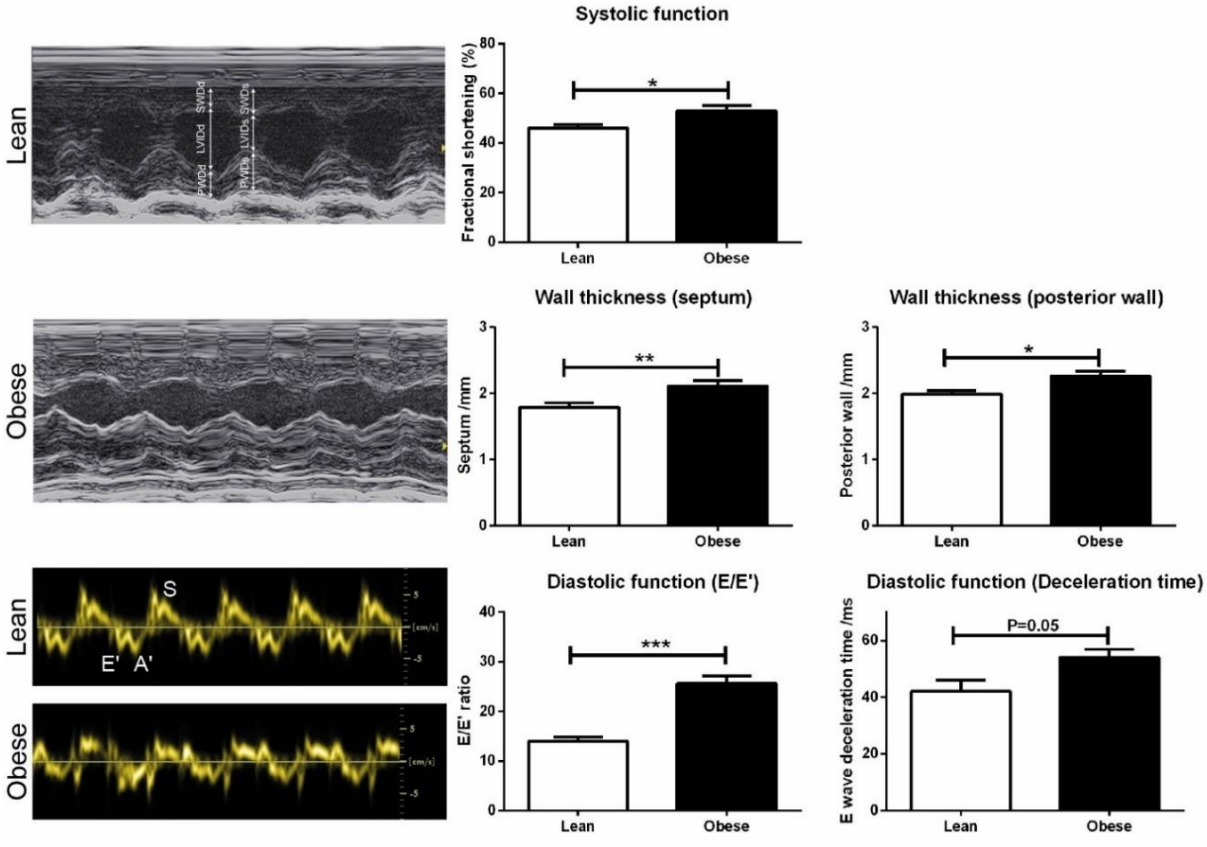


Figure 3.4: Structural and functional cardiac characterisation using echocardiography. Obesity was associated with increased LV wall thickness, mildly hyperdynamic systolic fucntion and marked diastolic dysfunction, broadly recapitulating the human phenotype. n = 18 (obese group) and n = 9 (lean controls); data are presented as mean ± SEM; statistical comparisons are by unpaired, two-tailed T-tests.

± 2 versus 46 ± 1%, P < 0.05) with marked diastolic dysfunction (E/E' ratio 26 ± 2 versus 14 ± 1, P < 0.001).

These changes occurred in the absence of significant hyperglycaemia, hyperinsulinemia, peripheral insulin resistance or hypertriglyceridemia although plasma high density lipoprotein (HDL) cholesterol levels were modestly reduced in obesity (Table 3.1, page 130). Similarly, cardiac lipotoxicity was not a major feature of this relatively mild model of obesity (myocardial triglyceride content 5.7 ± 1 versus 5.1 ± 1 mg/g wet weight, P = ns, Figure 3.5).

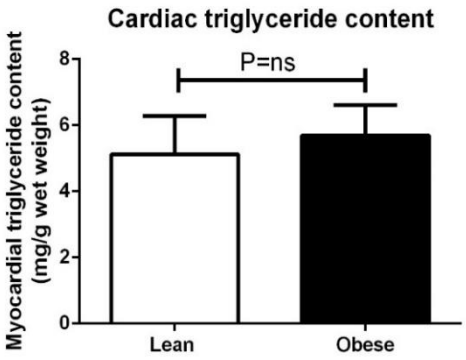


Figure 3.5: Cardiac lipotoxicity was not a major feature of this relatively mild model of obesity. n = 6 per group, mean ± SEM; unpaired, two-tailed T-test.

3.4.3.2 Obesity impaired myocardial PDH flux

Hyperpolarized cardiac magnetic resonance spectroscopy using [1-^{13}C]pyruvate was performed according to the method described in Appendix 2A with data acquisition from a single 10mm slice positioned over the heart.

Obesity reduced the rate of ^{13}C label incorporation into bicarbonate by 40% compared to lean controls (0.013 ± 0.002 s^{-1} versus 0.021 ± 0.002 s^{-1}, P < 0.01, Figure 3.6), with no change in the rate of label incorporation into lactate. The lack of an increase in label incorporation into lactate in the presence of reduced PDH flux is suggestive of reduced cellular glucose uptake, though this parameter cannot currently be measured using hyperpolarized MR.

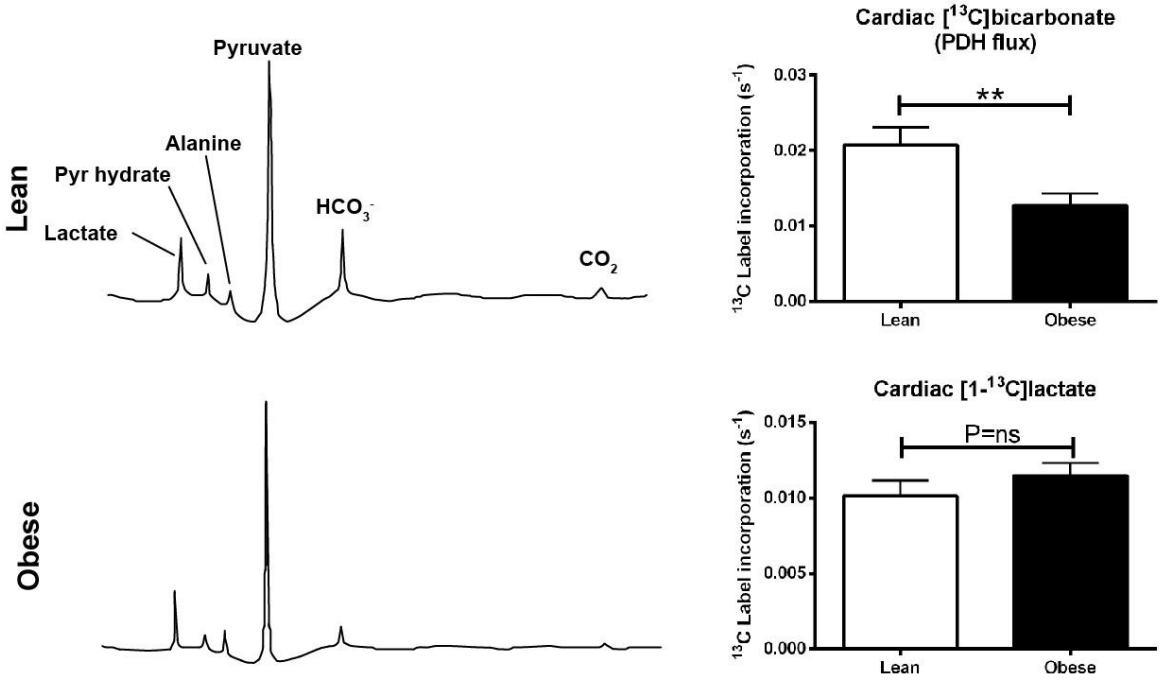


Figure 3.6: Obesity caused a 40% reduction in cardiac PDH flux, without increasing the rate of label incorporation into [1-^{13}C]lactate. n = 12 per group; mean ± SEM; statistical comparisons are by unpaired, two-tailed T-tests.

3.4.3.3 Obesity altered TCA cycle metabolism

As described fully in chapter 1, the ^{13}C label in hyperpolarized [2-^{13}C]pyruvate avoids oxidative decarboxylation by pyruvate dehydrogenase and instead enters the TCA cycle, providing information on select first span metabolite label incorporation. Because pyruvate dehydrogenase controls the rate of entry of this label into the TCA cycle, it is conventional to normalise [2-^{13}C]pyruvate metabolite data to PDH activity[43], and normalised values are presented in this chapter. Full methods for production, hyperpolarization and spectral acquisition of data from hyperpolarized [2-^{13}C]pyruvate experiments are described in Appendix 3A (page 141).

When compared to lean controls, obesity almost doubled the normalised rate of label incorporation into citrate (1.94 ± 0.3 versus 1.00 ± 0.3 AU, $P < 0.05$, Figure 3.7) and increased label incorporation into glutamate by over 50% (1.54 ± 0.1 versus 1.00 ± 0.1 AU, $P<0.05$). These findings imply an increase in the sizes of the citrate and glutamate pools.

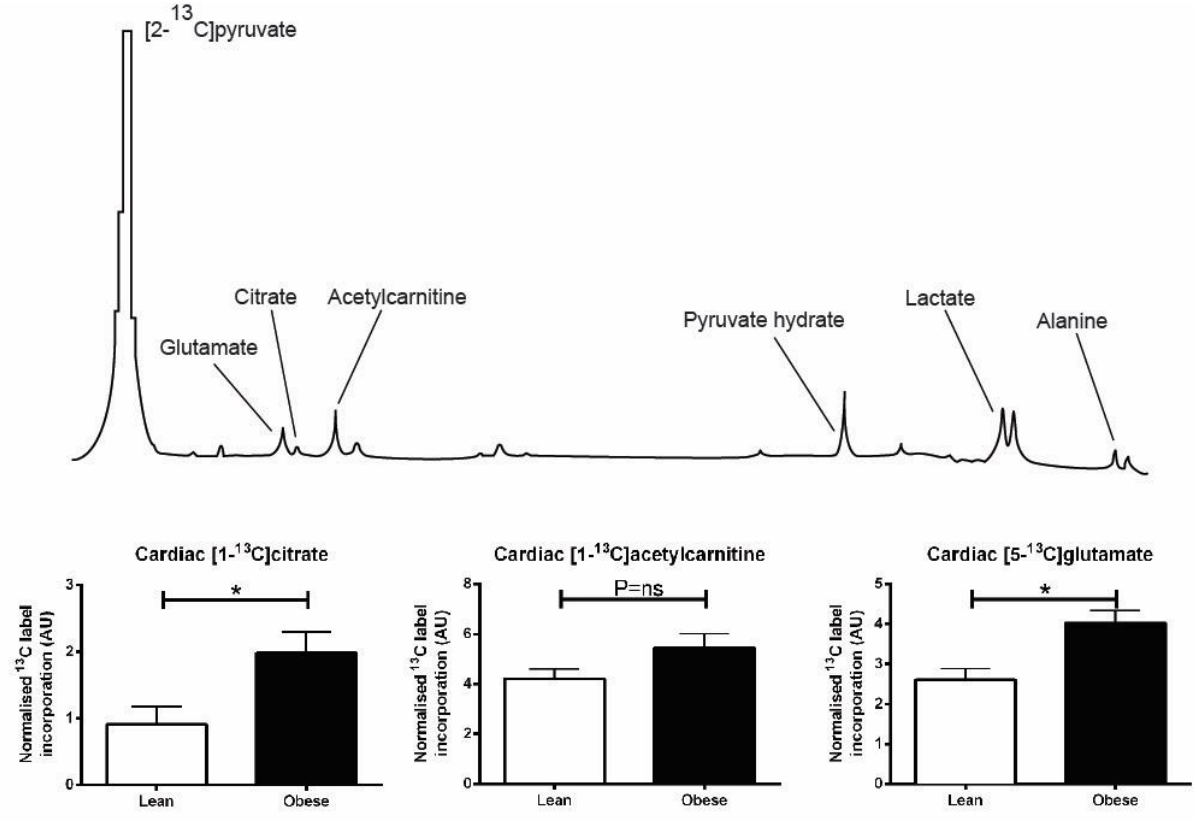


Figure 3.7: Hyperpolarized [1-2^{13}C]pyruvate demonstrates that obesity increases the rate of normalised cardiac ^{13}C label incorporation into [1-^{13}C] citrate and [5-^{13}C]glutamate, with no change in the rate of label incorporation into [1-^{13}C] acetycarnitine. n = 9 (lean group) and n = 15 (obese group) evaluable datasets; mean ± SEM; statistical comparisons are by unpaired, two-tailed T-tests.

In contrast, there was no change in the normalised rate of label incorporation into acetylcarnitine (1.30 ± 0.1 versus 1.00 ± 0.09 AU, P=ns), suggesting that the relative contribution of carbohydrate derived acetyl CoA to the acetylcarnitine pool was reduced due to low PDH flux.

3.4.4 Obesity compromised cardiac high energy phosphate metabolism

In order to determine whether obesity caused energetic deficit in this model, we performed ^{31}P MRS upon isolated perfused hearts using a perfusion rig colocated with a vertical bore 11.7 T magnet (methods described in detail in Appendix 3A (page 142)). This experimental design not only controls cardiac afterload and substrate availability, but also enables measurement of inorganic phosphate (Pi) which is precluded *in vivo* by the presence of 2,3 diphosphoglycerate. This in turn allows a more rigorous definition of cardiac

energetic state according to $\Delta G_{\sim ATP}$, the chemical driving force for ATPase reactions in the heart. $\Delta G_{\sim ATP}$ was derived according to equation 3.1:

$$\Delta G_{\sim ATP} = \Delta G^{0}{}_{\sim ATP} - RT\, ln \frac{[ATP]}{[ADP][Pi]} \quad 3.1$$

Where $\Delta G^{0}{}_{\sim ATP}$ is the constant value of for ATP hydrolysis under standard conditions (-30.J.mol^{-1}), ADP is adenosine diphosphate, R is the universal gas constant (8.3 J/mol/K) and T the absolute temperature. [ADP] was derived from the creatine kinase equation according to equation 3.2:

$$[ADP] = \frac{[ATP]\,[Creatine]}{K_{eq}\,[PCr]\,[H^{+}]} \quad 3.2$$

where K_{eq} is the equilibrium constant for the reaction, PCr is phosphocreatine, and [H^{+}] was estimated from the chemical shift of Pi.

High performance liquid chromatography (HPLC) metabolite quantitation (performed upon snap-frozen cardiac tissue) was used to calibrate spectroscopic metabolite content estimates and measure myocardial creatine concentration which was not different between obese and lean animals (22 ± 4 versus 19 ± 2 mM, P = ns).

Despite equivalent cardiac workload (rate-pressure product in obese versus lean animals 34000 ± 5000 versus 30000 ± 5000 mmHg.min^{-1}, P=ns), hearts from obese rats demonstrated significantly lower energetic reserve ($\Delta G_{\sim ATP}$ -59.2 ±0 .9 versus -64.8 ± 0.9 kJ.mol^{-1}, P<0.001, Figure 3.8) than hearts from lean rats. The PCr/ATP ratio, an alternative index of overall energetic state, was also significantly reduced in obesity (1.91 ± 0.07 versus 2.25 ± 0.09, P = 0.01). These findings confirm the presence of cardiac energetic

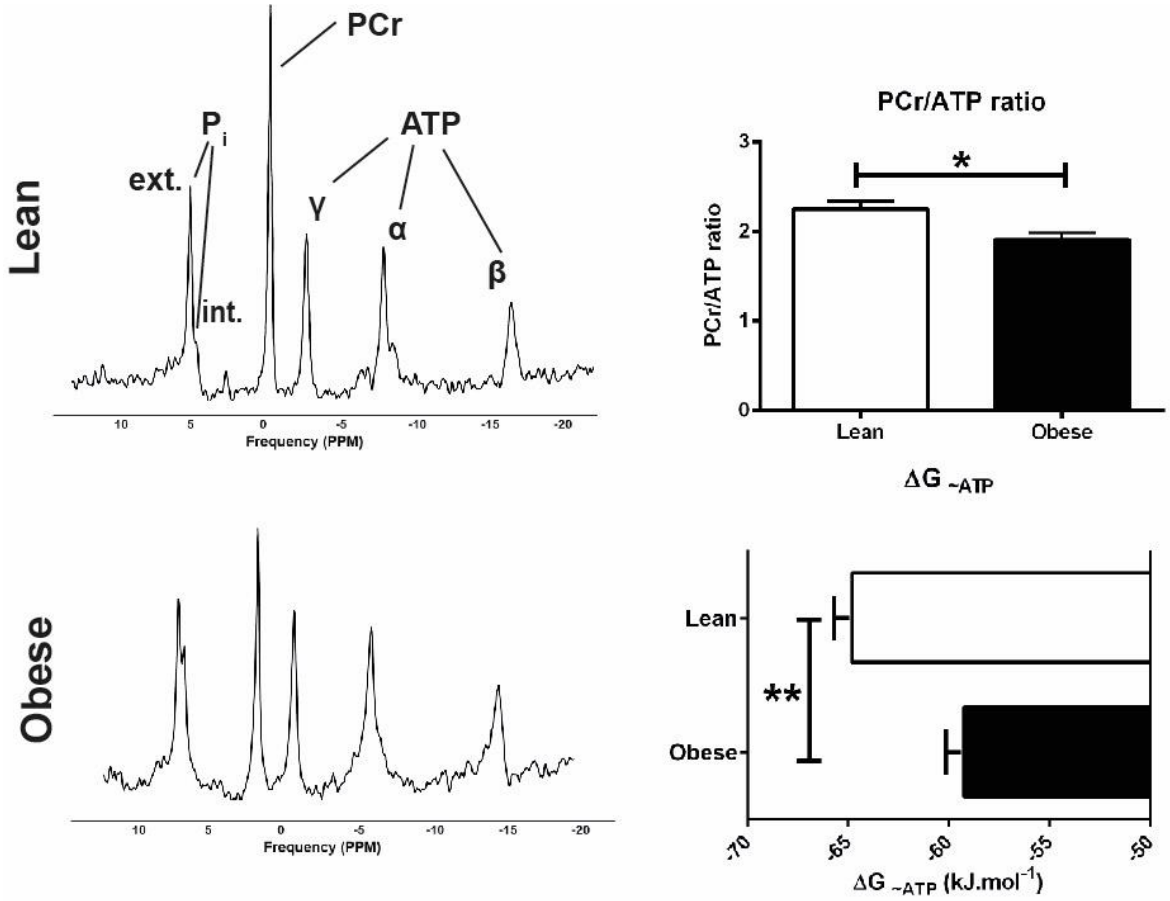


Figure 3.8: Obesity causes cardiac energetic deficit. Both $\Delta G_{\sim ATP}$ and the PCr/ATP ratio were significantly reduced. n = 10 evaluable datasets (lean group) and n = 12 (obese group); mean ± SEM; statistical comparisons are by unpaired, two-tailed T-tests.

deficit in this model, which may be due to mitochondrial dysfunction and provides a possible mechanistic link between the observed reduction in PDH flux and impairment of cardiac diastolic function.

3.4.5 Selection of pharmacological intervention to increase PDH flux

The manipulation of cardiac substrate metabolism has long been considered a potential therapeutic target in heart failure with reduced ejection fraction, but clinical studies have generally been small scale, and have been hampered by an inability to measure cardiac metabolism before and after the intervention, raising questions about the dosing and efficacy of the drugs involved. Pharmacological strategies that would be expected to reverse the suppression of PDH flux in this model can be grouped into three main classes:

3.4.5.1 Inhibitors of pyruvate dehydrogenase kinases

Dichloroacetate is a pyruvate mimetic which inhibits PDK activity and is the drug most commonly used to increase PDH activity in experimental settings. Although the mechanism by which DCA inhibits PDK activity varies between PDK isoforms, DCA binds to the pyruvate domain of PDK4 with ADP, and inhibits activity by locking the active site in a closed conformational state[44]. *In vivo*, DCA causes rapid inhibition of PDK activity, with measurable activity within 30 minutes of oral or parenteral administration[45]. In addition to its rapid effects on PDH via PDK inhibition, DCA may also have a further mechanism of action by reducing PDC turnover[46], though the mechanisms responsible for this effect remain to be elucidated. DCA has established antihyperglycaemic effects in diabetes[47, 48], increases PDH flux and improves diastolic function in rodent models of diabetes[49]. Although DCA has whole body effects, thus altering the circulating substrate profile, isolated perfused heart studies also show that DCA improves cardiac function[50], whilst an acute infusion of DCA improved cardiac oxygen efficiency and mechanical function in humans with heart failure[51]. These observations support the presence of a direct, myocardial mechanism of action.

The potential for clinical translation of dichloroacetate for obesity cardiomyopathy is limited by a narrow therapeutic window and toxicity, and some trials of this drug in mitochondrial diseases have been terminated early due to significant peripheral neuropathy[52]. These data suggest that dichloroacetate is therefore unlikely to be clinically translatable for obesity cardiomyopathy.

Sodium phenylbutyrate is a novel PDK inhibitor, and improved PDH activity in a model of congenital lactic acidosis[53]. Sodium phenylbutyrate is already approved for human use in some jurisdictions, but is also unlikely to be appropriate for cardiac applications as it is

primarily active against PDK1-3 with lower activity against PDK4[54], although the effect of phenylbutyrate on cardiac PDH activity has not been specifically tested.

3.4.5.2 Fatty acid oxidation inhibitors

Inhibitors of fatty acid oxidation indirectly increase cardiac carbohydrate metabolism and PDH activity, and are used as anti-anginal agents in some countries. Inhibition of fatty acid oxidation leads to a decrease in beta oxidation, thus decreasing acetyl CoA/CoA ratios and activating PDH, which leads to an improvement in cardiac oxygen efficiency. Perhexiline and etomoxir inhibit fatty acid oxidation by binding to carnitine palmitoyltransferase (CPT) -1 and -2 (competitively and non- competitively respectively), whilst trimetazidine is a weaker inhibitor of CPT-1 and inhibits fatty acid oxidation primarily by reducing the activity of specific enzymes of beta oxidation[55]. The effects of inhibiting fatty acid oxidation upon cardiac metabolism and function have most commonly been studied using trimetazidine, which causes substantial reductions in fatty acid oxidation with reciprocal increases in glucose oxidation[55]. Consistent with its effects upon metabolic substrate metabolism, trimetazidine improves cardiac energetics during experimental low flow ischaemia[56] and in human heart failure[57]. The use of trimetazidine to improve cardiac substrate and energetic metabolism in obesity cardiomyopathy has been limited by concern that inhibition of fatty acid oxidation in the presence of excess fatty acid levels might cause accumulation of toxic intermediates of lipid metabolism, including ceramides and diacylgylercols. However, recent studies of trimetazidine did not support these concerns and demonstrated instead that this drug prevented the development of both cardiac hypertrophy and diastolic dysfunction in a murine model of obesity cardiomyopathy[58]. Trimetazidine is difficult to obtain in the United Kingdom as it is listed on Schedule 1 of the Misuse of Drugs Regulations 2001, as the piperazine ring within the chemical structure of the molecule can be used as a substrate for the synthesis of the hallucinogen

benzylpiperazine (BZP). These limitations rendered trimetazidine unsuitable for use in this study.

3.4.5.3 Glucagon like peptide 1 (GLP-1) analogues

The incretin mimetics are a class of antihyperglycaemic drugs licensed for use in type II diabetes, which stimulate the glucagon like receptor 1 receptor (GLP-1R). The antihyperglycaemic effect of stimulation of the GLP-1R in diabetes is mediated by an increase in glucose dependent insulin section, by activation of G-protein coupled receptors in islet beta cells[59]. However, GLP-1Rs are expressed widely in peripheral tissues, including the heart, and the cardiovascular effects of incretin analogues are of increasing interest. In isolated rat hearts, recombinant GLP-1 increases glucose uptake and enhances recovery following ischaemia[60], whilst, in a canine model of heart failure, recombinant GLP-1 increases cardiac glucose uptake, insulin sensitivity and contractility[61]. In addition to administering GLP-1 analogues, the bioavailability of endogenous GLP-1 can also be enhanced by inhibiting dipeptidylpeptidase-4 (DPP-4), which catalyses GLP-1 breakdown. The DPP-4 inhibitor Linagliptin improved diastolic function in a rodent obesity model[62], whilst a different DPP-4 inhibitor, MK0626, also improved diastolic function in obese mice[63] though the effects upon cardiac metabolism *in vivo* are unclear.

In addition to their effects on myocardial substrate metabolism, GLP-1 analogues activate protective cell signalling pathways, ameliorating inflammation, nuclear factor of kappa B (NF-κB) translocation and other markers of apoptosis, fibrosis and hypertrophy[64]. One further benefit of GLP-1 analogues is to promote satiety, thus reducing energy intake and leading to weight loss[65]. These data suggested that GLP-1 analogues would be an effective pharmacological means of increasing PDH flux in this model obesity cardiomyopathy, and

a clinically available GLP-1 analogue, Liraglutide, was therefore selected for use in this study.

3.4.6 Liraglutide and calorie restriction restored myocardial carbohydrate metabolism, normalising energetics and diastolic function

Because prolonged GLP-1 treatment causes weight loss by reducing oral intake[66], a one-week treatment duration (0.2 mg/kg twice daily, analogous to human dosing in type II diabetes) was selected for use in this study, with the intention of studying the weight-neutral cardiac effects of the drug.

Treatment with Liraglutide did not lead to either significant weight loss over the one-week treatment period (mean weight post-treatment 453 ± 10 versus 467 ± 10 g pre-treatment, P=ns) or significant differences in plasma metabolite concentrations compared to obese controls (Table 3.1).

	Lean	Obese	Liraglutide	CR	P value
Glucose (mmol/L)	11.8 (0.3)	13.2 (1.6)	12.2 (2.7)	12.6 (0.4)	0.31
Insulin (μg/L)	1.06 (0.2)	1.23 (0.2)	1.22 (0.2)	0.89 (0.1)	0.48
Lactate (mmol/L)	4.0 (0.2)	3.78 (0.5)	4.62 (0.8)	3.35 (0.3)	0.32
LDL (mmol/L)	0.24 (0.02)	0.30 (0.02)	0.23 (0.01)	0.23 (0.01)	0.05
HDL (mmol/L)	0.63 (0.03)	0.56 (0.03)*	0.54 (0.03)**	0.69 (0.03)	0.002
Cholesterol (mmol/L)	2.01 (0.06)	2.01 (0.09)	2.11 (0.1)	2.08 (0.09)	0.89
Triglyceride (mmol/L)	1.07 (0.3)	1.58 (0.2)	1.51 (0.3)	1.51 (0.2)	0.43

Table 3.1: Plasma metabolite analysis. Obesity was associated with lower HDL but no other significant differences between the groups were noted. n = 10 datasets per group; mean (± SEM) with statistical comparison by ANOVA and multiple comparison correction by Tukey's method.

When compared to the pre-treatment obese group, myocardial PDH flux was significantly increased after Liraglutide treatment (0.023 ± 0.01 versus 0.013 ± 0.01 s^{-1}, P<0.05, Figure 3.9). Liraglutide treatment also reduced the normalised rates of ^{13}C label incorporation into citrate and glutamate to levels seen in the control group (0.7 ± 0.2 versus 1.9 ± 0.2 AU, P < 0.05 and 0.8 ± 0.2 versus 1.5 ± 0.1 AU, P < 0.001).

This was paralleled by a significant improvement in energetic reserve ($\Delta G_{\sim ATP}$ -64.8 ± 0.7 versus -59.2 ± 0.9 kJ.mol^{-1}, P < 0.01 and PCr/ATP ratio 2.45 ± 0.08 versus 1.91 ± 0.07, P < 0.01) and diastolic functional improvement (E/E' 18 ± 2 versus 26 ± 2, P = 0.01). These improvements occurred without change in LV wall thickness (septum 2.1 ± 0.1 versus 2.1 ± 0.1 mm, P = ns and posterior wall 2.3 ± 0.2 versus 2.3 mm ± 0.1, P = ns), cavity size (LVIDD 6.4 ± 0.3 versus 6.6 ± 0.1 mm, P = ns) or systolic function (fractional shortening 53 ± 2 versus 53 ± 2%, P = ns).

As expected, when compared to age matched obese rats the body weights of obese rats having undergone caloric restriction for four weeks were significantly lower (505 ± 9 versus 600 ± 10 g, P < 0.001). In addition, the epididymal fat pad weight, a marker of central obesity, was also significantly lower in the caloric restriction group (7.2 ± 0.4 versus 10.6 ± 1 g, P < 0.01). Myocardial PDH flux was increased in calorie restricted animals compared to pre-treatment (0.024 ± 0.002 versus 0.013 ± 0.002 s^{-1}, P < 0.01), whilst abnormal TCA cycle metabolism was also corrected (normalised rate of label incorporation into citrate 0.50 ± 0.06 versus 1.94 ± 0.3 AU, P < 0.01 and glutamate 0.92 ± 0.1 versus 1.54 ± 0.1 AU, P < 0.01). As with the Liraglutide treated group, this metabolic change was associated with improvements in both energetic reserve ($\Delta G_{\sim ATP}$ -62.8 ± 0.8 versus -59.2 ± 0.9 kJ.mol^{-1}, P<0.01 and PCr/ATP ratio 2.17 ± 0.05 versus 1.91 ± 0.07, P < 0.05) and diastolic function to levels seen in lean controls (E/E' ratio 15 ± 1 versus 26 ± 2, P < 0.05). Again, these effects occurred without change in LV wall thickness (septum 2.0 ± 0.1 versus 2.1 ± 0.1 mm and posterior wall 2.0 ± 0.1 versus 2.3 ± 0.3 mm, P = ns), cavity size (LVIDD 6.1 ± 0.3 versus 6.6 ± 0.1 mm, P = ns) or systolic function (fractional shortening 54 ± 3 versus 53 ± 2%, P = ns).

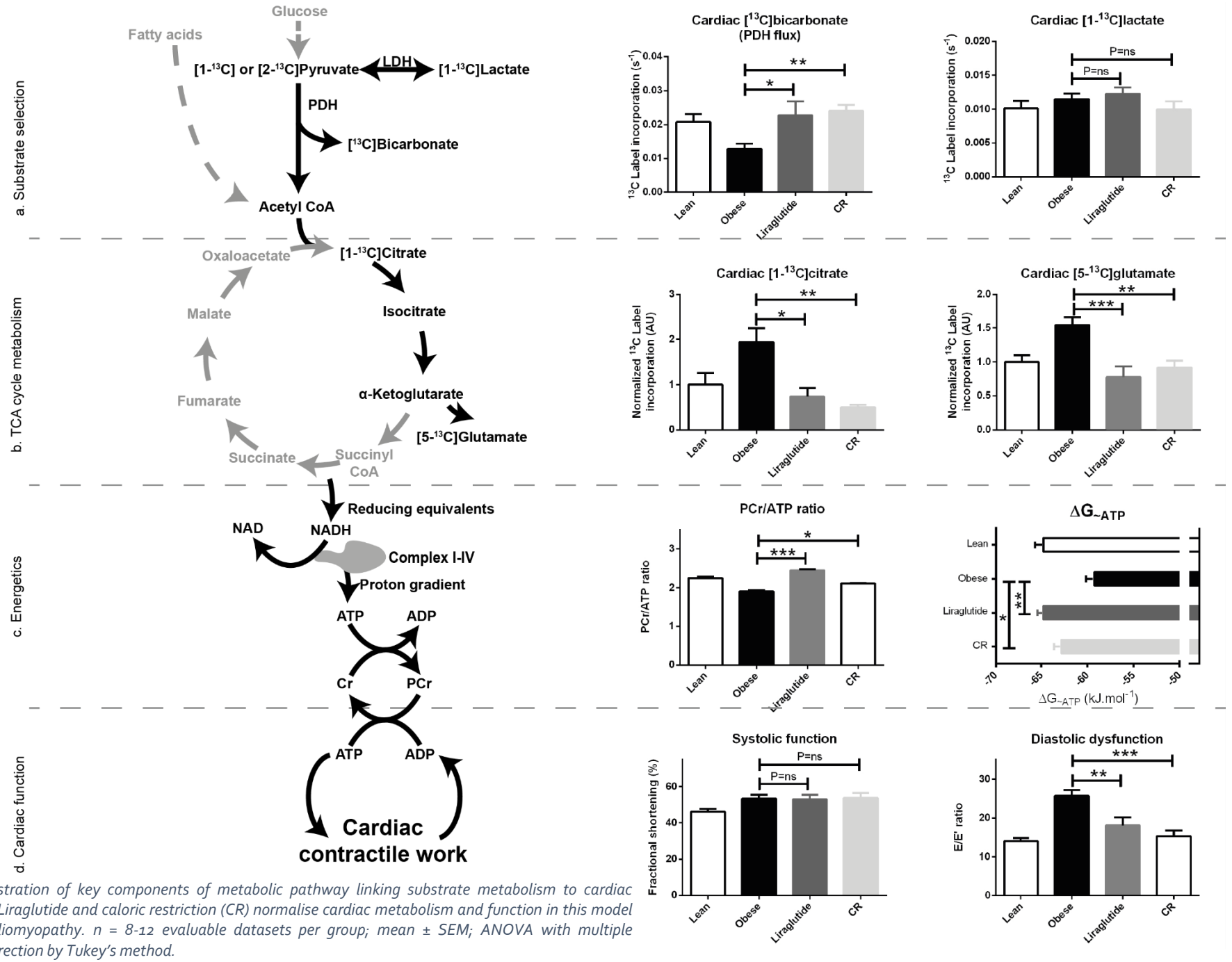


Figure 3.9: Illustration of key components of metabolic pathway linking substrate metabolism to cardiac function. Both Liraglutide and caloric restriction (CR) normalise cardiac metabolism and function in this model of obesity cardiomyopathy. n = 8-12 evaluable datasets per group; mean ± SEM; ANOVA with multiple comparison correction by Tukey's method.

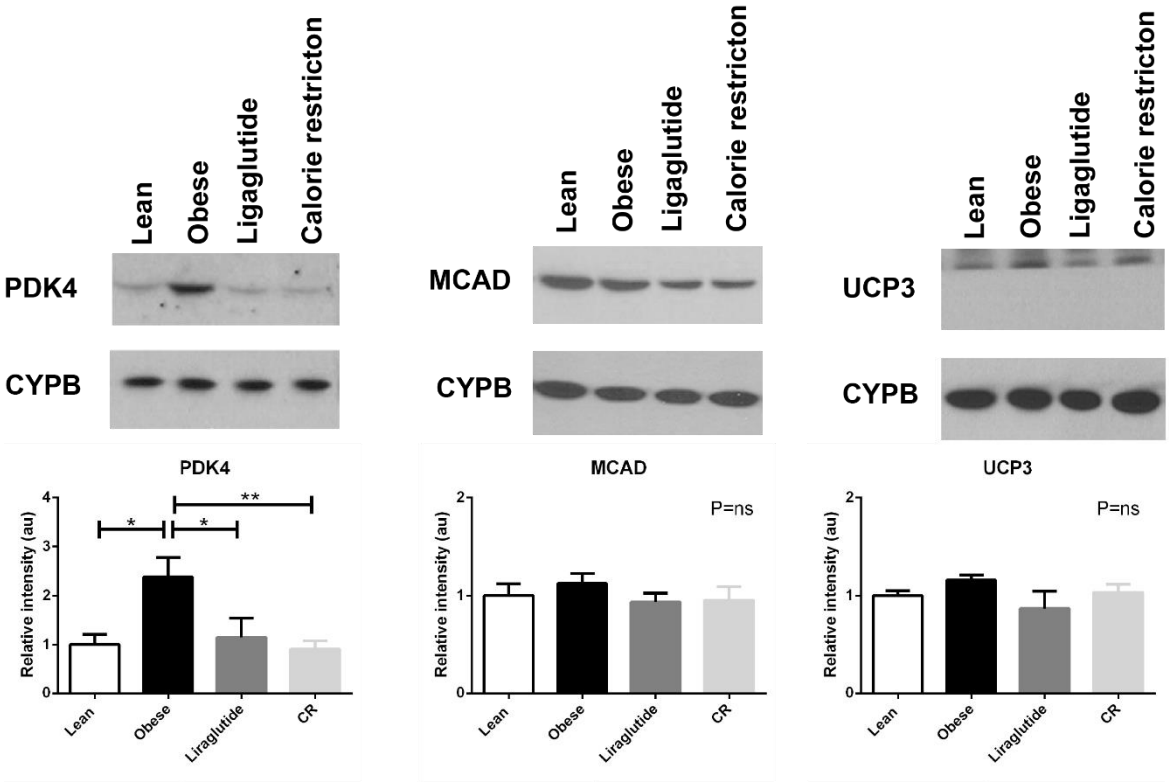


Figure 3.10: Western blot analysis of cardiac tissue. Obesity increased pyruvate dehydrogenase kinase 4 (PDK4) expression, with no change in medium-chain acyl-coenzyme A dehydrogenase (MCAD) or uncoupling-protein 3 (UCP3). Even protein loading was confirmed by expression of cyclophilin B (CYPB). n = 6 biological replicates, mean ± SEM; ANOVA with multiple comparison correction by Tukey's method when the ANOVA P-value was < 0.05 .

In order to help understand the mechanisms by which Liraglutide and caloric restriction restored PDH flux, Western blotting of key metabolic regulatory proteins was performed upon cardiac tissue (Figure 3.10). As expected, the PPAR target PDK4, the major regulatory of cardiac PDH activity, was increased in obesity and expression was normalised following either treatment. Surprisingly, there was no significant difference in UCP3 (uncoupling-protein 3) expression after statistical correction for multiple comparisons, whilst obesity did not increase expression of medium-chain acyl-coenzyme A dehydrogenase (MCAD) in this model. Cyclophilin B localises to the lumen of the endoplasmic reticulum and was chosen as a protein loading control as it is expressed in the heart without reported differential expression in cardiac metabolic disease states.

3.5 Discussion

The obesity and HFPEF epidemics mandate the identification of new treatment options for the symptomatic and prognostic implications of obesity related heart disease. Obesity in this model was associated with impaired myocardial carbohydrate metabolism, abnormal TCA cycle metabolism, impaired cardiac energetic reserve and diastolic but not systolic dysfunction. These changes were reversed following treatment with either the GLP-1 analogue Liraglutide or caloric restriction.

3.5.1 Cardiac metabolism as a therapeutic target in obesity cardiomyopathy

Abnormal metabolism has long been considered a candidate pathophysiologic mechanism in obesity cardiomyopathy, but the therapeutic potential of manipulating substrate selection has been unclear. One strength of this work was the use of hyperpolarized magnetic resonance spectroscopy to measure cardiac carbohydrate metabolism *in vivo* in conditions of physiological substrate availability. The finding of a dramatic reduction in PDH flux provides corroboration of findings from Golfman *et al*[67] and others that rates of glucose oxidation are reduced in perfused hearts from obese rats, in accordance with the Randle cycle[68]. Using hyperpolarized [2-^{13}C]pyruvate MRS experiments to probe TCA cycle metabolism *in vivo*, it was next demonstrated that obesity increased normalised rates of label incorporation into citrate and glutamate, suggesting an increase in their respective pool sizes. These findings most likely reflect increased citrate synthase and glutamate dehydrogenase flux, although the possibility of an increased pool size due to reduced activity of a downstream enzyme cannot be excluded from these data. However, increased citrate synthase activity was identified by Boudina *et al* in isolated mitochondria from hearts of obese *ob/ob* mice[69]. High citrate levels increase malonyl-CoA levels, which in turn reduce carnitine palmitoyltransferase-1 (CPT1) activity[70], limiting fatty acid uptake and oxidation which can predispose to toxic lipid intermediate accumulation. Although high PDH

activity has been linked to increased citrate levels[71], our contrasting findings suggest that alternative mechanisms of regulation of citrate synthase activity may be dominant in this model. In particular, high ADP/ATP ratios, as were observed in these ^{31}P spectroscopy studies, and high NAD^+/NADH ratios increase citrate synthase activity[72], as a homeostatic mechanism to increase TCA cycle flux and maintain a sufficiently elevated chemical driving force for ATPase reactions in states of energetic deficit which may therefore account for these findings.

Our finding that interventions leading to normalisation of PDH flux were associated with normalisation of diastolic function is consistent with the hypothesis that reduced carbohydrate metabolism contributes to cardiac functional impairment in obesity. A mechanistic link through energetics cannot, however, currently be proven experimentally on account of a lack of molecular tools to manipulate and measure the ratios of key adenine nucleotides with the necessary degree of subcellular compartmental specificity. Alternative,

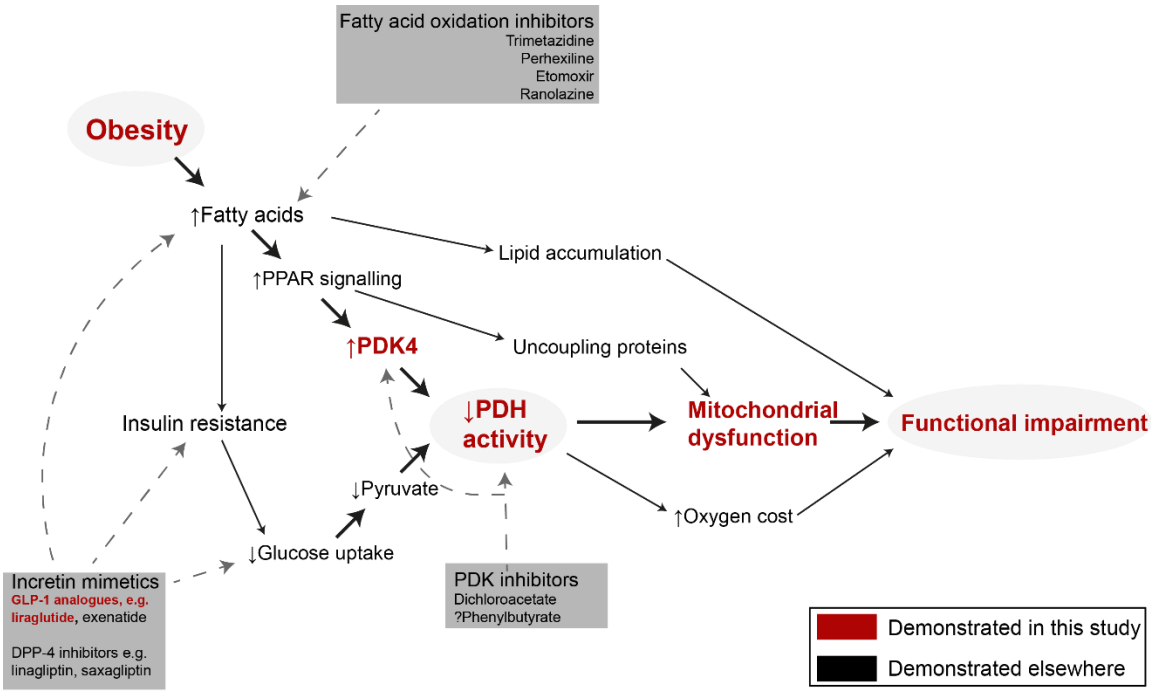


Figure 3.11: Summary of possible mechanistic links between impaired PDH flux and cardiac functional impairment in obesity cardiomyopathy along with targets of the major classes of metabolic modulator therapy. Points highlighted in red reflect mechanisms demonstrate d in the experiments presented in this chapter; remaining mechanisms are demonstrated elsewhere.

passive mechanisms of diastolic dysfunction in obesity include left ventricular hypertrophy and cardiac lipotoxicity and may be contributory to the clinical phenotype (summarised with potential clinical pharmacological therapeutic approaches in Figure 3.11), although significant triglyceride accumulation did not occur in this model, whilst LV wall thickness did not change following either treatment.

Some questions regarding the systems interplay of cardiac PDH flux, energetics and function in obesity remain to be answered. Although the free energy change of ATP hydrolysis was significantly impaired in obese rats compared to lean and treated animals in our study (to -59 $kJ.mol^{-1}$), this value still remains more negative than the estimated minimum for sarcoplasmic Ca^{2+} ATPase function (~-53 $kJ.mol^{-1}$ [73]) and thus would not be predicted to limit diastolic function at rest. Furthermore, despite the profound metabolic consequences of dominant fat metabolism, the healthy heart is energetically resilient and it is therefore unlikely that an acute shift in substrate metabolism from carbohydrates to fat (as occurs in healthy hearts whilst fasting) is sufficient in isolation to cause energetic deficit of a degree sufficient to impair cardiac function[74]. One possibility that may reconcile these observations is that the presence of additional, subclinical myocardial pathology in obesity might increase the energetic cost of contraction and relaxation. Furthermore, as a shift towards predominant carbohydrate metabolism (reversion to the so-called "fetal phenotype") is an early, and likely adaptive, metabolic shift in hypertrophied and failing hearts[75, 76], the presence of insulin resistance and inhibition of the machinery of carbohydrate metabolism may abrogate this shift, exacerbating energetic deficit. This view would also be consistent with clinical evidence suggesting that obesity does not cause heart failure abruptly, but rather increases the likelihood of its development over years[77].

The development of a better understanding of the temporal changes in cardiac energy metabolism and impaired function in metabolic diseases would be an important goal in future clinical hyperpolarized MR studies.

3.5.2 Clinical translational approaches

The findings of this study have translational potential as both calorie restriction and GLP-1 analogues are immediately available for human use, though neither have been tested specifically for obesity cardiomyopathy in randomized trials. However, Liraglutide, at a dose lower than that used in this study, caused modest weight loss in patients with obesity but without diabetes[78], and improved cardiovascular outcomes in patients with established type II diabetes[79]. These findings support the cardiovascular safety profile of GLP-1 analogues, and are remarkable as many antihyperglycaemic therapies for type II diabetes either promote weight gain or increase the risk of heart failure[80, 81].

Licensing authorities would be likely to require a phase III trial of GLP-1 analogue therapy powered to detect changes in cardiovascular outcomes in obesity as a precursor to regulatory approval for this indication, though it would be clearly desirable to establish signals of efficacy and optimise the dosing strategies in smaller phase II trials first. Both clinical hyperpolarized ^{13}C MR and ^{31}P spectroscopy[82, 83] could, in conjunction with detailed measures of systolic and diastolic function, provide surrogate end-point biomarkers that would enable careful dose titration and improve the accuracy of power calculations to maximise the likelihood of success at phase III.

As an initial step to test the feasibility of using metabolic MR in phase II pharmaceutical studies in obesity, diabetes and other metabolic disease states, regulatory approval has been granted and funding secured for a pilot clinical study in OCMR to use hyperpolarized [1-^{13}C]pyruvate MRS and ^{31}P MRS to assess the cardiac metabolic and functional response to

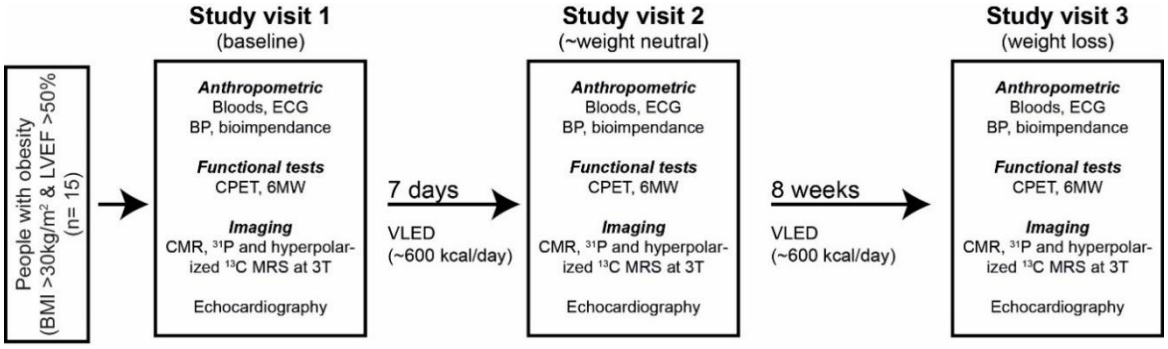


Figure 3.12: Overview of proposed clinical study investigating the cardiovascular effects of caloric restriction using VLEDs in obesity. Visit 2 (7 days) tests the effects of reversal of insulin resistance; visit 3 tests the effects of weight loss.

a very low energy diet (VLED, approximately 600 kcal per day as commercially available milkshakes) in obesity. The study design includes a baseline assessment, which is repeated one week after the start of the VLED (to test the effects of marked insulin sensitisation without substantial weight loss; an effect which is well documented with this intervention[84]) and again after two months (to test the effects of weight loss, design summarised in Figure 3.12). This study will begin when a sufficient number of sterile fluid paths become available, which is currently anticipated to be in autumn 2016.

3.5.3 Limitations and future work

The applicability of results from experiments performed in rodent models to complex human diseases such as obesity remains unclear. There is substantial variability in the cardiac phenotype between different models of obesity, and none fully recapitulate important variability in human obesity driven by fat depots heterogeneity and waist:hip circumference ratios. One key strength of hyperpolarized MR is the potential for rapid translation of the technique to the human disease states, which should help to confirm or refute the validity of the findings in this rodent model.

3.6 Conclusions

Obesity cardiomyopathy is an under-recognised clinical problem which lacks specific therapeutic options. Work presented in this chapter identifies major changes in cardiac energy metabolism and diastolic function in a model of obesity cardiomyopathy, which were reversed following treatment with either a clinically available GLP-1 analogue or caloric restriction leading to weight loss. These findings help to establish a role for multinuclear ^{13}C and ^{31}P MRS in providing a more comprehensive assessment of cardiac energy metabolism than is possible with conventional imaging technologies and supports a role for altered energy metabolism in the development of obesity cardiomyopathy. Ongoing work by the group will investigate the translational potential of this work, by piloting hyperpolarized cardiovascular MR in humans with obesity which may set the scene for hyperpolarized MR to become a surrogate endpoint in future clinical trials of drugs active in cardiovascular metabolism.

3.7 Appendix 3A: Methods

3.7.1 Model

All procedures were carried out in accordance with the UK Animals (Scientific Procedures) Act 1986. Obesity was induced in Long Evans rats by high fat feeding for at least 12 weeks (Teklad Custom Research Diet TD.06414, 60% KCal from fat, 19 % KCal from protein, 21 % KCal from carbohydrate *ad libitum)* by Harlan Laboratories, Indianapolis, US. Control animals were maintained on Teklad Global Diet 2014S (13 % KCal from fat, 20% KCal from protein, 67 % KCal from carbohydrate *ad libitum*).

3.7.2 Echocardiography

To characterise the cardiac phenotype of the model, we elected to use echocardiography rather than cine MRI, as the higher temporal resolution of ultrasound enables a more comprehensive assessment of diastolic function. A clinical GE Vivid I scanner was available in the department, and a compatible 10S-RS phased array paediatric probe with frequency range of 4.5 – 11.5 MHz was purchased for use in these studies. In pilot work, the ability to assess diastolic function reproducibly was confirmed and standardised and the clinically established E/E' ratio was selected for use as the primary index of diastolic function, as it is a relatively pre-load independent measure and is less susceptible to potentially confounding pseudonormalisation of the E/A ratio due to increased left atrial pressure in advanced diastolic dysfunction. Wall thickness and left ventricular (LV) dimensions were derived from M-mode images using a short-axis view at the level of the papillary muscles. Pulsed-wave Doppler recordings of LV inflow were obtained from the subcostal 4-chamber view to measure maximal early diastolic peak velocity (E) and late peak velocity (A). Tissue Doppler Imaging was recorded from the medial mitral valve annulus to record early (E') and active (A') left ventricular diastolic myocardial velocities.

3.7.3 Hyperpolarized [1-^{13}C] and [2-^{13}C]pyruvate magnetic resonance spectroscopy

Rats were anaesthetised (2.5 % isoflurane with 2 L.min^{-1} oxygen) and positioned in a custom-built MR cradle with ^{1}H/^{13}C butterfly coil (loop diameter, 2 cm) over the thorax. The cradle was positioned in a 7 T horizontal bore MR scanner linked to a Direct Drive console (Varian Medical Systems, Yarnton, UK). Correct positioning was confirmed by the acquisition of an axial proton FLASH image (TE/TR, 1.17/2.33 ms; matrix size, 64 x 64; FOV, 60 x 60 mm; slice thickness, 2.5 mm; excitation flip angle, 15°). An ECG-gated shim was used to reduce the proton line width to <120 Hz. Hyperpolarized [1-^{13}C]pyruvate (Sigma-Aldrich, Gillingham, UK) was prepared by ~30 minutes of hyperpolarization at ~1K, before being rapidly dissolved in a heated and pressurised alkaline solution. Hyperpolarized [2-^{13}C]pyruvate was prepared in an identical fashion, with hyperpolarization for 45 minutes. This procedure produced a solution of ~80 mM hyperpolarized sodium [1-^{13}C] or [2-^{13}C]pyruvate at physiological temperature and pH, with a polarization of ~30%. One millilitre of this solution was injected over ten seconds via a tail vein cannula (dose of ~0.16 mmol/kg). Individual ECG-gated ^{13}C MR slice selective cardiac spectra (n = 120) were acquired over 120s after injection (TR, 1 s; excitation flip angle, 5°; slice thickness 10 mm, sweep width, 13,593 Hz; acquired points, 2,048; frequency centred relative to the C1/C2 pyruvate resonance as appropriate).

3.7.4 Cardiac perfusion

Hearts were removed following anesthesia with sodium pentobarbital via intraperitoneal injection. Hearts were then rapidly placed in ice-cold Krebs-Henseleit-Buffer to induce arrest and immediately mounted on the perfusion system. The aorta was cannulated and hearts were perfused in a recirculating retrograde Langendorff mode at a pressure of 85 mmHg pressure. The perfusion buffer was modified Krebs-Henseleit-Buffer in nanopure water containing 118 mM NaCl, 4.7 mM KCl, 1.2 mM $MgSO_4$, 1.35 mM $CaCl_2$, 0.5 mM

Na_2EDTA, 11 mM glucose, 25 mM $NaHCO_3$ and 1.2 mM KH_2PO_4, oxygenated with a mix of 95% O_2/5%CO_2 and maintained at 37°C. The left ventricle was ventilated via a polyethylene tube inserted through the apex. A small water-filled balloon was inserted into the LV cavity via the mitral valve, and connected to a pressure transducer in turn linked to a recording device (PowerLab 45P, AD instruments, New Zealand). End diastolic pressure was set between 2-8 mmHg. At the end of all experiments the hearts were frozen using aluminium tongs cooled to the temperature of liquid nitrogen and stored at -80°C for subsequent analysis.

3.7.5 ^{31}P spectroscopy

Perfused hearts were positioned in an 11.7T MR system (Bruker, Germany) and spectra were acquired at 202.5 MHz using a 90° RF pulse. PCr resonance was set at 0 ppm, the chemical shifts of Pi, Υ-ATP, α-ATP, β-ATP were referenced to this resonance. An unsaturated, fully relaxed spectrum was acquired using a 90° pulse (repetition time, 15 seconds, averages, 40, acquisition time, 10 minutes).

3.7.6 Western blotting

Total frozen hearts were crushed and a sample (20-30 mg) lysed in standard lysis buffer using a rotor-stator homogeniser. Protein concentration was determined using a commercially available spectrophotometric assay (Thermo Fisher Scientific Inc) according to the manufacturer's instructions.

Polyacrylamide gel electrophoresis (PAGE) was performed upon 18μL of protein sample using GE Amersham ECL precast gels, and transferred to nitrocellulose membranes with Western blotting. Protein expression of PDK4 (AB38242, Abcam plc, 1:10000), ACADM (AB92461, Abcam plc, 1:10000), UCP3 (AB3477, Abcam plc, 1/1000), and the loading control cyclophilin B (AB16045, Abcam plc, 1:1000) was assessed. All samples were run

in duplicate on separate 15-well gels containing a gradient of 4 to 12% acrylamide (Amersham ECL gel, GE Healthcare) and were normalized with loading control protein.

3.7.7 High performance liquid chromatography

The myocardial total creatine pool size was assessed using HPLC. 5-10mg crushed heart tissue was homogenised in perchloric acid and neutralised with sodium hydroxide. The homogenate was centrifuged and filtered, before being loaded onto an HPLC system with a Supelcosil™ LC-18-T column. Results were quantified with reference to standards using Azure software (Kromatek, UK) and normalised to non-collagenous protein content using the assay of Lowry.

3.8 Appendix 3B: References

1. Kenchaiah S, Evans J C, Levy D, Wilson P W, Benjamin E J, Larson M G, Kannel W B, and Vasan R S *Obesity and the risk of heart failure.* New England Journal of Medicine 2002;347(5):305-313

2. Alpert M A *Obesity Cardiomyopathy:: Pathophysiology and Evolution of the Clinical Syndrome.* The American Journal of the Medical Sciences 2001;321(4):225-236

3. Wong C and Marwick T H *Obesity cardiomyopathy: pathogenesis and pathophysiology.* Nature Clinical Practice Cardiovascular Medicine 2007;4(8):436-443

4. Owan T E, Hodge D O, Herges R M, Jacobsen S J, Roger V L, and Redfield M M *Trends in prevalence and outcome of heart failure with preserved ejection fraction.* New England Journal of Medicine 2006;355(3):251-259

5. Rayner J, Neubauer S, and Rider O *The paradox of obesity cardiomyopathy and the potential for weight loss as a therapy.* Obesity Reviews 2015;16(8):679

6. Abel E D, Litwin S E, and Sweeney G *Cardiac remodeling in obesity.* Physiological Reviews 2008;88(2):389-419

7. Peterson L R, Herrero P, Schechtman K B, Racette S B, Waggoner A D, Kisrieva-Ware Z, Dence C, Klein S, Marsala J, and Meyer T *Effect of obesity and insulin resistance on myocardial substrate metabolism and efficiency in young women.* Circulation 2004;109(18):2191-2196

8. Luiken J J, Arumugam Y, Dyck D J, Bell R C, Pelsers M M, Turcotte L P, Tandon N N, Glatz J F, and Bonen A *Increased rates of fatty acid uptake and plasmalemmal fatty acid transporters in obese Zucker rats.* Journal of Biological Chemistry 2001;276(44):40567-40573

9. Wu P, Sato J, Zhao Y, Jaskiewicz J, Popov K, and Harris R *Starvation and diabetes increase the amount of pyruvate dehydrogenase kinase isoenzyme 4 in rat heart.* Biochemical Journal 1998;329:197-201

10. Barger P M and Kelly D P *PPAR signaling in the control of cardiac energy metabolism.* Trends in Cardiovascular Medicine 2000;10(6):238-245

11. Varga T, Czimmerer Z, and Nagy L *PPARs are a unique set of fatty acid regulated transcription factors controlling both lipid metabolism and inflammation.* Biochimica et Biophysica Acta (BBA)-Molecular Basis of Disease 2011;1812(8):1007-1022

12. Jensen M D, Haymond M W, Rizza R A, Cryer P E, and Miles J *Influence of body fat distribution on free fatty acid metabolism in obesity.* Journal of Clinical Investigation 1989;83(4):1168

13. Vyska K, Machulla H, Stremmel W, Fassbender D, Knapp W, Notohamiprodjo G, Gleichmann U, Meyer H, Knust E, and Körfer R *Regional myocardial free fatty acid extraction in normal and ischemic myocardium.* Circulation 1988;78(5):1218-1233

14. Zhou Y-T, Grayburn P, Karim A, Shimabukuro M, Higa M, Baetens D, Orci L, and Unger R H *Lipotoxic heart disease in obese rats: implications for human obesity.* Proceedings of the National Academy of Sciences 2000;97(4):1784-1789

15. Keller H R, Dreyer C, Medin J, Mahfoudi A, Ozato K, and Wahli W *Fatty acids and retinoids control lipid metabolism through activation of peroxisome proliferator-activated receptor-retinoid X receptor heterodimers.* Proceedings of the National Academy of Sciences 1993;90(6):2160-2164

16. Wende A R, Huss J M, Schaeffer P J, Giguère V, and Kelly D P *PGC-1α coactivates PDK4 gene expression via the orphan nuclear receptor ERRα: a mechanism for transcriptional control of muscle glucose metabolism.* Molecular and Cellular Biology 2005;25(24):10684-10694

17. Kirchner H, Nylen C, Laber S, Barrès R, Yan J, Krook A, Zierath J R, and Näslund E *Altered promoter methylation of PDK4, IL1 B, IL6, and TNF after Roux-en Y gastric bypass.* Surgery for Obesity and Related Diseases 2014;10(4):671-678

18. Young M E, Guthrie P H, Razeghi P, Leighton B, Abbasi S, Patil S, Youker K A, and Taegtmeyer H *Impaired long-chain fatty acid oxidation and contractile dysfunction in the obese Zucker rat heart.* Diabetes 2002;51(8):2587-2595

19. Buchanan J, Mazumder P K, Hu P, Chakrabarti G, Roberts M W, Yun U J, Cooksey R C, Litwin S E, and Abel E D *Reduced cardiac efficiency and altered substrate metabolism precedes the onset of hyperglycemia and contractile dysfunction in two mouse models of insulin resistance and obesity.* Endocrinology 2005;146(12):5341-5349

20. Kolter T, Uphues I, and Eckel J *Molecular analysis of insulin resistance in isolated ventricular cardiomyocytes of obese Zucker rats.* American Journal of Physiology-Endocrinology And Metabolism 1997;273(1):E59-E67

21. Chatham J C and Seymour A-M L *Cardiac carbohydrate metabolism in Zucker diabetic fatty rats.* Cardiovascular Research 2002;55(1):104-112

22. Labbé S M, Grenier-Larouche T, Noll C, Phoenix S, Guérin B, Turcotte E E, and Carpentier A C *Increased myocardial uptake of dietary fatty acids linked to cardiac dysfunction in glucose-intolerant humans.* Diabetes 2012;61(11):2701-2710

23. Rosa G, Rocco P, Manco M, Greco A V, Castagneto M, Vidal H, and Mingrone G *Reduced PDK4 expression associates with increased insulin sensitivity in postobese patients.* Obesity Research 2003;11(2):176-182

24. Viljanen A P, Karmi A, Borra R, Pärkkä J P, Lepomäki V, Parkkola R, Lautamäki R, Järvisalo M, Taittonen M, and Rönnemaa T *Effect of caloric restriction on myocardial fatty acid uptake, left ventricular mass, and cardiac work in obese adults.* The American Journal of Cardiology 2009;103(12):1721-1726

25. Sidhu S, Gangasani A, Korotchkina L G, Suzuki G, Fallavollita J A, Canty J M, and Patel M S *Tissue-specific pyruvate dehydrogenase complex deficiency causes cardiac*

hypertrophy and sudden death of weaned male mice. American Journal of Physiology-Heart and Circulatory Physiology 2008;295(3):H946-H952

26. Finck B N, Lehman J J, Leone T C, Welch M J, Bennett M J, Kovacs A, Han X, Gross R W, Kozak R, and Lopaschuk G D *The cardiac phenotype induced by PPARα overexpression mimics that caused by diabetes mellitus.* The Journal of Clinical Investigation 2002;109(109 (1)):121-130

27. Ritov V B, Menshikova E V, He J, Ferrell R E, Goodpaster B H, and Kelley D E *Deficiency of subsarcolemmal mitochondria in obesity and type 2 diabetes.* Diabetes 2005;54(1):8-14

28. Neubauer S, Krahe T, Schindler R, Horn M, Hillenbrand H, Entzeroth C, Mader H, Kromer E, Riegger G, and Lackner K *^{31}P magnetic resonance spectroscopy in dilated cardiomyopathy and coronary artery disease. Altered cardiac high-energy phosphate metabolism in heart failure.* Circulation 1992;86(6):1810-1818

29. Rider O, Francis J, Tyler D, Byrne J, Clarke K, and Neubauer S *Effects of weight loss on myocardial energetics and diastolic function in obesity.* The International Journal of Cardiovascular Imaging 2013;29(5):1043-1050

30. Rider O J, Francis J M, Ali M K, Holloway C, Pegg T, Robson M D, Tyler D, Byrne J, Clarke K, and Neubauer S *Effects of catecholamine stress on diastolic function and myocardial energetics in obesity.* Circulation 2012;125(12):1511-1519

31. Phan T T and Frenneaux M *The pathophysiology of diastolic heart failure.* F1000 Biology Reports 2010;2(16)

32. Ingwall J S and Weiss R *G Is the failing heart energy starved? On using chemical energy to support cardiac function.* Circulation Research 2004;95(2):135-145

33. Tian R, Nascimben L, Ingwall J S, and Lorell B H *Failure to maintain a low ADP concentration impairs diastolic function in hypertrophied rat hearts.* Circulation 1997;96(4):1313-1319

34. Bers D M *Sarcoplasmic reticulum Ca uptake, content and release,* in *Excitation-contraction coupling and cardiac contractile force* 2001, Springer. p. 161-202.

35. Kammermeier H, *High energy phosphate of the myocardium: concentration versus free energy change,* in *Cardiac Energetics* 1987, Springer. p. 31-36.

36. Boudina S, Sena S, Theobald H, Sheng X, Wright J J, Hu X X, Aziz S, Johnson J I, Bugger H, and Zaha V G *Mitochondrial energetics in the heart in obesity-related diabetes: direct evidence for increased uncoupled respiration and activation of uncoupling proteins.* Diabetes 2007;56(10):2457-2466

37. Murray A J, Anderson R E, Watson G C, Radda G K, and Clarke K *Uncoupling proteins in human heart.* The Lancet 2004;364(9447):1786-1788

38. Boudina S, Han Y H, Pei S, Tidwell T J, Henrie B, Tuinei J, Olsen C, Sena S, and Abel E D *UCP3 regulates cardiac efficiency and mitochondrial coupling in high fat–fed mice but not in leptin-deficient mice.* Diabetes 2012;61(12):3260-3269

39. Essop M F, Razeghi P, McLeod C, Young M E, Taegtmeyer H, and Sack M N *Hypoxia-induced decrease of UCP3 gene expression in rat heart parallels metabolic gene switching but fails to affect mitochondrial respiratory coupling.* Biochemical and Biophysical Research Communications 2004;314(2):561-564

40. Muoio D M *Metabolic inflexibility: when mitochondrial indecision leads to metabolic gridlock.* Cell 2014;159(6):1253-1262

41. Veech R L *The therapeutic implications of ketone bodies: the effects of ketone bodies in pathological conditions: ketosis, ketogenic diet, redox states, insulin resistance, and mitochondrial metabolism.* Prostaglandins, Leukotrienes and Essential Fatty Acids 2004;70(3):309-319

42. Sverdlov A L, Elezaby A, Behring J B, Bachschmid M M, Luptak I, Tu V H, Siwik D A, Miller E J, Liesa M, and Shirihai O S *High fat, high sucrose diet causes cardiac mitochondrial dysfunction due in part to oxidative post-translational modification of mitochondrial complex II.* Journal of Molecular and Cellular Cardiology 2015;78:165-173

43. Atherton H J, Dodd M S, Heather L C, Schroeder M A, Griffin J L, Radda G K, Clarke K, and Tyler D J *Role of pyruvate dehydrogenase inhibition in the development of hypertrophy in the hyperthyroid rat heart a combined magnetic resonance imaging and hyperpolarized magnetic resonance spectroscopy study.* Circulation 2011;123(22):2552-2561

44. Wynn R M, Kato M, Chuang J L, Tso S-C, Li J, and Chuang D T *Pyruvate dehydrogenase kinase-4 structures reveal a metastable open conformation fostering robust core-free basal activity.* Journal of Biological Chemistry 2008;283(37):25305-25315

45. Curry S H, Chu P I, Baumgartner T G, and Stacpoole P W *Plasma concentrations and metabolic effects of intravenous sodium dichloroacetate.* Clinical Pharmacology & Therapeutics 1985;37(1):89-93

46. Evans O B and Stacpoole P W *Prolonged hypolactatemia and increased total pyruvate dehydrogenase activity by dichloroacetate.* Biochemical Pharmacology 1982;31(7):1295-1300

47. Eichner H L, Stacpoole P W, and Forsham P H *Treatment of streptozotocin diabetes with di-isopropylammonium dichloroacetate (DIPA).* Diabetes 1974;23(3):179-182

48. Stacpoole P W, Moore G W, and Kornhauser D M *Metabolic effects of dichloroacetate in patients with diabetes mellitus and hyperlipoproteinemia.* New England Journal of Medicine 1978;298(10):526-530

49. Le Page L M, Rider O J, Lewis A J, Ball V, Clarke K, Johansson E, Carr C A, Heather L C, and Tyler D J *Increasing Pyruvate Dehydrogenase Flux as a Treatment for Diabetic*

Cardiomyopathy: A Combined ^{13}C Hyperpolarized Magnetic Resonance and Echocardiography Study. Diabetes 2015:db141560

50. Nicholl T A, Lopaschuk G D, and McNeill J H *Effects of free fatty acids and dichloroacetate on isolated working diabetic rat heart.* American Journal of Physiology-Heart and Circulatory Physiology 1991;261(4):1053-1059

51. Bersin R M, Wolfe C, Kwasman M, Lau D, Klinski C, Tanaka K, Khorrami P, Henderson G N, de Marco T, and Chatterjee K *Improved hemodynamic function and mechanical efficiency in congestive heart failure with sodium dichloroacetate.* Journal of the American College of Cardiology 1994;23(7):1617-1624

52. Kaufmann P, Engelstad K, Wei Y, Jhung S, Sano M, Shungu D, Millar W, Hong X, Gooch C, and Mao X *Dichloroacetate causes toxic neuropathy in MELAS: a randomized, controlled clinical trial.* Neurology 2006;66(3):324-330

53. Ferriero R, Manco G, Lamantea E, Nusco E, Ferrante M I, Sordino P, Stacpoole P W, Lee B, Zeviani M, and Brunetti-Pierri N *Phenylbutyrate therapy for pyruvate dehydrogenase complex deficiency and lactic acidosis.* Science Translational Medicine 2013;5(175):175ra31

54. Ferriero R, Iannuzzi C, Manco G, and Brunetti-Pierri N *Differential inhibition of PDKs by phenylbutyrate and enhancement of pyruvate dehydrogenase complex activity by combination with dichloroacetate.* Journal of Inherited Metabolic Disease 2015:1-10

55. Kantor P F, Lucien A, Kozak R, and Lopaschuk G D *The antianginal drug trimetazidine shifts cardiac energy metabolism from fatty acid oxidation to glucose oxidation by inhibiting mitochondrial long-chain 3-ketoacyl coenzyme A thiolase.* Circulation Research 2000;86(5):580-588

56. Allibardi S, Chierchia S L, Margonato V, Merati G, Neri G, Dell'Antonio G, and Samaja M *Effects of trimetazidine on metabolic and functional recovery of postischemic rat hearts.* Cardiovascular Drugs and Therapy 1998;12(6):543-549

57. Fragasso G, Perseghin G, De Cobelli F, Esposito A, Palloshi A, Lattuada G, Scifo P, Calori G, Del Maschio A, and Margonato A *Effects of metabolic modulation by trimetazidine on left ventricular function and phosphocreatine/adenosine triphosphate ratio in patients with heart failure.* European Heart Journal 2006;27(8):942-948

58. Ussher J R, Fillmore N, Keung W, Mori J, Beker D L, Wagg C S, Jaswal J S, and Lopaschuk G D *Trimetazidine Therapy Prevents Obesity-Induced Cardiomyopathy in Mice.* Canadian Journal of Cardiology 2014;30(8):940-944

59. Drucker D J *The biology of incretin hormones.* Cell Metabolism 2006;3(3):153-165

60. Zhao T, Parikh P, Bhashyam S, Bolukoglu H, Poornima I, Shen Y-T, and Shannon R P *Direct effects of glucagon-like peptide-1 on myocardial contractility and glucose uptake in normal and postischemic isolated rat hearts.* Journal of Pharmacology and Experimental Therapeutics 2006;317(3):1106-1113

61. Nikolaidis L A, Elahi D, Hentosz T, Doverspike A, Huerbin R, Zourelias L, Stolarski C, Shen Y-t, and Shannon R P *Recombinant glucagon-like peptide-1 increases myocardial glucose uptake and improves left ventricular performance in conscious dogs with pacing-induced dilated cardiomyopathy.* Circulation 2004;110(8):955-961

62. Aroor A R, Sowers J R, Bender S B, Nistala R, Garro M, Mugerfeld I, Hayden M R, Johnson M S, Salam M, and Whaley-Connell A *Dipeptidylpeptidase inhibition is associated with improvement in blood pressure and diastolic function in insulin-resistant male Zucker obese rats.* Endocrinology 2013;154(7):2501-2513

63. Bostick B, Habibi J, Ma L, Aroor A, Rehmer N, Hayden M R, and Sowers J R *Dipeptidyl peptidase inhibition prevents diastolic dysfunction and reduces myocardial fibrosis in a mouse model of Western diet induced obesity.* Metabolism 2014;63(8):1000-1011

64. Noyan-Ashraf M H, Shikatani E A, Schuiki I, Mukovozov I, Wu J, Li R-K, Volchuk A, Robinson L A, Billia F, and Drucker D J *A glucagon-like peptide-1 analog reverses the molecular pathology and cardiac dysfunction of a mouse model of obesity.* Circulation 2013;127(1):74-85

65. Flint A, Raben A, Astrup A, and Holst J J *Glucagon-like peptide 1 promotes satiety and suppresses energy intake in humans.* Journal of Clinical Investigation 1998;101(3):515

66. Raun K, von Voss P, Gotfredsen C F, Golozoubova V, Rolin B, and Knudsen L B *Liraglutide, a long-acting glucagon-like peptide-1 analog, reduces body weight and food intake in obese candy-fed rats, whereas a dipeptidyl peptidase-IV inhibitor, vildagliptin, does not.* Diabetes 2007;56(1):8-15

67. Golfman L S, Wilson C R, Sharma S, Burgmaier M, Young M E, Guthrie P H, Van Arsdall M, Adrogue J V, Brown K K, and Taegtmeyer H *Activation of PPARγ enhances myocardial glucose oxidation and improves contractile function in isolated working hearts of ZDF rats.* American Journal of Physiology-Endocrinology and Metabolism 2005;289(2):E328-E336

68. Randle P, Garland P, Hales C, and Newsholme E *The glucose fatty-acid cycle its role in insulin sensitivity and the metabolic disturbances of diabetes mellitus.* Lancet 1963;281(7285):785-789

69. Boudina S, Sena S, O'Neill B T, Tathireddy P, Young M E, and Abel E D *Reduced mitochondrial oxidative capacity and increased mitochondrial uncoupling impair myocardial energetics in obesity.* Circulation 2005;112(17):2686-2695

70. Saha A, Vavvas D, Kurowski T, Apazidis A, Witters L, Shafrir E, and Ruderman N *Malonyl-CoA regulation in skeletal muscle: its link to cell citrate and the glucose-fatty acid cycle.* American Journal of Physiology-Endocrinology And Metabolism 1997;272(4):E641-E648

71. Jeoung N H and Harris R A *Role of pyruvate dehydrogenase kinase 4 in regulation of blood glucose levels.* Korean Diabetes Journal 2010;34(5):274-283

72. Shepherd D and Garland P *The kinetic properties of citrate synthase from rat liver mitochondria.* Biochemical Journal 1969;114(3):597-610

73. Ingwall J S, *Energetic basis for heart failure,* in *Heart Failure: A Companion to Braunwald's Heart Disease,* D.Mann, Editor 2002, Kluwer Academic Publishers: London.

74. Mjøs O D *Effect of free fatty acids on myocardial function and oxygen consumption in intact dogs.* Journal of Clinical Investigation 1971;50(7):1386

75. Chokshi A, Drosatos K, Cheema F H, Ji R, Khawaja T, Yu S, Kato T, Khan R, Takayama H, and Knöll R *Ventricular assist device implantation corrects myocardial lipotoxicity, reverses insulin resistance, and normalizes cardiac metabolism in patients with advanced heart failure.* Circulation 2012;125(23):2844-2853

76. Barger P M and Kelly D P *Fatty acid utilization in the hypertrophied and failing heart: molecular regulatory mechanisms.* The American Journal of the Medical Sciences 1999;318(1):36

77. Scaglione R, Dichiara M, Indovina A, Lipari R, Ganguzza A, Parrinello G, Capuana G, Merlino G, and Licata G *Left ventricular diastolic and systolic function in normotensive obese subjects: influence of degree and duration of obesity.* European Heart Journal 1992;13(6):738-742

78. Pi-Sunyer X, Astrup A, Fujioka K, Greenway F, Halpern A, Krempf M, Lau D C, le Roux C W, Violante Ortiz R, and Jensen C B *A randomized, controlled trial of 3.0 mg of liraglutide in weight management.* New England Journal of Medicine 2015;373(1):11-22

79. Marso S P, Daniels G H, Brown-Frandsen K, Kristensen P, Mann J F, Nauck M A, Nissen S E, Pocock S, Poulter N R, and Ravn L S *Liraglutide and cardiovascular outcomes in type 2 diabetes.* New England Journal of Medicine 2016;

80. Scirica B M, Bhatt D L, Braunwald E, Steg P G, Davidson J, Hirshberg B, Ohman P, Frederich R, Wiviott S D, and Hoffman E B *Saxagliptin and cardiovascular outcomes in patients with type 2 diabetes mellitus.* New England Journal of Medicine 2013;369(14):1317-1326

81. Graham D J, Ouellet-Hellstrom R, MaCurdy T E, Ali F, Sholley C, Worrall C, and Kelman J A *Risk of acute myocardial infarction, stroke, heart failure, and death in elderly Medicare patients treated with rosiglitazone or pioglitazone.* Journal of the American Medical Association 2010;304(4):411-418

82. Rodgers C T, Clarke W T, Snyder C, Vaughan J T, Neubauer S, and Robson M D *Human cardiac 31P magnetic resonance spectroscopy at 7 Tesla.* Magn Reson Med 2013;

83. Rodgers C T, Clarke W T, Snyder C, Vaughan J T, Neubauer S, and Robson M D *Human cardiac ^{31}P magnetic resonance spectroscopy at 7 Tesla.* Magnetic Resonance in Medicine 2014;72(2):304-315

84. Maggio C A and Pi-Sunyer F X *Obesity and type 2 diabetes.* Endocrinology and metabolism clinics of North America 2003;32(4):805-822

Chapter 4: Hyperpolarized MRI of cardiac inflammation and repair

4.1 Abstract

Myocardial infarction (MI) remains a major cause of premature death despite highly optimised systems for the delivery of primary reperfusion, highlighting a need for novel therapeutic approaches that can be administered in the days following the event. Inflammation in the healing myocardium is one potential post-MI therapeutic target, though clinical exploration of this process has been hampered as conventional imaging techniques cannot reliably assess inflammation. In this chapter, we have shown that metabolic reprogramming in activated macrophages results in an expansion of the intracellular lactate pool in these cells, providing a method for detection of cardiac inflammation using hyperpolarized [1-^{13}C]pyruvate imaging in rodent models. Separate MR spectroscopic experiments using cell suspensions demonstrated that macrophage activation upregulates a panel of glycolytic genes, and that this high glycolytic rate is essential for the production of key proinflammatory cytokines. Finally, specific targeting of the hyperpolarized lactate signal using glycolytic inhibitors *in vivo* attenuated both the lactate signal and also improved cytokine levels within healing myocardium. Hyperpolarized MRI therefore provides a novel method for the detection of myocardial inflammation, with high translational potential.

4.2 Background

4.2.1 Myocardial infarction

MI is the most common cause of cardiac injury, and results in the loss of large numbers of cardiomyocytes[1]. Arrhythmia has historically been the most common cause of death from myocardial infarction in the acute phase[2], whilst patients who survive the initial event, representing the majority of such patients, have an increased risk of developing ventricular remodelling and heart failure[3, 4].

Contemporary therapeutic strategies for acute MI with ST segment elevation include rapid reperfusion with primary percutaneous coronary intervention (PPCI) to restore myocardial perfusion[5] and subsequent neurohormonal blockade to improve long-term ventricular remodelling[6, 7]. These treatments have been effective in reducing the mortality rate following MI[8, 9], though the burden of disease remains unacceptably high. Furthermore, as systems for the delivery of rapid reperfusion are now highly developed, opportunities to improve outcomes by delivering PPCI more rapidly appear to be limited. The identification of therapeutic approaches that could be administered in the days that follow myocardial infarction therefore now represents a major goal of the field[10-12].

4.2.2 Inflammation following myocardial infarction

Inflammation in the myocardium in the days following an MI is a biological process which has historically been less extensively investigated as a potential therapeutic target than either reperfusion or neurohormonal blockade. Despite an increasing body of preclinical work, no immunomodulatory therapies are currently licensed to improve wound healing or clinical outcomes for patients who have experienced an MI.

The presence of a significant cellular inflammatory response in the healing myocardium was documented in post-mortem histological studies in the 1960s[13], prompting investigation of the potential utility of corticosteroids to improve wound healing. Despite apparently reducing infarct size in animal models[14], early clinical experiments demonstrated that this non-selective immunosuppressive approach was associated with impaired scar formation[15] and an increased risk of catastrophic ventricular rupture[16]. Not all clinical trials of corticosteroids following MI have demonstrated the same results[17], though their use in this setting remains considered to be relatively contraindicated. These observations suggest that the development of novel therapeutic strategies targeting cardiac inflammation will only be successful if they are selective, are based on an improved understanding of the molecular mechanisms involved and are, ideally, individualised, given the high degree of clinical variability in this disease process.

Renewed interest in cardiac inflammation as a therapeutic target following MI has prompted a series of investigations which have contributed to important improvements in the understanding of the cellular mechanisms involved in cardiac injury and repair. In the days and weeks following MI, the healing myocardium is highly biologically active, with rapid cellular turnover and a complex cascade of processes which lead to mature scar formation[18]. Neutrophils are the first inflammatory cells to accumulate in the infarcted myocardium, and do so in the hours following the event in chemokine driven recruitment via C-X-C motif ligand 1 (CXCL1), CXCL8, P-selectin and L-selectin[19]. Marginated neutrophils, which have a primary evolutionary role in infection control, are potently cytotoxic and release proteolytic enzymes and reactive oxidant species[20]. Because myocardial infarction leads to sterile inflammation, neutrophil driven toxicity may be at least partially maladaptive and may contribute to an increase in infarct size.

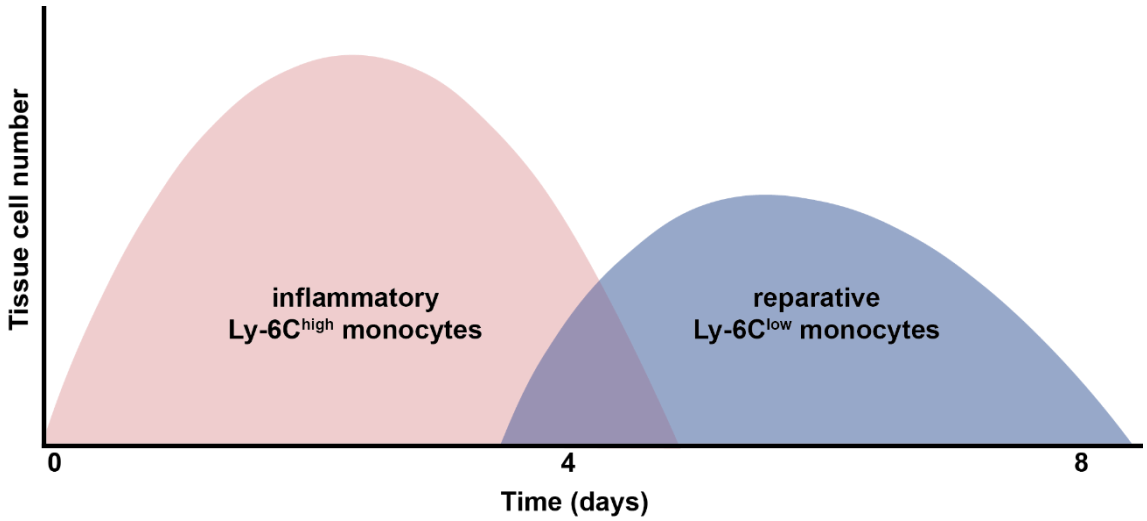


Figure 4.1: Biphasic monocyte/macrophage resposnse to myocardial infarction; redrawn from Nahrendorf et al[11].

In hours 24 - 72 following MI, the milieu of innate immune cells within the healing myocardium becomes dominated by monocytes, which are the precursors of macrophages and dendritic cells[21]. Monocytes and macrophages have a complex role in wound healing, with functions as mediators of both tissue destruction and also of tissue repair. These seemingly contradictory findings were reconciled by the discovery that the monocyte response to MI in mice is biphasic, with an initial pro-inflammatory response, characterised by monocytes highly expressing the cell surface marker Ly-6C and peaking in number at day 3[18]. This is then followed by a second phase in which monocytes with a reparative function and low expression of Ly-6C predominate (Figure 4.1):

The spleen was subsequently shown to be a major source of both Ly-6C^{high} and Ly-6C^{low} monocytes[22]. Reparative cells including Ly-6C^{low} monocytes/macrophages have roles in the deposition of extracellular matrix and the formation of mature scar and help to explain the increased risk of ventricular rupture following non-selective immunosuppression or pan-macrophage depletion[23].

More nuanced approaches to the manipulation of key macrophage activation and polarization pathways have since been shown to be a promising strategy to improve cardiac

repair following MI[24, 25]. Providing proof-of-concept, selective targeting of inflammatory monocytes via C-C chemokine receptor type 2 (CCR2) reduced infarct size and improved wound healing following MI[26]. Recently, recombinant vascular endothelial growth factor C (VEGF-C) was shown to enhance the development of lymphatic vessels following myocardial infarction, improving systolic function[27] in a mechanism that may involve enhanced clearance of inflammatory macrophages.

4.2.3 Imaging cardiac inflammation

One important limitation of our ability to translate this improved understanding of inflammation biology to therapies that could improve the function of human hearts following MI is a shortage of clinical biomarkers of cardiac inflammation. Whilst it is likely that any degree of inflammation is maladaptive in transient ischaemia/reperfusion injury with minimal cardiomyocyte death, inflammation may be essential for mature scar formation in patients with more extensive myocardial injury. New imaging techniques are therefore needed to better understand inflammation in a clinical context following MI, to aid in the identification of patient subgroups who would be most likely to respond favourably to immunomodulatory therapies, and as surrogate biomarkers of clinical response in phase II pharmacological trials.

4.2.3.1 Current strategies for imaging cardiac inflammation are limited

Although a mild peripheral blood leucocytosis is common following myocardial infarction[28], this lacks either sensitivity or specificity for cardiac injury. Recently, T_2 weighted oedema imaging using ^{1}H CMR was shown to demonstrate a bimodal pattern following myocardial infarction[29], with high signal immediately following reperfusion, which fell to a nadir at 24 hours before increasing to a second peak at day 4 - 7. However, ^{1}H T_1 and T_2 measures are inevitably confounded by the water content of oedema, collagen,

and paramagnetic effects from iron within areas of myocardial haemorrhage. As a result, T_2 signal was not changed by the administration of corticosteroids in a subsequent study by the same group[30], despite markedly reducing the inflammatory cell count.

Positron emission tomography using ^{18}FDG demonstrates regionally increased tracer uptake in MI in the days following the event[31], but the use of this tracer for inflammation imaging is limited by high background signal from surrounding myocardium. This necessitates the artificial suppression of cardiac carbohydrate metabolism prior to imaging, which has an unknown effect upon non-cardiomyocyte cell metabolism. The long acquisition times and high ionising radiation dose of ^{18}FDG PET also limits the use of this technique for longitudinal studies in the same patient.

4.2.3.2 Potential role for hyperpolarized magnetic resonance in the assessment of cardiac inflammation

The cellular processes of differentiation, inflammatory cytokine production, phagocytosis, and collagen deposition pose a significant cellular energetic challenge to monocytes/macrophages within the hypoxic microenvironment of an MI. In general, the primary metabolic pathway by which ATP synthesis is sustained in hypoxia is anaerobic glycolysis[32]. In immune cells, metabolic reprogramming results in an increase in glycolytic rates following activation from their quiescent state[33]. This increase in anaerobic glycolysis would be expected to expand the intracellular lactate pool size in immune cells post MI, providing a potential opportunity to non-invasively assess inflammation using hyperpolarized ^{13}C magnetic resonance imaging of regional [1-^{13}C]lactate label incorporation in the heart[34, 35]. Unlike current CMR techniques, hyperpolarized [1-^{13}C]lactate signal should not be significantly confounded by the presence of oedema or collagen. These characteristics represent potential advantages over existing techniques.

4.3 Hypotheses

Accordingly, it was hypothesised that metabolic reprogramming of activated inflammatory cells within injured myocardial tissue would be detectable using hyperpolarized [1-^{13}C]pyruvate magnetic resonance. Specifically, that:

- high hyperpolarized lactate signal would be detected in healing myocardial segments at time-points corresponding to the peaks of the 'inflammatory' and 'reparative' monocyte/macrophage responses.
- activation of macrophages *in vitro* would increase the cellular glycolytic rate, thus expanding the intracellular lactate pool and increasing [1-^{13}C]lactate label flux rates in hyperpolarized MR experiments.
- blockade of glycolysis in activated macrophages would abrogate any increase in [1-^{13}C]lactate label flux rates and alter the inflammatory phenotype of the cell.

The identification of a non-invasive biomarker of cardiac inflammation would help to develop our understanding of human cardiac inflammation biology and would set the scene for future studies involving potential clinical therapies that modulate cardiac inflammation.

4.4 Methods development and results

4.4.1 Development of a model of myocardial infarction

The most commonly used experimental models of MI are created by surgical coronary artery ligation, with or without subsequent reperfusion. In pilot work to establish feasibility and test the sensitivity of the [1-^{13}C]pyruvate imaging sequence to inflammation, MI was induced by coronary artery ligation for 40 minutes (with subsequent reperfusion) in a rodent model. Hyperpolarized magnetic resonance using [1-^{13}C]pyruvate was performed at day 3, corresponding to the predicted peak of the 'inflammatory'-type monocyte-macrophage response. Details of the experimental methods are provided in Appendix 4A (page 199). The resulting [1-^{13}C]lactate images demonstrated strikingly higher lactate signal in the region corresponding to the infarct than in the remote myocardium (Figure 4.2).

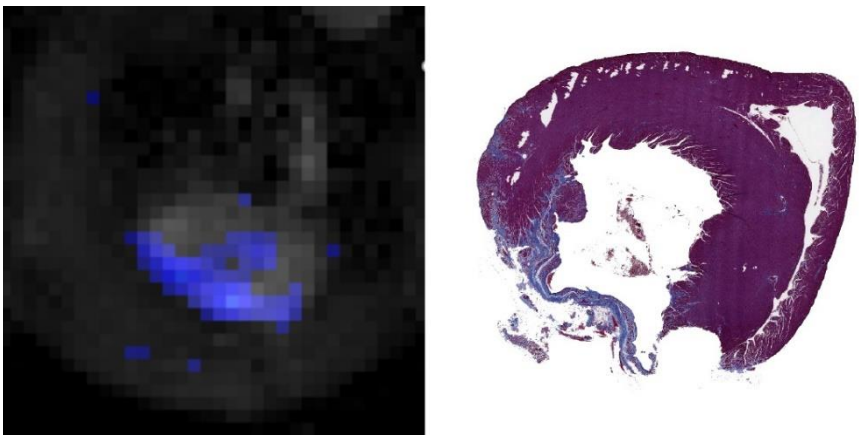


Figure 4.2: Hyperpolarized [1-^{13}C]lactate imaging demonstrates high lactate signal at day 3 (n = 1) corresponding to the histologically defined infarct (Masson trichrome stained).

Despite helping to prove the concept of the experiment, these coronary artery ligation experiments also highlighted the very high degree of variability in infarct size and location that is associated with this model. Out of three biological replicates, a large myocardial infarction was demonstrated histologically in only one. This feature of the model posed a particular problem in the context of an MR experiment in which some inhomogeneity of the coverage of the ^{13}C surface coil was present. Although the variability in infarct size and

location with ligation models is well recognised and is sometimes controlled for retrospectively[36], the need for enzymatic digestion of hearts to liberate cell suspensions for the measurement of inflammatory cells precluded the use of histological assessment of infarct size. Indicative power calculations suggested the need for an unfeasibly high number of experiments (>20 per group) using coronary artery ligation, demonstrating the need for a different model with a more consistent infarct size and location.

Cryoinjury is an alternative model of MI in which a cryoprobe, usually manufactured from aluminium and cooled to the temperature of liquid nitrogen, is applied to the surface of the heart to cause injury. Although arguably less physiological than coronary artery ligation, this model is extensively used in zebrafish[37, 38] and, importantly, induces an injury of a consistent size, in a consistent location. The pathological features of cryoinjury are similar to those seen following coronary artery ligation and include cardiomyocyte apoptosis and necrosis, with a degree of scar transmurality that is dependent upon the duration of application of the cryoprobe. In pilot work, this method was more reproducible, quicker and was associated with lower intraoperative mortality rates than coronary artery ligation[39]. Histological analysis demonstrated similar mature scar formation, with a lower degree of transmurality of injury than was seen with coronary artery ligation (Figure 4.3).

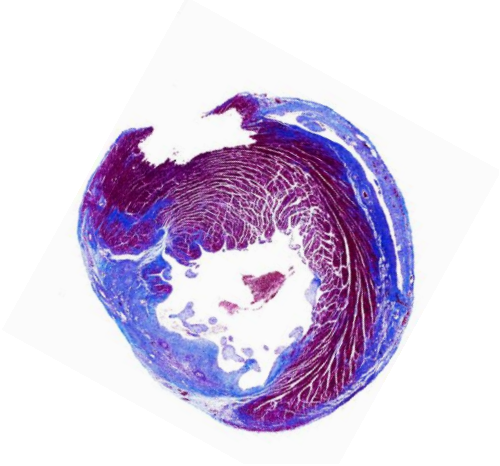


Figure 4.3: Cryoinjury produces mature scar formation with a similar appearance to that of coronary artery ligation, though with a lower degree of transmurality.

4.4.2 Development of flow cytometric approach

In addition to a robust model of myocardial injury, it was next necessary to develop a method for the quantitation of immune cell number within the healing myocardium. Flow cytometry is the method of choice for identifying and sorting cells within complex populations and was therefore used in these experiments.

Flow cytometry uses lasers to interrogate cells as they pass through the cytometric apparatus in stream of single cells[40]. The apparatus initially records the scattering pattern of the laser light caused by the cell, which provides information about the size and granularity of the cells. More detailed cellular identification and phenotyping is possible by staining the cells with flourochrome conjugated antibodies, which are interrogated by lasers with specific emission frequencies to provide information about cell surface marker expression.

A method for disruption and collagenase digestion of cardiac tissue to liberate single cell suspensions was adapted and optimised from a previously described method for mouse heart cell isolation[41], using an increased volume of collagenase II solution to compensate for the higher tissue mass. This method yielded reasonably consistent numbers of viable cells in pilot work (~100,000 cells per mg tissue, estimated from trypan blue excursion). An optional additional digestion step using dispase was proposed in the original method, but did not substantially increase cell yield in this model and was therefore subsequently omitted.

4.4.2.1 Initial experiments: four colour flow cytometry panel

As murine models and human samples are commonly used in immunological studies, well established antibody panels for immunophenotyping are available and require minimal optimisation[42]. However, fewer studies have used flow cytometry for rat

immunophenotyping, which necessitated the development of an appropriate antibody panel for these experiments.

The expense and technical difficulty of flow cytometric experiments increases with the number of antibodies used in the panel. The aim when designing a multi-colour antibody panel is therefore to use the minimum necessary number of flourochromes to reliably identify and phenotype the cells of interest. The major challenge in experiments using a higher number of antibodies and flourochromes is to minimise the overlap in flourochrome emission spectra, particularly between cell surface markers where a high degree of separation is desirable.

The use of the surface marker cluster of differentiation 45 (CD45) as a marker to select all leucocytes in a cell population is well established, though specific rodent macrophage and neutrophil markers are less clearly defined[43]. The marker CD68 is used as a pan-macrophage marker in fixed rodent tissue specimens[44], though it is expressed predominantly intracellularly, necessitating undesirable cell permeabilisation and fixation processes prior to flow cytometry. CD11b/c is an alternative macrophage cell surface marker[45], but may be expressed on other cell types in addition to monocytes/macrophages. Furthermore, phenotypic differentiation of macrophages with predominantly 'inflammatory' or 'reparative' phenotypes is also challenging. The murine marker Ly6C is not expressed on rat macrophages, though CD43 has been identified as a marker which may be differentially expressed by rat macrophage subsets[46].

In initial experiments, a four colour panel using antibodies against CD45 (to select leucocytes), CD11b/c (to select monocyte-macrophages) and CD43 (to phenotype monocyte-macrophages) as well as a cell viability dye (Zombie Violet™, BioLegend®) was selected (Table 4.1). These flourochromes were selected to be either separately excited by

each of the 3 lasers on a Dako Cyan™ flow cytometer (emitting at 405 nm, 488 nm, and 635 nm), or alternatively to have well separated fluorescence emission spectra, thus minimising the need for compensation.

Antibody target	Flourochrome	Excitation laser (nm)	Maximum fluorescence emission (nm)	Supplier
Live/Dead	Zombie Violet	405	450	BioLegend®
CD45	Alexa Fluor 488	488	517	BioLegend®
CD43	Phycoerythrin (PE)	488	575	BioLegend®
CD11b/c	Alexa Fluor 647	633	675	BioLegend®

Table 4.1: Panel of flourochrome conjugated monoclonal antibodies used in initial flow cytometric experiments.

In a pilot experiment using this antibody cocktail, it was possible to identify a population of $CD45^+$ $CD11b/c^+$ cells in both heart and spleen cell suspensions and to demonstrate that their number was higher in the heart (and fewer in the spleen) following cryoinfarction, behaviour that is consistent with a predominantly macrophage population (Figure 4.4).

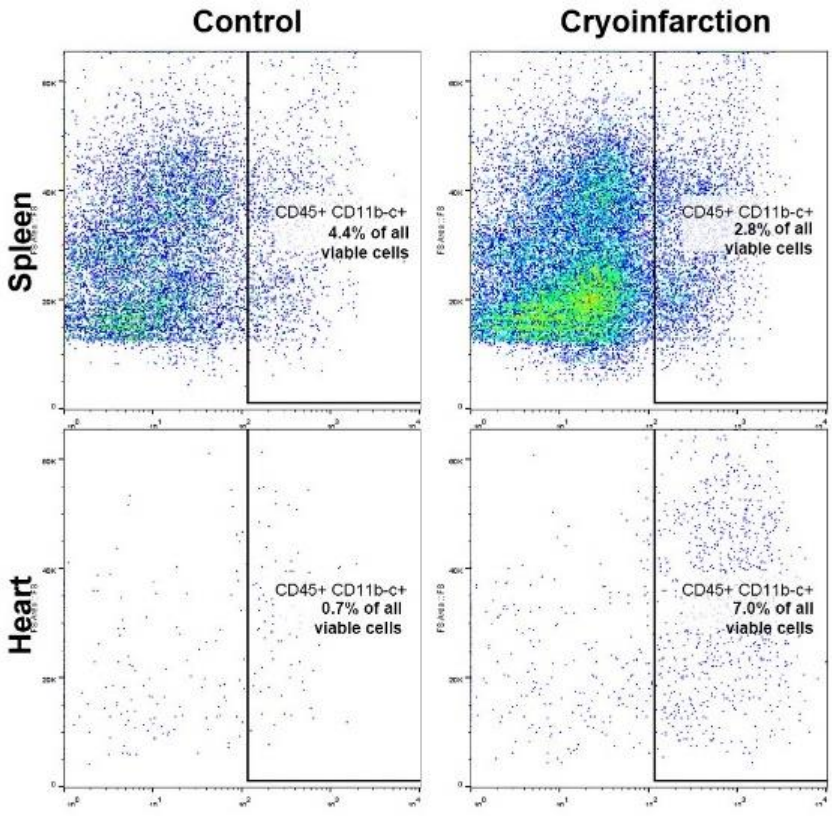


Figure 4.4: Initial flow cytometric experiments using a 4 colour panel identified a population of $CD45^+$ $CD11b/c^+$ cells whose number increase in the heart and decrease in the spleen following myocardial infarction.

However, no clear separation in CD43 staining was observed in $CD45^+$ $CD11b/c^+$ cells (Figure 4.5). Thus, although this strategy identified a population of inflammatory cells, monocyte-macrophage phenotyping was not possible, which demonstrated that this gating strategy was not sufficiently sophisticated for use in the planned experiment. CD11b/c staining of neutrophils has been reported[47]; it is likely that the failure of this strategy to differentiate $CD43^{hi}$ and $CD43^{lo}$ monocyte-macrophage subsets may have reflected contamination of the $CD45^+$ $CD11b/c^+$ cell populations with a large number of neutrophils.

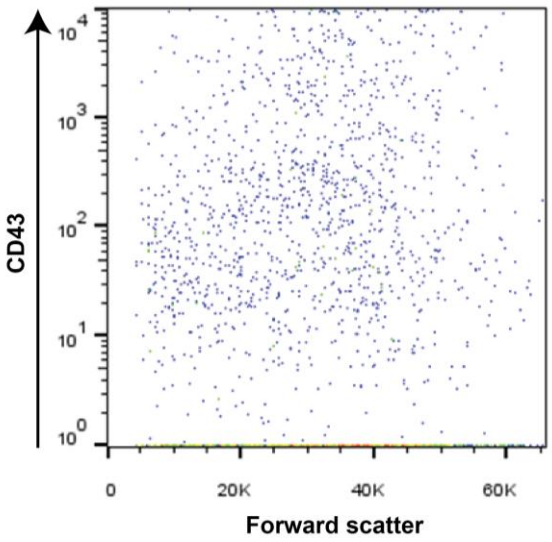


Figure 4.5: No clear separation in CD43 expression in $CD45^+$ $CD11b/c^+$ cells, suggesting that this antibody panel does not allow macrophage phenotyping using the CD43 marker.

4.4.2.2 *Optimisation of an improved, seven colour flow cytometry panel*

Given the failure of the initial four colour panel to adequately assess the post MI monocyte-macrophage response, a new panel design was adapted from a method recently described and validated in rat inflammatory responses to lung injury[48]. This panel was adapted for use in these experiments by removing antibodies included to assess T-cell subsets (as MI causes predominantly innate, rather than adaptive, immune responses), which reduces the potential for experimental confounding due to fluorescence spectral overlap. The final list

of antibodies, flourochromes and suppliers is presented in Table 4.2; gating strategies are presented for splenocytes (Figure 4.7) and heart (Figure 4.8).

This strategy not only enabled assessment of all major inflammatory cell groups, but also enabled clear separation of monocytes/macrophages into two groups: $CD43^{hi}His48^{lo/int}$ ((‘reparative’ phenotype, analogous to $Ly6C^{lo}$ monocytes/macrophages in mice) and $CD43^{lo}His48^{hi}$ (‘inflammatory’ phenotype, analogous to $Ly6C^{hi}$).

Antibody target	Flourochrome	Excitation laser (nm)	Maximum fluorescence emission (nm)	Supplier
Live/Dead	Zombie Violet	405	450	BioLegend®
His48	FITC	488	530	eBioscience®
CD45	APC-Cy7	633	750	BioLegend®
CD3	Viogreen	405	530	Miltenyi®
CD161	APC	633	665	BioLegend®
CD45r	PE-Cy7	488	750	eBioscience®
CD43	PE	488	575	BioLegend®

Table 4.2: Antibodies and flourochromes used for seven colour flow cytometric panel.

Having established the flow cytometric gating strategy, antibody titration experiments were performed to optimise the mass of antibody used in each experiment (Figure 4.6). The advantages of optimised antibody concentrations include improved cell separation and, usually, reduced the cost of the reagents (manufacturer recommended concentrations tend to be higher than are necessary for most applications). All antibodies were used at the concentration demonstrated to achieve the highest stain index (SI), which was calculated from the median fluorescence intensity (MFI) of the positive and negative cell populations according to the equation 4.1[49]:

$$SI = \frac{(MFI_{\text{signal}} - MFI_{\text{background}})}{[(84^{\text{th}}\ \text{percentile}\ MFI_{\text{signal}} - MFI_{\text{background}})/0.995]} \qquad 4.1$$

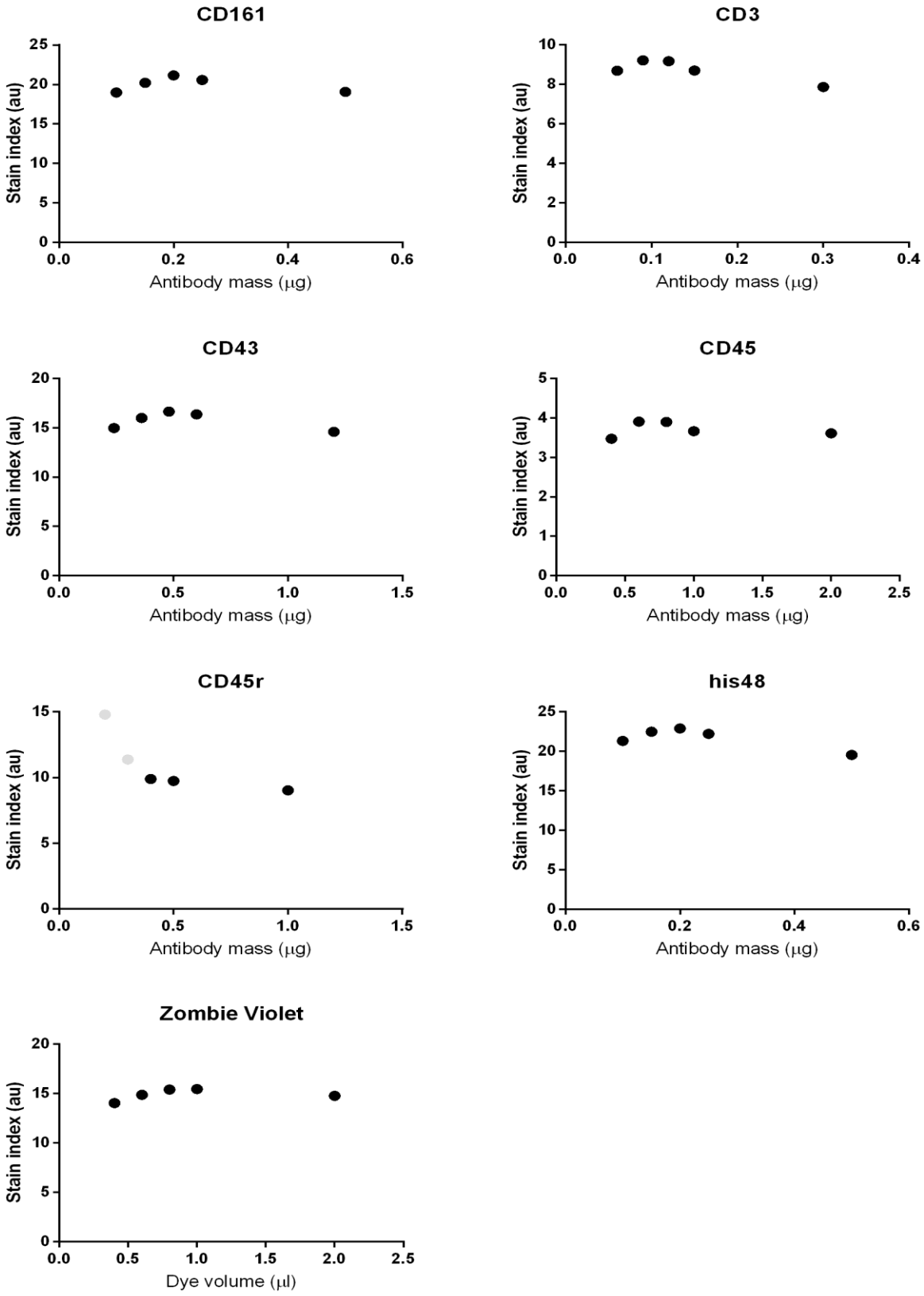


Figure 4.6: Antibody titration experiments for flow cytometry. The optimal mass of antibody to optimise staining index (calculated as a modified ratio of median positive cell flouresence to background flouresence) was determined for all antibodies. High background signal led to anomolous results for the two lowest concentrations of CD45 (grey points).

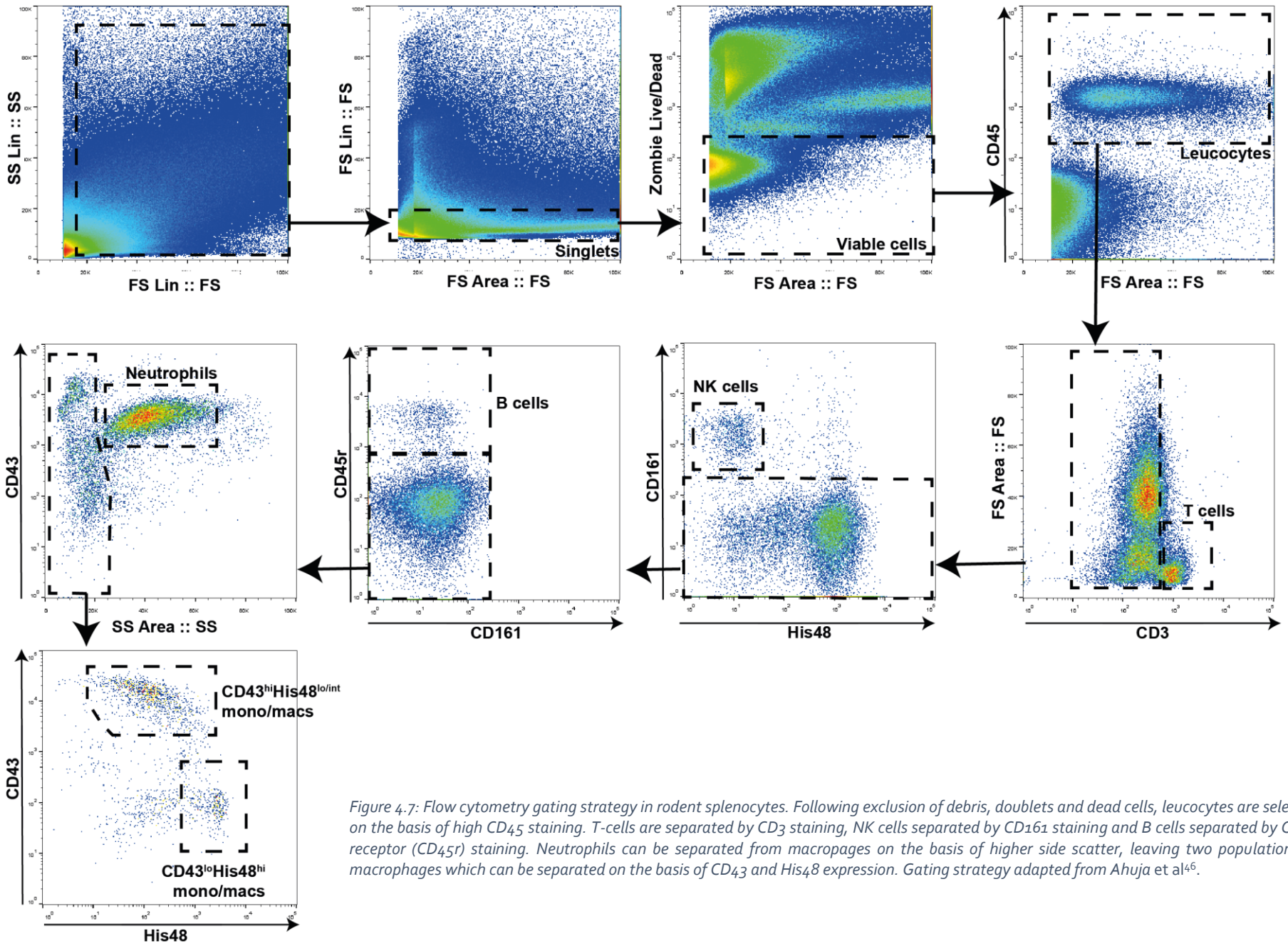


Figure 4.7: Flow cytometry gating strategy in rodent splenocytes. Following exclusion of debris, doublets and dead cells, leucocytes are selected on the basis of high CD45 staining. T-cells are separated by CD3 staining, NK cells separated by CD161 staining and B cells separated by CD45 receptor (CD45r) staining. Neutrophils can be separated from macropages on the basis of higher side scatter, leaving two populations of macrophages which can be separated on the basis of CD43 and His48 expression. Gating strategy adapted from Ahuja et al[46].

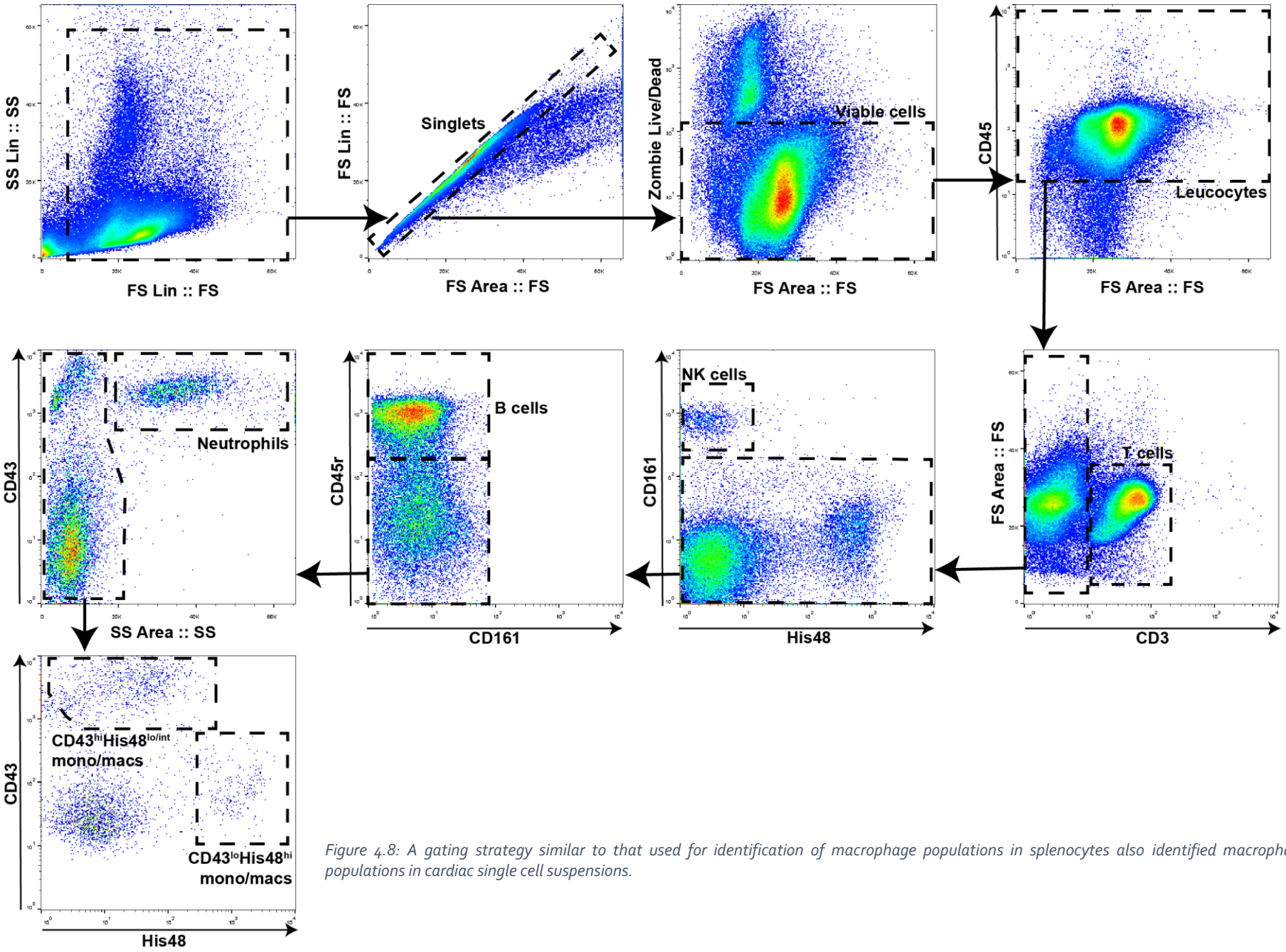


Figure 4.8: A gating strategy similar to that used for identification of macrophage populations in splenocytes also identified macrophage populations in cardiac single cell suspensions.

4.4.3 MI causes high hyperpolarized [1-^{13}C]lactate signal at both day 3 and 7, reflecting macrophage driven inflammation

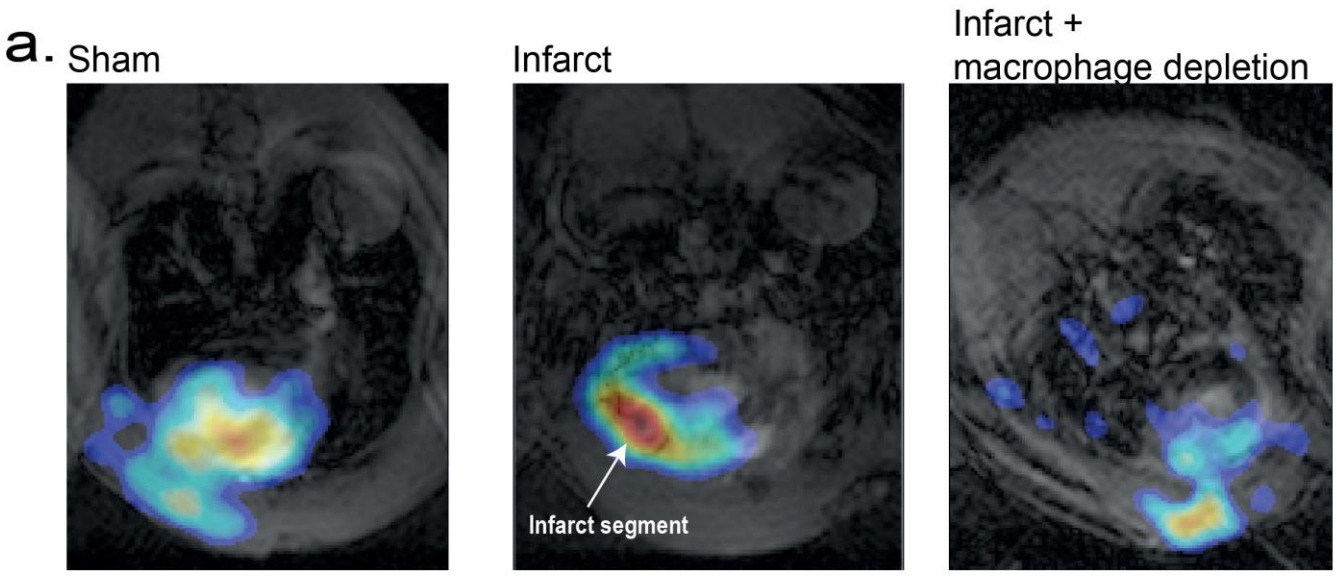
Following development and optimisation of the methods, we next proceeded to combine these techniques in an experiment designed to test the hypothesis that hyperpolarized [1-^{13}C]lactate production might be a novel method for assessing cardiac inflammation. Cryoinjury or sham procedure were performed in rodents prior to hyperpolarized MRI and flow cytometry at day 3 and 7.

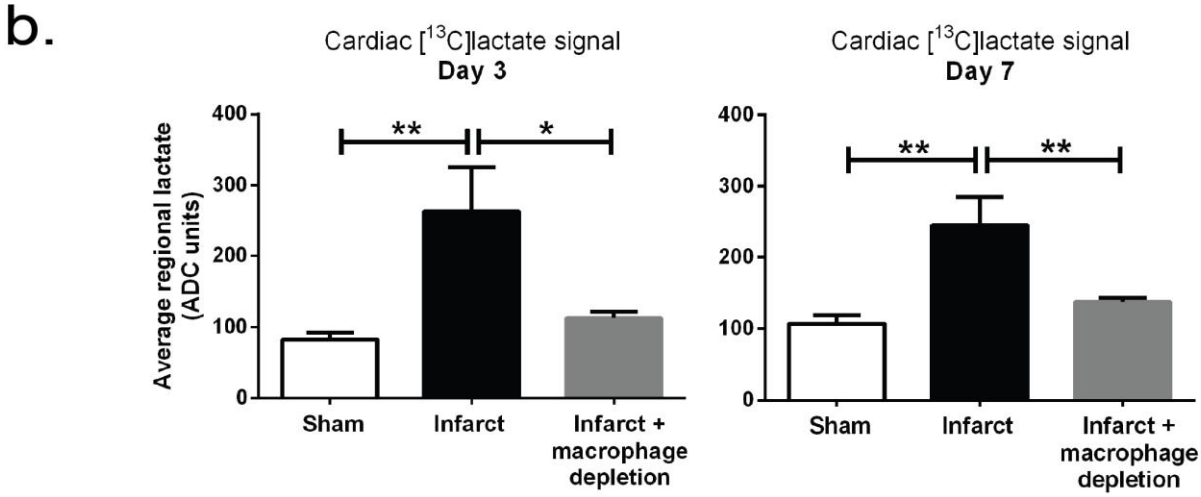
Myocardial cryoinfarction caused intense hyperpolarized [1-^{13}C]lactate signal in healing myocardial segments at both day 3 and day 7 (Figure 4.9, panel a and b, n = 5-6 evaluable biological replicates per time-point), which was associated with a marked influx of both macrophages and neutrophils (Figure 4.9, panel c). The majority of these macrophages were CD43^{lo}His48^{hi} at day 3 and were CD43^{hi}His48$^{lo/int}$ at day 7. This finding is highly consistent with previous studies in mice and suggests that CD43 expression in rat monocytes/macrophages is reciprocal to Ly6C expression in mouse monocytes/macrophages. High hyperpolarized [1-^{13}C]lactate signal was also seen in both the sham and infarct groups in the adjacent thoracotomy site, providing further evidence that [1-^{13}C]lactate reflects inflammation in healing tissues.

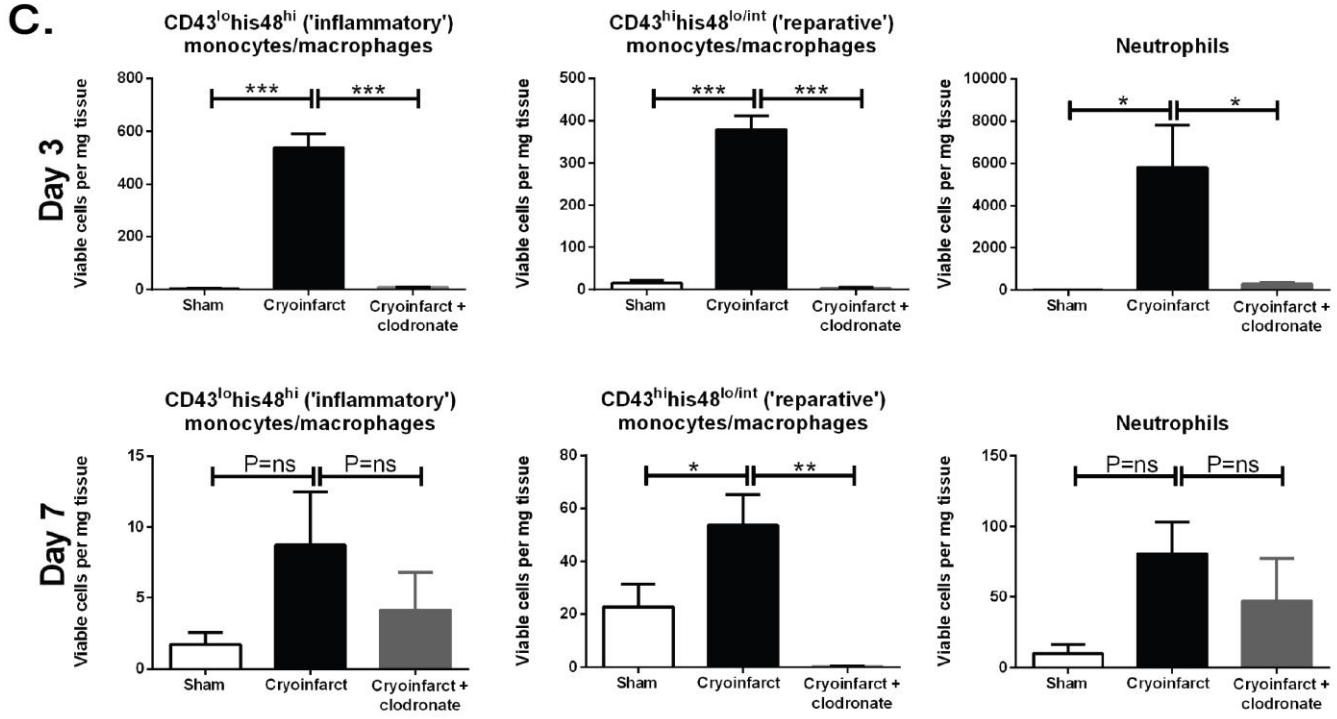
To determine unambiguously whether the hyperpolarized [1-^{13}C]lactate signal reflected macrophage driven inflammation, macrophage depletion was next performed in a two separate groups by intravenous administration of liposome encapsulated clodronate at the time of cryoinfarction. Liposomes are selectively phagocytosed by macrophages, which releases the clodronate intracellularly and induces macrophage depletion[50]. Flow cytometry confirmed that clodronate liposomes caused essentially complete macrophage depletion at day 3, with some repopulation of the CD43^{lo}His48^{hi} by day 7 (Figure 4.9, panel c). Macrophage depletion with clodronate liposomes also abrogated the increase in

hyperpolarized [1-^{13}C]lactate signal seen in the cryoinjury group, a finding which suggests that macrophage driven inflammation is causative for the high [1-^{13}C]lactate signal. Cardiac neutrophil numbers were lower in hearts from the clodronate treated group, suggesting that pro-inflammatory cytokine secretion by macrophages may be important in preventing neutrophil regress.

The cardiac cine imaging protocol included standard long axis views and a short axis cine stack covering the base to apex ((Figure 4.9, panel d). Contours were placed using the cmr$^{42®}$ software package to derive left ventricular volumes, mass and function and demonstrated a modest, though highly consistent, impairment of systolic function at both day 3 and day 7, which was driven primarily by an increase in end systolic volume ((Figure 4.9, panel e). Despite the presence of a significant wall motion abnormality in all hearts, the remote myocardial segments appeared hyperdynamic, preserving the overall ejection fraction.


a.
Sham
Infarct
Infarct +
macrophage depletion
Infarct segment


b.
Cardiac [13C]lactate signal
Day 3
Average regional lactate (ADC units)
400
300
200
100
0
**
*
Sham
Infarct
Infarct + macrophage depletion
Cardiac [13C]lactate signal
Day 7
400
300
200
100
0
**
**
Sham
Infarct
Infarct + macrophage depletion


c.
CD43loHis48hi ('inflammatory') monocytes/macrophages
CD43hiHis48lo/int ('reparative') monocytes/macrophages
Neutrophils
Day 3
Viable cells per mg tissue
800
600
400
200
0
***
***
Sham
Cryoinfarct
Cryoinfarct + clodronate
500
400
300
200
100
0
***
***
10000
8000
6000
4000
2000
0
*
*
Day 7
15
10
5
0
P=ns
P=ns
80
60
40
20
0
*
**
150
100
50
0
P=ns
P=ns

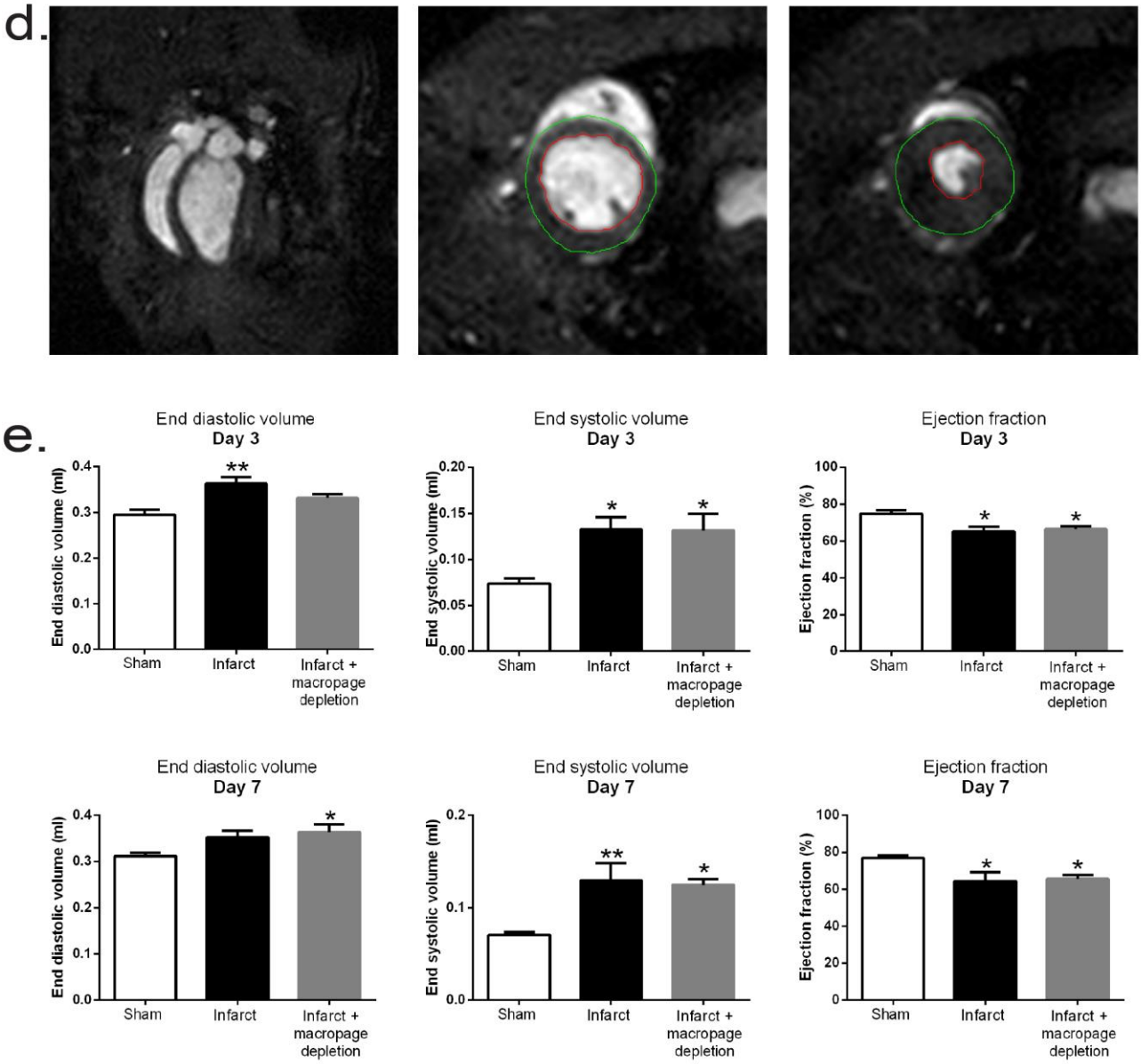


Figure 4.9: Panels a and b; hyperpolarized [1-^{13}C]lactate images show intense lactate signal in injured myocardial segments at both day 3 and 7, which was near-normalised by macrophage depletion. Panel c; myocardial infarction caused a marked macrophage and neutrophil inflammatory reponse at day 3 which persisted to day 7, though total cell number was lower at day 7. Panel d; representative long- and short-axis cine images; cardiac volumetric and functional information was assessed by placing contours on short axis images in end-diastole and end-systole; MI caused a modest reduction in systolic function which was driven primarily by an increase in end-systolic volume. n = 4-6 evaluable datasets per timepoint; statistical comparisons by ANOVA with multiple comparison testing by Holm-Sidak's method

4.4.4 Development of hyperpolarized MR in cell suspensions

One potential strength of hyperpolarized MR as a tool for translational experiments is the ability for use across cell lines, animal models and humans. Having established that high hyperpolarized [1-^{13}C]lactate signal post-MI reflected macrophage driven inflammation, we next sought to understand whether the high signal reflected macrophage number or whether the lactate signal was also influenced by macrophage inflammatory phenotype. To understand this, it was necessary to develop an *in vitro* model system in which lactate signals could be recorded from a precisely defined number of cells in suspension. The rate of label exchange from hyperpolarized [1-^{13}C]pyruvate to [1-^{13}C]lactate and other reactions has been used as a biomarker of treatment response in cancer cell lines[51, 52], though no cardiovascular applications of DNP in cell suspensions have yet been described.

Large numbers of cells are generally required for DNP experiments using clinical or preclinical MR systems, though the number of cells can be reduced when using high-end NMR systems with high sensitivity RF coils[53]. The immortalized RAW264.7 macrophage-like cell line was used to generate a sufficient number of cells. Cells were maintained under standard tissue culture conditions, the full methods for which are formally described in Appendix 4A (page 201).

In pilot phantom experiments, round bottomed NMR tubes were associated with poor magnetic field homogeneity during shimming, leading to broad spectral line-widths (Figure 4.10). This poor homogeneity was likely to be due to the complex fluid/air interface, and, in subsequent experiments, agar gel was added to the bottom of the NMR tube in order to reduce this effect. This approach improved shim line-widths from around 100Hz to around 50Hz.

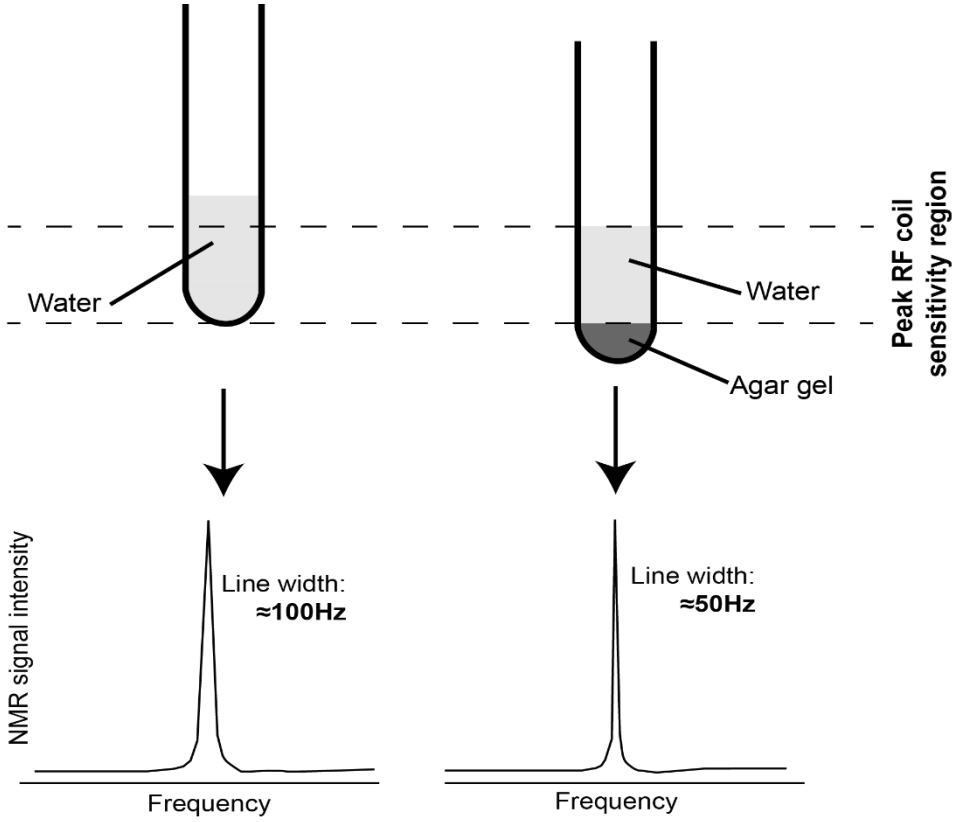


Figure 4.10: Improved shimming of cell suspensions was achieved by adding agar gel to the bottom of the NMR tube.

In pilot cell suspension experiments, little or no label exchange into [1-^{13}C]lactate was detectable using an 11.7 T preclinical MRI scanner following the addition of 1 ml of 6.1 mM hyperpolarized [1-^{13}C]pyruvate to a 1 ml cell suspension containing either 10^7, 20^7, or 40^7 RAW264.7 macrophages (40^7 RAW264.7 cells corresponds to around four 75ml tissue culture flasks when grown in monolayers to 80% confluency).

However, when 80^7 macrophage-like cells were placed in a 1 ml suspension, a degree of lactate exchange sufficient to enable robust fitting to standard kinetic models was detected. Large format 175 ml flasks were used for cell culture thereafter.

4.4.5 RAW264.7 activation increases hyperpolarized [1-^{13}C]lactate label flux

Having established a protocol for estimation of [1-^{13}C]lactate label incorporation rates in cell suspensions, this method was then used to test the effect of activation/polarizing RAW264.7 macrophages to an inflammatory phenotype by comparing addition of lipopolysaccharide (LPS, 1 μg/ml) to cell culture medium for 24 hours versus an equivalent volume of sterile phosphate buffered saline (PBS, 80^7 cells in a 1ml suspension was used in both groups). The resulting signal intensity curves (Figure 4.11, lactate signal normalised to mean [1-^{13}C]pyruvate signal to control for variability in sample polarization) demonstrated significantly higher lactate signal in LPS activated cells. Hypothesising that this might reflect intracellular lactate pool expansion due to higher glycolytic rates, we next tested the effect of addition of the glycolytic inhibitor 2-deoxyglcuose (2-DG) to LPS activated macrophages. 2-DG treatment normalised the lactate signal in activated macrophages, suggesting that high glycolytic rates are responsible for the increase in [1-^{13}C]lactate signal.

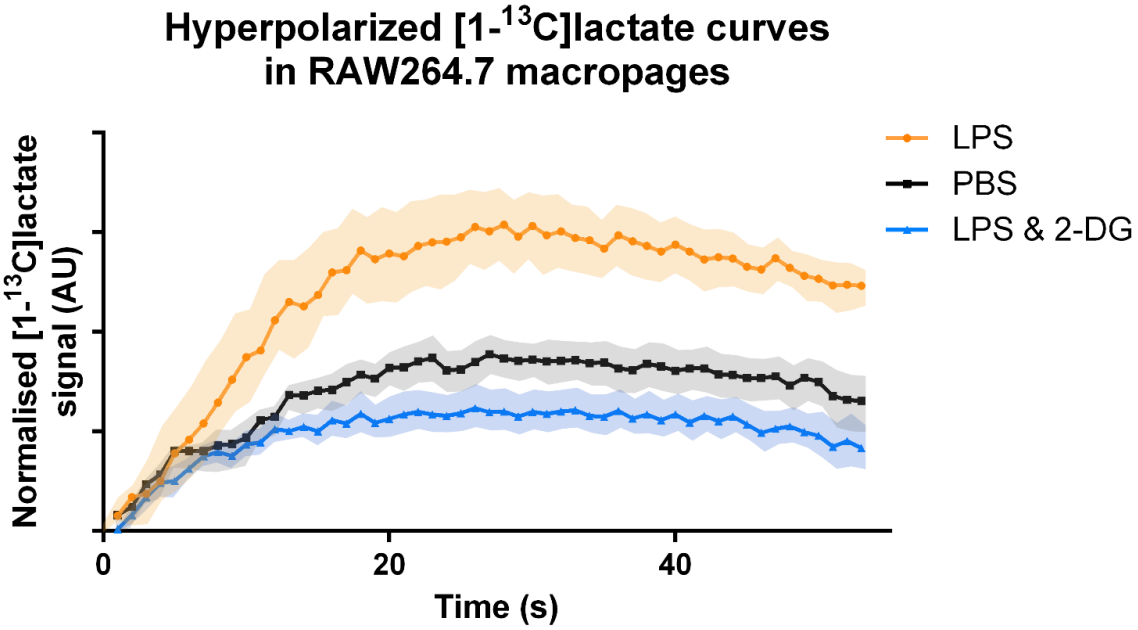


Figure 4.11: [1-^{13}C]lactate production following addition of hyperpolarized [1-^{13}C]pyruvate in cells treated with lipopolysaccharide was higher than in control cells; this rise was abrogated by addition of the glycolytic inhibitor 2-DG. n = 5-6 experiments per group, lactate curves are presented as mean normalised to pyruvate signal ± SEM.

These data were subsequently fitted to the kinetic model of Zierhut[54] as previously described. As the volume and concentration of pyruvate in the resulting cell suspension are known, it is possible to estimate lactate label flux by multiplying the lactate label exchange rate by the final pyruvate concentration in the cell suspension (calculated to be 3.05 nmol/ml). Again, activated RAW264.7 macrophages demonstrated significantly higher rates of [1-^{13}C]lactate label flux, which was normalised by co-incubation with 2-DG.

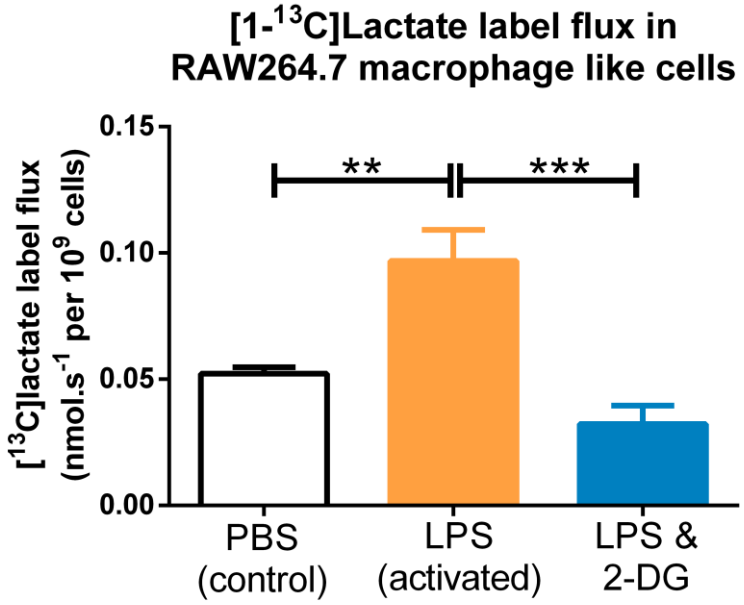


Figure 4.12: Kinetic modelling yields lactate flux estimates in RAW264.7 macrophages, which is increased in LPS activated macrophages through a glycolysis dependent mechanism. n = 5-6 experiments per group; statistical comparison by ANOVA with correction for multiple comparisons by Tukey's method.

4.4.6 Glycolysis is essential for macrophage proinflammatory cytokine production

Having established that activated macrophages demonstrate high hyperpolarized lactate signal due to high glycolytic rates, quantitative polymerase chain reaction (qPCR) was next used to determine the transcriptional mechanisms by which LPS stimulation leads to an increase in cellular glycolysis.

Validation of qPCR reaction efficiency in both singleplex and duplex reactions

Real time quantitative polymerase chain reaction (qPCR) is the method of choice for the assessment of relative gene expression in biological samples. First, single-stranded ribonucleic acid (RNA) is extracted from the biological sample and used as a template for the synthesis of double-stranded complementary deoxyribonucleic acid (cDNA). This cDNA is then amplified in a thermal cycling reaction, in which the double stranded DNA is melted to two single strands. Each of these single strands then serves as the template for the synthesis of two further identical double-stranded sequences, according to the DNA polymerase chain reaction. Unlike the standard polymerase chain reaction however, qPCR incorporates either fluorescently labelled sequence specific primers (TaqMan™ chemistry) or double stranded DNA binding dyes (SYBR® Green chemistry) to enable fluorescence quantitation using a thermal cycler equipped with fluorescence detectors. The measured fluorescent signal is proportional to the quantity of the gene sequence of interest, which doubles with every thermal cycle (until the reaction becomes limited). The cycle number at which fluorescence is detected can therefore be used to estimate the quantity of the gene sequence present at the start of the reaction; a higher input quantity of the sequence will lead to detection at an earlier thermal cycle. All qPCR values are expressed relative to the expression of an endogenous control ('housekeeping') gene expected to be stably expressed in both the control and treatment groups, to control for unavoidable differences in cDNA input quantity.

One important factor to consider in qPCR experimental design is the selection of appropriate reagents, of which there are two competing chemistry systems, TaqMan™ and SYBR® Green. Although TaqMan™ reagents are more expensive than SYBR® Green reagents, they generally offer superior specificity and sensitivity to low-copy number genes, require less optimisation, and enable duplex reaction design – i.e. both the housekeeping

gene and gene of interest can be run in the same reaction, minimising a potential source of bias. TaqMan™ reagents were therefore selected for use in these experiments.

Following literature review, the following genes were selected to interrogate both glycolytic function and proinflammatory cytokine expression in macrophages (Table 4.3):

Gene symbol	Protein encoded by gene	Protein function
Pkm	Pyruvate kinase	Enzyme of glycolysis
Ldha	Lactate dehydrogenase	Enzyme of glycolysis
Pdk1	Pyruvate dehydrogenase kinase 1	Enzyme of glycolysis
Pfkfb3	6-phosphofructo-2-kinase	Enzyme of glycolysis
IL1b	Interleukin 1β	Inflammatory cytokine
IL6	Interleukin 6	Inflammatory cytokine
Rn18S	Pre-ribosomal RNA	Endogenous control gene

Table 4.3: qPCR primers evaluating key glycolytic and inflammatory genes were selected.

Having selected genes of interest, it was next necessary to confirm PCR reaction efficiency in order to ensure that the assumptions made in copy number estimation were valid. qPCR efficiency describes the rate at which the PCR amplicon is generated, and is usually expressed in percentage terms. In order for the comparative cycle threshold (Ct) value method of quantitation to be reliable, the efficiency of the target and endogenous control genes must be approximately equal. Reaction efficiency can be reduced by the presence of reaction inhibitors, a suboptimal primer/probe design or inaccurate pipetting and it is therefore important to exclude these potentially confounding factors prior to gene quantitation experiments. In a 100% efficient PCR reaction, the amplicon signal will double every cycle, i.e. there will be a 10-fold increase in amplicon every 3.32 cycles ($\log_2 10 = 3.32$). A qPCR curve is a regression line plot of Ct value versus the log of nucleic acid input; reaction efficiency is calculated as $10^{-1/\text{slope}}-1 \times 100$.

In order to validate the efficiency of qPCR reactions with the selected cDNA input concentrations and reagents, 10-fold dilution series were constructed for each gene of

interest (Figure 4.14). The results from these dilution series confirmed that all reactions were at least 90% efficient in both singleplex and duplex reaction (both gene of interest and housekeeping gene assessed in the same reaction). These findings demonstrate satisfactory reagent performance and confirm that the selected cDNA input quantity was appropriate, validating subsequent assumptions made during quantitation using the $2^{-\Delta\Delta CT}$ method (which converts Ct values for both the gene of interest and housekeeping gene to a single fold change value).

18s ribosomal RNA demonstrated highly stable Ct values across all experimental groups implying that it is an effective endogenous control gene. Additional housekeeping genes were therefore not investigated.

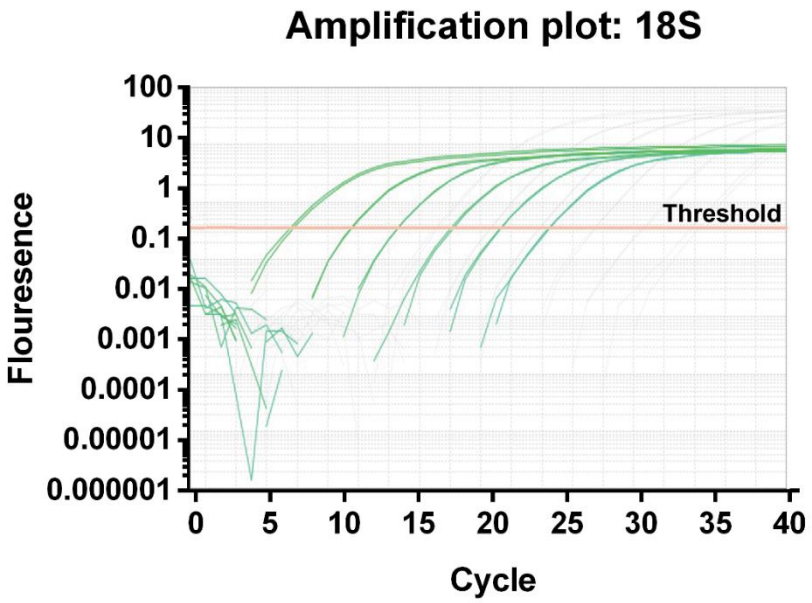
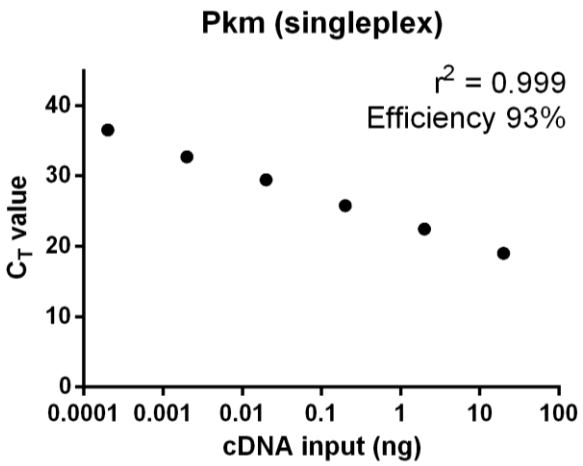
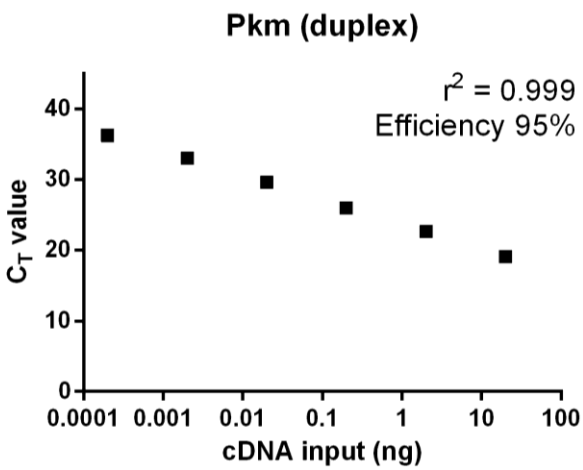
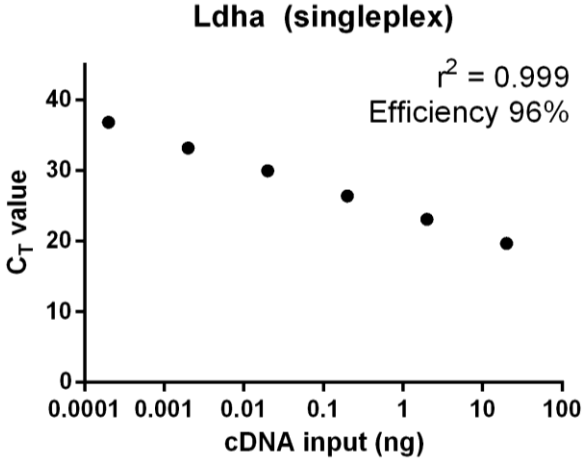
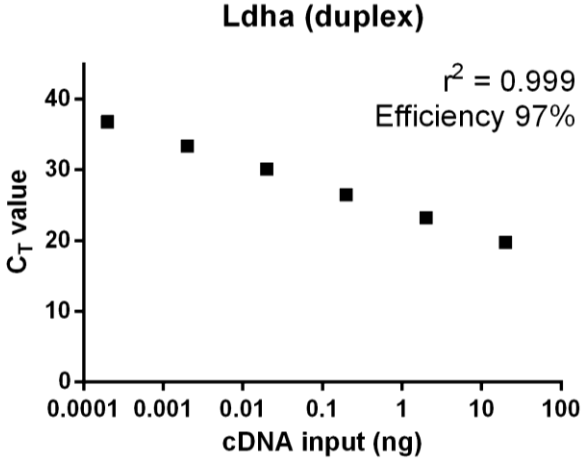


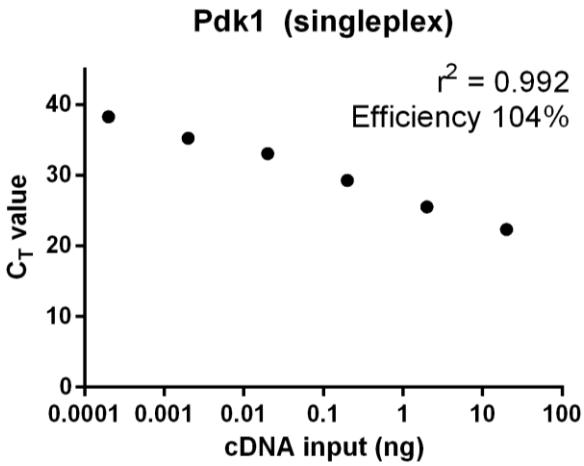
Figure 4.13: Amplification plot for 10-fold dilution series of cDNA input quantity in 18s (also performed in all other genes).

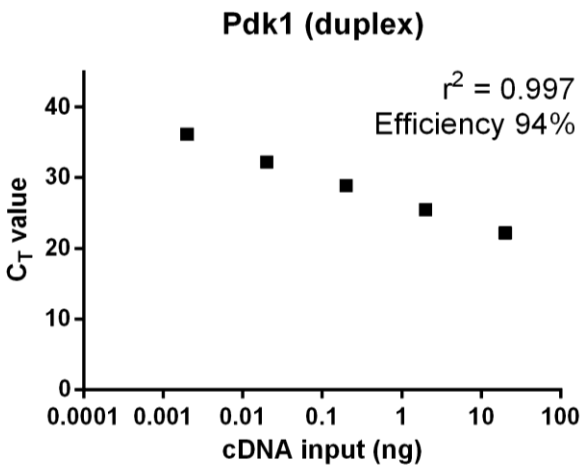

Pkm (singleplex)
r2 = 0.999
Efficiency 93%
CT value
cDNA input (ng)

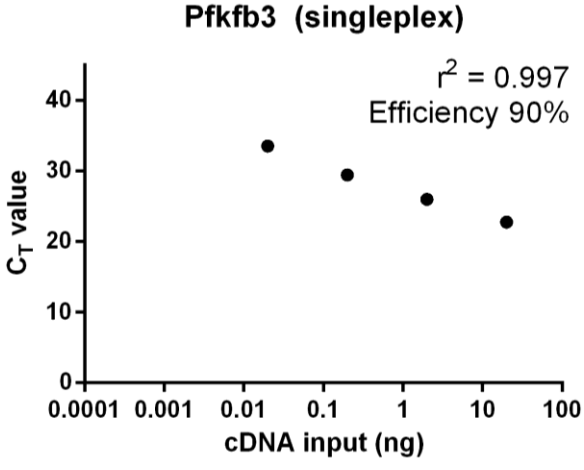

Pkm (duplex)
r2 = 0.999
Efficiency 95%
CT value
cDNA input (ng)

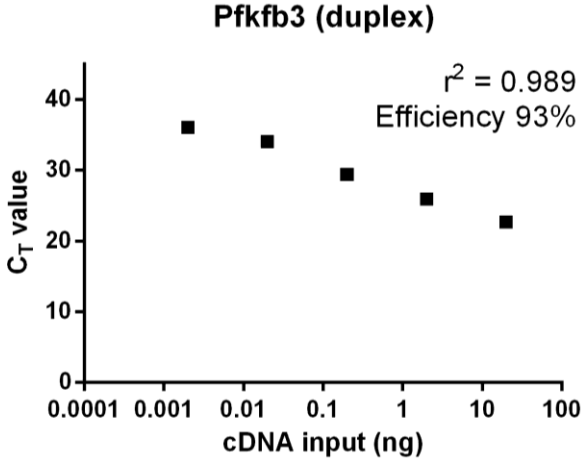

Ldha (singleplex)
r2 = 0.999
Efficiency 96%
CT value
cDNA input (ng)


Ldha (duplex)
r2 = 0.999
Efficiency 97%
CT value
cDNA input (ng)


Pdk1 (singleplex)
r2 = 0.992
Efficiency 104%
CT value
cDNA input (ng)


Pdk1 (duplex)
r2 = 0.997
Efficiency 94%
CT value
cDNA input (ng)


Pfkfb3 (singleplex)
r2 = 0.997
Efficiency 90%
CT value
cDNA input (ng)


Pfkfb3 (duplex)
r2 = 0.989
Efficiency 93%
CT value
cDNA input (ng)

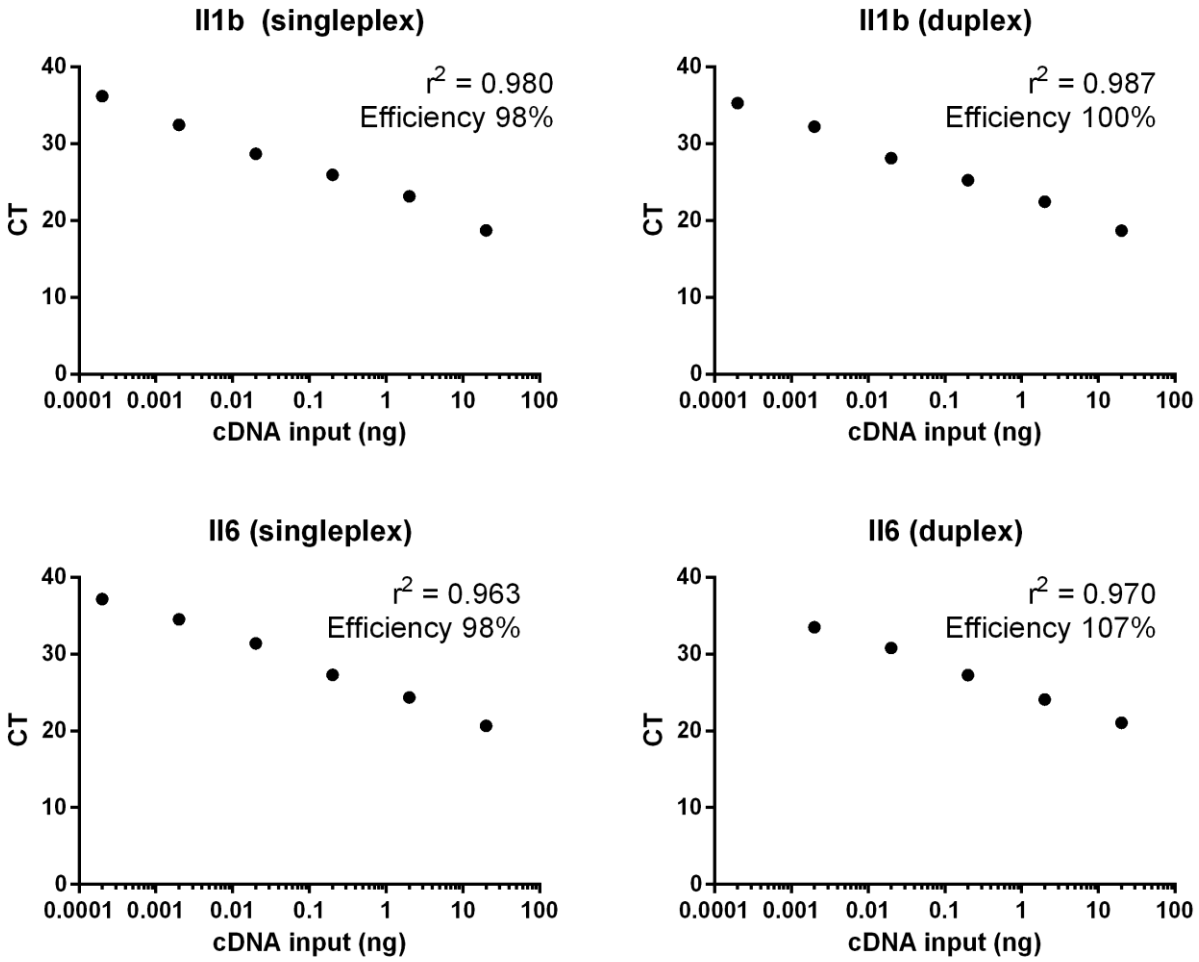


Figure 4.14: 10-fold dilution series for each gene of interest were constructed to estimate reaction efficiency. All reaction efficiencies were > 90% in both singleplex and duplex.

4.4.6.1 qPCR results

qPCR analysis of the relative expression of genes encoding key glycolytic enzymes demonstrated that LPS stimulation caused upregulation of a panel of glycolytic genes, including those encoding lactate dehydrogenase (LDH), pyruvate kinase (PKM) and 6-phosphofructo-2-kinase (PFKFB3). These findings suggest a transcriptionally mediated increase in glycolytic rate (Figure 4.15). Although pyruvate dehydrogenase kinase 1 (PDK1) was downregulated, PDK1 negatively regulates pyruvate dehydrogenase activity and this therefore suggests an increased in oxidative glucose metabolism, as well as glycolysis. Many of these genes are established targets of the transcription factor hypoxia inducible factor 1A (HIF-1α). Subsequent qPCR analysis of Hif1a gene expression confirmed HIF-1α upregulation, suggesting normoxic HIF-1α activation. As expected, genes encoding the inflammatory cytokines interleukin 1β (IL-1β) and interleukin 6 (IL-6) were both strongly upregulated following LPS simulation.

Blockade of glycolysis with 2-DG prevented normoxic Hif1a activation and abrogated the upregulation of genes encoding LDH, PKM and PFKFB3. No significant difference in PDK1 regulation was demonstrated. Interestingly, 2-DG also markedly reduced expression of IL-1β (confirming the findings of a previous study[33]) and, to a lesser extent, IL-6. These findings suggest that an increase in glycolytic rate is essential for complete macrophage activation and polarization, highlighting a key link between cellular metabolism and function. Furthermore, the findings suggest that the high hyperpolarized [1-^{13}C]lactate signal measured in activated macrophages is determined not just by their number, but also by their inflammatory activation status and cellular phenotype.

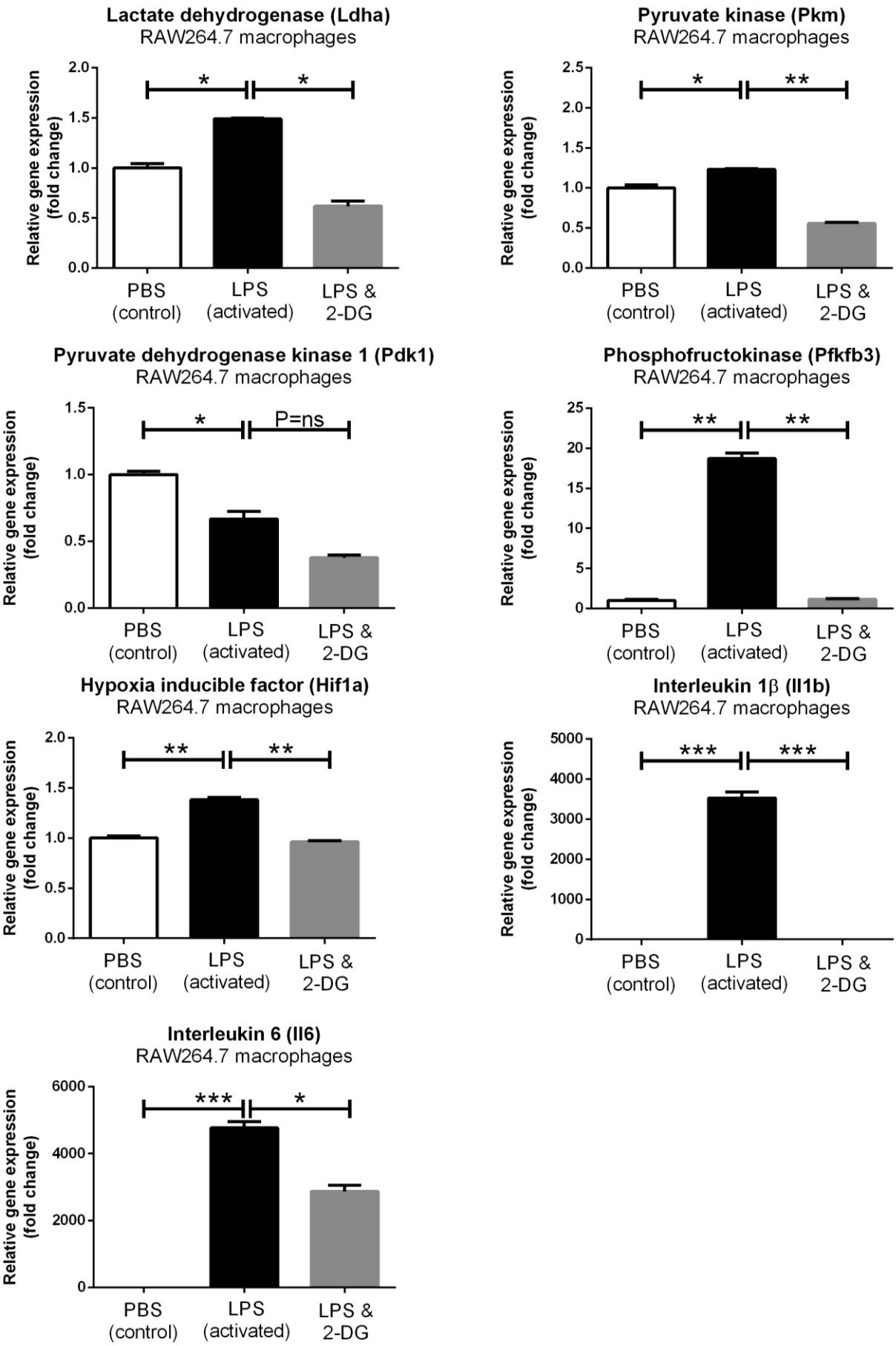


Figure 4.15: Activation of RAW264.7 macrophages using LPS regulates a panel of glycolytic and inflammatory genes. Glycolytic blockade using 2-DG tends to block the increase in both glycolytic and also inflammatory genes. n = 3 biological replicates per group; statistical comparison by ANOVA with correction for multiple comparisons by Tukey's method.

4.4.6.2 *Validation of qPCR findings at protein level*

To investigate whether the changes in inflammatory cytokine gene expression were also recapitulated at the protein (i.e. functional) level, concentrations of key inflammatory cytokines were measured in cell lysates using enzyme linked immunosorbent assays (ELISA). Methodological details are provided in Appendix 4A (page 203). As expected, LPS caused increases in IL-β, IL-6 and TNF- α protein expression, which was reduced if the cells were co-incubated with 2-DG. It is perhaps surprising that TNF-α protein levels were lower following 2-DG treatment as, unlike IL-β and IL-6, preformed TNF-α is stored intracellularly in macrophages and is released following stimulation in a largely non-transcriptional process. Subsequent measurement of TNF-α in cell culture medium supernatants (rather than in cell lysates) confirmed that 2-DG did not change TNF-α release.

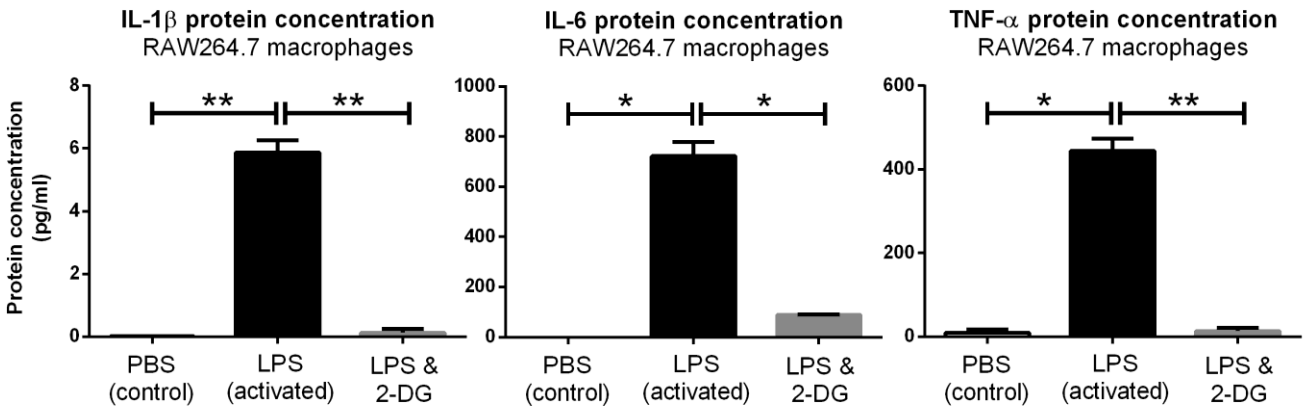


Figure 4.16: Cytokine levels in RAW264.7 cell lysates were measured using ELISA; 2-DG treatment reduced the protein levels of key pro-inflammatory cytokines. n = 3 biological replicates per group; statistical comparison by ANOVA with correction for multiple comparisons by Tukey's method.

4.4.6.3 Validation in primary macrophages

Although an immortalised cell line is the only practical way of generating a sufficient number of cells for hyperpolarized MRS experiments in cell suspensions, it is necessary to validate findings from cell lines using primary cells. Bone marrow derived macrophages are widely used for this purpose by immunologists, though there is evidence that they are not necessarily identical to macrophages derived from other sources[55] whilst the spleen is the major source of monocytes/macrophages in myocardial infarction[22]. It was therefore decided to develop a method for the production of spleen derived macrophages, to investigate whether primary cells would show similar patterns of gene regulation to RAW264.7 macrophages.

Full details of the optimised protocol for generating spleen derived macrophages are provided in Appendix 4A (page 201). In brief, mouse splenocytes were plated at 4-6 $x10^6$ cells per well of a 6 well plate and incubated with 5 ng/ml of murine macrophage colony stimulating factor (M-CSF) for 6 days. This method produced monolayers of 70-80 % confluent cells with the morphology of mature macrophages. Flow cytometric analysis confirmed that whereas $Ly6C^{lo}$ monocytes/macrophages formed just 2 % of all viable cells within non-cultured murine splenocytes (Figure 4.17), this differentiation protocol yielded a >95 % pure population of pure primary macrophages (Figure 4.18).

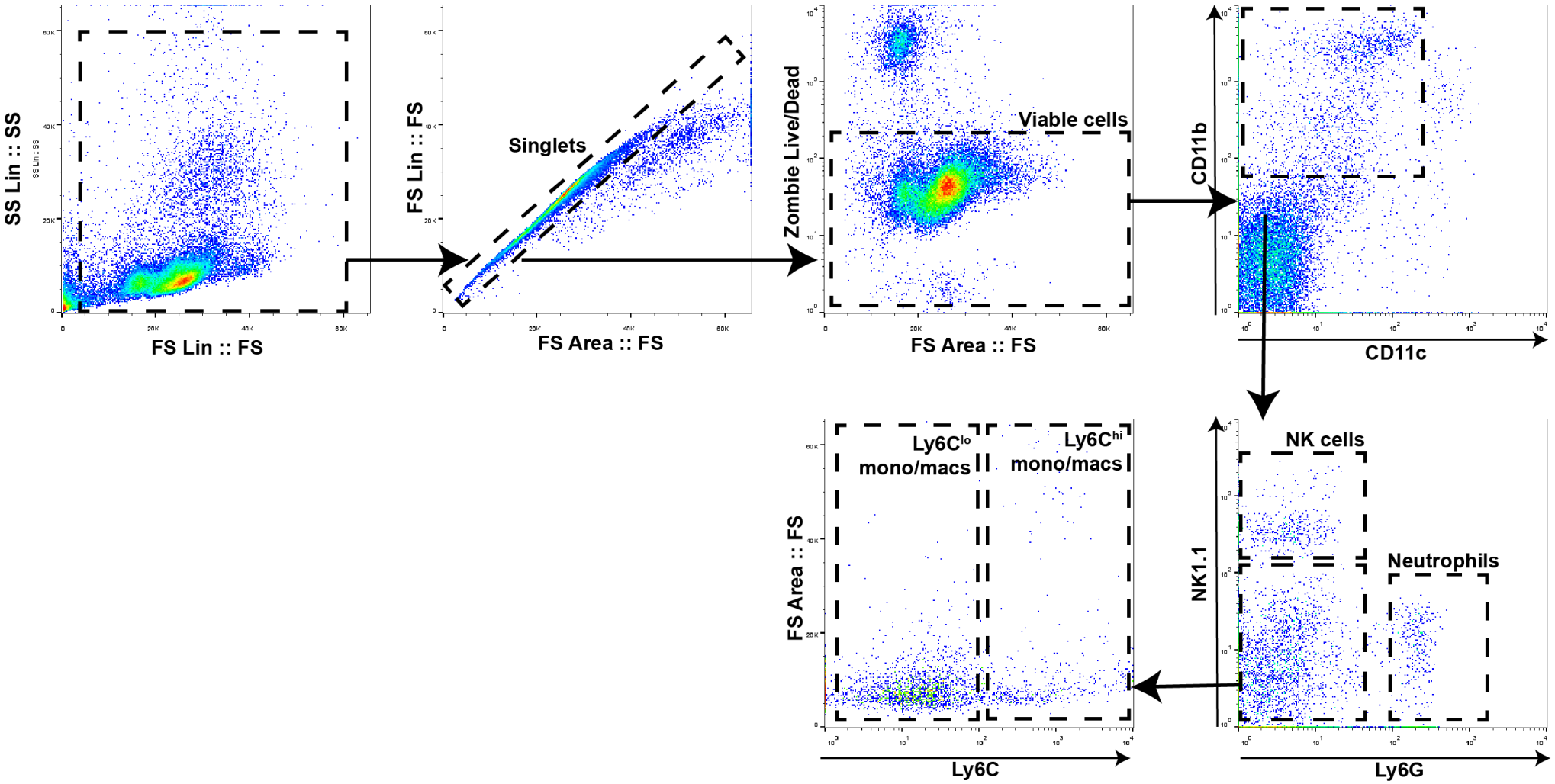


Figure 4.17: Gating strategy for mouse splenocytes. Ly6C^{lo} monocytes/macrophages represented approximately 2 % of all viable cells.

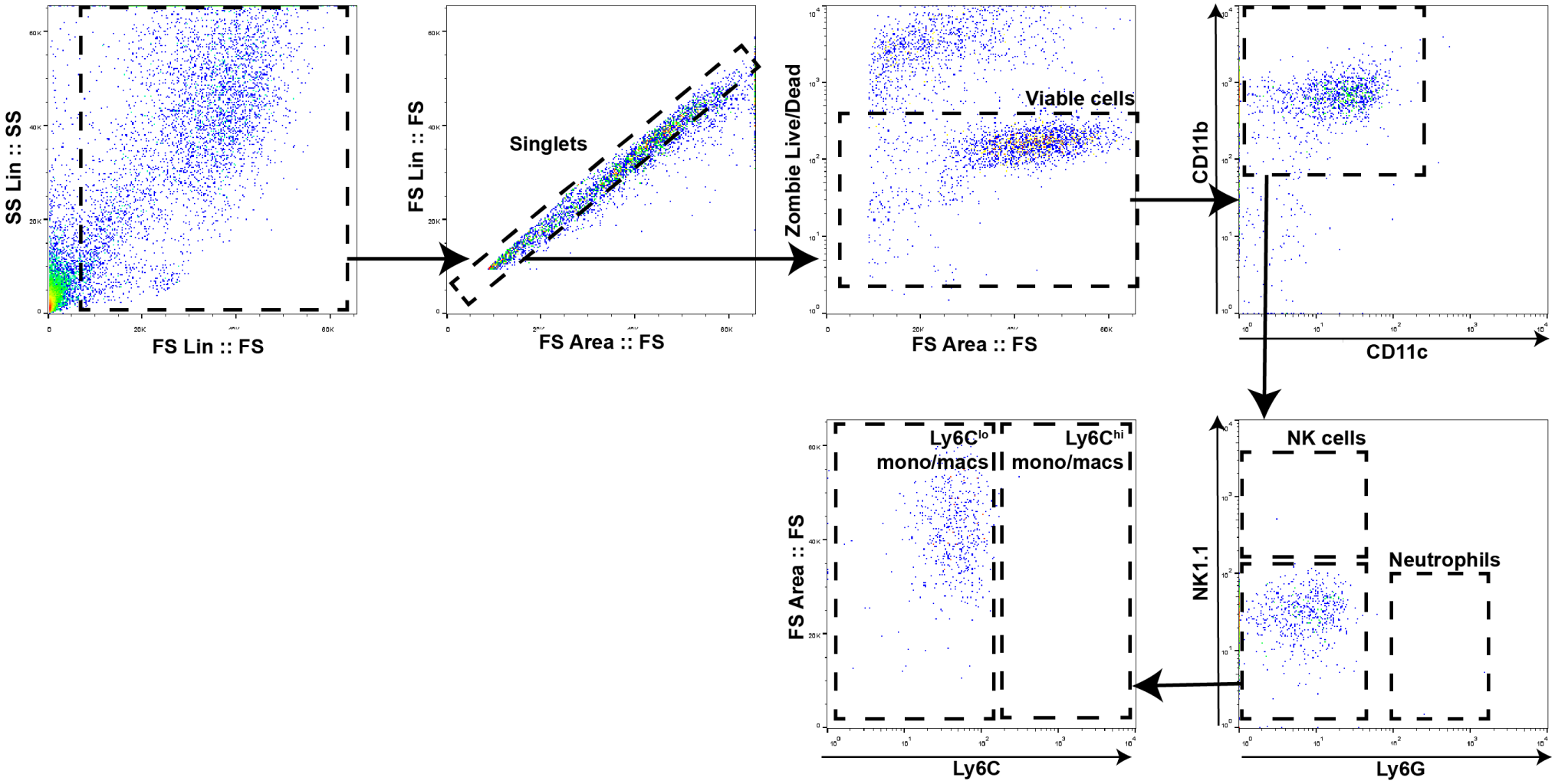


Figure 4.18: Gating strategy for spleen derived macrophages produced from murine splenocytes at day 6. Viable cells were a >95 % pure population of Ly6C^{lo} monocytes/macrophages.

4.4.6.4 *Primary spleen derived macrophages show similar patterns of gene regulation to RAW264.7 cells*

Primary spleen derived macrophages were then treated with LPS with or without 2-DG and qPCR was used to evaluate patterns of glycolytic and inflammatory gene expression. In a pattern identical to that seen with RAW264.7 macrophages, activation of primary macrophages with LPS caused marked upregulation of LDH, PKM, PFKFB3 and HIF-1α, with downregulation of PDK1 (Figure 4.19). Again, 2-DG markedly attenuated regulation of IL-1β though, in contrast to RAW264.7 cells, there was no significant difference in IL-6 regulation.

In general, the fold changes in gene expression demonstrated in these primary cells were higher than those seen with RAW264.7 cells. Although the RAW264.7 cells were used at low passage number (< 20), their responsiveness to polarization stimuli is known to decrease over time due to genetic drift potentially explaining this finding.

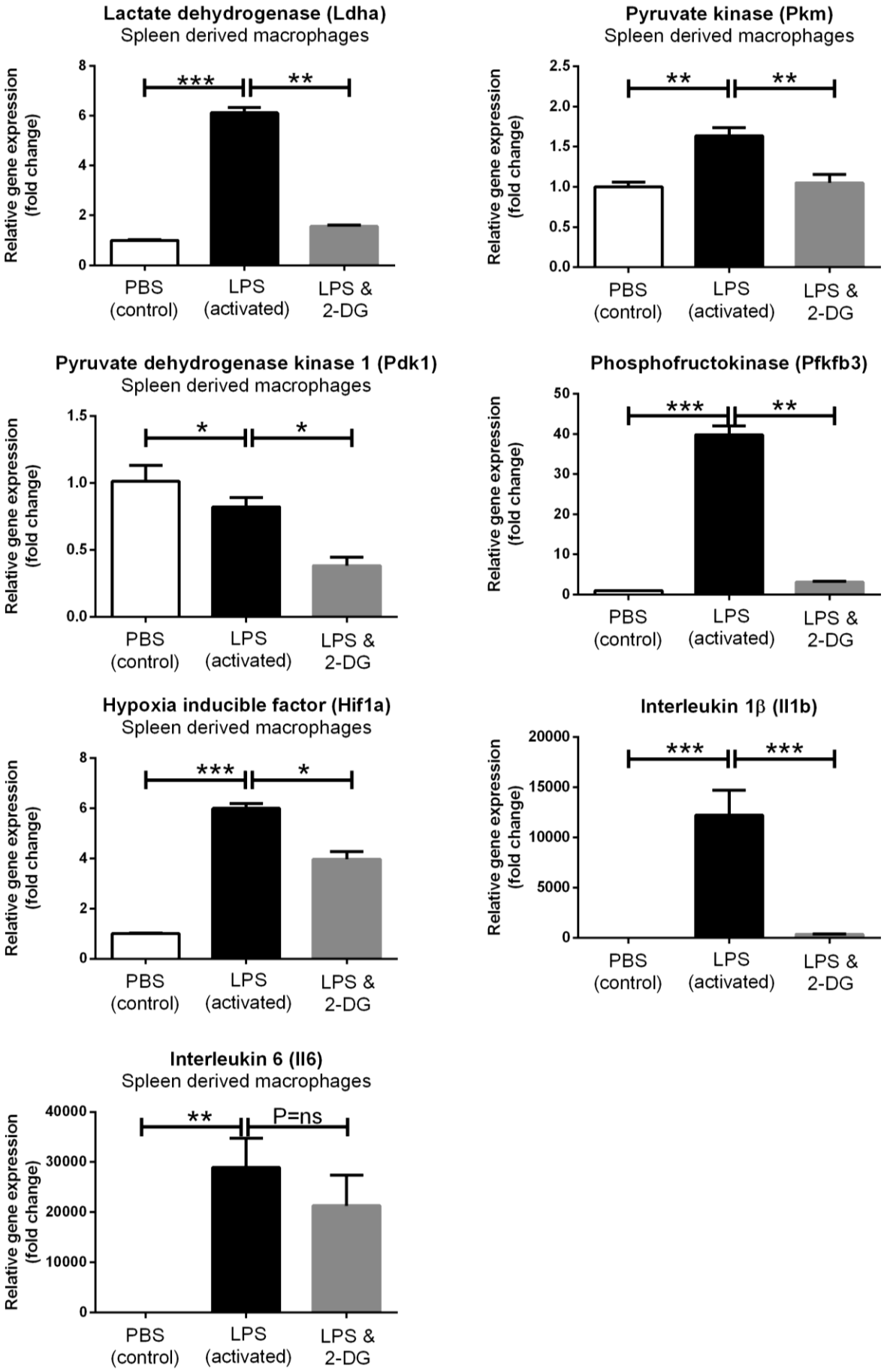


Figure 4.19: Validation of qPCR gene expression profiles following LPS stimulation and 2-DG treatment in primary spleen derived macrophages. Patterns of gene regulation were identical to RAW264.7 cells with a tendency to higher fold changes. n = 3 biological replicates per group; statistical comparison by ANOVA with correction for multiple comparisons by Tukey's method.

4.4.7 Hyperpolarized [1-^{13}C]lactate signal as a potential therapeutic target

Having established that high hyperpolarized [1-^{13}C]lactate signal in healing myocardium reflects macrophage driven inflammation due to glycolytic/inflammatory reprogramming in these cells, we next asked whether the [1-^{13}C]lactate signal might be a potential therapeutic target in its own right. To determine this, two further groups of rats underwent cryoinfarction and were treated with either 2-DG (500 mg/kg per day in two divided doses) or an equivalent volume of sterile 0.9% saline until hyperpolarized MRI was performed on day 3. 2-DG administration was commenced 3 hours following cryoinjury in order to test the concept that novel therapies targeting macrophage immune-metabolism could be administered following reperfusion in humans.

2-DG at a dose of 500 mg/kg caused no apparent toxicity and significantly reduced hyperpolarized [1-^{13}C]lactate signal at day 3 (Figure 4.20).

Cardiac tissue from the infarct zone was next evaluated using qPCR. MI caused a greater than 50-fold increase in IL-1β expression in infarct tissue compared to normal myocardium acquired from a separate group. There was a non-significant reduction in IL-1β gene expression in infarct tissue following 2DG treatment at a dose of 500 mg/kg. This result may have reflected the fact that 500 mg/kg is a relatively low dose of 2-DG, and treatment

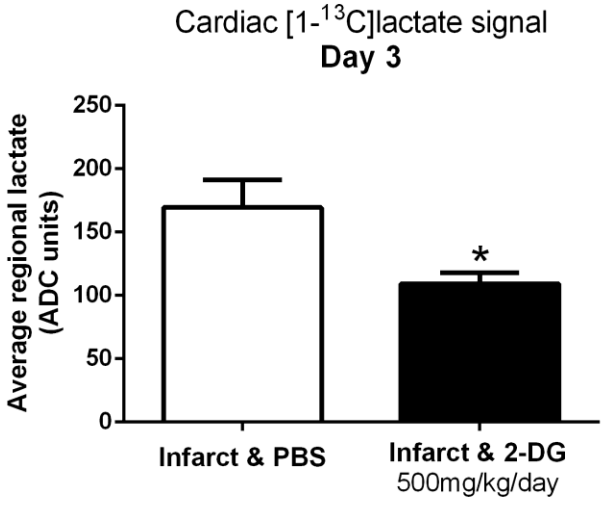


Figure 4.20: 2-deoxyglucose treatment reduced hyperpolarized [1-^{13}C]lactate signal at day 3. n = 4-5 evaluable datasets per group; statistical comparison by unpaired T-test.

of a subsequent group with 1 g/kg again demonstrated no toxicity but caused further, statistically significant, reduction in IL-1β gene expression in healing myocardium. These findings help to establish the concept that specific targeting of the molecular mechanisms underlying the hyperpolarized [1-^{13}C]lactate signal can also modify inflammatory processes in the healing myocardium, providing initial evidence of 'MR visible' immunomodulation. As expected, no difference was seen in LV systolic function at day 3, however ongoing work will determine the effect of 2-DG treatment upon longer term myocardial remodelling and scar formation.

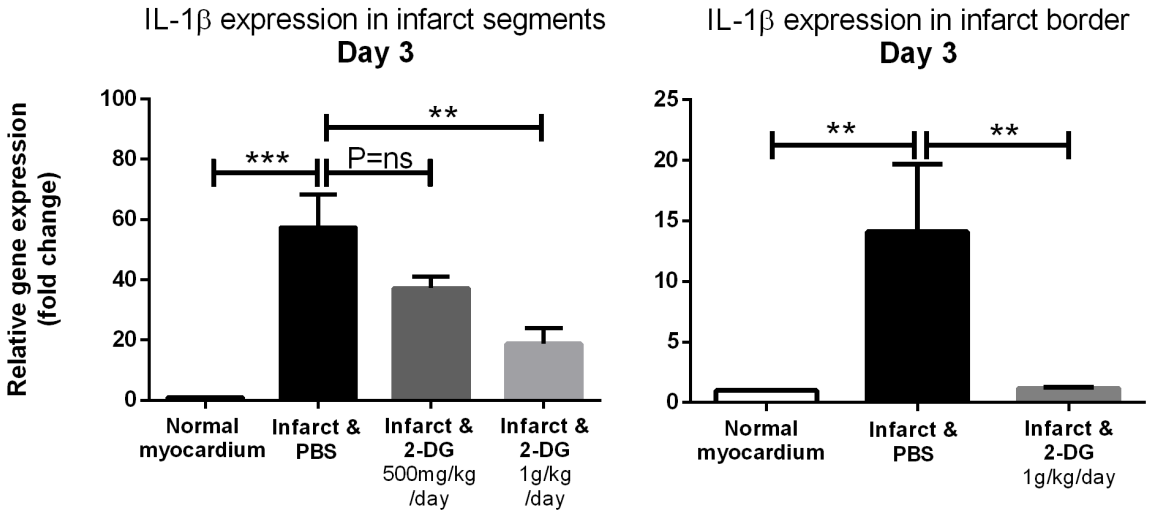


Figure 4.21: Post MI treatment with 2-deoxyglucose caused dose-dependent down-regulation of IL-1β gene expression in infarct tissue and border zones in addition to reducing the hyperpolarized [1-^{13}C]lactate signal. n = 6 biological replicates treated with PBS or 2-DG (n = 3 at 500 mg/kg/day and n=3 at 1 g/kg/day).

4.5 Discussion

Innate immune cells are increasingly recognised to be key regulators of myocardial healing and remodelling following MI. However, despite significant advances in the understanding of the biology of these cells, no specific therapy targeting immune cells is currently available to patients to improve cardiac remodelling post MI. One limitation of clinical translation in this field is a shortage of clinical biomarkers that could be used to assess the degree of inflammation present in individual patients, and to assess their response to treatment.

Work presented in this chapter demonstrates that high hyperpolarized [1-^{13}C]lactate signal is present in healing myocardial segments in the days following MI, and reflects macrophage driven inflammation. Although it is possible that ischaemic myocardium could also contribute to a high lactate signal, the near-normalisation of hyperpolarized [1-^{13}C]lactate signal following systemic depletion of macrophages suggests that the signal is primarily caused by inflammation. In probing the mechanisms underlying the lactate signal and macrophage activation, we show that the metabolic phenotype of macrophages shifts towards dominant glycolysis following activation, expanding the intracellular lactate pool and subsequent hyperpolarized [1-^{13}C]lactate signal in cell suspension experiments. These findings suggest that the high hyperpolarized [1-^{13}C]lactate signal seen post MI reflects not just the number of inflammatory cells infiltrating the tissue, but also that the signal provides fundamental information about the inflammatory phenotype of the cells. Finally, testing potential therapeutic relevance, specific targeting of macrophage glycolysis using the glycolytic inhibitor 2-DG significantly attenuated both the hyperpolarized [1-^{13}C]lactate signal in injured myocardial segments and also modified inflammatory cytokine production, highlighting the link between the measured [1-^{13}C]lactate signal and the biological process of wound healing. Ethical approval has subsequently been granted for a pilot study to

investigate hyperpolarized [1-^{13}C]lactate production in patients following myocardial infarction.

4.5.1 Mechanisms of macrophage activation in MI

The mechanisms underlying the activation of macrophages infiltrating the myocardium following MI remain to be fully elucidated. Recently, circulating monocytes (the precursors of macrophages) were shown to be 'pre-programmed' with distinct transcriptional profiles following MI in both patients and mice[10]. A preliminary retrospective analysis of transcriptome data from monocytes in this study however did not indicate significant regulation of key glycolytic genes (N Ruparelia, personal communication). This suggests that in addition to pre-programming, further monocyte activation and differentiation to a final inflammatory phenotype occurs within the myocardium, which is likely to be driven by local signals. Although the precise mechanisms remain to be determined, one key candidate mechanism is macrophage toll like receptor (TLR) activation.

4.5.1.1 TLRs in MI

A family of cell surface receptors called pattern recognition receptors (PRRs) are the primary means by which the innate immune system detects molecules unique to foreign microbes[56, 57]. PRRs formed the basis of what was initially classified as 'self' versus 'non-self' differentiation, a model proposed by Burnet to explain the specificity of the healthy immune response to pathogens, but not self[58]. PRRs include TLRs, nod-like receptors and glycation end product receptors and a family of 10 human TLRs have now been identified[59]. Although an immunological model in which PRRs recognise unique microbial epitopes (termed pathogen associated molecular patterns, PAMPs) and initiate inflammatory signalling pathways is consistent with the appropriate response to infection in healthy

people, this model would not explain the presence of significant inflammation in a sterile MI, where no microbial products would usually be present.

A new paradigm of innate immunity was proposed by Matzinger in the 1990s, in which the innate immune system does not simply differentiate on the basis of 'self' and 'non-self' but rather recognises immunological 'danger'[60, 61]. According to the 'danger model', the innate immune system recognises not just microbial PAMPs, but also host intracellular molecules to which the immune system is not normally exposed. This may reflect an evolutionary adaptation to minimise the risk of infection in superficial injury, though the innate immune system also has a crucial role in tissue and wound healing.

In the *in vitro* aspects of work in this chapter, LPS was used as an immunologic 'danger' signal to activate macrophages and polarise them to an inflammatory phenotype. LPS is primarily an agonist of TLR4, which is one of the best studied TLRs in MI and is recognised as an important mediator of myocardial wound healing[62, 63]. The precise danger signals responsible for activating/polarising macrophages in the injured myocardium are of interest to several groups[64], and it may be that TLRs other than TLR4 are important in the post MI inflammatory response. This could be investigated in future work by comparing the transcriptomic profiles of quiescent splenic monocytes, of circulating monocytes during MI, and cardiac post MI monocytes/macrophages. Adoptive transfer techniques using specific TLR deletion in macrophages could also help to determine precisely the key signals and receptors leading to macrophage activation (and high hyperpolarized [1-^{13}C]lactate signal) post MI.

4.5.2 Clinical translational challenges and opportunities of inflammation imaging

Hyperpolarized MRI offers a number of potential advantages over current imaging technologies for the assessment of post-MI cardiac inflammation. Current ^{1}H CMR

imaging techniques show high T_1 and T_2 signal in the days following myocardial infarction due to high water content, reflecting myocardial oedema and collagen deposition[65]. However, conflicting findings regarding the kinetics of T_2 signal over the first week following MI have been reported. Although traditionally thought to provide a stable index of the total myocardial area-at-risk[66], porcine studies from the laboratory of Fuster report a biphasic T_2 signal response with high signal in the hours following reperfusion which fell before the arrival of a second peak at day 7[29]. However, whilst systemic administration of corticosteroids significantly reduced the inflammatory cell count at day 7, they did not change myocardial T_2 signal[30]. These findings suggest that an array of processes, including reperfusion injury, collagen deposition, and oedema, contribute significantly to the measured T_2 signal, which therefore lacks sensitivity to inflammatory cell count. T_1/T_2 signal and hyperpolarized [1-^{13}C]lactate production may therefore provide complementary information about myocardial healing processes, reflecting both inflammatory cell count and also the tissue composition of the underlying myocardium.

^{18}FDG PET studies show high tracer uptake in healing myocardium at day 5, which is attenuated by immunosuppression[31]. It is likely that this signal has a similar biological basis to the processes leading to high [1-^{13}C]lactate signal, though hyperpolarized MR arguably offers several advantages over PET in this setting. Firstly, all cardiac ^{18}FDG PET studies are challenging as normal myocardium has high glucose uptake which can obscure signal resulting from the inflammatory processes of interest. As a result, high ^{18}FDG uptake was initially not detected in the hearts of mice post MI [31], requiring an alternative anaesthesia protocol to suppress the background signal from myocardial glucose uptake. Most cardiac ^{18}FDG PET clinical protocols advocate suppression of myocardial carbohydrate metabolism using high fat drinks, heparin administration and fasting, but these measures may also suppress glucose uptake in inflammatory cells. The safety of suppression of cardiac

glucose metabolism post MI is also uncertain, as glucose metabolism is thought to be relatively oxygen sparing[67]. Furthermore, the high radiation dose of ^{18}FDG PET precludes serial studies in human participants. Finally, hyperpolarized MR offers quicker acquisition times than PET: the hyperpolarized MR acquisitions in this study were performed in 2 minutes, whereas cardiac PET acquisitions normally require 30 - 90 minutes.

One further strength of hyperpolarized MR is its unusual suitability for use across all three major biological model systems (cells, animal models and humans). This offers the opportunity for investigators to design imaging experiments in which both a high degree of mechanistic insight and also clinical relevance can be established to provide mutually supportive findings Figure 4.22). In this study, the cell based assays provided complementary mechanistic information to the rodent findings, and future pilot clinical work may provide validation of rodent models.

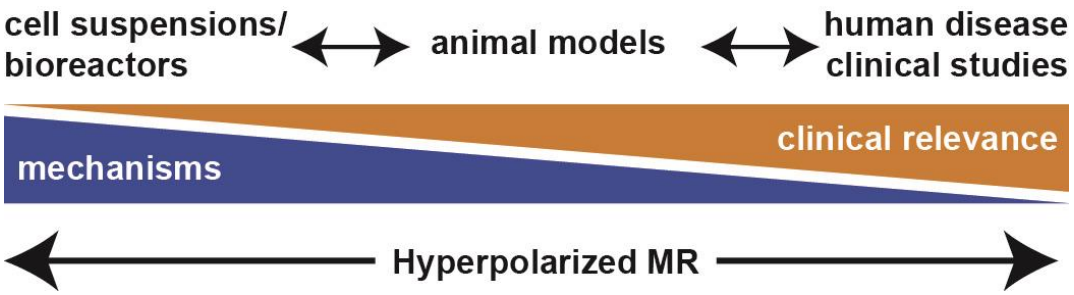


Figure 4.22: Potential role of hyperpolarized MR in translational research across all three major model systems.

4.5.3 Technical developments in hyperpolarized MRI of inflammation

This study highlighted several technical limitations with our current preclinical MR hardware, which could be overcome for future studies. Firstly, ^{13}C surface coil inhomogeneity is likely to have contributed to apparently lower signal acquired from regions of the heart further from the coil. Although a new ^{13}C volume coil has since been acquired (Figure 4.23), the sensitivity of this coil was not sufficient for imaging in these

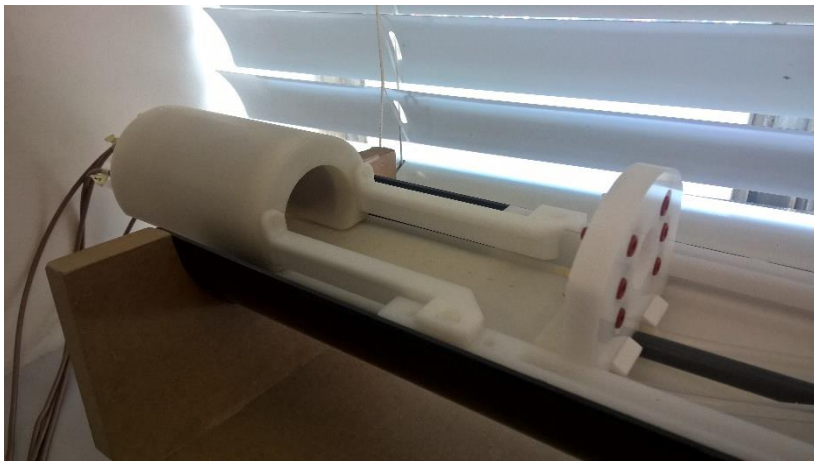


Figure 4.23: New ^{13}C coil to improve homogeneity in future preclinical imaging studies.

studies, and the effect of inhomogeneity was controlled for experimentally by the use of the cryoinjury model to cause reproducible antero-apical injury (where coverage is good). Work in underway to install a series of pre-amplifiers to the ^{13}C coil to improve sensitivity.

Rapid ^{13}C imaging sequences using echo planar imaging require high gradient field strength and slew rates to optimise spatial resolution. The current gradient set is suboptimal and was one factor which contributed to a spatial resolution of approximately 1 x 1 x 3 mm for ^{13}C imaging. Nevertheless, this resolution remains comparable with preclinical PET imaging, and the resolution of hyperpolarized MR may in future begin to exceed the theoretical limits of PET[68].

Finally, we did not perform late gadolinium enhancement imaging in this study as pilot work suggested that insufficient RF power was available to generate the inversion pulses necessary for phase-sensitive inversion recovery sequences. LGE would have been valuable as an additional indicator of infarct size and location and would have enabled more precise co-registration of lactate signals and infarct area. This could be included in future studies following an upgrade of the RF amplifier.

4.5.4 Clinical applications of hyperpolarized MR inflammation imaging

The finding that administration of 2-DG following myocardial infarction suppresses both hyperpolarized [1-^{13}C]lactate signal and also inflammatory cytokine expression in infarcts highlights a potential role for hyperpolarized MR as a surrogate end-point of efficacy in dose ranging and phase II studies of novel therapies that target cardiac inflammation. For example, if a new molecule is thought to be active through selective suppression of inflammatory cytokine production in healing myocardium, hyperpolarized MR could be used to demonstrate the minimum dose needed to cause an effect in small pilot studies, thus reducing the costs of development and improving the probability of success at phase III[69]. Several molecules are under development for this indication, though 2-DG, whilst useful for proof-of-concept studies in animal models, is unlikely to be a viable candidate for human studies on account of its narrow therapeutic window and complex pharmacodynamics. However, drugs such as losmapimod, a p38 mitogen activated protein (MAP) kinase inhibitor with potent anti-inflammatory effects, or recombinant VEGF-c may well benefit from such an approach. Losmapimod substantially reduced infarct size in a phase II trial in myocardial infarction with ST segment elevation (STEMI)[70], but did not show a beneficial effect in an early phase III trial in which patients with both STEMI and NSTEMI were included[71], though an efficacy signal in STEMI persisted. These findings highlight that cardiac immunomodulatory therapies may need to individualised to provide optimal outcomes.

4.5.5 Limitations

In the cell experiments presented in this study, no experiments to determine the effect of 2-deoxyglucose upon cells which had not been activated with lipopolysaccharide were performed. This could be investigated in future experiments.

4.5.6 Conclusions

Work presented in this chapter demonstrates that high [1-^{13}C]lactate signal observed in healing myocardium at day 3 and 7 following MI reflects macrophage driven inflammation. Activation of quiescent macrophages using LPS induces a transcriptional programme that markedly increases key glycolytic genes, leading to high glycolytic rate and expansion in the intracellular lactate pool that is likely to be the mechanistic basis for the increase in [1-^{13}C]lactate signal. This glycolytic gene programme was also shown to be essential for the production of the key proinflammatory cytokine IL-1β. Specific targeting of the lactate signal with glycolytic inhibitors post MI attenuated myocardial inflammation, highlighting a fundamental link between the [1-^{13}C]lactate signal and wound healing biology. These findings suggest that hyperpolarized MR could provide a novel method for the assessment of cardiac inflammation, with significant potential advantages over current imaging strategies.

4.6 Appendix 4A: Methods

4.6.1 Myocardial infarction

All procedures were performed in collaboration with Prof Carolyn Carr. Anaesthesia was induced in female Wistar rats using 4 % isoflurane in medical oxygen, the trachea was intubated and the lungs ventilated, and a left thoracotomy performed. In initial experiments using ischaemia reperfusion injury, a polyethylene tube was sutured across the left anterior descending coronary artery for 40 minutes and removed. In subsequent experiments using the cryoinjury method, the heart was exteriorised and a 9 mm aluminium cryoprobe cooled to the temperature of liquid nitrogen applied to the antero-apical myocardium for 15 seconds. The chest was closed in layers and analgesia provided with meloxicam and buprenorphine.

4.6.2 Macrophage depletion

Clodronate liposomes were supplied by N van Rooijen (Haarlem, The Netherlands). The dose used was 0.1 ml / 100 g body weight, which was administered by intravenous injection following cryoinjury.

4.6.3 Hyperpolarized MR imaging

[1-^{13}C]pyruvic acid was hyperpolarized using a prototype hyperpolarizer according to the method described fully in Appendix 2A (page 101). Hyperpolarized magnetic resonance imaging was performed in collaboration with Dr Jack Miller using a 7 T MR system. Full details of the design and operation of this ^{13}C imaging sequence have been previously published[72]. A custom designed analysis workflow was designed by Dr Miller; this package uses a modified Markov Chain Monte Carlo method with adaptive sampling and delayed rejection to return regional [1-^{13}C]lactate label rate constants which discriminate between signal and noise and control for spatial variation introduced by the use of a surface coil.

4.6.4 Flow cytometry

4.6.4.1 Creation of cell suspensions

Following perfusion with 50 ml cold Hanks' balanced salt solution (HBSS) to remove circulating immune cells, hearts were isolated and the infarcted region was excised from the heart, including the border zone. The mass of both the remote and infarct segments was recorded prior to trituration using surgical scissors. The resulting fine tissue fragments underwent digestion in a collagenase II solution (500 units/ml in Hanks' balanced salt solution) for 30 minutes at 37 °C with intermittent agitation. The digestion reaction was terminated by the addition of cold HBSS; the resulting mixture was passed through a 70 μm mesh filter. The filtered cell suspension was washed and the cells resuspended at a concentration of approximately 2 x10^7 cells per ml following a semi-automated cell count.

Splenic tissue

Spleens were passed through a 70 μm mesh filter and red blood cells lysed by incubation for 2 minutes in a hypotonic lysis solution (Insight Biotechnology Ltd.) at 37 °C. The lysis reaction was terminated by the addition of cold HBSS and cells within the resulting mixture resuspended at approximately 2 x 10^7 cells per ml following a semi-automated cells count.

4.6.4.2 Antibody staining

1 x 10^6 cells from either heart or spleen were incubated with 1 μl mouse anti-rat CD32 to minimise non-specific binding of Fc expressing cells. Cells were stained with 1 μl Zombie Violet™ Live/Dead for 20 minutes at 4 °C, prior to further staining with the antibody cocktail for 30 minutes at 4 °C. Cells were washed twice, resuspended in 1 ml flow cytometry buffer (HBSS with 10 mM 4-(2-hydroxyethyl)-1-piperazineethanesulfonic acid (HEPES) and 2% FBS) and analysed immediately.

4.6.4.3 Flow cytometry

Flow cytometric experiments were performed using instruments located at the flow cytometry core facility at the Sir William Dunn School of Pathology, University of Oxford. For cytometric experiments, cell suspensions were analysed using either a Beckman Coulter CyAn™ flow cytometer or a MoFlo® Astrios™ cell sorter. Compensation was adjusted manually using single colour controls or in accordance with the principle of fluorescence minus one (FMO) where necessary. Gating strategies are provided in the relevant section of this chapter. Excellent technical support from Nigel Rust with the development of these experiments is gratefully acknowledged.

4.6.5 Cell culture

RAW264.7 cells were supplied by ATCC® and maintained in RPMI-1640 medium supplemented with 10 % foetal bovine serum at 37 ^{o}C and 5 % CO_2 using either 75 ml or 175 ml tissue culture flasks (Corning Life Sciences, Arizona, US). Cells were passaged when they reached > 70 % confluency.

To create primary spleen derived macrophages, mouse spleens were passed through a 70 μm mesh filter and red blood cells lysed by incubation for 2 minutes in a hypotonic lysis solution (Insight Biotechnology). The resulting splenocytes were washed and plated at 4-6 x10^6 cells per well of a 6 well plate. Culture medium was RPMI-1640 medium supplemented with 10% FBS, 5 ng/ml M-CSF and 1 % penicillin/streptomycin. Non-adherent cells were removed and the medium changed every other day. Experiments were performed upon cells at day 6.

Lipopolysaccharides derived from Escherichia Coli were supplied by Sigma and were used at 1 μg/ml. 2-DG was also supplied by Sigma and was used at a final concentration of 1mM

following pilot dose ranging experiments which demonstrated effective suppression of lactate production and minimal cytotoxicity.

4.6.6 Hyperpolarized MR in cell suspensions

Pyruvic acid and radical (5 µl) was mixed with gadolinium (0.5 µl of 1:50 gadoterate meglumine) and hyperpolarized for 30 minutes using a HyperSense™ hyperpolarizer. RAW264.7 cells were detached from culture flask using Accutase® cell detachment solution (BioLegend®) and washed prior to a semi-automated cell count and resuspension at a concentration of 8 x 10^7 cells in 1 ml medium at 37 °C. The cell suspension was added to an NMR tube and placed in an 11.7 T magnet. Warm air was blown across the tube to maintain a sample temperature of approximately 37 °C. Hyperpolarized [1-^{13}C]pyruvate solution was then produced by dissolution of the pyruvic acid using 4.5 ml Tris/NaOH buffer. 1 ml of the resulting solution was mixed with the cell suspension by injection through a polyethylene tube. The time between cell resuspension and dissolution was approximately 5 minutes. ^{13}C NMR signals were acquired over 1 minute.

4.6.7 qPCR

Approximately 30 mg heart tissue was homogenised in RLT lysis buffer (QIAGEN) and RNA extracted using RNeasy mini columns (Qiagen). The integrity of the extracted RNA was confirmed by NanoDrop™ spectrophotometry (Thermo Scientific); all samples had A_{260}:A_{280} ratio of > 2. RNA was reverse transcribed using a high-capacity cDNA reverse transcription kit (Thermo Scientific).

TaqMan® primers were used in 20 µl qPCR reactions which were run in duplicate using a StepOnePlus™ qPCR system (Thermo Scientific). Gene expression was normalised to expression of 18s RNA (RAW264.7 or primary spleen derived macrophage studies) or 45s

pre-ribosomal RNA (Rn03928990_g1, rat tissues) and expressed according to the $2^{-\Delta\Delta CT}$ method. Details of the gene expression assays used are provided in Table 4.4.

Gene symbol	Gene name	TaqMan® assay identity
Pkm	Pyruvate kinase	Mm00834102_gH
Ldha	Lactate dehydrogenase	Mm01612132_g1
Pdk1	Pyruvate dehydrogenase kinase 1	Mm00554300_m1
Pfkfb3	6-phosphofructo-2-kinase	Mm00504650_m1
IL1b	Interleukin 1β	Mm00434228_m1
IL6	Interleukin 6	Mm00446190_m1
hif1A	Hypoxia inducible factor 1	Mm00468869_m1
Rn18S	Pre-ribosomal RNA	Mm03928990_g1

Table 4.4: List of Taqman® gene expression assays used in this study.

4.6.8 Enzyme linked immunosorbent assay (ELISA)

Cells were harvested from 6-well plates using a cell scraper and resuspended in 1ml phosphate buffered saline prior to homogenisation using spin columns (Qiashredder, Qiagen). Enzyme linked immunosorbent assays were performed upon the resultant cell homogenates using assay kits according the manufacturers' instructions. IL-1β and TNF-α kits were supplied by eBioscience; an IL-6 assay kit was supplied by BioLegend®.

4.7 Appendix 4B: References

1. Thygesen K, Alpert J S, and White H D. *Universal definition of myocardial infarction.* Journal of the American College of Cardiology, 2007. 50(22): p. 2173-2195.

2. Zaman S and Kovoor P. *Sudden cardiac death early after myocardial infarction pathogenesis, risk stratification, and primary prevention.* Circulation, 2014. 129(23): p. 2426-2435.

3. Bursi F, Enriquez-Sarano M, Nkomo V T, Jacobsen S J, Weston S A, Meverden R A, and Roger V L. *Heart failure and death after myocardial infarction in the community the emerging role of mitral regurgitation.* Circulation, 2005. 111(3): p. 295-301.

4. Opie L H, Commerford P J, Gersh B J, and Pfeffer M A. *Controversies in ventricular remodelling.* The Lancet, 2006. 367(9507): p. 356-367.

5. Keeley E C, Boura J A, and Grines C L. *Primary angioplasty versus intravenous thrombolytic therapy for acute myocardial infarction: a quantitative review of 23 randomised trials.* The Lancet, 2003. 361(9351): p. 13-20.

6. Capricorn Investigators. *Effect of carvedilol on outcome after myocardial infarction in patients with left-ventricular dysfunction: the CAPRICORN randomised trial.* The Lancet, 2001. 357(9266): p. 1385-1390.

7. Pitt B, Remme W, Zannad F, Neaton J, Martinez F, Roniker B, Bittman R, Hurley S, Kleiman J, and Gatlin M. *Eplerenone, a selective aldosterone blocker, in patients with left ventricular dysfunction after myocardial infarction.* New England Journal of Medicine, 2003. 348(14): p. 1309-1321.

8. Schmidt M, Jacobsen J, Lash T L, Bøtker H E, and Sørensen H T. *25-year trends in first-time hospitalization for acute myocardial infarction, subsequent short-and long-term mortality, and the prognostic impact of gender and comorbidity: a Danish nationwide cohort study.* Circulation, 2011. 124(21): p. 9577-9577.

9. Smolina K, Wright F L, Rayner M, and Goldacre M J. *Determinants of the decline in mortality from acute myocardial infarction in England between 2002 and 2010: linked national database study.* BMJ, 2012. 344: p. d8059.

10. Ruparelia N, Godec J, Lee R, Chai J T, Dall'Armellina E, McAndrew D, Digby J E, Forfar J C, Prendergast B D, Kharbanda R K, Banning A P, Neubauer S, Lygate C, Channon K M, Haining W N, and Choudhury R P. *Acute myocardial infarction activates distinct inflammation and proliferation pathways in circulating monocytes, prior to recruitment, and identified through conserved transcriptional responses in mice and humans.* European Heart Journal, 2015. 36(29): p. 1923-1934.

11. Swirski F K and Nahrendorf M. *Leukocyte behavior in atherosclerosis, myocardial infarction, and heart failure.* Science, 2013. 339(6116): p. 161-166.

12. Nahrendorf M and Swirski F K. *Monocyte and macrophage heterogeneity in the heart.* Circulation Research, 2013. 112(12): p. 1624-1633.

13. Fishbein M C, Maclean D, and Maroko P R. *The histopathologic evolution of myocardial infarction.* Chest, 1978. 73(6): p. 843-849.

14. Maclean D, Fishbein M C, Braunwald E, and Maroko P R. *Long-term preservation of ischemic myocardium after experimental coronary artery occlusion.* Journal of Clinical Investigation, 1978. 61(3): p. 541.

15. Bulkley B H and Roberts W C. *Steroid therapy during acute myocardial infarction: a cause of delayed healing and of ventricular aneurysm.* The American Journal of Medicine, 1974. 56(2): p. 244-250.

16. Roberts R, DeMello V, and Sobel B. *Deleterious effects of methylprednisolone in patients with myocardial infarction.* Circulation, 1976. 53(3): p. 204-6.

17. Giugliano G R, Giugliano R P, Gibson C M, and Kuntz R E. *Meta-analysis of corticosteroid treatment in acute myocardial infarction.* The American Journal of Cardiology, 2003. 91(9): p. 1055-1059.

18. Nahrendorf M, Swirski F K, Aikawa E, Stangenberg L, Wurdinger T, Figueiredo J-L, Libby P, Weissleder R, and Pittet M J. *The healing myocardium sequentially mobilizes two monocyte subsets with divergent and complementary functions.* The Journal of Experimental Medicine, 2007. 204(12): p. 3037-3047.

19. Frangogiannis N G, Smith C W, and Entman M L. *The inflammatory response in myocardial infarction.* Cardiovascular Research, 2002. 53(1): p. 31-47.

20. Ren G, Dewald O, and Frangogiannis N G. *Inflammatory mechanisms in myocardial infarction.* Current Drug Targets - Inflammation & Allergy, 2003. 2(3): p. 242-256.

21. Dewald O, Zymek P, Winkelmann K, Koerting A, Ren G, Abou-Khamis T, Michael L H, Rollins B J, Entman M L, and Frangogiannis N G. *CCL2/monocyte chemoattractant protein-1 regulates inflammatory responses critical to healing myocardial infarcts.* Circulation Research, 2005. 96(8): p. 881-889.

22. Swirski F K, Nahrendorf M, Etzrodt M, Wildgruber M, Cortez-Retamozo V, Panizzi P, Figueiredo J-L, Kohler R H, Chudnovskiy A, and Waterman P. *Identification of splenic reservoir monocytes and their deployment to inflammatory sites.* Science, 2009. 325(5940): p. 612-616.

23. van Amerongen M J, Harmsen M C, van Rooijen N, Petersen A H, and van Luyn M J. *Macrophage depletion impairs wound healing and increases left ventricular remodeling after myocardial injury in mice.* The American Journal of Pathology, 2007. 170(3): p. 818-829.

24. Sager H B, Heidt T, Hulsmans M, Dutta P, Courties G, Sebas M, Wojtkiewicz G R, Tricot B, Iwamoto Y, and Sun Y. *Targeting Interleukin-1β Reduces Leukocyte Production After Acute Myocardial Infarction.* Circulation, 2015. 132(20): p. 1880-1890.

25. Bujak M, Dobaczewski M, Gonzalez-Quesada C, Xia Y, Leucker T, Zymek P, Veeranna V, Tager A M, Luster A D, and Frangogiannis N G. *Induction of the CXC*

chemokine interferon-γ-inducible protein 10 regulates the reparative response following myocardial infarction. Circulation Research, 2009. 105(10): p. 973-983.

26. Leuschner F, Dutta P, Gorbatov R, Novobrantseva T I, Donahoe J S, Courties G, Lee K M, Kim J I, Markmann J F, and Marinelli B. *Therapeutic siRNA silencing in inflammatory monocytes in mice.* Nature Biotechnology, 2011. 29(11): p. 1005-1010.

27. Klotz L, Norman S, Vieira J M, Masters M, Rohling M, Dubé K N, Bollini S, Matsuzaki F, Carr C A, and Riley P R. *Cardiac lymphatics are heterogeneous in origin and respond to injury.* Nature, 2015. 522(7554): p. 62-67.

28. Menon V, Lessard D, Yarzebski J, Furman M I, Gore J M, and Goldberg R J. *Leukocytosis and adverse hospital outcomes after acute myocardial infarction.* The American Journal of Cardiology, 2003. 92(4): p. 368-372.

29. Fernández-Jiménez R, Sánchez-González J, Agüero J, García-Prieto J, López-Martín G J, García-Ruiz J M, Molina-Iracheta A, Rosselló X, Fernández-Friera L, and Pizarro G. *Myocardial edema after ischemia/reperfusion is not stable and follows a bimodal pattern: imaging and histological tissue characterization.* Journal of the American College of Cardiology, 2015. 65(4): p. 315-323.

30. Fernández-Jiménez R, García-Prieto J, Sánchez-González J, Agüero J, López-Martín G J, Galán-Arriola C, Molina-Iracheta A, Doohan R, Fuster V, and Ibáñez B. *Pathophysiology underlying the bimodal edema phenomenon after myocardial ischemia/reperfusion.* Journal of the American College of Cardiology, 2015. 66(7): p. 816-828.

31. Lee W W, Marinelli B, van der Laan A M, Sena B F, Gorbatov R, Leuschner F, Dutta P, Iwamoto Y, Ueno T, and Begieneman M P. *PET/MRI of inflammation in myocardial infarction.* Journal of the American College of Cardiology, 2012. 59(2): p. 153-163.

32. Kim J W, Tchernyshyov I, Semenza G L, and Dang C V. *HIF-1-mediated expression of pyruvate dehydrogenase kinase: a metabolic switch required for cellular adaptation to hypoxia.* Cell Metabolism, 2006. 3(3): p. 177-185.

33. Tannahill G, Curtis A, Adamik J, Palsson-McDermott E, McGettrick A, Goel G, Frezza C, Bernard N, Kelly B, and Foley N. *Succinate is an inflammatory signal that induces IL-1β through HIF-1α.* Nature, 2013. 496(7444): p. 238-242.

34. Schroeder M A, Cochlin L E, Heather L C, Clarke K, Radda G K, and Tyler D J. *In vivo assessment of pyruvate dehydrogenase flux in the heart using hyperpolarized carbon-13 magnetic resonance.* Proceedings of the National Academy of Sciences, 2008. 105(33): p. 12051-12056.

35. Schroeder M A, Clarke K, Neubauer S, and Tyler D J. *Hyperpolarized magnetic resonance: a novel technique for the in vivo assessment of cardiovascular disease.* Circulation, 2011. 124(14): p. 1580-1594.

36. Lygate C. *Surgical models of hypertrophy and heart failure: Myocardial infarction and transverse aortic constriction.* Drug Discovery Today: Disease Models, 2006. 3(3): p. 283-290.

37. González-Rosa J M, Martín V, Peralta M, Torres M, and Mercader N. *Extensive scar formation and regression during heart regeneration after cryoinjury in zebrafish.* Development, 2011. 138(9): p. 1663-1674.

38. González-Rosa J M and Mercader N. *Cryoinjury as a myocardial infarction model for the study of cardiac regeneration in the zebrafish.* Nature Protocols, 2012. 7(4): p. 782-788.

39. van den Bos E J, Mees B M, de Waard M C, de Crom R, and Duncker D J. *A novel model of cryoinjury-induced myocardial infarction in the mouse: a comparison with coronary artery ligation.* American Journal of Physiology - Heart and Circulatory Physiology, 2005. 289(3): p. 1291-1300.

40. Shapiro H M. *Practical flow cytometry.* 2005: John Wiley & Sons.

41. Pinto A R, Chandran A, Rosenthal N A, and Godwin J W. *Isolation and analysis of single cells from the mouse heart.* Journal of Immunological Methods, 2013. 393(1-2): p. 74-80.

42. Rose S, Misharin A, and Perlman H. *A novel Ly6C/Ly6G-based strategy to analyze the mouse splenic myeloid compartment.* Cytometry Part A, 2012. 81(4): p. 343-350.

43. Campanella M, Sciorati C, Tarozzo G, and Beltramo M. *Flow cytometric analysis of inflammatory cells in ischemic rat brain.* Stroke, 2002. 33(2): p. 586-592.

44. Dijkstra C, Döpp E, Van Den Berg T, and Damoiseaux J. *Monoclonal antibodies against rat macrophages.* Journal of Immunological Methods, 1994. 174(1): p. 21-23.

45. Robinson A, White T, and Mason D. *Macrophage heterogeneity in the rat as delineated by two monoclonal antibodies MRC OX-41 and MRC OX-42, the latter recognizing complement receptor type 3.* Immunology, 1986. 57(2): p. 239.

46. Ahuja V, Miller S E, and Howell D N. *Identification of two subpopulations of rat monocytes expressing disparate molecular forms and quantities of CD43.* Cellular Immunology, 1995. 163(1): p. 59-69.

47. Yamazaki T, Seko Y, Tamatani T, Miyasaka M, Yagita H, Okumura K, Nagai R, and Yazaki Y. *Expression of intercellular adhesion molecule-1 in rat heart with ischemia/reperfusion and limitation of infarct size by treatment with antibodies against cell adhesion molecules.* The American Journal of Pathology, 1993. 143(2): p. 410.

48. Barnett-Vanes A, Sharrock A, Birrell M A, and Rankin S. *A single 9-colour flow cytometric method to characterise major leukocyte populations in the rat: validation in a model of LPS-induced pulmonary inflammation.* PloS ONE, 2016. 11(1): p. e0142520.

49. Telford W G, Babin S A, Khorev S V, and Rowe S H. *Green fiber lasers: An alternative to traditional DPSS green lasers for flow cytometry.* Cytometry Part A, 2009. 75(12): p. 1031-1039.

50. van Rooijen N and van Kesteren-Hendrikx E. *Clodronate liposomes: perspectives in research and therapeutics.* Journal of Liposome Research, 2002. 12(1-2): p. 81-94.

51. Gallagher F A, Kettunen M I, Hu D-E, Jensen P R, Karlsson M, Gisselsson A, Nelson S K, Witney T H, Bohndiek S E, and Hansson G. *Production of hyperpolarized [1, 4-$^{13}C_2$] malate from [1, 4-$^{13}C_2$] fumarate is a marker of cell necrosis and treatment response in tumors.* Proceedings of the National Academy of Sciences, 2009. 106(47): p. 19801-19806.

52. Harris T, Eliyahu G, Frydman L, and Degani H. *Kinetics of hyperpolarized $^{13}C_1$-pyruvate transport and metabolism in living human breast cancer cells.* Proceedings of the National Academy of Sciences, 2009. 106(43): p. 18131-18136.

53. Breukels V, Jansen K, Heijster F H, Capozzi A, Bentum P J M, Schalken J A, Comment A, and Scheenen T W. *Direct dynamic measurement of intracellular and extracellular lactate in small-volume cell suspensions with ^{13}C hyperpolarised NMR.* NMR in Biomedicine, 2015. 28(8): p. 1040-1048.

54. Zierhut M L, Yen Y-F, Chen A P, Bok R, Albers M J, Zhang V, Tropp J, Park I, Vigneron D B, and Kurhanewicz J. *Kinetic modeling of hyperpolarized $^{13}C_1$-pyruvate metabolism in normal rats and TRAMP mice.* Journal of Magnetic Resonance, 2010. 202(1): p. 85-92.

55. Wang C, Yu X, Cao Q, Wang Y, Zheng G, Tan T K, Zhao H, Zhao Y, Wang Y, and Harris D C. *Characterization of murine macrophages from bone marrow, spleen and peritoneum.* BMC Immunology, 2013. 14(1): p. 1.

56. Medzhitov R and Janeway C A. *Decoding the patterns of self and nonself by the innate immune system.* Science, 2002. 296(5566): p. 298-300.

57. Janeway C A and Medzhitov R. *Innate immune recognition.* Annual Review of Immunology, 2002. 20(1): p. 197-216.

58. Burnet F M. *Immunological recognition of self.* Science, 1961. 133(3449): p. 307-311.

59. Takeda K, Kaisho T, and Akira S. *Toll-like receptors.* Annual Review of Immunology, 2003. 21(1): p. 335-376.

60. Matzinger P. *Tolerance, danger, and the extended family.* Annual review of immunology, 1994. 12(1): p. 991-1045.

61. Matzinger P. *The danger model: a renewed sense of self.* Science, 2002. 296(5566): p. 301-305.

62. Timmers L, Sluijter J P, van Keulen J K, Hoefer I E, Nederhoff M G, Goumans M-J, Doevendans P A, van Echteld C J, Joles J A, and Quax P H. *Toll-like receptor 4 mediates*

maladaptive left ventricular remodeling and impairs cardiac function after myocardial infarction. Circulation Research, 2008. 102(2): p. 257-264.

63. Oyama J-i, Blais C, Liu X, Pu M, Kobzik L, Kelly R A, and Bourcier T. *Reduced myocardial ischemia-reperfusion injury in toll-like receptor 4-deficient mice.* Circulation, 2004. 109(6): p. 784-789.

64. De Haan J, Smeets M, Pasterkamp G, and Arslan F. *Danger signals in the initiation of the inflammatory response after myocardial infarction.* Mediators of Inflammation, 2013. 2013.

65. Ferreira V M, Piechnik S K, Dall'Armellina E, Karamitsos T D, Francis J M, Choudhury R P, Friedrich M G, Robson M D, and Neubauer S. *Non-contrast T1-mapping detects acute myocardial edema with high diagnostic accuracy: a comparison to T2-weighted cardiovascular magnetic resonance.* Journal of Cardiovascular Magnetic Resonance, 2012. 14(42): p. 1.

66. Aletras A H, Tilak G S, Natanzon A, Hsu L-Y, Gonzalez F M, Hoyt R F, and Arai A E. *Retrospective determination of the area at risk for reperfused acute myocardial infarction with T2-weighted cardiac magnetic resonance imaging histopathological and displacement encoding with stimulated echoes (DENSE) functional validations.* Circulation, 2006. 113(15): p. 1865-1870.

67. Mehta S R, Yusuf S, Díaz R, Zhu J, Pais P, Xavier D, Paolasso E, Ahmed R, Xie C, and Kazmi K. *Effect of glucose-insulin-potassium infusion on mortality in patients with acute ST-segment elevation myocardial infarction: the CREATE-ECLA randomized controlled trial.* JAMA, 2005. 293(4): p. 437-446.

68. Levin C S and Hoffman E J. *Calculation of positron range and its effect on the fundamental limit of positron emission tomography system spatial resolution.* Physics in Medicine and Biology, 1999. 44(3): p. 781.

69. Matthews P M, Rabiner I, and Gunn R. *Non-invasive imaging in experimental medicine for drug development.* Current Opinion in Pharmacology, 2011. 11(5): p. 501-507.

70. Newby L K, Marber M S, Melloni C, Sarov-Blat L, Aberle L H, Aylward P E, Cai G, De Winter R J, Hamm C W, and Heitner J F. *Losmapimod, a novel p38 mitogen-activated protein kinase inhibitor, in non-ST-segment elevation myocardial infarction: a randomised phase 2 trial.* The Lancet, 2014. 384(9949): p. 1187-1195.

71. O'Donoghue M L, Glaser R, Cavender M A, Aylward P E, Bonaca M P, Budaj A, Davies R Y, Dellborg M, Fox K A, and Gutierrez J A T. *Effect of losmapimod on cardiovascular outcomes in patients hospitalized with acute myocardial infarction: a randomized clinical trial.* JAMA, 2016. 315(15): p. 1591-1599.

72. Miller J J, Lau A Z, Teh I, Schneider J E, Kinchesh P, Smart S, Ball V, Sibson N R, and Tyler D J. *Robust and high resolution hyperpolarized metabolic imaging of the rat heart at 7T with 3D spectral-spatial EPI.* Magnetic Resonance in Medicine, 2015.

This page is intentionally left blank

Chapter 5: Future perspectives

5.1 Hyperpolarized cardiovascular MR: the next decade

The clinical translation of hyperpolarized magnetic resonance using dynamic nuclear polarization from a simple, brilliant idea to initial human studies has proved to be more challenging than was anticipated by any of the leading figures in the field. In particular, the manufacture of sterile fluid paths has been, and to some extent remains, the surprise rate-limiting step. Nevertheless, there are strong grounds for a belief that hyperpolarized MR will be a disruptive technology in medical imaging, with broad and clinically relevant applications across cardiovascular science, metabolic disease, oncology, immuno-inflammation, and beyond. There is perhaps potential for 10-year adoption across academic health science centres on a scale comparable with PET. The keys to achieving success on this scale will be the judicious development of key clinical applications for [1-^{13}C]pyruvate, and, in parallel, a renewed focus upon the development of the next generation of hyperpolarization molecules and hardware.

5.1.1 Hyperpolarized [1-^{13}C]pyruvate as a clinical tool

Initial studies using any new imaging technology should arguably be designed to establish feasibility, safety, and to provide proof-of-concept by demonstrating novel, though unsurprising, findings. With such studies now well underway in cardiovascular science, we

now need to move rapidly to a new programme of clinical studies designed to demonstrate the scenarios in which hyperpolarized MR can add meaningful value over existing imaging techniques. Hyperpolarized MR is particularly well suited to such studies in the heart, for reasons including its rapid acquisition times, the absence of ionising radiation, and the potential for detailed structural and functional cardiac assessment in the same examination.

With respect to the most prevalent cardiovascular diseases, the ability to image regional [1-^{13}C]lactate production holds real promise as a novel and fundamental marker of ischaemia in both epicardial and microvascular coronary disease, and may avoid many of the limitations of existing techniques, such as non-linear concentration/signal curves and dark-rim artefacts in first-pass GBCA perfusion imaging. In failing, pressure-loaded, and volume-loaded ventricles, serial metabolic imaging studies will provide new insights into the mechanisms underlying the transition from compensated to decompensated states, and may refine the timing and selection of clinical interventions. In cardiomyopathies, where cardiac metabolic dysregulation is increasingly recognised as an early manifestation of phenotype, regional metabolic maps may highlight previously unrecognised areas of abnormality, even prior to the development of macroscopic structural changes. In cardiovascular inflammation, [1-^{13}C]lactate imaging will assess not just post-MI inflammation, but may also become a marker of inflammation in atherosclerotic plaques, myocarditis, and surveillance of transplanted hearts.

In tandem with studies to test diagnostic performance in disease states, we also need to investigate the role of hyperpolarized [1-^{13}C]pyruvate for proof-of-mechanism studies in trials of new pharmaceuticals for metabolic diseases. Tens of promising molecules which are active at an array of newly recognised targets are currently in pipelines for obesity, diabetes, and other metabolic diseases. Given the new focus of regulatory bodies upon

effects of such drugs upon cardiovascular outcomes, there is a strong case for the use of hyperpolarized [1-^{13}C]pyruvate imaging at a relatively early stage of the development of this new generation of metabolic therapies. Prime candidate drug classes for this approach include glucagon receptor modulators and apolipoprotein mimetics (both currently at phase I/II), as well as the newer SGLT-2 inhibitors and GLP-1 mimetics, where metabolic imaging may provide insights into the mechanisms by which these drugs exert their cardiovascular benefits. These studies will require the development of new connections and collaborations between academic cardiovascular imaging scientists and drug development scientists within the pharmaceutical industry.

5.1.2 New molecules in hyperpolarized magnetic resonance

In parallel with work to define the clinical roles of [1-^{13}C]pyruvate, we also need to develop and translate the next generation of hyperpolarized substrates. Although over eighty molecules suitable for hyperpolarization and biological administration have been identified (and patent protected), many of the products of metabolism of these substrates are not biologically regulated in disease states to the same extent as [1-^{13}C]pyruvate. Ongoing preclinical work will be essential to define the most promising candidates for clinical translation.

5.1.2.1 The next generation of molecules for clinical DNP sites

In the short-medium term, the next generation of molecules for clinical hyperpolarization will include [^{13}C]urea and [2-^{13}C]pyruvate. It is likely that [^{13}C]urea will be co-polarized and co-administered with hyperpolarized [1-^{13}C]pyruvate, thus enabling an unprecedented simultaneous assessment of regional cardiac perfusion and metabolism. This approach has potential to transform strategies for the assessment of myocardial viability, and other clinical problems.

Hyperpolarized [2-^{13}C]pyruvate has high translational potential, and shares the same excellent safety profile as [1-^{13}C]pyruvate. Hyperpolarized [2-^{13}C]pyruvate will provide a unique assessment of human cardiac TCA cycle metabolism, dysregulation of which is increasingly recognised in hypertrophic and other cardiomyopathies and may represent a therapeutic target.

Looking further ahead, the extraordinarily long T_1 times of silicon nanoparticles bode well for the development of a new generation of molecular imaging agents. Methods for the conjugation of nanoparticles to antibodies are well established, and the huge signal benefits of hyperpolarization may help to overcome the currently limited MR contrast created by existing nanoparticle technologies. Major potential applications of hyperpolarized antibody conjugated nanoparticles exist in vascular disease and atherosclerosis.

As well as developing molecules, we need to redouble our collaborations with industry to inform the design of the next generation of hyperpolarization hardware and consumables. The SPINlab™ has achieved its goal of enabling hyperpolarized MR in humans, and considerations for the design of a next generation system will include a greater degree of reliability, automation, and user-friendliness. With ongoing close collaboration between development engineers and the current SPINlab™ sites, it should be possible to achieve major improvements in the usability and cost of next generation hyperpolarizers, which will be essential to open hyperpolarization to a far wider range of academic institutions than are currently invested in the technique.

5.1.2.2 New methods for hyperpolarization

The introduction of clinical hyperpolarization using dynamic nuclear polarization is shortly to be followed by clinical parahydrogen hyperpolarization. Parahydrogen hyperpolarization

is in principle capable of creating a very wide range of molecules, and the identification of the most promising agents will be a major focus of a number of research groups worldwide.

5.1.3 Conclusions

The continued development of hyperpolarized MR from a research method to a mainstream clinical tool will require a concerted effort from a growing and international group of scientists, engineers, and clinicians, as well as continued support from their research funding bodies and companies. Nevertheless, the potential to help people with cardiovascular, and other, diseases to live longer, healthier lives is substantial, providing a compelling rationale for continued research in this field.